METEOROLOGY HYDROLOGY AND WATER MANAGEMENT
IMGW-PIB Science Journal since 2013

VOL. 14 | ISSUE 1 | 2026

ISNN 2299-3835

Coupled urban-topographic interactions in a complex mountainous valley: A WRF-based evaluation of urban morphology effects on pre-monsoon temperature regimes in the Doon Valley, India

Ujjwal Kumar, Deepak Kumar

School of Environment & Natural Resources, Doon University, Dehradun, India

Vikas Singh

National Atmospheric Research Laboratory (NARL), ISRO, Tirupati, India

Abstract

In this study, we investigate the influence of urban morphology on pre-monsoon temperature regimes in the Doon Valley, a complex intermontane basin in the western Himalayas, using high-resolution (2×2 km²) Weather Research and Forecasting (WRF) model simulations for the year 2021. The model employed a threefold nested domain (18-6-2 km) configuration with National Centers for Environmental Prediction – Final Analysis (NCEP-FNL) (0.25°×0.25°) global analyses as boundary conditions. To represent the rapidly expanding built environment of Dehradun, a simulation incorporating the Urban Canopy Model with the Building Effect Parameterization (WRF-UCM-BEP) was conducted and validated against ground-based observations from both Dehradun (urbanized valley, ~640 m ASL) and Mussoorie (hill station, ~2005 m ASL). The inclusion of urban canopy physics markedly improved model performance in Dehradun, reducing mean absolute error and root mean square error by 15-20% relative to the control run and increasing correlation and agreement for ambient (2 m) air temperature ($r = 0.83 \rightarrow 0.86$; index of agreement = 0.72 → 0.78). In contrast, improvements in Mussoorie were marginal, confirming that urbanization-driven heat storage and morphology dominate thermal behavior within the valley city. The WRF-UCM-BEP simulation effectively reproduced the ambient urban heat island (UHI), with persistent nighttime warming of 1-2°C over Dehradun's city core and a more realistic diurnal cycle. The model also improved representation of the surface UHI, showing stronger spatial coherence and closer agreement with MODIS 1 km land-surface temperature patterns. Vertical diagnostics revealed that WRF-UCM-BEP improved the vertical depiction of boundary-layer structure, weakening katabatic winds (-1.5 to -2 m s^{-1}), suppressing nocturnal inversion, and capturing elevated warm layers consistent with observed mixing profiles. The results demonstrate that urban morphology exerts dominant control over both ambient and surface thermal environments in Dehradun, underscoring the importance of realistic multilayer urban-canopy parameterizations in high-resolution, nested mesoscale modeling of Himalayan cities.

Keywords

WRF model, Urban Canopy Model, Building Effect Parameterization, mountain breeze circulation, Himalayan Terrain, Urban Heat Island, High-Resolution Simulation.

Submitted 12 July 2025, revised 29 October 2025, accepted 15 December 2025

DOI: 10.26491/mhwm/215597

1. Introduction

Numerical weather prediction (NWP) models such as the Weather Research and Forecasting (WRF) model (Skamarock et al. 2019) have become indispensable tools for simulating atmospheric processes, and have been extensively used over complex mountainous terrains (Zhang et al. 2013; Karki et al. 2017; Arthur et al. 2018; Luna et al. 2020; Navale, Singh 2020; Golzio et al. 2021; Min et al. 2021; Singh et al. 2021; Zhang et al. 2022; Liu et al. 2023; Biswasharma et al. 2024). However, the performance of these models is sensitive to topography, grid size, and the choice of physical parameterization schemes,

including planetary boundary layer (PBL) schemes, microphysics, and cumulus parameterizations (Arthur et al. 2018; Navale, Singh 2020; Singh et al. 2021; Golzio et al. 2021; Liu et al. 2024; Singh et al. 2024b).

Previous studies have demonstrated the importance of high-resolution WRF simulations in improving meteorological representation in mountainous regions. For example, Zhang et al. (2013) applied a probability matching approach to correct satellite rainfall biases using WRF simulations, while Karki et al. (2017) evaluated WRF performance at multiple resolutions (25, 5, and 1 km) over the Khumbu and Rolwaling regions, highlighting that finer resolutions capture monsoonal precipitation peaks more realistically. Arthur et al. (2018) introduced topographic shading and slope effects in WRF through the Immersed Boundary Method, showing improvements in surface energy fluxes and thermally driven flows. Similarly, Luna et al. (2020) improved meteorological simulations over Bogotá by replacing the default elevation with Alos-PALSAR DEM data. These examples demonstrate that WRF's ability to represent local climate strongly depends on topographic representation and resolution.

Topographic modifications also alter atmospheric instability. For instance, Navale and Singh (2020) used WRF experiments over the Northwest Himalayas, finding that variables such as relative humidity, convective available potential energy (CAPE), and wind speed respond significantly to changes in elevation and valley representation. Golzio et al. (2021) emphasized the influence of land-use datasets on simulations over the Italian Alps, while Singh et al. (2021) showed that finer resolution reduces biases in Central Himalayan simulations compared to Ganges Valley Aerosol Experiment (GVAX) observations. More recently, Liu et al. (2023, 2024) highlighted the sensitivity of WRF precipitation to microphysics, cumulus, and Planetary Boundary Layer (PBL) schemes over the Tibetan Plateau. Collectively, these studies stress that WRF simulations over complex terrain demand careful design of physics options and boundary conditions.

Urban morphology adds another layer of complexity. The incorporation of UCM and BEP into WRF has enabled researchers to capture urban heat island (UHI) effects and altered boundary-layer processes. For example, Lin et al. (2016) demonstrated improvements in diurnal air temperature simulation over Taiwan with UCM modifications, while Gaur et al. (2021) and Silva et al. (2021) showed that multilayer urban schemes better represent wind, humidity, and temperature extremes in Ottawa and Lisbon, respectively. Bilang et al. (2022) applied WRF-UCM to Manila and found improved simulation of high-heat events, and Roukounakis et al. (2023) highlighted the statistical significance of UCM inclusion over Athens. These findings confirm that representing urban morphology is essential for simulating near-surface meteorology in cities.

Despite these advances, studies coupling WRF-UCM over complex mountainous valleys that host rapidly urbanizing cities remain scarce. Intermontane basins such as the Doon Valley in Uttarakhand, India, present a unique challenge where urban expansion interacts with steep topography and thermally driven circulation. These considerations motivate the present study, which aims to evaluate high-resolution WRF simulations (2×2 km²) over the Doon Valley, compare them with ERA5, validate them against ground-

based observations, and explicitly assess the role of urban morphology through the UCM-BEP scheme. Specifically, we test whether including urban morphology improves simulation of temperature regimes during the pre-monsoon season, when urban heat effects are climatologically strongest.

2. Methodology

2.1. Study area

The Doon Valley, in the western Himalayan region of India within the state of Uttarakhand, forms an elongated intermontane depression bordered by the Siwalik Hills to the south and the Mussoorie Range (Lesser Himalaya**)** to the north. The domain spans 29.8°N – 31.2°N and 77.2°E – 78.8°E (Fig. 1). The valley's physiographic configuration results from the tectonic interplay between the Main Boundary Thrust (MBT) and the Himalayan Frontal Fault (HFF), which created a broad synclinal basin filled with Quaternary alluvium and piedmont deposits (Valdiya 1980; Thakur, Rawat 1992). Elevation ranges from about 400 m in the southern plains to over 2000 m along the northern ridges, establishing a steep north-south gradient that strongly influences thermal stratification and wind systems.

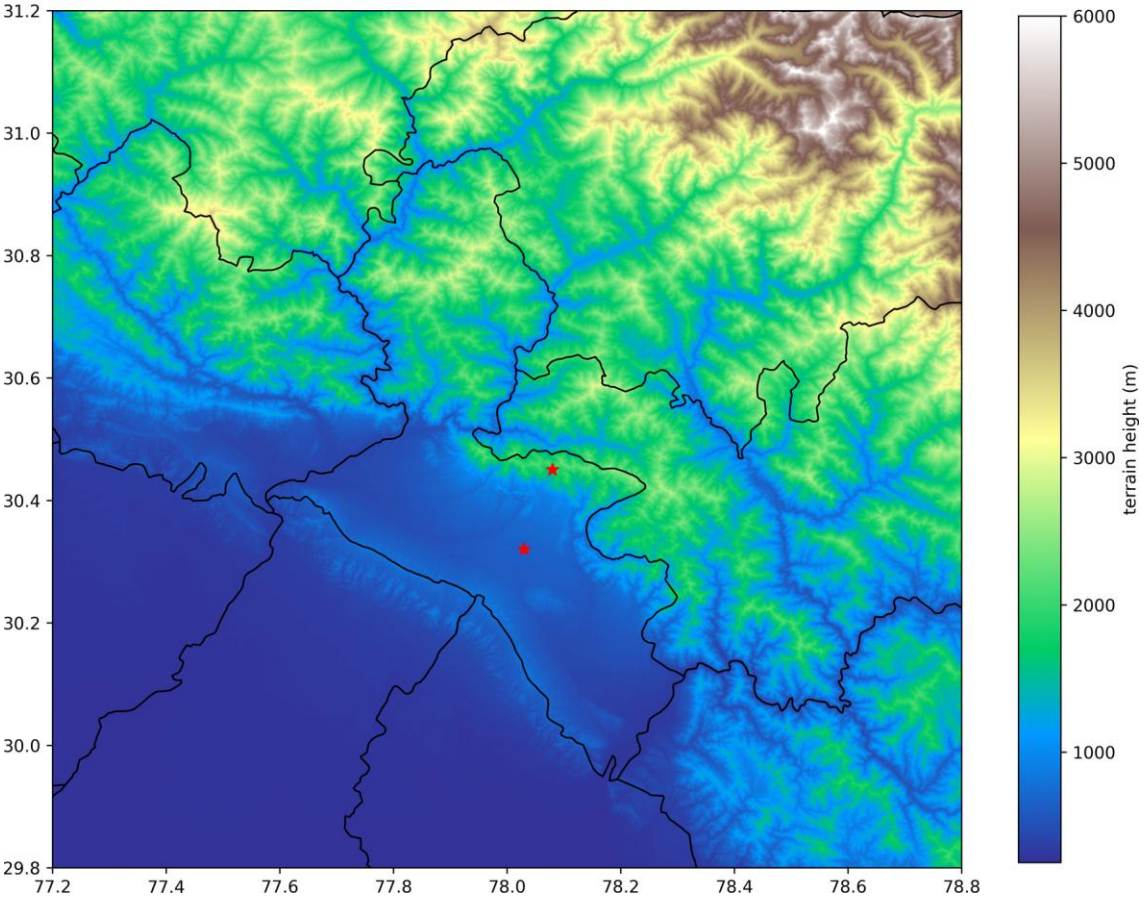

Fig. 1. Terrain of the study domain. The central area is the Dehradun district (Doon Valley area). The two red stars are the locations of IMD observation stations: Dehradun Mokhampur (30.32°N, 78.03°E, ~640 m altitude) and Mussoorie (30.45°N, 78.08°N, ~2005 m altitude). The map was prepared from the data of SRTM V3 product (SRTM Plus) provided by NASA JPL at a resolution of 1 arc-second (Farr et al. 2007).

This complex topography fosters diurnally reversing thermally driven circulations, characterized by daytime upslope (anabatic) and nighttime downslope (katabatic) winds, which play a crucial role in regulating the valley's temperature and ventilation (Karki et al. 2017). At the basin floor lies Dehradun, the capital of Uttarakhand (~640 m ASL), which has undergone rapid urban expansion in recent decades. The juxtaposition of this highly urbanized valley city with the adjacent Mussoorie hill station (~2005 m ASL) – a relatively undisturbed, forest-dominated region – creates a natural laboratory for studying urban-topographic interactions and the modulation of temperature regimes and urban heat island (UHI) effects in a mountainous environment.

Figure 1 shows the terrain configuration of the study domain derived from the SRTM V3 (1-arc-second) digital elevation model (DEM) provided by NASA JPL (Farr et al. 2007). The Dehradun district (central area) represents the core of the Doon Valley; the two red stars indicate the locations of the India Meteorological Department (IMD) stations at Dehradun Mokhampur (30.32°N, 78.03°E, ~640 m) and Mussoorie (30.45°N, 78.08°E, ~2005 m). The steep elevation contrast between these stations highlights the valley's orographic control on local meteorology.

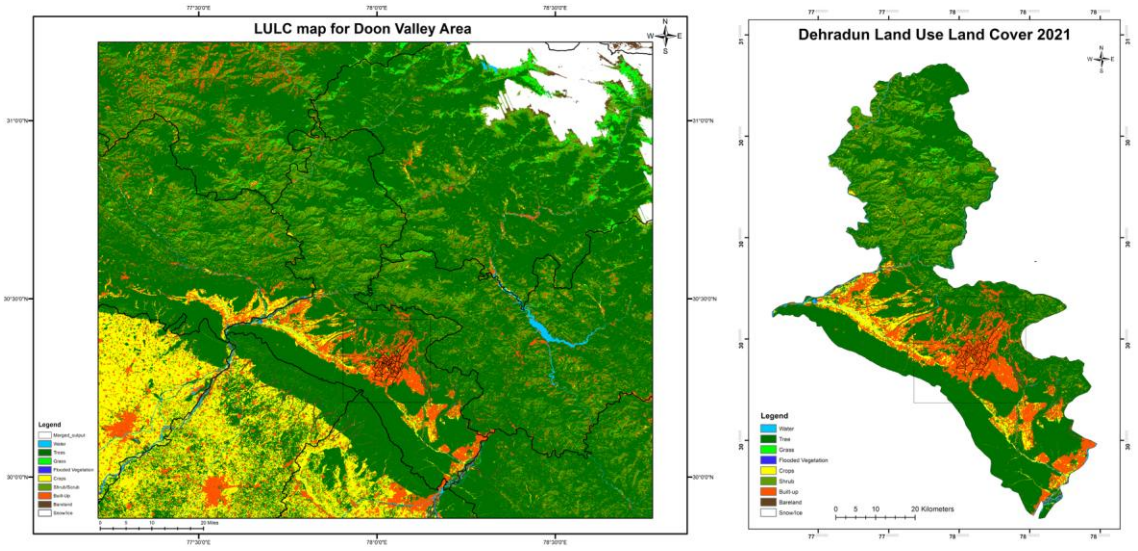

Fig. 2. Land use/land cover (LULC) for: the Doon Valley area (left map); the Dehradun district. The region shaded in red shows the built-up area (urban region) (right map). The region inside the dotted rectangular boundary in both (a) and (b) is the Dehradun city municipal area. The LULC map was obtained using a dynamic world dataset, which is a 10 m near-real-time (NRT) LULC dataset derived from Sentinel-2 L1C collection (Brown et al. 2022). The region shown within the dotted line in (a) shows Dehradun city and its surroundings.

Figure 2 presents the LULC distribution derived from the Dynamic World 10 m near-real-time dataset (Brown et al. 2022). Built-up areas (shown in red) are concentrated around the Dehradun municipal region, delineated by the dotted rectangular boundary, whereas surrounding areas are predominantly agricultural or forested. This spatial heterogeneity emphasizes the interplay between urban surfaces and natural terrain, which governs energy exchange, boundary-layer structure, and diurnal thermal gradients.

Thus, the Doon Valley offers a natural laboratory to study coupled urban-topographic interactions under pre-monsoon conditions, where both steep terrain and rapid urbanization jointly shape temperature distribution, local circulations, and the evolution of UHI phenomena.

2.2. WRF model

The Advanced Research WRF (ARW) modeling system version 4.2 (Skamarock et al. 2019) was used to simulate meteorology over the Doon Valley from 22 December 2020 to 1 January 2022, covering the full calendar year 2021. The first 10 days (22-31 December 2020) were treated as the model spin-up period. The year 2021 was selected because: (1) it represents a recent year with complete availability of high-quality IMD station data at both valley (Dehradun) and hill (Mussoorie) sites, and (2) it exhibited typical pre-monsoon conditions (March-June) with multiple heat events, making it suitable for UHI evaluation.

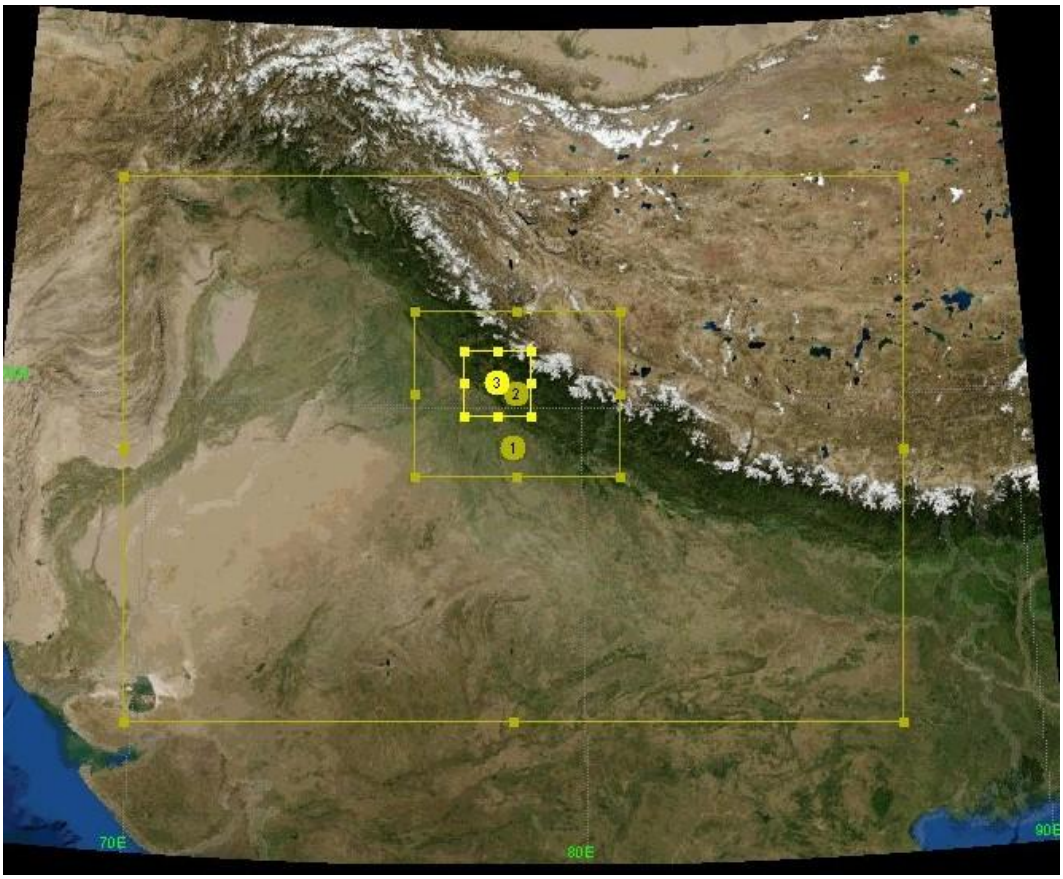

Fig. 3. The three-fold (1:3 ratio) nested domain (D01: 18×18 km², D02: 6×6 km², D03: 2×2 km²) for WRF model set-up in the present study [obtained through WRF-domain wizard (NCAR 2008)]. The yellow circles 1, 2, and 3 depict the centers of domains D01, D02, and D03.

The WRF model employs a fully compressible, non-hydrostatic dynamical core with terrain-following vertical coordinates. Three nested domains (1:3 ratio) were used at 18 km, 6 km, and 2 km resolution, respectively, with the innermost domain focused on the Doon Valley (Fig. 3). Boundary conditions were derived from NCEP GDAS/FNL 0.25° global analyses. The following physical parameterizations were applied, based on prior Himalayan studies (Navale, Singh 2020; Singh et al. 2021; 2024b):

- Microphysics: WSM 3-class scheme (Hong et al. 2004).
- Planetary Boundary Layer (PBL): YSU scheme (Hong et al. 2006).
- Cumulus physics: Kain-Fritsch scheme (Kain 2004).
- Surface layer: Monin-Obukhov scheme (Monin, Obukhov 1954; Namdev et al. 2024).
- Land surface: Noah LSM (Ek et al. 2003).
- Longwave radiation: RRTM (Mlawer et al. 1997).

2.3. Urban Canopy Model – Building Effect Parameterization (UCM-BEP)

To represent urban canopy, we used the multilayer Building Effect Parameterization (BEP) scheme (Martilli et al. 2002; Mussetti et al. 2020; Hendricks, Knievel 2022), an option in WRF v4.2. The Urban Canopy Model BEP simulation was run for the pre-monsoon period (21 March – 30 June 2021, considering 21-Mar to 31-Mar as the spin-up period), during summer when UHI effects are strongest.

Unlike the single-layer UCM, BEP discretizes the urban canopy into multiple vertical layers and explicitly treats heat and momentum exchanges between roofs, walls, and roads. The momentum equation in BEP is:

$$\frac{\partial u}{\partial t} = -\frac{1}{\rho}\frac{\partial p}{\partial x} + \nu\frac{\partial^2 u}{\partial z^2} - C_D.\frac{A(z)}{V(z)}.u|u| \quad (1)$$

where:

- u is the horizontal wind component,
- C_D is the drag coefficient for buildings,
- $\frac{A(z)}{V(z)}$ is the ratio of building frontal area to volume at height z,
- ν is the eddy viscosity.

The energy balance in each urban layer is calculated for three distinct surfaces: roof**,** wall, and road. Each surface has its own surface energy balance:

$$Q^* = Q_H + Q_E + Q_C + Q_A \quad (2)$$

where:

- Q^* is the net radiation,
- Q_H is the sensible heat flux,
- Q_E is the latent heat flux,
- Q_G is the ground (or conductive) heat flux,
- Q_A is the anthropogenic heat flux (redundant in this study).

The vertical profiles of temperature, humidity, and wind are updated using these energy and momentum exchanges at each model level within the urban canopy, thereby improving the representation of the urban boundary layer (UBL) structure (Mussetti et al. 2020).

In this study, the NOAH land surface model (LSM) (Ek et al. 2003) was used in conjunction with the BEP-UCM framework to provide realistic treatment of soil moisture, evapotranspiration, and urban land-use interactions. The NOAH LSM supports the coupling of BEP with surface processes by enabling separate treatment of vegetated and impervious surfaces. The urban classification in the land-use data set (based on MODIS/USGS) triggers the UCM-BEP parameterizations over urban grid cells. Further, the BEP module enables building morphology parameters (e.g., average building height, street width, building fraction) to be user-specified or retrieved from lookup tables, facilitating more accurate representation of urban heterogeneity in grid-scale simulations. The default values used for Dehradun city were: average building height = 7.5 m, building width = 15 m, street width = 20 m, and impervious fraction = 0.9, typical of high-density urban cores (Garuma 2018). By explicitly resolving radiative trapping and dynamic drag in street canyons, the WRF-UCM-BEP system captures the thermal inertia of urban areas, their delayed nighttime cooling, and their suppression of thermally driven flows, which are critical to simulating urban heat island (UHI) effects in mountainous regions like the Doon Valley.

2.4. ERA-5 data

The ERA5 global reanalysis from the European Centre for Medium-Range Weather Forecasts (ECMWF) was used to evaluate large-scale temperature patterns. ERA5 employs the Integrated Forecasting System (IFS) Cycle 41r2 with a four-dimensional variational (4D-Var) data assimilation scheme that incorporates satellite, radiosonde, aircraft, and land observations. It provides hourly data at 0.25° (~31 km) resolution on 137 model levels. For improved near-surface representation, we used the ERA5-Land subset at 0.1°×0.1° (~9 km) resolution, which re-runs the IFS land component (HTESSEL) with enhanced land-surface and boundary-layer physics (Copernicus Climate Data Store 2024). ERA5-Land provides hourly temperature, soil, and flux variables with better land heterogeneity and topographic detail. In this study, ERA5-Land data for January-December 2021 were retrieved from the Copernicus Climate Data Store (CDS) and bilinearly interpolated to the WRF outer domain for consistent comparison with model outputs over the Doon Valley.

2.5. Surface observation data

Hourly meteorological observations were obtained from India Meteorological Department (IMD) stations at Dehradun Mokhampur (30.32°N, 78.03°E, 640 m) and Mussoorie (30.45°N, 78.08°E, 2005 m) (locations shown in Fig. 1). These served as the reference for validating WRF outputs.

2.6. Evaluation metrics

To evaluate the WRF simulation against the ground-based observations, we used the statistical metrics correlation (r), root mean square error ($RMSE$), index of agreement (IOA), mean absolute error (MAE), mean absolute percentage error ($MAPE$), and normalized root mean square error ($NRMSE$) (Willmott 1981; Karppinen et al. 2000; Borrego et al. 2008).

$$CORR = \frac{\sum_{i=1}^{n}(S_i-\bar{S})(O_i-\bar{O})}{\sqrt{\sum_{i=1}^{n}(S_i-\bar{S})^2}\sqrt{\sum_{i=1}^{n}(O_i-\bar{O})^2}} \quad (3)$$

$$IOA = 1 - \frac{\sum_{i=1}^{n}(S_i-O_i)^2}{\sum_{i=1}^{n}(|S_i-\bar{O}|+|O_i-\bar{O}|)^2} \quad (4)$$

$$RMSE = \sqrt{\frac{1}{n}\sum_{i=1}^{n}(S_i - O_i)^2} \quad (5)$$

$$MAE = \frac{1}{n}\sum_{i=1}^{n}|S_i - O_i| \quad (6)$$

$$MAPE = \frac{100}{n}\sum_{i=1}^{n}\left|\frac{S_i-O_i}{O_i}\right| \quad (7)$$

$$NRMSE = \frac{RMSE}{\bar{O}} \times 100 \quad (8)$$

where S_i and O_i are simulated and observed values, n is the number of samples, and $\bar{O}$ and $\bar{S}$ are the means of observed and simulated values.

3. Results and discussion

The WRF simulation was run for the entire year 2021, spanning from 22 Dec 2020 to 01 Jan 2022, with a model spin-up period of 22-31 Dec 2020. The simulation covered the domain 29.8°N to 31.2°N and 77.2°E to 78.8°E, the Doon Valley region, at 2×2 km² resolution. The WRF simulation was carried out in three nested domains (18×18 km², 6×6 km², 2×2 km²). As discussed in the Methods section, the WRF physics schemes were chosen in view of earlier WRF studies of the same region that provided optimum results, i.e., the YSU scheme for the boundary layer (Navale, Singh 2020; Singh et al. 2024b). The high-resolution WRF meteorological simulations have been compared with 0.1°×0.1° resolution ERA-5 to assess the effect of high-resolution distinctive features. The WRF simulated meteorology has been evaluated against ground-based observations for an entire year at the valley site (Dehradun) and the hill site (Mussoorie). Dehradun has become highly urbanized in recent decades; hence, WRF with the Urban Canopy Model (UCM) using the BEP scheme has been run over the region, and the performance of WRF and WRF-UCM has been compared.

3.1. High resolution features: WRF simulation at 2×2 km resolution vs. ERA-5 Land data at 0.1°×0.1° resolution

The WRF meteorological simulation for 2 m temperature and 2 m relative humidity, and its comparison with ERA-5 Land data at 0.1°×0.1° resolution, are presented in Figures 4 and 5. The WRF simulated at higher resolution, allowing it to capture small-scale temperature variations in greater detail. This feature is evident in the more granular patterns (Jun-2021), especially in the valley and hilly regions. The ERA-5 Land data (right) has a coarser resolution (~10 km), leading to a smoother representation of temperature variations over the region; however, the finer details, such as local temperature variations in valleys and ridges, are not well captured. The WRF model is better at capturing local heating and cooling effects, likely

influenced by elevation, land use, and terrain. This enhancement is important for valleys like Doon, where complex topography plays a significant role in temperature distribution. The ERA-5 data set, while useful for large-scale trends, cannot resolve fine-scale topographic influences as effectively as WRF's higher resolution simulation. The wintertime (January 2021) comparison shows that WRF exhibits stronger cooling in the north (blue shading), corresponding to hill and mountainous areas, while southern valley regions remain warmer, showing the expected winter temperature inversion. Colder regions are less pronounced in ERA-5, suggesting weaker resolution of temperature inversion effects in the valley.

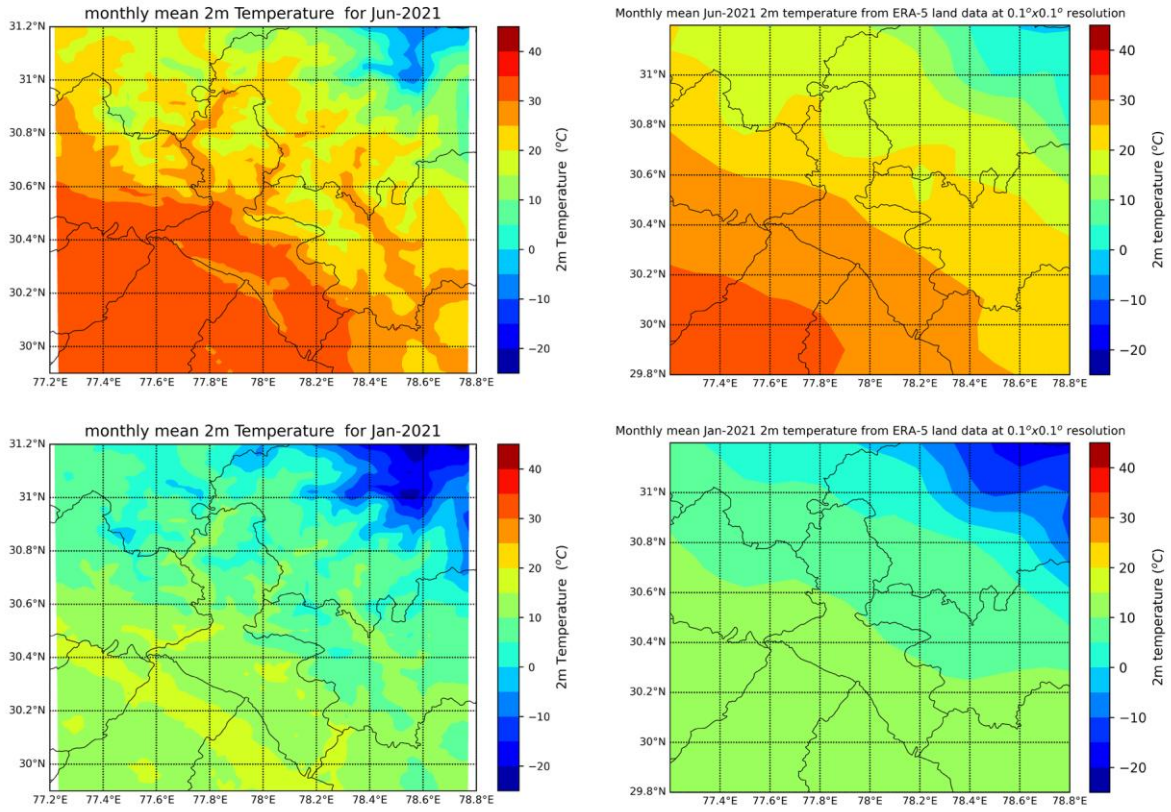

Fig. 4. Comparison of 2 m temperature from WRF (2×2 km² resolution) simulation (left) and ERA-5 (0.1°×0.1°) resolution (right) for June 2021 (upper panels) and January 2021 (lower panels).

Figure 5 compares 2 m relative humidity (RH) between the WRF (2×2 km²) simulation and ERA-5 (0.1°×0.1°) data for the monsoon season (July 2021) and the pre-monsoon season (April 2021). In the monsoon season (July 2021), WRF captures significant spatial variability in RH, especially over hilly areas where RH is locally higher. It shows pockets of high RH (>80%) in northern and central regions, likely the effect of orographic lifting causing moisture accumulation. Sharp humidity gradients are evident, reflecting terrain influence on moisture distribution. The ERA-5 results show a smoother distribution of RH with a large-scale gradient from south (~40-50%) to north (~80%). It lacks the fine-scale humidity variations caused by local terrain effects. The WRF's high resolution simulation captures orographic moisture enhancement due to monsoon winds interacting with the terrain. As seen in WRF, orographic lifting causes higher RH over hills, an effect not well-represented in ERA-5. Evidently, the local

convective systems, which increase humidity locally, are better captured in WRF. In the pre-monsoon season (April 2021), the WRF shows widespread lower RH (<40%), especially in the southern and central parts of the region, while there is higher RH in some northern areas, likely due to local moisture retention in higher-altitude regions.

The ERA-5 depicts a more uniform humidity field, lacking the local variations seen in WRF, showing higher RH (~50-60%) over northern areas, but the distribution of lower RH is smoother.

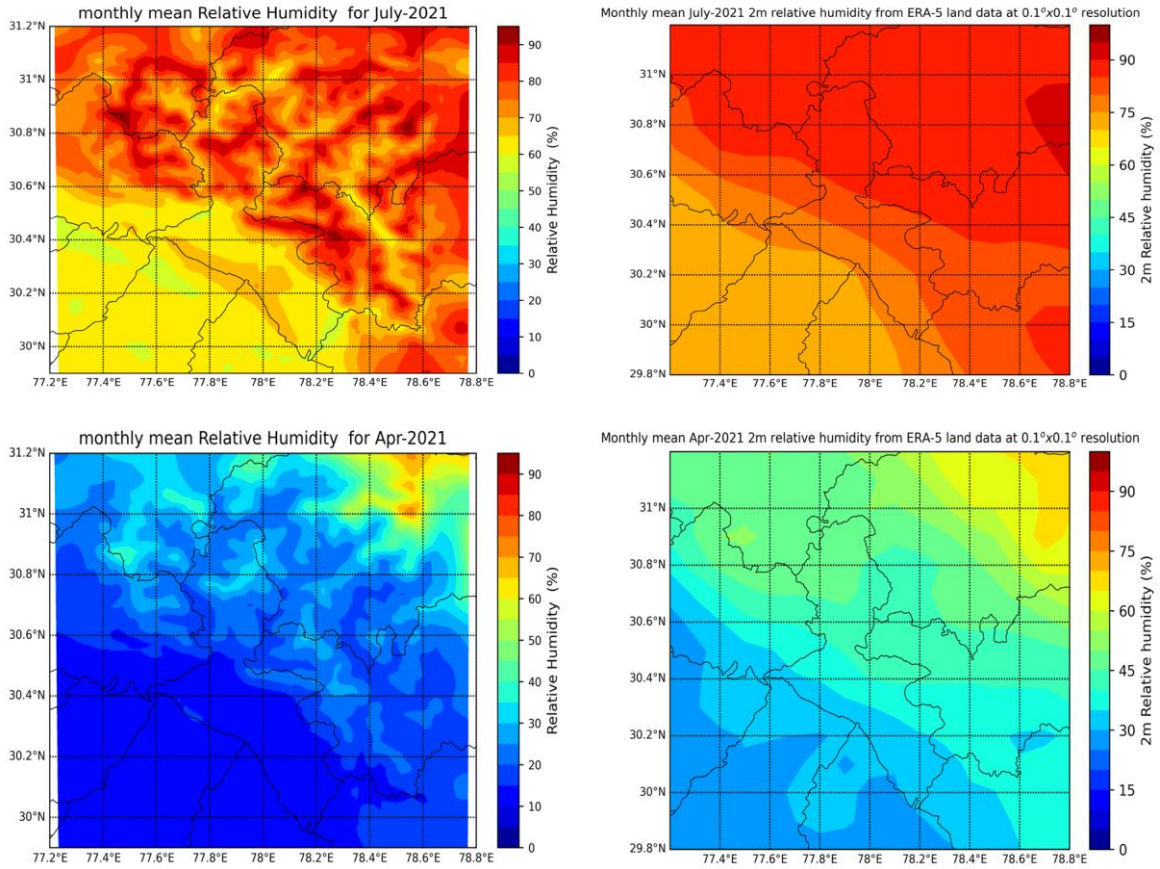

Fig. 5. Comparison of 2 m relative humidity from WRF (2×2 km² resolution) simulation (left) and ERA-5 (0.1°×0.1°) resolution (right) for July 2021 (monsoon season) (upper panels) and April 2021 (pre-monsoon season) (lower panels).

3.2. Evaluation of WRF simulation with ground observations

The year-long (1 January 2021 through 30 December 2021) validation of WRF-simulated 2 m temperature was compared with observations from two ground-based meteorological stations of the India Meteorological Department (IMD) within the simulated domain. Figure 6 presents the WRF-simulated hourly temperature variations (2 m temperature) versus the ground meteorological observations for 2021 at two locations, Dehradun Mokhampur and Mussoorie. The model was validated against ground observations for hourly temperature, the daily median temperature, and the daily peak 90th percentile temperature. The validation metrics (*r*, *IOA*, *MAE*, and *RMSE*) for both locations are presented in Table 1. The hourly temperature simulations provide insight into the model's ability to capture diurnal variations,

but daily median temperature is a robust metric better reflecting the central tendency of temperature variations while minimizing the influence of extreme values. The 90th percentile temperature represents peak daytime warming events, which are crucial for assessing extreme heat conditions.

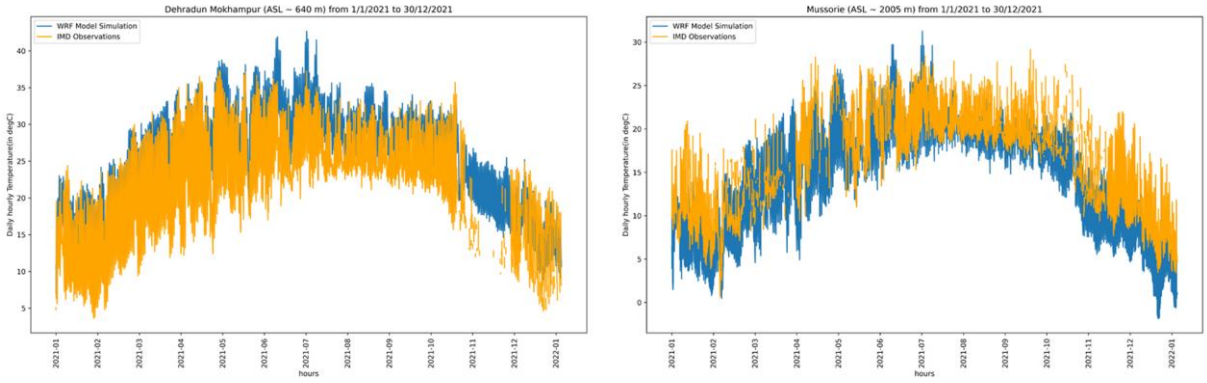

Fig. 6. The time series of hourly 2 m temperature variations obtained from WRF simulation and the observations from the IMD meteorological stations from 1 January 2021 through 30 December 2021 at Dehradun (left) and Mussoorie (right).

The comparison between WRF-simulated and observed temperatures shows that WRF performs reasonably well in both locations but exhibits greater discrepancies in Dehradun compared to Mussoorie. The correlation coefficient and *IOA* are relatively high for both locations (Table 1), indicating a general agreement between simulations and observations. The *MAE* and *RMSE* are larger for Dehradun than Mussoorie (Table 1), suggesting that WRF is less precise in urban conditions. The validation metric results for daily median temperature show that the correlation and *IOA* remain high, but slightly better than for hourly temperatures, indicating that WRF can capture the overall temperature trend more accurately. The errors (*MAE* and *RMSE*) are still higher for Dehradun, implying that urban dynamics such as heat retention and urban canyon effect are not well represented in the model. The validation metrics for daily peak 90th percentile temperature reveal lower correlation and *IOA* compared to median temperature, indicating greater difficulty in capturing peak temperature events. The error metrics were larger, especially in Dehradun, where extreme daytime temperatures are more affected by urban morphology.

For Mussoorie, WRF performs better, likely because WRF accurately incorporates the land-atmosphere interactions over complex mountainous terrain. However, for the Dehradun region, the *MAE* and *RMSE* are higher, possibly because the city has grown rapidly and the WRF simulation has not included all of the urban features. In the next section, the performance of the WRF simulation, after including urban features, is discussed.

3.3. Impact of urban features: WRF-UCM (BEP) simulation and its evaluation

The WRF-UCM with BEP scheme incorporates urban morphology by considering three-dimensional urban structures, urban canyon effects, and heat exchange between buildings and the atmosphere. The WRF-UCM with BEP scheme was run for the pre-monsoon season (22 Mar 2021 to 20 Jun 2021, where

the period 22 Mar 2021 to 31 Mar 2021 is the model's spin-up period) to assess the urban effects as effectively as possible. The impact of these modifications is assessed using key statistical metrics: *r*, *IOA*, *MAE*, and *RMSE* for three temperature categories: hourly temperature, daily median temperature, and daily peak 90th percentile temperature (Fig. 7).

Table 1. Validation metrics of WRF simulations against IMD observations for 2021.

Location	Metric	Hourly T2	Daily Median T2	Daily 90th Percentile T2
Dehradun	*r*	0.80	0.84	0.71
	IOA	0.72	0.77	0.65
	MAE (°C)	4.9	5.3	6.1
	RMSE (°C)	5.7	5.7	6.8
	MAPE (%)	14.2	12.7	15.8
	NRMSE (%)	13.5	12.9	15.1
Mussoorie	*r*	0.87	0.89	0.81
	IOA	0.79	0.83	0.74
	MAE (°C)	3.4	3.1	4.2
	RMSE (°C)	4.2	3.9	4.8
	MAPE (%)	9.8	8.9	10.7
	NRMSE (%)	10.4	9.2	11.0

Table 2. Comparison of validation metrics for WRF and WRF-UCM (BEP) during the pre-monsoon season (March-June 2021) at Dehradun and Mussoorie.

Location	Variable	Model	*r*	*IOA*	*MAE* (°C)	*RMSE* (°C)	*MAPE* (%)	*NRMSE* (%)
Dehradun	Hourly T2	WRF	0.80	0.72	4.9	5.7	14.2	13.5
		WRF-UCM (BEP)	0.83	0.78	4.1	4.9	12.0	11.6
	Median T2	WRF	0.84	0.73	5.3	5.7	13.0	13.2
		WRF-UCM (BEP)	0.86	0.78	4.3	4.7	11.4	11.0
	90th Percentile T2	WRF	0.71	0.65	6.1	6.8	15.8	15.1
		WRF-UCM (BEP)	0.78	0.70	5.0	5.9	13.2	13.0
Mussoorie	Hourly T2	WRF	0.87	0.79	3.4	4.2	9.8	10.4
		WRF-UCM (BEP)	0.88	0.80	3.2	4.0	9.4	9.9
	Median T2	WRF	0.89	0.81	3.1	3.9	9.2	9.4
		WRF-UCM (BEP)	0.90	0.82	3.0	3.8	8.8	9.1
	90th Percentile T2	WRF	0.81	0.74	4.2	4.8	10.7	11.0
		WRF-UCM (BEP)	0.82	0.75	4.0	4.6	10.3	

At Dehradun, for hourly temperature simulation, the WRF-UCM (BEP) scheme demonstrates a marginal improvement in *IOA* (0.72 to 0.78) and r (0.80 to 0.83) over the standard WRF model (Table 2). The noticeable reduction in *MAE* (4.9 to 4.1) and *RMSE* (5.7 to 4.9) for the WRF-UCM (BEP) simulation suggests a more accurate representation of diurnal temperature variations. This improvement is the result of including urban heat storage and canyon radiative trapping in the WRF through UCM (BEP scheme). At Mussoorie, the improvement is less or negligible, indicating that BEP modifications primarily benefit urban regions, where the representation of building-energy interactions is crucial. The performance

remains comparable to WRF, as the model is already capable of simulating natural terrain with limited urban influence. For daily median temperature at Dehradun, noticeable improvement is observed with WRF-UCM (BEP), as reflected in higher *IOA* values (0.53 to 0.58). The reduction in *MAE* (5.3 to 4.3) and *RMSE* (5.7 to 4.7) indicates a more precise simulation of overall daily temperature trends. The standard WRF model underestimates urban heat retention, leading to biases that BEP corrects. At Mussoorie, the results remain relatively unchanged compared to WRF, reinforcing that the urban modifications in BEP are less relevant in high-altitude, rural settings. For daily peak 90th percentile temperature performance at Dehradun, the inclusion of BEP significantly improves high-temperature peak prediction. The urban heat island (UHI) effect amplifies peak temperatures in cities, which WRF-UCM (BEP) captures better than the standard WRF model. The reduction in *MAE* and *RMSE* highlights the importance of including urban morphology in WRF for accurate extreme temperature simulation. At Mussoorie, the differences between WRF and WRF-UCM (BEP) are minor, reaffirming that urban parameterization has little influence at a hill station where urbanization is less, and therefore, the urban effect is less pronounced. The BEP scheme improves WRF's performance significantly in Dehradun by incorporating urban physics, whereas its impact in Mussoorie is minimal. Hourly and peak temperatures benefit the most from urban modifications, as they are more sensitive to urban heat storage and canyon effects.

Figure 7 illustrates the spatial distribution of the daily peak 90th percentile temperature over Dehradun averaged for May 2021, as simulated by the WRF and WRF-UCM (BEP). The results highlight the temperature variations across the region, emphasizing the impact of urbanization on local thermal conditions. The upper panels of Figure 7 compare the temperature distribution from WRF (left) and WRF-UCM (BEP scheme) (right) for the entire Dehradun region. Both simulations depict a clear spatial gradient, with elevated temperatures in the southern urban areas and cooler temperatures in the northern high-altitude regions. However, the inclusion of the urban canopy model (BEP scheme) leads to a more pronounced urban morphology effect, with higher temperatures over the city center compared to the standard WRF simulation.

The lower panel of Figure 7 focuses on the section of Dehradun that includes the urban core of Dehradun, where the temperature differences between the WRF and WRF-UCM (BEP) simulations become more apparent. The WRF-UCM simulation shows systematically higher temperatures in built-up areas due to better representation of urban geometry, thermal properties of buildings, and reduced evaporative cooling. In contrast, the standard WRF model underestimates these effects, leading to relatively lower temperatures. The enhanced warming in the WRF-UCM simulation is consistent with the urban heat island phenomenon, which is driven by increased sensible heat flux and a lower fraction of latent heat flux in urban environments.

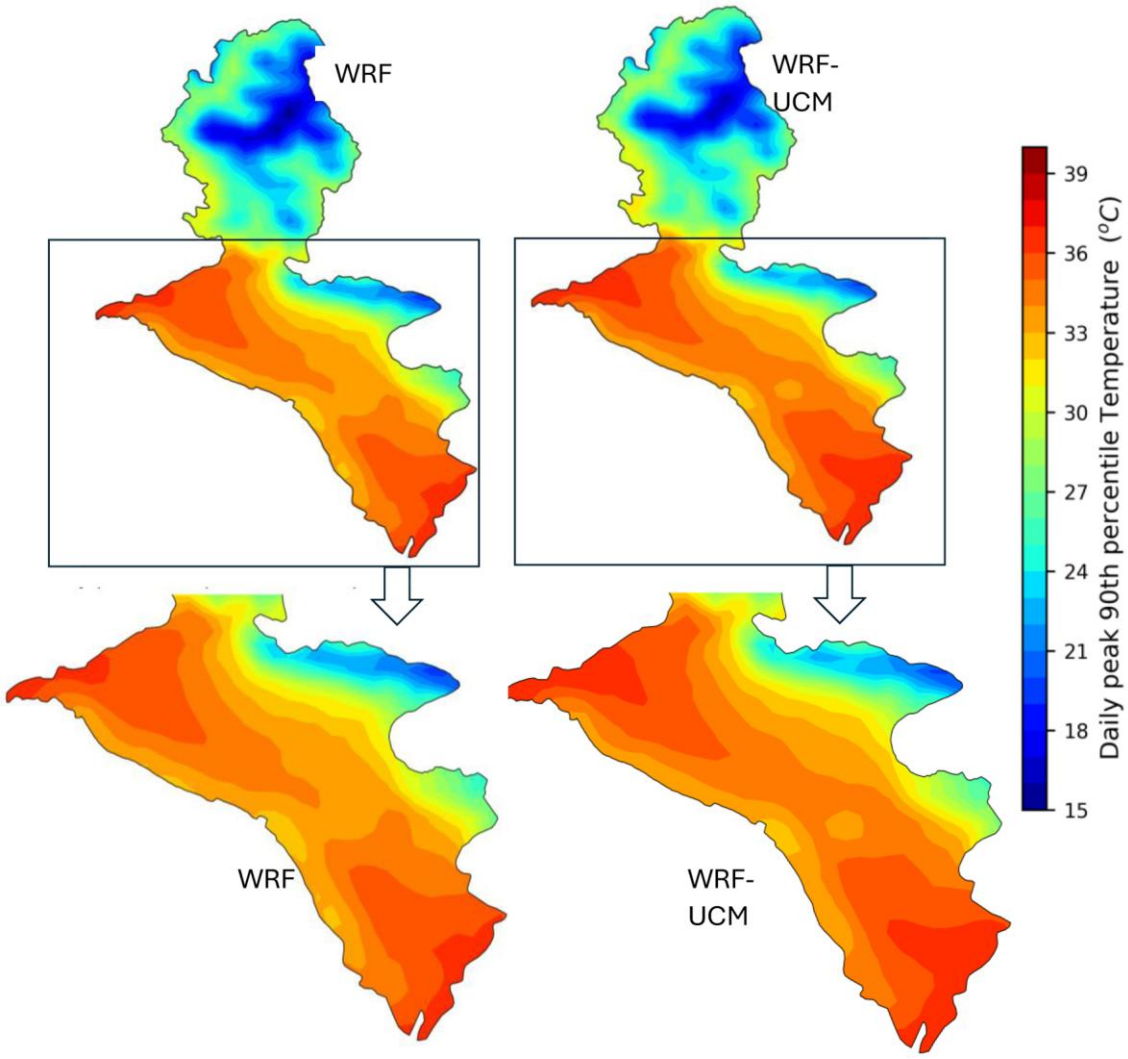

Fig. 7. May 2021 mean of daily peak 90th percentile temperature of Dehradun by WRF and WRF-UCM (BEP). The upper panel shows all of Dehradun; the lower panel shows the urban core of Dehradun that experiences higher temperatures.

3.4. Assessment of UHI effect

The UHI effect was evaluated in two complementary ways: (1) UHI based on near-surface air temperature (2-m temperature (T2)) to assess the atmospheric manifestation of the phenomenon, and (2) Surface UHI based on skin temperature (TSK) and satellite-derived MODIS LST to examine the radiative surface imprint of urban warming. Both approaches provide a comprehensive understanding of nocturnal UHI dynamics. The UHI effect is evaluated for the Dehradun city areas (municipal localities) where build-up is predominant and administratively regulated by urban municipal corporations.

3.4.1. UHI (air temperature-based):

During April, the WRF-BEP simulation produced higher nocturnal UHI intensities compared to the control WRF run, with maximum ΔT exceeding 6 K at 00:00 UTC (05:30 IST) (Fig. 8). The enhancement is attributable to the representation of urban canopy processes in BEP, which trap heat more effectively during nighttime. The UHI then diminished rapidly after sunrise, reaching near-neutral or slightly negative

values between 04:00 – 10:00 UTC (09:30 – 15:30 IST), before re-emerging in the late afternoon. Spatial maps for April indicate a clear warming core over central Dehradun, more pronounced in WRF-BEP, highlighting the importance of urban morphology in shaping near-surface temperature fields (Fig. 8).

In May, both WRF and WRF-BEP runs reproduced consistent nocturnal UHI peaks, but the magnitude was slightly lower than in April, with maximum ΔT values of about 4-4.5 K. Interestingly, the WRF simulation exhibited somewhat larger UHI magnitudes than WRF-BEP during late evening hours. This reversal suggests seasonal modulation, where stronger background heating in May reduces the relative contribution of urban canopy effects. Spatial plots show localized hot-spots over the city core during afternoon hours, although the areal extent of elevated temperatures remains broader in WRF compared to the more spatially confined but sharper warming simulated by WRF-BEP.

By June, the nocturnal UHI weakened further, with peak intensities generally below 3.5 K. The WRF control runs simulated higher UHI magnitudes than WRF-BEP, particularly during late evening (18:00 – 22:00 UTC). The weaker UHI during June can be attributed to enhanced convective activity and stronger mixing, which diminished the urban–rural thermal contrast. Spatial fields for June confirm this, showing more diffuse warming signatures with reduced intensity compared to April and May. The observational analyses in an earlier study (Dhankar et al. 2024) report that increased cloud cover and moisture during the monsoon transition dampen UHI signatures in Dehradun, matching the attenuation we diagnose in June.

Across all months, the UHI was strongest during the late evening and early nighttime hours, while it weakened substantially during the forenoon and was nearly absent around sunrise.

These results indicate a strong seasonal (monthly) modulation of UHI intensity, with maximum nocturnal intensities in April, a moderate decline in May, and a further reduction in June. The inclusion of the BEP scheme enhances the simulation of nocturnal warming during April, when stable atmospheric conditions prevail, but produces weaker signals during late pre-monsoon months when convective mixing dominates. This highlights the sensitivity of UHI representation to both urban canopy processes and background meteorological conditions. Prior Dehradun-focused UHI works (Mishra, Arya 2024) emphasize the role of built-up growth and vegetation gradients in setting the magnitude and timing of thermal contrasts; our ambient UHI diagnostics reproduce those space-time features at high resolution and attribute the April peak to stronger stability and reduced evaporative cooling over the urban core.

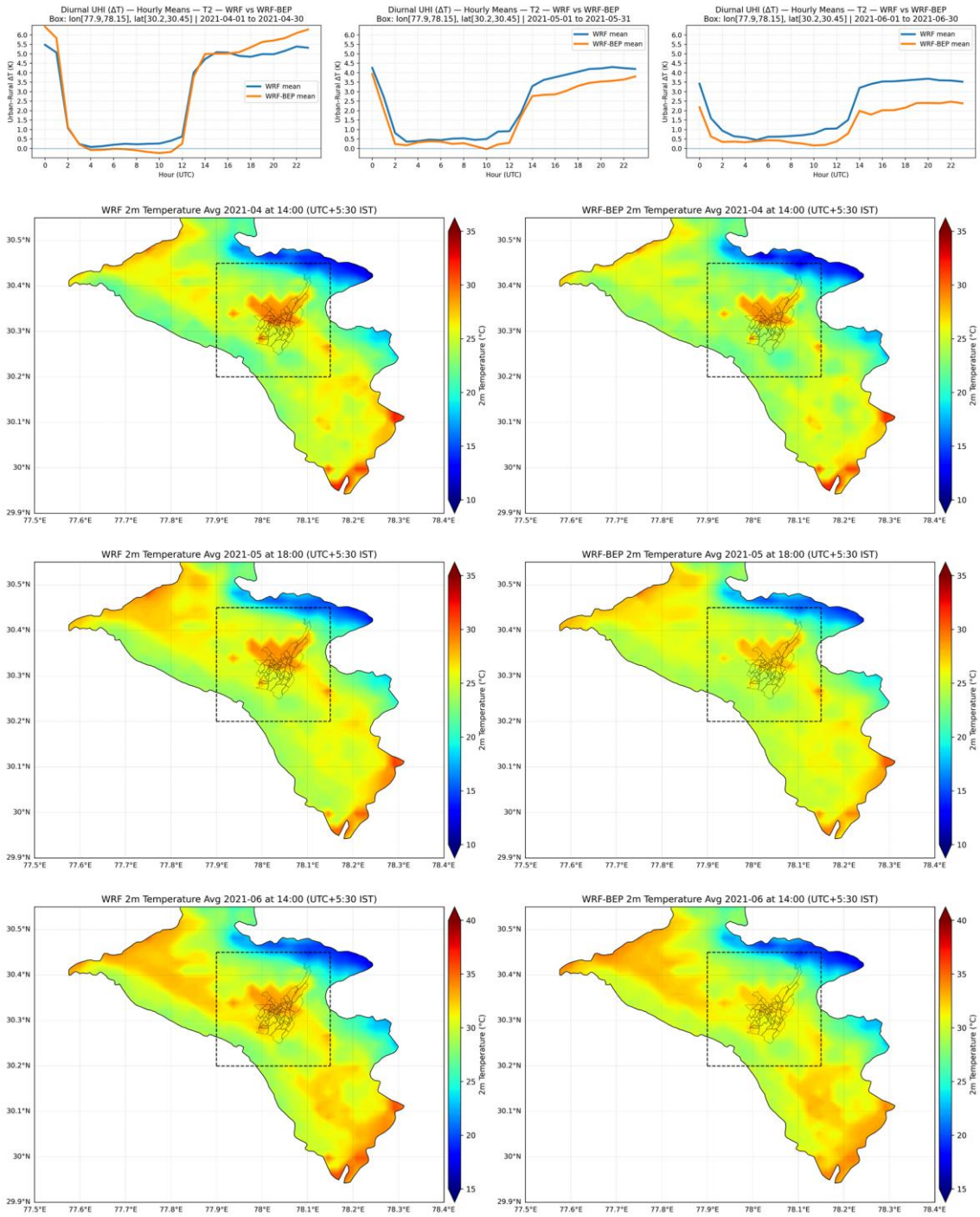

Fig. 8. Monthly variation of evening-time ambient urban heat-island (UHI) intensity ($\Delta T = T_{urban} - T_{rural}$) derived from WRF and WRF-UCM-BEP simulations for the pre-monsoon months of April, May, and June 2021. The top panel represents the monthly averaged diurnal cycles of ambient ΔT, showing stronger daytime and evening UHI development in the WRF-UCM-BEP run than in the standard WRF simulation. The lower panels include sets of maps illustrating spatial distributions of UHI intensity at 14:00 UTC (≈ 19:30 IST) for the same months, enabling consistent inter-month comparisons under peak-heating conditions. Warm anomalies exceeding 4-6°C are concentrated over the Dehradun urban core, while weaker contrasts occur in June due to enhanced convective mixing. The WRF-UCM-BEP configuration produces a more compact and realistic UHI footprint, emphasizing the role of urban morphology in regulating late-afternoon ambient temperature.

3.4.2. Surface UHI (skin temperature/MODIS LST)

To assess the surface expression of the UHI, we compared monthly composites of MODIS 1-km LST with modeled skin temperature (TSK) from the control WRF run and the urban-canopy run (WRF-BEP) over Doon Valley.

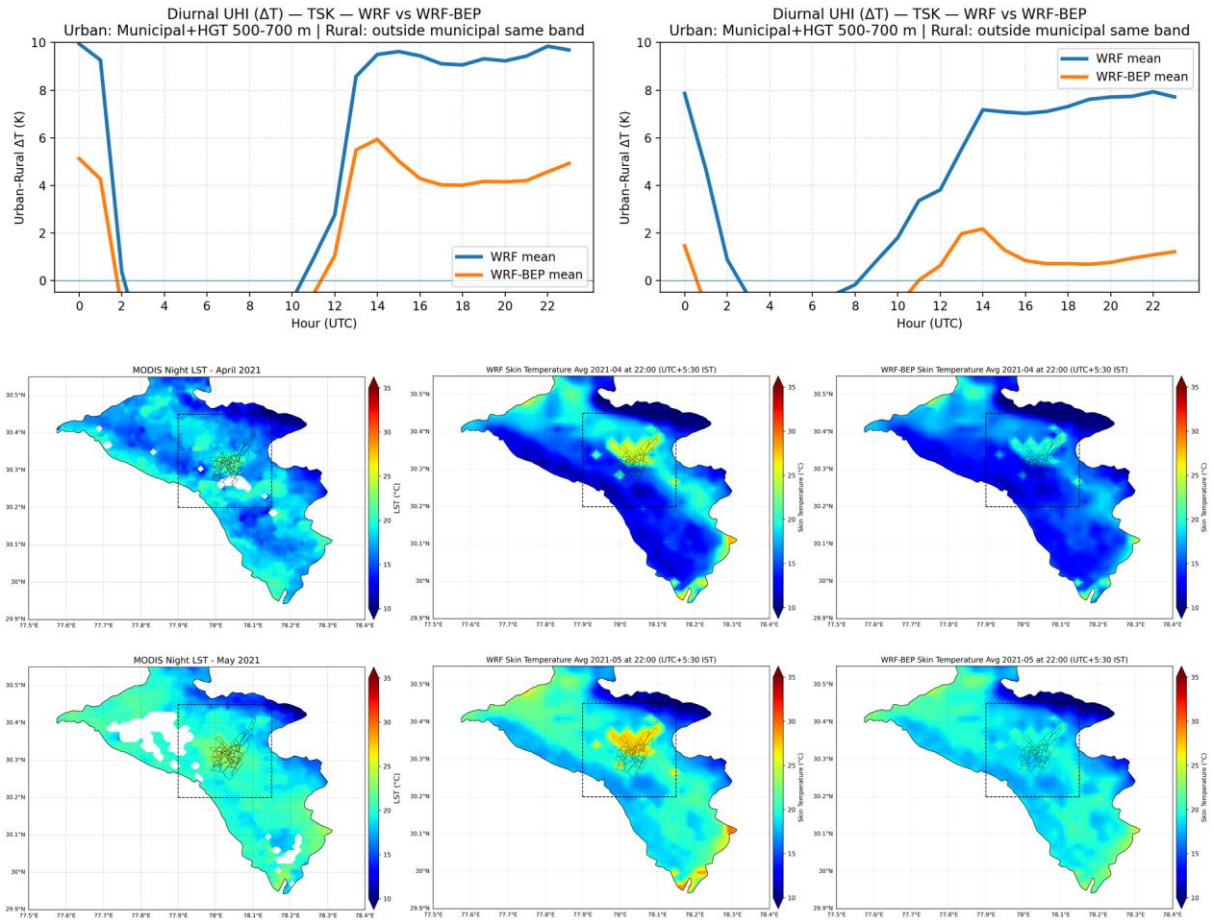

Fig. 9. Monthly variation of nighttime surface UHI ($\Delta T\_skin = TSK_{urban} - TSK_{rural}$) from WRF and WRF-UCM-BEP simulations compared with MODIS 1 km land-surface-temperature (LST) for April and May 2021. The top panel shows the monthly average diurnal cycles of surface ΔT_skin, demonstrating stronger nocturnal UHI intensity and slower post-sunset cooling in the WRF-UCM-BEP simulation. The subsequent maps depict spatial distributions of nighttime surface UHI at 01:00 UTC (≈ 06:30 IST) for each month. MODIS LST (Aqua night 1:30 to 1:50 local overpass time) maps (top row of each month) serve as observational references; WRF and WRF-UCM-BEP maps illustrate modeled skin-temperature and UHI intensity fields. The WRF-UCM-BEP configuration captures a compact, warmer surface core centered over Dehradun in close agreement with MODIS observations, whereas the control WRF run exhibits diffuse heating extending into rural surroundings. These results confirm the improved capability of the BEP scheme to reproduce nocturnal surface-UHI magnitude, structure, and monthly variability under pre-monsoon conditions.

The surface UHI was computed as $\Delta T_{surf} = \bar{T}_{urban} - \bar{T}_{rural}$. We focus on April and May 2021, when the pre-monsoon dry and clear conditions make surface temperature contrasts most distinct.

Hourly means of surface ΔT (urban − rural) from modeled skin temperature show a clear pre-monsoon diurnal rhythm. In April, ΔT builds from late morning, peaks during late afternoon and early evening, and then weakens overnight; May follows the same shape with a slightly muted amplitude, while June is flatter and weaker as humidity and cloudiness rise toward the monsoon. Over these months, the control WRF generally produces a larger and more persistent afternoon plateau than expected. Adding the urban canopy (WRF-BEP) dampens the peak by roughly 20-40% in April and May and slightly sharpens the rise and decay, yielding timing and magnitude that align better with typical dry-season surface heating over the valley. A 2020 Dehradun analysis (Maithani et al. 2020) using Landsat/MODIS shows compact, recurrent hot-spots over the municipal corridor with the strongest pre-monsoon contrasts and a damped diurnal amplitude as humidity increases – patterns mirrored by our MODIS-constrained evaluation and improved by WRF-BEP.

The spatial LST fields for April and May reinforce this behavior. MODIS 1-km (Aqua night: 1:30 to 1:50 local overpass time) composites consistently show a compact warm core along the Dehradun urban corridor, with cooler forested slopes and higher terrain surrounding it. The control WRF reproduces a warm center but spreads it too broadly and sometimes displaces warmth onto adjacent hills, indicating an overly diffuse hot-spot and mild warm bias outside built-up areas. WRF-BEP concentrates the hot-spot more tightly over the valley floor, reduces spurious warming on the slopes, and matches the observed placement of the warm core more closely in both months.

Thus, WRF-BEP explains the surface UHI more credibly than the control WRF: it lowers exaggerated afternoon ΔT, improves the timing of the diurnal cycle, and better captures the compact spatial footprint of the urban warm core observed by MODIS, while limiting artificial spillover of heating onto surrounding terrain. A recent Dehradun-specific study (Singh et al. 2024a) documents seasonal dynamics and multi-decadal warming of surface thermal conditions, with intensified warm cores coincident with expansion of built-up areas in the valley floor; our MODIS, WRF-BEP comparison reproduces those compact hot-spots and their pre-monsoon amplification, indicating that explicit urban morphology helps constrain both magnitude and footprint of surface UHI in Dehradun.

3.5. Role of mountain-breeze circulation and the dominance of urban morphology in regulating valley temperature

The Doon Valley's north-south relief, bounded by the Siwalik Hills and Mussoorie Range, supports strong diurnal thermally driven winds, i.e., daytime upslope (anabatic) and nighttime downslope (katabatic) flows, that naturally ventilate the basin (Karki et al. 2017; Singh et al. 2021). Under clear pre-monsoon conditions, these circulations promote nocturnal cooling and maintain valley-slope temperature contrasts.

In the standard WRF simulation, the nocturnal pattern at 01:00 UTC on 15 May 2021 (Fig. 10a) clearly depicts cooler air pooled within the valley and a temperature gradient toward the northern slopes, indicating organized katabatic drainage. The WRF-UCM (BEP) run (Fig. 10b) alters this structure substantially: valley temperatures remain elevated, horizontal gradients flatten, and the difference map

(Fig. 10c) reveals localized warming of +1.5-2°C across the urbanized Doon-Rispana corridor. Cooler anomalies confined to forested ridges imply that radiative trapping and heat storage within built surfaces suppress nocturnal cold-air formation.

Vertical cross-sections of temperature and potential temperature (Fig. 11) reinforce these contrasts. The control WRF simulation shows a shallow inversion around 700-800 m ASL and steep potential-temperature gradients typical of stable stratification. In WRF-BEP, this inversion nearly vanishes, and vertical gradients weaken, producing a more mixed boundary layer. The added urban heat flux erodes surface stability and limits nocturnal cooling.

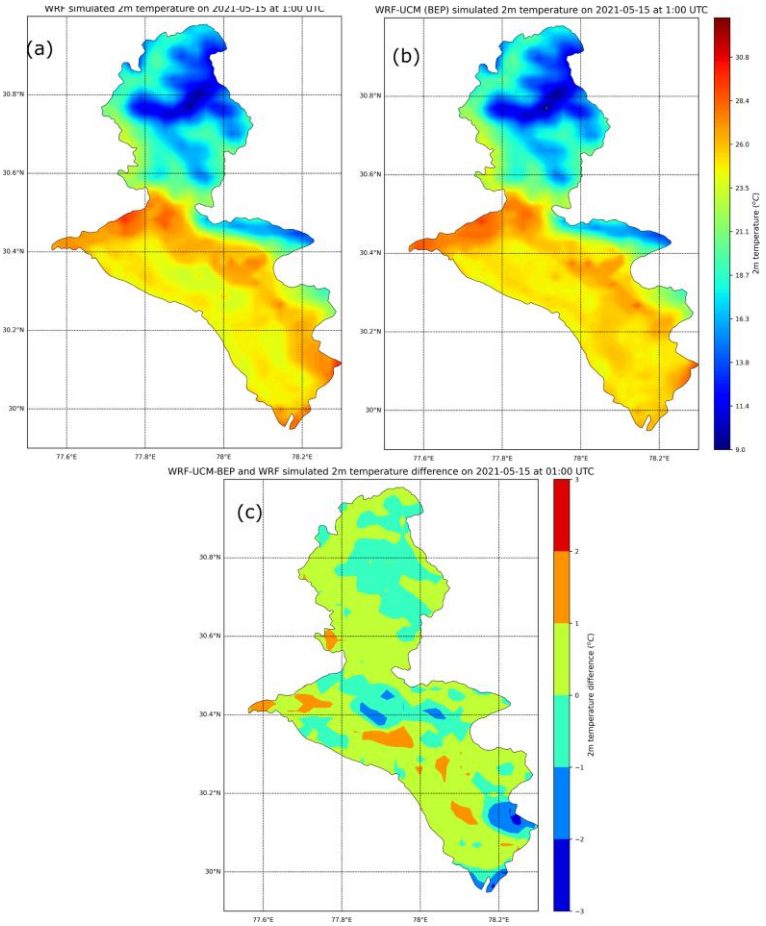

Fig. 10. Simulated 2 m temperature (WRF) at 01:00 UTC on 15 May (a); Simulated 2 m temperature (WRF-BEP) at 01:00 UTC on 15 May 2025 (b); Difference in 2 m temperature (WRF-BEP − WRF) (c).

The wind cross-sections (Fig. 12) depict a similar transition. In WRF, downslope winds of ~1-2 m s^{-1} descend from the Mussoorie slopes toward the valley floor, forming a coherent mountain-breeze cell. In WRF-BEP, these flows become disorganized and weaker, occasionally reversing near the surface above the city core. Difference plots (Figs. 13-14) quantify this effect: warming of +1-2°C and wind-speed reductions up to 1.8 m s^{-1} within 0-2 km AGL show that urban heat alters both thermal and dynamical structures. Surface warming enhances near-surface stability, weakening katabatic momentum and reducing natural nighttime ventilation.

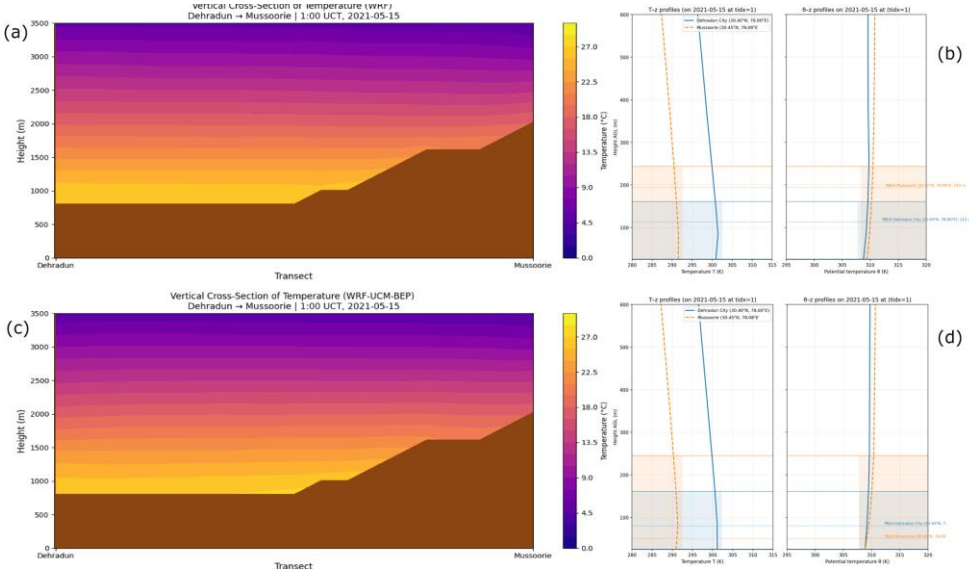

Fig. 11. (a) Vertical cross-section of temperature (from WRF run); (b) temperature vs. height (from surface) and θ (potential temperature) vs. height (from surface) profile (from WRF run); (c) vertical cross-section of temperature (from WRF-UCM-BEP run); (d) temperature vs. height (from surface) and θ (potential temperature) vs. height profile (from surface) (from WRF-UCM-BEP). The temperature inversion is suppressed in the WRF-UCM-BEP run.

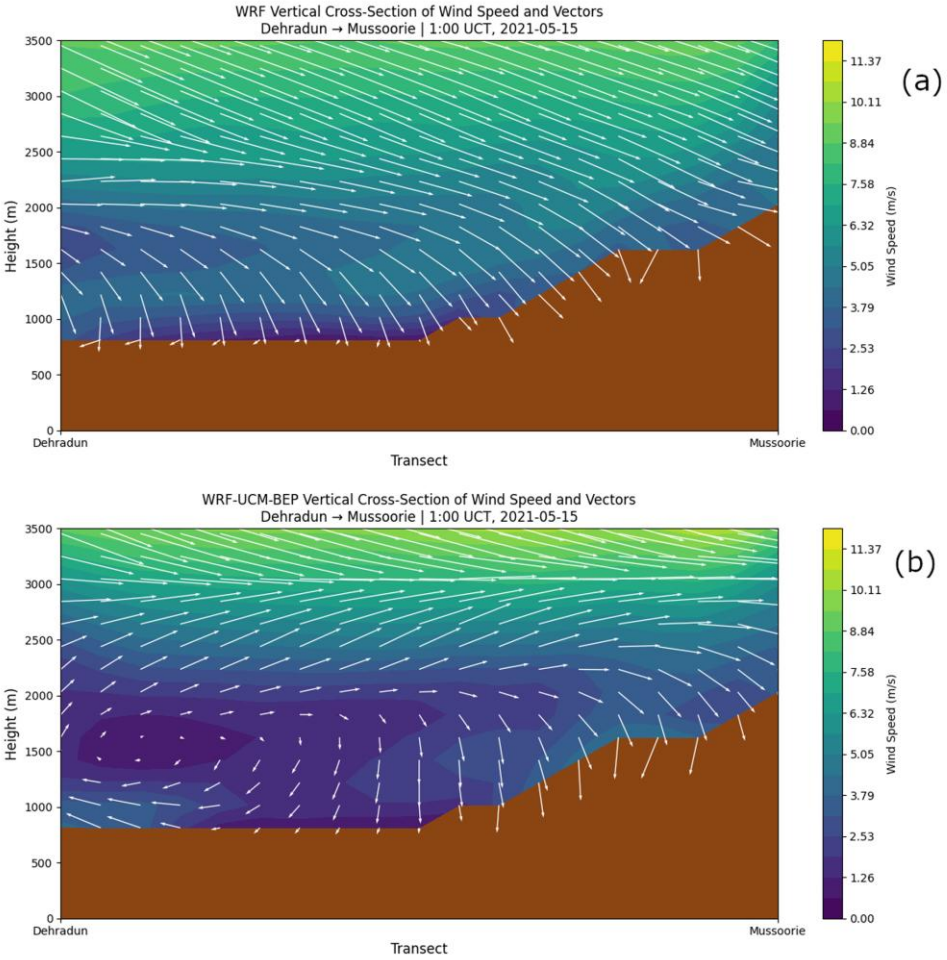

Fig. 12. (a) Vertical cross-section of wind speed and vectors (WRF), (b) Vertical cross-section of wind speed and vectors (WRF-BEP).

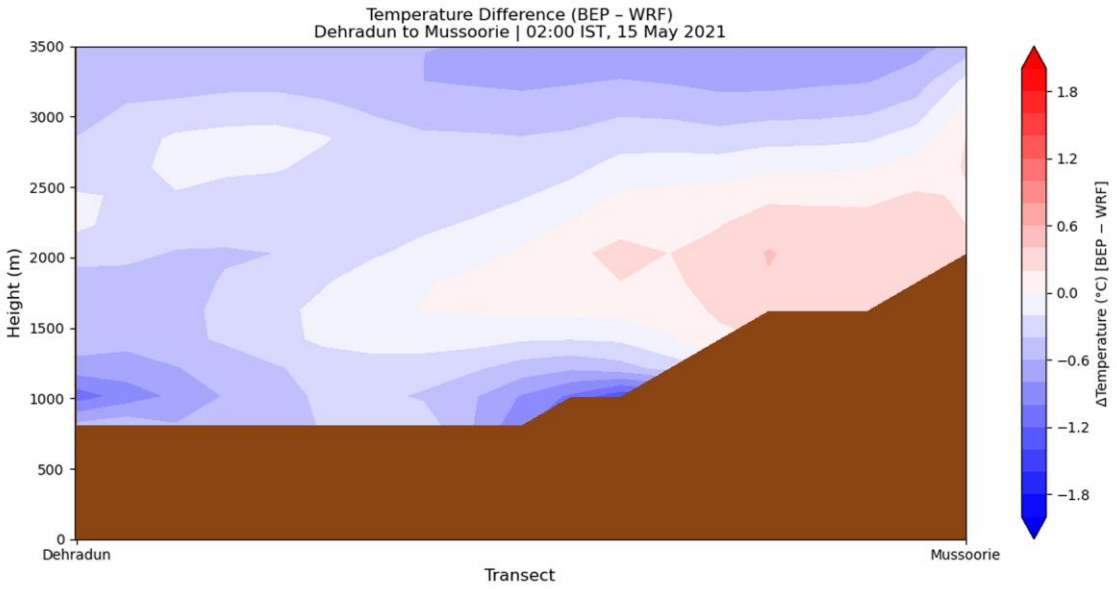

Fig. 13. Vertical cross-section of temperature difference (WRF-BEP − WRF).

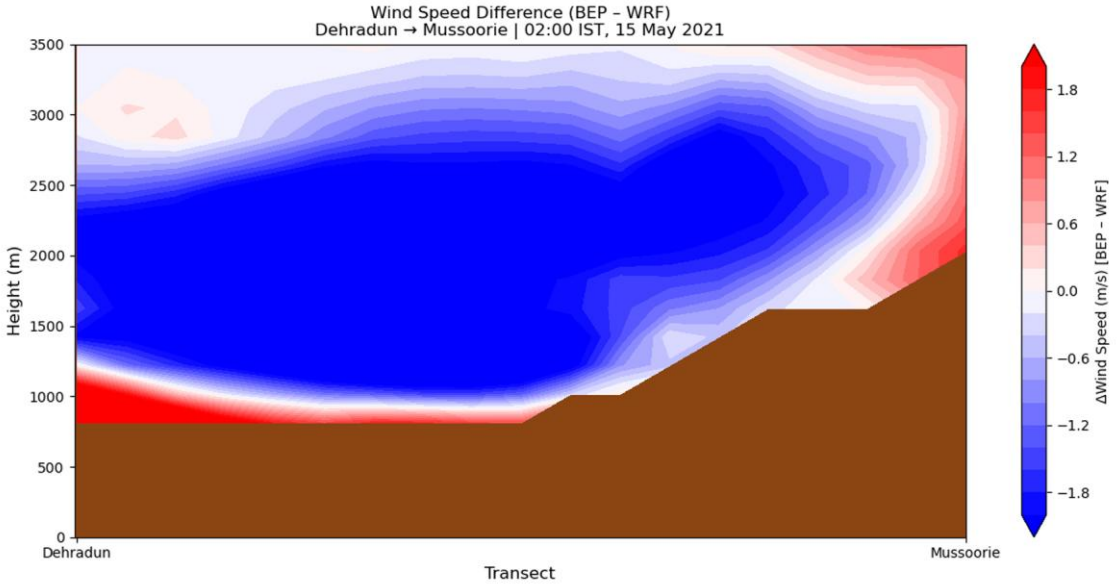

Fig. 14. Vertical cross-section of wind speed difference (WRF-BEP − WRF).

Collectively, these diagnostics demonstrate that urban morphology dominates over terrain-induced thermodynamics in controlling nocturnal conditions within the Doon Valley. The multilayer BEP scheme captures how building geometry, high heat capacity, and canyon radiation trapping disrupt cold-air drainage and maintain persistent nighttime warmth. Such suppression of mountain-breeze circulation implies reduced ventilation efficiency, elevated heat stress, and potential deterioration of nighttime air quality.

Comparable results have been reported for other mountainous cities – Lisbon (Silva et al. 2021), Manila (Bilang et al. 2022), and Athens (Roukounakis et al. 2023) – but this study extends the evidence to the western Himalayas, demonstrating how rapid urbanization can override natural cooling processes in

intermontane basins. The findings highlight the necessity of incorporating realistic urban morphology in mesoscale modeling to accurately represent thermal dynamics and inform climate-responsive urban planning for Himalayan valleys such as Dehradun.

The analysis revealed that the WRF-BEP framework provides a more realistic representation of urban–topography interactions in the Doon Valley, highlighting the dominance of built environment characteristics in controlling nocturnal temperature and wind patterns. These findings have critical implications for urban planning, nighttime heat stress management, and air quality regulation, particularly in rapidly urbanizing intermontane basins like Dehradun.

4. Conclusion

This study demonstrates the capability of high-resolution (2×2 km^2) WRF model simulations, configured with a threefold nested domain (18-6-2 km) and NCEP-FNL (0.25°) boundary conditions, to capture the complex meteorological and thermal dynamics of the Doon Valley, a rapidly urbanizing intermontane basin in the western Himalayas. The model effectively resolved the valley's topographic gradients and diurnal variability, providing a robust basis to assess how urban morphology modifies local temperature regimes.

The integration of the Urban Canopy Model coupled with the Building Effect Parameterization (WRF-UCM-BEP) substantially enhanced model fidelity, particularly in Dehradun (urbanized valley). Quantitative validation against India Meteorological Department (IMD) observations showed improvements in correlation ($r = 0.83 \rightarrow 0.86$) and index of agreement ($IOA = 0.72 \rightarrow 0.78$), along with a 15-20% reduction in *MAE* and *RMSE* for ambient (2 m) air temperature. These improvements were most pronounced during the pre-monsoon season, when urban heat storage, radiative trapping, and reduced evaporative cooling strongly influence temperature extremes. In contrast, the Mussoorie (hill station) site exhibited negligible improvement, underscoring that WRF-UCM-BEP primarily benefits simulations in urbanized low-lying valleys where built morphology governs local energy exchange.

The WRF-UCM-BEP configuration successfully reproduced the ambient urban heat island (UHI) in Dehradun, characterized by persistent nocturnal warming of 1-2°C and improved simulation of diurnal temperature cycles. It also improved the surface UHI representation by producing a compact and spatially coherent warm core that closely aligned with MODIS 1-km land surface temperature (LST) observations. This dual agreement between ambient and surface temperature patterns confirms the model's effectiveness in capturing both the atmospheric and radiative imprints of urbanization.

Vertical diagnostics further revealed that WRF-UCM-BEP improved the representation of boundary-layer structure, capturing realistic vertical mixing profiles while weakening katabatic winds (-1.5 to -2 m s^{-1}) and suppressing nocturnal inversion layers that ordinarily develop under stable nighttime conditions. The resulting disruption of mountain-breeze circulation indicates that urban morphology reduces nocturnal cooling and natural ventilation, thereby intensifying heat retention within the valley atmosphere.

Collectively, these findings highlight that urban morphology exerts a dominant control on both ambient and surface thermal environments in Dehradun, while exerting minimal influence over higher, less-urbanized terrain such as Mussoorie. The results emphasize the necessity of incorporating multilayer urban canopy schemes into high-resolution mesoscale models for topographically complex and rapidly urbanizing regions.

In addition to improving model realism, these insights have direct implications for urban planning, heat-stress mitigation, and air-quality management in Himalayan cities. Integrating urban morphological parameters into weather and climate modeling frameworks can support climate-resilient design strategies, improve urban ventilation planning, and inform sustainable growth policies for intermontane basins such as the Doon Valley.

References

Arthur R.S., Lundquist K.A., Mirocha J.D., Chow F.K., 2018, Topographic effects on radiation in the WRF model with the immersed boundary method: implementation, validation, and application to complex terrain, Monthly Weather Review, 156, 3277-3292, DOI: 10.1175/MWR-D-18-0108.1.

Bilang R.G.J.P., Blanco A.C., Santos J.A.S., Olaguera L.M.P., 2022, Simulation of Urban Heat Island during a high-heat event using WRF urban canopy models: a case study for Metro Manila, Atmosphere, 13 (10), DOI: 10.3390/atmos13101658.

Biswasharma R., Umakanth N., Pongener I., Longkumer I., Rao K.M.M., Pawar S.D., Gopalkrishnan V., Sharma S., 2024, Sensitivity analysis of cumulus and microphysics schemes in the WRF model in simulating Extreme Rainfall Events over the hilly terrain of Nagaland, Atmospheric Research, 304, DOI: 10.1016/j.atmosres.2024.107393.

Borrego C., Monteiro A., Ferreira J., Miranda A.I., Costa A.M., Carvalho A.C., Lopes M., 2008, Procedures for estimation of modelling uncertainty in air quality assessment, Environment International, 34 (5), 613-620, DOI: 10.1016/j.envint.2007.12.005.

Brown C.F., Brumby S.P., Guzder-Williams B., Birch T., Hyde S.B., Mazzariello J., Czerwinski W., Pasquarella V.J., Haertel R., Ilyushchenko S., Schwehr K., Weisse M., Stolle F., Hanson G., Guinan O., Moore R., Tait A.M., 2022, Dynamic World, near real-time global 10 m land use land cover mapping, Scientific Data, 9, DOI: 10.1038/s41597-022-01307-4.

Dhankar S., Singh G., Kumar K., 2024, Impacts of urbanization on land use, air quality, and temperature dynamics in Dehradun district of Uttarakhand, India: a comprehensive analysis, Frontiers in Environmental Science, 12, DOI: 10.3389/fenvs.2024.1324186

Dilawar A., Chen B., Guo L., Liu S., Shafeeque M., Arshad A., Hussain Y., Qureshi M.A., Kayiranga A., Wang F., Measho S., Zhang H., 2021, Evaluation the WRF model with different land surface schemes: Heat wave event simulations and its relation to pacific variability over Ccoastal region, Karachi, Pakistan, Sustainability, 13 (22), DOI: 10.3390/su132212608.

Ek M.B., Mitchell K.E., Lin Y., Rogers E., Grunmann P., Koren V., Gayno G., Tarpley J.D., 2003, Implementation of Noah land surface model advances in the National Centers for Environmental Prediction operational mesoscale Eta model, Journal of Geophysical Research: Atmospheres, 108 (D22), DOI: 10.1029/2002JD003296.

Farr T.G., Rosen P.A., Caro E., Crippen R., Duren R., Hensley S., Kobrick M., Paller M., Rodriguez E., Roth L., Seal D., Shaffer S., Shimada J., Umland J., Werner M., Oskin M., Burbank D., Alsdorf D.E., 2007, The shuttle radar topography mission, Reviews of Geophysics, 45 (2), DOI: 10.1029/2005RG000183.

Garuma G.F., 2018, Review of urban surface parameterizations for numerical climate models, Urban Climate, 24, 830-851, DOI: 10.1016/j.uclim.2017.10.006.

Gaur A., Lacasse M., Armstrong M., Lu H., Shu C., Fields A., Palou F.S., Zhang Y., 2021, Effects of using different urban parametrization schemes and land-cover datasets on the accuracy of WRF model over the City of Ottawa, Urban Climate, 35, DOI: 10.1016/j.uclim.2020.100737.

Golzio A., Ferrarese S., Cassardo C., Diolaiuti G.A., Pelfini M., 2021, Land-use improvements in the weather research and forecasting model over complex mountainous terrain and comparison of different grid sizes, Boundary-Layer Meteorology, 180, 319-351, DOI: 10.1007/s10546-021-00617-1.

Gupta P., Verma S., Mukhopadhyay P., Bhatla R., Payra S., 2024, Fidelity of WRF model in simulating heat wave events over India, Scientific Reports, 14 (1), DOI: 10.1038/s41598-024-52541-2.

Hendricks E.A., Knievel J.C., 2022, Evaluation of urban canopy models against near-surface measurements in Houston during a strong frontal passage, Atmosphere, 13 (10), DOI: 10.3390/atmos13101548.

Hong S.-Y., Dudhia J., Chen S.-H., 2004, A revised approach to ice microphysical processes for the bulk parameterization of clouds and precipitation, Monthly Weather Review, 132 (1), 103-120, DOI: 10.1175/1520-0493(2004)132<0103:ARATIM>2.0.CO;2.

Hong S.-Y., Noh Y., Dudhia J., 2006, A new vertical diffusion package with an explicit treatment of entrainment processes, Monthly Weather Review, 134 (9), 2318-2341, DOI: 10.1175/MWR3199.1.

Kain J.S., 2004 The Kain-Fritsch convective parameterization: an update, Journal of Applied Meteorology, 43 (1), 170-181, DOI: 10.1175/1520-0450(2004)043<0170:TKCPAU>2.0.CO;2.

Karki R., Hasson S., Gerlitz L., Schickhoff U., Scholten T, Böhner J., 2017, Quantifying the added value of convection-permitting climate simulations in complex terrain: a systematic evaluation of WRF over the Himalayas, Earth System Dynamics, 8 (3), 507-528, DOI: 10.5194/esd-8-507-2017.

Karppinen A., Kukkonen J., Elolähde T., Konttinen M., Koskentalo T., Rantakransa E., 2000, A modelling system for predicting urban air pollution: Model description and applications in the Helsinki metropolitan area, Atmospheric Environment, 34 (22), 3735-3743, DOI: 10.1016/S1352-2310(00)00074-1.

Lin C.-Y., Su C.-J., Kusaka H., Akimoto Y., Sheng Y.-F., Huang J.-C., Hsu H.-H., 2016, Impact of an improved WRF urban canopy model on diurnal air temperature simulation over northern Taiwan, Atmospheric Chemistry and Physics, 16 (3), 1809-1822, DOI: 10.5194/acp-16-1809-2016.

Liu H., Shang L., Li M., Zheng X., Shi P., 2024, WRF numerical simulation of summer precipitation and its application over the mountainous southern Tibetan Plateau based on different cumulus parameterization schemes, Atmospheric Research, 309, DOI: 10.1016/J.ATMOSRES.2024.107608.

Liu H., Zhao X., Duan K., Shang W., Li M., Shi P., 2023, Optimizing simulation of summer precipitation by weather research and forecasting model over the mountainous southern Tibetan Plateau, Atmospheric Research, 281, , DOI: 10.1016/J.ATMOSRES.2022.106484.

Liu S., 2024, Sensitivity of WRF-simulated 2 m temperature and precipitation to physics options over the Loess Plateau, Advances in Meteorology, 2024 (1), DOI: 10.1155/2024/6633255.

Luna M.A.G., Casallas A., Cerón L.C.B., Clappier A., 2020, Implementation and evaluation of WRF simulation over a city with complex terrain using Alos-Palsar 0.4 s topography, Environmental Science and Pollution Research, 27, 37818-37838, DOI: 10.1007/s11356-020-09824-8.

Maithani S., Nautiyal G., Sharma A., 2020, Investigating the effect of lockdown during COVID-19 on land surface temperature: study of Dehradun City, India, Journal of the Indian Society of Remote Sensing, 48 (9), 1297-1311,DOI: 10.1007/s12524-020-01157-w.

Martilli A., Clappier A., Rotach M.W., 2002, An urban surface exchange parameterization for mesoscale models, Boundary-Layer Meteorology, 104 (2), 261-304, DOI: 10.1023/A:1016099921195.

Min Y., Huang W., Ma M., Zhang Y., 2021, Simulations in the topography effects of Tianshan mountains on an extreme precipitation event in the Ili River valley, China, Atmosphere, 12 (6), DOI: 10.3390/atmos12060750.

Mishra A., Arya D.S., 2024, Assessment of land-use land-cover dynamics and urban heat island effect of Dehradun city, North India: a remote sensing approach, Environment, Development and Sustainability, 26 (9), 22421-22447, DOI: 10.1007/s10668-023-03558-6.

Mlawer E.J., Taubman S.J., Brown P.D., Iacono M.J., Clough S.A., 1997, Radiative transfer for inhomogeneous atmosphere: RRTM, a validated correlated-k model for the longwave, Journal of Geophysical Research: Atmospheres, 102 (D14), 16663-16682, DOI: 10.1029/97JD00237.

Monin A.S., Obukhov A.M., 1954, Basic laws of turbulent mixing in the surface layer of the atmosphere, Contributions of the Geophysical Institute, Academy of Sciences USSR, 24 (151), 163-187.

Mussetti G., Brunner D., Henne S., Allegrini J., Scott Krayenhoff E., Schubert S., Feigenwinter C., Vogt R., Wicki A., Carmeliet J., 2020, COSMO-BEP-Tree v1.0: a coupled urban climate model with explicit representation of street trees, Geoscientific Model Development, 13 (3), 1685-1710, DOI: 10.5194/gmd-13-1685-2020.

Namdev P., Sharan M., Srivastava A., Mishra S.K., 2024, An updated parameterization of the unstable atmospheric surface layer in the WRF model, Geoscientific Model Development, 17 (22), 8093-8115, DOI: 10.5194/gmd-17-8093-2024.

Navale A., Singh C., 2020, Topographic sensitivity of WRF-simulated rainfall patterns over the North West Himalayan region, Atmospheric Research, 242, DOI: 10.1016/j.atmosres.2020.105003.

NCAR, 2008, WRF Domain Wizard User Guide, National Center for Atmospheric Research, available online at https://www2.mmm.ucar.edu/wrf/users/ (data access 19.12.2025).

NCAR, 2024, available online at https://www.mmm.ucar.edu/models/wrf (data access 19.12.2025).

Noble E., Druyan L.M., Fulakeza M., 2014, The sensitivity of WRF daily summertime simulations over West Africa to alternative parameterizations. Part I: African wave circulation, Monthly Weather Review, 142 (4), 1588-1608, DOI: 10.1175/MWR-D-13-00194.1.

Ntoumos A., Hadjinicolaou P., Zittis G., Constantinidou K., Tzyrkalli A., Lelieveld J., 2023, Evaluation of WRF model boundary layer schemes in simulating temperature and heat extremes over the Middle East-North Africa (MENA) region, Journal of Applied Meteorology and Climatology, 62 (9), 1315-1332, DOI: 10.1175/JAMC-D-22-0108.1.

Politi N., Sfetsos A., Vlachogiannis D., Nastos P.T., Karozis S., 2020, A sensitivity study of high-resolution climate simulations for Greece, Climate, 8 (3), DOI: 10.3390/cli8030044.

Roukounakis N., Varotsos K.V., Katsanos D., Lemesios I., Giannakopoulos C., Retalis A., 2023, High resolution WRF modelling of extreme heat events and mapping of the Urban Heat Island characteristics in Athens, Greece, Sustainability, 15 (23), DOI: 10.3390/su152316509.

Silva R., Carvalho A.C., Carvalho D., Rocha A., 2021, Study of urban heat islands using different urban canopy models and identification methods, Atmosphere, 12 (4), DOI: 10.3390/atmos12040521.

Singh G., Ojha P.K., Sharma S.K., Kumari P., Pandey A.K., Mishra A.K., Kumar K., 2024a, Implications of urbanization on the seasonal dynamics and long-term trends in the thermal climate of a city in the Himalayan foothills of India, Journal of Geovisualization and Spatial Analysis, 8 (2), DOI: 10.1007/s41651-024-00178-0.

Singh J., Singh N., Ojha N., Dimri A.P., Singh R.S., 2024b, Impacts of different boundary layer parameterization schemes on simulation of meteorology over Himalaya, Atmospheric Research, 298, DOI: 10.1016/j.atmosres.2023.107154.

Singh J., Singh N., Ojha N., Sharma A., Pozzer A., Kiran Kumar N., Rajeev K., Gunthe S.S., Kotamarthi V.R., 2021, Effects of spatial resolution on WRF v3.8.1 simulated meteorology over the central Himalaya, Geoscience Model Development, 14 (3), 1427-1443, DOI: 10.5194/gmd-14-1427-2021.

Skamarock W.C., Klemp J.B., Dudhia J., Gill D.O., Liu Z., Berner J., Wang W., Powers J.G., Duda M.G., Barber D.M., Huang X.-Y., 2019, A description of the advanced research WRF Version 4, NCAR TECHNICAL NOTE, NCAR/TN–556+STR.

Thakur V.C., Rawat B.S., 1992, Geological Map of the Western Himalaya. Wadia Institute of Himalayan Geology, Dehradun.

Valdiya K.S., 1980, Geology of the Kumaun Lesser Himalaya, Wadia Institute of Himalayan Geology, Dehradun, India. 21 pp.

Wang Y., Brasseur G.P., Ma Y.-F., Peuch V.-H., Wang T., 2023, Does downscaling improve the performance of urban ozone modeling?, Geophysical Research Letters, 50 (23), DOI: 10.1029/2023GL104761.

Willmott C.J., 1981, On the validation of models, Physical Geography, 2 (2), 184-194, DOI: 10.1080/02723646.1981.10642213.

Zhang G., Zhu S., Zhang N., Zhang G., Xu Y., 2022, Downscaling hourly air temperature of WRF simulations over complex topography: a case study of Chongli District in Hebei Province, China, Journal of Geophysical Research: Atmospheres, 127 (3), DOI: 10.1029/2021JD035542.

Zhang X., Anagnostou E.N., Frediani M., Solomos S., Kallos G., 2013, Using NWP simulations in satellite rainfall estimation of heavy precipitation events over mountainous areas, Journal of Hydrometeorology, 14 (6), 1844-1858, DOI: 10.1175/JHM-D-12-0174.1.

Zittis G., Hadjinicolaou P., Lelieveld J., 2014, Comparison of WRF model physics parameterizations over the MENA-CORDEX domain, American Journal of Climate Change, 3 (5), 490-511, DOI: 10.4236/ajcc.2014.35042.

Trends and variability of seasonal rainfall in Ethiopian River basins: implications for water resource management

Melkamu Belay Mekonnen[1], Menale Wondie[2], Solomon Addisu[3]

[1] Ethiopian Meteorology Institute, Bahir Dar Center, Bahir Dar, Ethiopia

[2] Amhara Agricultural Research Institute, Bahir Dar, Ethiopia

[3] Bahir Dar University, Bahir Dar, Ethiopia

Abstract

This study examines the spatial and temporal variability of seasonal and annual rainfall across Ethiopia's major river basins using gauge observations and CHIRPS data for the period 1981-2023. Ethiopia's estimated mean annual rainfall is ~813.8 mm, but its distribution is highly uneven. The western basins Abay, Baro, and Omo receive more than 52% of the national total, highlighting their central role in the country's hydrology. Kiremit (June-September) is the dominant rainy season, contributing about 58.2% of annual rainfall nationwide. In contrast, Belg (February-May) and Bega (October-January) rainfall amounts are especially important in southeastern basins such as Genale and Shebele-Ogaden, where agriculture and pastoral livelihoods depend heavily on seasonal rainfall outside the main rainy period.

Trend analysis shows that rainfall has generally increased across Ethiopia, with about 88% of the time series exhibiting positive trends. The strongest increases are observed in the Abay and Baro basins, where annual rainfall has risen by up to 8.1 mm per year. In contrast, Belg rainfall shows declining trends in the Awash, Genale, and Shebele-Ogaden basins, and the Shebele-Ogaden basin also exhibits decreases in both Kiremit and annual rainfall. Variability analysis indicates that rainfall is most stable in the Abay and Baro basins (CV ≈ 0.09) and most variable in the Tekeze-Mereb and Denakil basins (coefficient of variation, CV >0.3). Overall, the results highlight growing basin-to-basin differences in rainfall behavior and point to the need for basin-specific water and agricultural management strategies to strengthen climate resilience.

Keywords

CHIRPS, climate adaptation, Ethiopia, rainfall variability, seasonal patterns, spatial analysis, water resource management.

Submitted 30 October 2025, revised 21 January 2026, accepted 23 January 2026

DOI: 10.26491/mhwm/217299

1. Introduction

Rainfall is the main driver of water availability and hydrological variability, and it strongly shapes how water resources are distributed across space and time (Trenberth, Shea 2005). Changes in rainfall directly affect runoff generation, flood occurrence, and drought development, making precipitation a central factor in water resource assessment and risk management (Mishra, Singh 2011). In Ethiopia, where agriculture is predominantly rain-fed, seasonal rainfall variability has far-reaching consequences for crop production, livestock, public health, and the wider economy. The country is especially sensitive to climate extremes because even modest shifts in rainfall timing or intensity can affect food security, land degradation, and water availability (Viste, Sorteberg 2013; Fazzini et al. 2015). Ethiopia also plays a critical regional role as a source for several major transboundary river basins in northeastern Africa, increasing the importance of understanding its rainfall dynamics (D'Souza, Jolliffe 2017).

Ethiopia's rainfall regime is commonly divided into three seasons: Bega (October-January), Belg (February-May), and Kiremit (June-September). These seasons are mainly controlled by the seasonal movement of the Intertropical Convergence Zone and its interaction with large-scale atmospheric circulation systems (Gissila et al. 2004; Jury 2018; Nicholson 2018; Aniley et al. 2025). Bega is generally dry and dominated by northeasterly winds, although limited rainfall occurs in southern and southeastern parts of the country (Jury, Funk 2013; Jury 2023). Belg is a shorter and more variable rainy season, influenced by tropical convection and moisture transport from the Arabian Sea (Ding, Sikka 2006; Jury 2010; Viste, Sorteberg 2013; Camberlin 2018). This season is particularly important for the Rift Valley, Genale, Shebelle, and Ogaden basins, but recent studies report a declining trend in Belg rainfall over eastern Ethiopia linked to ocean warming and circulation changes (Jury, Funk 2013; Mera 2018; Stojanovic et al. 2022; Jury 2023). Kiremit, driven by the summer monsoon and enhanced by tropical jet systems, is the main rainy season and provides most of the country's annual rainfall (Segele, Lamb 2005; Korecha, Barnston 2007; Viste, Sorteberg 2013; Jury 2022). Supporting the bulk of national food production, Kiremit is the most critical season for both agriculture and water resources (Fazzini et al. 2015; World Bank 2018; Abebe et al. 2022).

Variability in these rainfall seasons often leads to extreme events such as droughts and floods, with direct impacts on ecosystems, water availability, and agricultural productivity (Wagesho et al. 2013; Nicholson 2017; Zeleke, Damtie 2017; Mera 2018). Understanding how seasonal rainfall is changing across different river basins is therefore essential for climate adaptation, sustainable water management, and policy development in Ethiopia (de Sherbinin et al. 2008; Shortridge 2019; Moges, Bhat 2021; Gashaw et al. 2023; Kobe 2023).

While several studies have examined rainfall trends in Ethiopia, most focus on individual regions, short time periods, or single seasons. Basin-wide comparisons that consistently assess seasonal rainfall variability across all major river basins using long-term datasets remain limited. To address this gap, this study combines gauge observations and satellite-based rainfall data to analyze seasonal and annual rainfall trends and variability across Ethiopian river basins. By identifying basin-specific patterns and contrasts, the study aims to provide information directly relevant to agricultural planning, water resource management, and climate resilience efforts.

2. Materials and methods

2.1. Description of the study area

Ethiopia, spanning approximately 1.13 million km² between 3.30°–15°N and 33°–48°E, is characterized by diverse and complex topography, including highlands, rugged terrain, low plains, and the Great Rift Valley, which divides the country into distinct regions (Fig. 1). Elevations range from 144 m below sea level in the Danakil Depression to 4,620 m asl at Ras Dashen peak (Awulachew et al. 2007). This varied terrain contributes to significant spatial and temporal climate variability, including diverse rainfall regimes (Abbate et al. 2015; Fazzini et al. 2015; Camberlin 2018). The country is divided into several major river

basins that differ in size, flow, and elevation, with the Abay (Upper Blue Nile) Basin being the most prominent in terms of flow and tributaries, while the Rift Valley Basin is the smallest, yet known for its numerous lakes (Williams 2016).

Ethiopia's economy is heavily reliant on rain-fed agriculture, which employs the majority of the population and contributes significantly to GDP. However, frequent droughts have led to persistent food insecurity, affecting about 10% of households with high levels of malnutrition and dependence on food aid (WBG 2018; Abebe, Cirella 2023). The country also possesses a large livestock population, highlighting the critical importance of water and climate variability for both livelihoods and food security (WBG 2021; Zerssa et al. 2021).

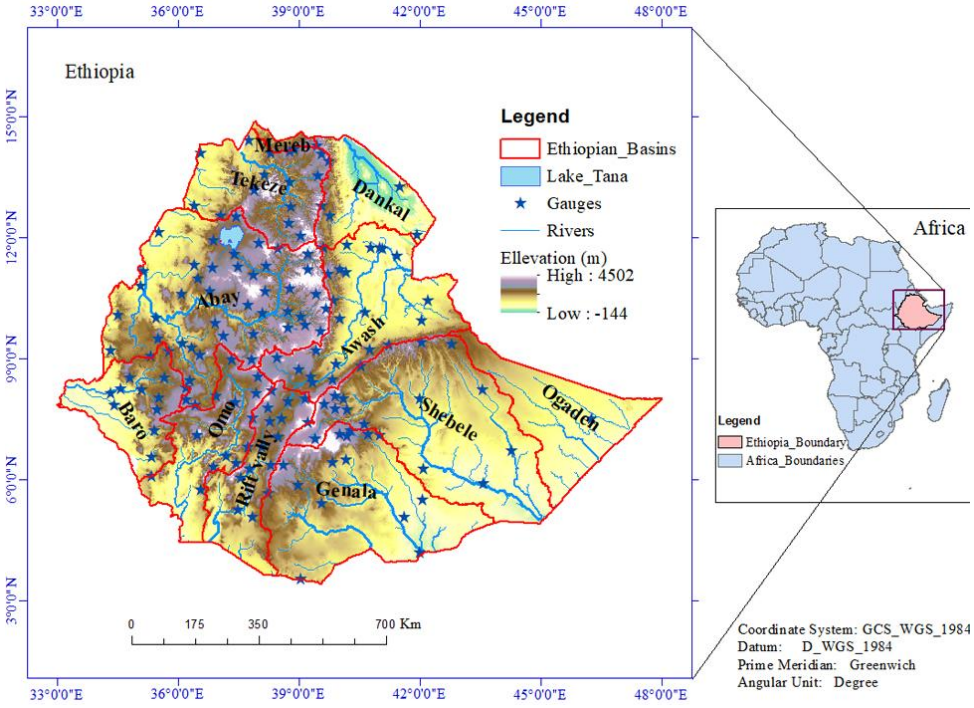

Fig. 1. Study area showing Ethiopia's river basins, elevation, and the locations of rain gauge stations used in the analysis.

2.2. Rainfall data sources

Daily rainfall data from 1981 to 2023 were obtained from 158 spatially representative rain gauge stations operated by the Ethiopian Meteorology Institute (EMI) (Fig. 1). Seasonal rainfall totals were derived from the daily records following the standard definitions of Bega, Belg, and Kiremit seasons. To complement gauge observations and improve spatial coverage, three gridded rainfall products were evaluated: CRU TS version 4.07 (Harris et al. 2020), CHIRPS version 2 (Funk et al. 2015), and TAMSAT, a long-term satellite-based rainfall dataset developed for Africa (Maidment et al. 2020). The performance of these products was assessed against gauge observations using multiple statistical metrics implemented in the Climate Data Tool (CDT). Among the three datasets, CHIRPS showed the best overall agreement with gauge data across most metrics (Table 1).

2.3. Data quality control and homogeneity testing

Quality control procedures were applied to ensure the reliability of the rainfall time series. These included outlier detection, trend testing, and homogeneity assessment following established approaches (Hamed, Rao 1998; Mudelsee 2019; Taylor 2022). Outliers were identified using the interquartile range (IQR) method, where values below Q1 − 1.5 IQR or above Q3 + 1.5 IQR were flagged (Tukey's method).

Homogeneity of the rainfall series was assessed using the Standard Normal Homogeneity Test (SNHT) (Alexandersson, Moberg 1998), implemented in CDT (Dinku et al. 2022). The SNHT is widely used in climatological studies for its ability to detect artificial shifts caused by changes in instrumentation or station location.

2.4. Seasonal rainfall contribution

The contribution of each season to annual rainfall was calculated as the ratio of the long-term seasonal mean to the long-term annual mean, expressed as a percentage. This allowed comparison of seasonal importance across river basins.

2.5. Temporal and spatial trends

Temporal rainfall trends were analyzed using the modified Mann–Kendall (MK) test, which accounts for serial correlation in hydroclimatic time series (Yue, Wang 2004). The Theil–Sen estimator was used to quantify the magnitude of trends, as it is robust to outliers and non-normal distributions. Spatial trends were analyzed using CDT to ensure consistency across basins.

To minimize the influence of autocorrelation, a pre-whitening procedure was applied before performing the MK test. This approach removes serial dependence while preserving the underlying trend signal, improving the reliability of trend detection.

2.6. Areal rainfall estimation

Areal mean rainfall for each basin was estimated using the Thiessen polygon method (Thiessen 1911; Mair, Fares 2011). This method assigns weights to each gauge based on the area it represents, assuming that rainfall within each polygon is best represented by the gauge located at its centroid.

The areal rainfall over the basin (R_T) is computed from:

$$R_T = T_i R_i \tag{1}$$

Where R_T is the observed rainfall at the center of the i^{th} polygon, and the weighting factor T_i is given by:

$$T_i = \frac{A_i}{A_T} \tag{2}$$

Where A_T is the total area of the basin or boundary and A_i is the area of each Thiessen polygon.

2.7. Rainfall variability

Rainfall variability was quantified using the coefficient of variation (CV), defined as the ratio of the standard deviation to the mean rainfall, expressed as a percentage (Blöschl, Sivapalan 1997; Pedersen et al. 2010). The CV was computed for individual stations and basin-wide areal means at both seasonal and annual scales. This metric provides a standardized measure for comparing variability across regions and seasons.

3. Results and discussion

3.1. Quality control and homogeneity

Quality control checks were carried out using a randomly selected subset of 50 rain gauge stations. Outlier analysis showed that 11 stations contained lower outliers, while only the Amba Maryam station exhibited both lower and upper outliers. These values correspond to known extreme conditions during drought-prone years, such as 1984, and are therefore considered physically plausible rather than erroneous. One upper outlier was detected at the Nedjo station for May 2014 and was traced to an encoding error; this value was removed from the analysis.

Trend and homogeneity testing indicated that most stations did not exhibit statistically significant trends. However, nine stations, including Amba Maryam, Lalibela, Elidar, Jimma, Filtu, Ime, Kebridihar, Axum Airport, and Maytsebri, showed increasing rainfall; Shoa Robit was the only station with a decreasing trend. Five stations (Elidar, Moyale, Filtu, Ime, and Kebridihar) were identified as non-homogeneous and non-stationary. This behavior is likely linked to data gaps and subsequent infilling, which can introduce artificial shifts in the time series.

Overall, the quality control results confirm that the majority of stations provide reliable rainfall records for trend analysis. At the same time, the presence of inhomogeneities in a small number of stations highlights the need for careful screening of long-term rainfall data, particularly when assessing trends at local scales.

3.3.1. Data validation

Data validation was carried out by comparing three satellite-based rainfall products (CHIRPS, CRU, and TAMSAT) to gauge observations using several statistical performance metrics. The aim was to assess how well each product represents observed rainfall and to identify the most suitable dataset for subsequent analysis.

Overall, CHIRPS shows the strongest performance across most evaluation metrics, indicating a high level of accuracy and reliability in capturing rainfall amounts (Table 1). CRU also performs reasonably well but exhibits slightly higher errors and bias compared to CHIRPS. TAMSAT generally shows weaker performance in terms of error-based metrics such as RMSE and MAE. However, it performs better in terms of bias and false detection rates, suggesting fewer false rainfall events and lower systematic error.

Although TAMSAT may therefore be considered a more conservative dataset, CHIRPS provides the best overall balance between accuracy and reliability among the three products. Based on these results, CHIRPS was selected, together with gauge data, for further analysis and graphical presentation in this study.

Table 1. Performance ranking of CHIRPS, CRU, and TAMSAT rainfall datasets based on selected statistical evaluation metrics.

Performance	CHIRPS	CRU	TAMSAT
	Weakest		Strongest
CORR	0.977	0.944	0.876
BR2	0.953	0.868	0.744
BIAS	1.054	1.092	0.989
PBIAS	5.422	9.249	-1.053
ME	3.467	5.915	-0.673
MAE	8.584	12.32	14.586
RMSE	11.265	17.221	25.518
NSE	0.947	0.876	0.728
MNSE	0.797	0.708	0.655
RNSE	-7.759	-11.434	0.482
IOA	0.986	0.967	0.935
MIOA	0.895	0.853	0.834
RIOA	-1.37	-2.268	0.876
POD	1	0.998	0.921
POFD	1	1	0.385
FAR	0.028	0.028	0.012
FBS	1.029	1.026	0.932
CSI	0.972	0.97	0.911
HSS	0	-0.004	0.248
MQB	1.082	1.153	1.061
MQE	-2.535	2.277	3.552
VHI	0.975	0.953	0.887
QPOD	0.966	0.937	0.869
VFAR	0.118	0.159	0.142
QFAR	0.146	0.196	0.178
VMI	0.025	0.047	0.113
QMISS	0.034	0.063	0.131
VCSI	0.863	0.807	0.773
QCSI	0.828	0.763	0.731

3.2. Seasons of Ethiopia and their contributions to annual total rainfall

Ethiopia's three distinct rainfall seasons are Bega (October-January), the dry season with little rainfall; Belg (Feb-May), the second rainy season following the main Kiremit; and Kiremit (June-September), the primary rainy season that supplies the majority of the country's annual rainfall.

3.2.1. Bega

In southern and southeastern Ethiopia, the Bega season (October-January) represents the second most important rainfall period. Rainfall during this season is mainly associated with the retreat of the summer monsoon and the southward movement of the Intertropical Convergence Zone (ITCZ). Precipitation typically peaks in October and ranges from about 290 to 510 mm in parts of the southeastern Rift Valley, southern Omo, and the southwestern Baro basin (Fig. 2).

At the basin scale, the contribution of Bega rainfall to annual totals varies considerably. The Baro and Omo basins receive the highest seasonal mean rainfall during Bega, with averages of 244.7 mm and 258.1 mm, respectively. In contrast, the Tekeze-Mereb and Denakil basins receive much lower rainfall during this season and show relatively high variability. The Genale and Wabishebele-Ogaden basins stand out in terms of proportional contribution, with Bega rainfall accounting for up to 48% of their annual totals (Table 3).

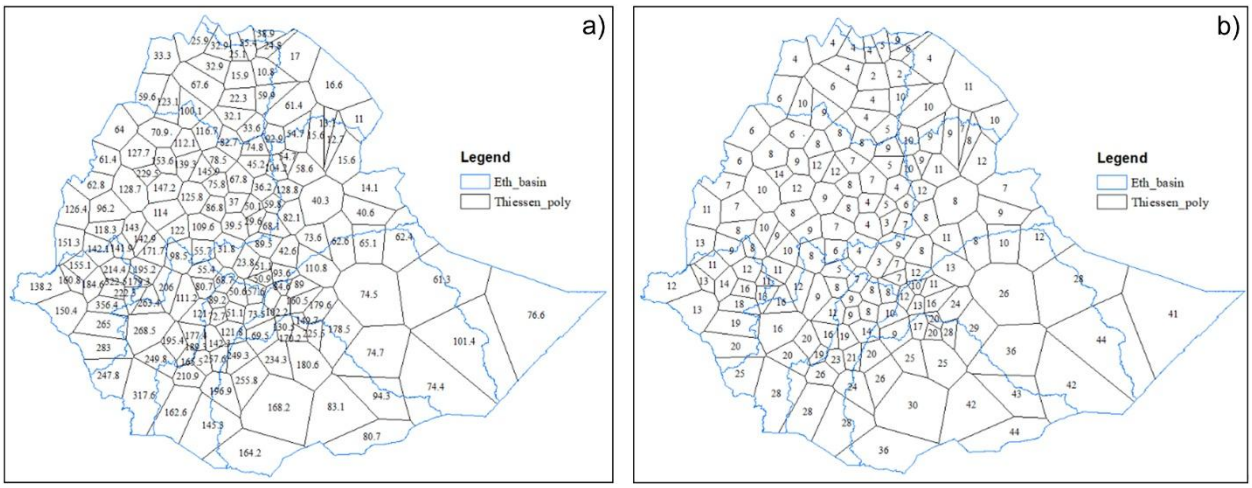

Fig. 2. (a) Spatial distribution of mean Bega seasonal precipitation and (b) its percentage contribution to annual rainfall, based on gauge observations and corresponding Thiessen polygons.

Other basins, including Abay, Awash, and the Rift Valley, receive comparatively modest Bega rainfall, accompanied by marked spatial and temporal variability. These differences highlight the diverse hydrological behavior of Ethiopian river basins during the Bega season and underline the importance of considering basin-specific rainfall characteristics in water resource planning.

3.2.2. Belg

The Belg season (February-May) is the main rainy period for the Rift Valley, Genale, Shebele, and Ogaden river basins, whereas it functions as a shorter secondary rainy season in other parts of Ethiopia. This season is marked by high temperatures, particularly from March to May, and by strong rainfall variability. In lowland areas, these conditions can increase the risk of wildfires and place additional stress on water and agricultural systems.

Rainfall amounts during Belg vary widely across the country. Southern and southwestern basins such as Abay, Baro, and Omo receive moderate to high rainfall, typically between 250 and 800 mm. In contrast, northern and eastern basins, including Tekeze-Mereb and Denakil, receive much lower amounts, in some locations as little as 17 mm (Fig. 3). Over the past four decades, Belg rainfall has declined by approximately 10-25% in eastern Ethiopia, reinforcing concerns about increasing moisture stress in these regions. Among the basins, Baro stands out as both the wettest and most stable during Belg, whereas Tekeze-Mereb remains one of the driest and most variable.

At the basin level, Belg rainfall contributes a substantial share of the annual total in southeastern Ethiopia. The Genale Basin receives about 100-500 mm during Belg, accounting for 36-60% of its annual rainfall, with a long-term mean of 324 mm (54%), making Belg the wettest season for this basin (Tables 2 and 3). The Wabishebele-Ogaden Basin shows a similar dependence, with Belg rainfall contributing 31-52% of the annual total (mean of 188 mm). The Denakil Basin receives considerably less rainfall, but Belg still accounts for up to one-third of its annual total.

Despite the long-term declining trend, recent years (since 2020) show signs of recovery in Belg rainfall over parts of southeastern and eastern Ethiopia (Fig. 3).

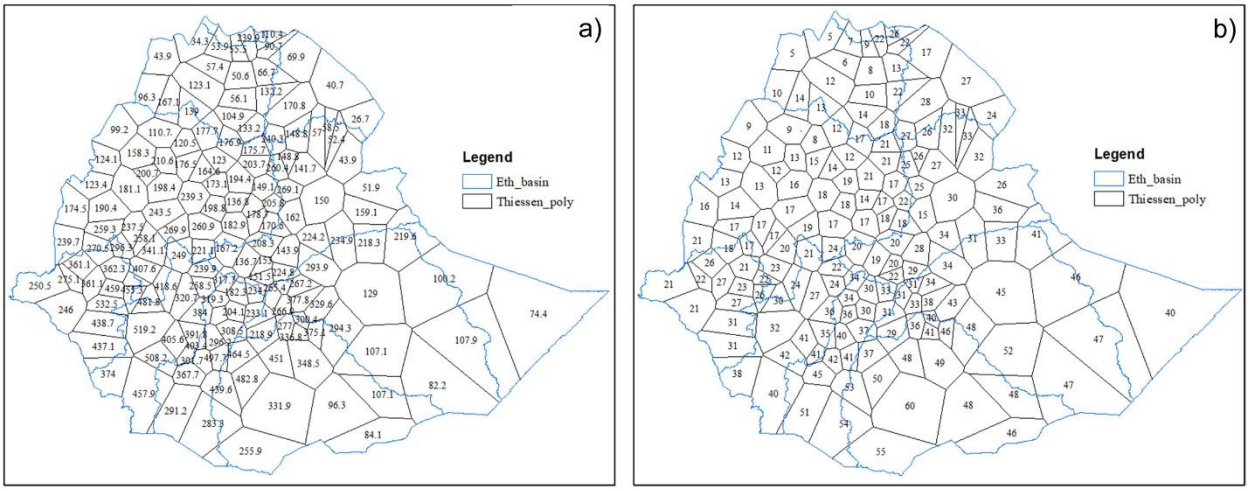

Fig. 3. (a) Spatial distribution of mean Belg seasonal precipitation and (b) its percentage contribution to annual rainfall, based on gauge observations and corresponding Thiessen polygons.

3.2.3. Kiremit

The Kiremit season (June-September) is Ethiopia's main rainy period, providing the bulk of annual rainfall across most river basins. Rainfall during this season is widespread and relatively consistent, with peaks typically occurring in July and August, coincident with limited temperature variability. Because of its dominant contribution to water availability and crop production, Kiremit is the most economically important rainfall season in the country.

During Kiremit, the Abay, Tekeze–Mereb, and northeastern Denakil basins receive 70-92% of their annual rainfall. Other basins, including Awash, Baro, southern Abay, northern Omo, and the northeastern Rift Valley, receive about 60-70% of their yearly totals during this season. Rainfall amounts show strong spatial contrasts, with western basins receiving the highest totals. Central parts of the Abay Basin and northeastern Baro receive up to 1600 mm, whereas eastern basins such as Genale and Wabishebele-Ogaden receive much lower amounts, typically between 50 and 300 mm (Fig. 4).

The Abay Basin stands out with the highest seasonal mean rainfall (941.2 mm, accounting for 73% of the annual total) and the lowest variability (CV = 0.07). Baro, Tekeze-Mereb, and Omo also receive substantial Kiremit rainfall, though with higher variability. In contrast, eastern basins such as Genale, Wabishebele-Ogaden, and Denakil receive limited rainfall and show greater spatial variability, particularly in Denakil and Awash, which exhibit the highest CV values during Kiremit (Tables 2 and 3).

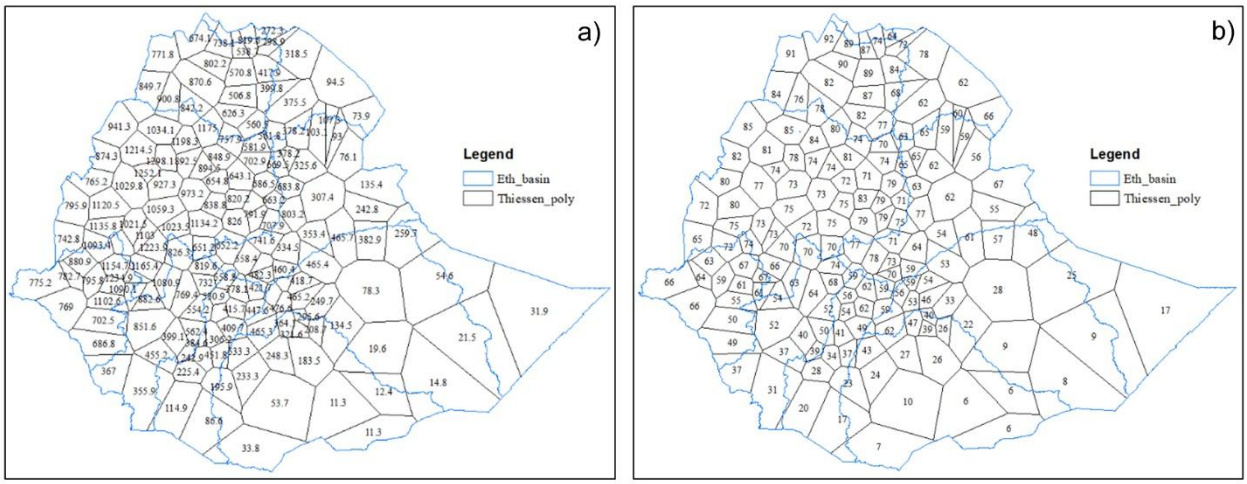

Fig. 4. (a) Spatial distribution of mean Kiremit seasonal precipitation and (b) its percentage contribution to annual rainfall, based on gauge observations and corresponding Thiessen polygons.

3.3. Basin-scale annual areal mean precipitation

Analysis based on CHIRPS rainfall data for 1981-2023 provides a consistent view of the spatial distribution of annual rainfall across Ethiopian river basins. The relatively high spatial resolution of CHIRPS (0.05°, approximately 5 km × 5 km) allows a more detailed representation of rainfall patterns than gauge data alone, particularly in regions with sparse station coverage.

The highest annual rainfall occurs in western and southwestern Ethiopia, notably in the central and southern parts of the Abay Basin, western Baro, and central to northwestern Omo, including areas around Jimma. In these regions, annual rainfall commonly exceeds 1800 mm, with some locations receiving more than 2000 mm. Among all basins, the Abay Basin stands out not only for receiving the largest volume of rainfall but also for its relatively low interannual variability (CV = 0.09), indicating a more stable rainfall regime (Table 3). At the national scale, Ethiopia's mean annual rainfall is estimated at 813.8 mm, although this average masks strong regional contrasts (Table 2).

Table 2. Basins' contribution to national annual rainfall total.

Basin	Area (km^2)	Precipitation (mm)	Areal precipitation (BMC)	Percentage contribution in Ethiopian total rainfall
Abay	199,811.85	1282.8	256.3	28.6
Awash	116,865.20	569.3	66.5	7.4
Baro	75,912.10	1442.9	109.5	12.2
Dankal	63,137.04	343.6	22.0	2.5
Genala	173,383.08	598.8	103.8	11.6
Omo	78,616.94	1357.8	106.7	11.9
Riftvally	52,749.83	893.8	47.1	5.3
Shebele-Ogaden	280,892.86	396.0	111.2	12.4
Tekeze-Mereb	89,712.86	827.0	74.1	8.3

In terms of areal contribution, the Abay Basin, covering 199,812 km^2, accounts for 28.6% of the country's total annual rainfall, while the Denakil Basin contributes the smallest share, 2.5% (Table 2).

These results underline the dominant role of the Abay Basin in Ethiopia's water resources. Together with the Tekeze and Baro basins, it supplies more than 80% of the annual flow of the Nile River system, highlighting its regional hydrological importance (Yitayew Melesse 2011).

Table 3. Areal mean seasonal rainfall contribution (%) and coefficient of variation (CV) across Ethiopian river basins.

No	Basin name	Area (km^2)	Areal mBega	Cv	Areal mBelg	Cv	Areal mKirem.	Cv	Areal mAnn.	Cv	Annual percentage contribution		
											Bega	Belg	Kiremit
1	Abay	199,812	117.6	0.31	224.1	0.21	941.2	0.07	1282.8	0.07	9	17	73
2	Awash	116,865	52.4	0.45	177.1	0.30	339.9	0.17	569.3	0.12	9	31	60
3	Baro	75,912	244.7	0.25	377.8	0.13	820.6	0.09	1442.9	0.09	17	26	57
4	Dankal	64,137	44.1	0.27	124.4	0.35	175.3	0.29	343.6	0.17	13	36	51
5	Genala	173,383	180.7	0.45	324.0	0.25	94.2	0.16	598.8	0.18	30	54	16
6	Omo	78,617	258.1	0.38	466.7	0.17	633.9	0.12	1357.8	0.10	19	34	47
7	Riftvally	52,750	208.5	0.35	377.4	0.20	308.4	0.15	893.8	0.11	23	42	35
8	Shebele-Ogaden	280,893	114	0.58	187.7	0.25	94.4	0.14	396.0	0.20	29	47	24
9	Tekeze-Mereb	89,713	50.9	0.38	113.9	0.32	662.3	0.12	827.0	0.10	6	14	80

The mean annual precipitation map for 1981-2023 highlights the strong hydroclimatic contrasts across Ethiopia, largely shaped by complex topography and large-scale atmospheric circulation. The western river basins Abay, Baro, and Omo together receive 52.7% of the country's total rainfall (Table 2), whereas the eastern basins remain persistently in water-deficit due to their arid and semi-arid conditions. These marked spatial and temporal differences in rainfall underline the uneven distribution of water resources across the country. A clear understanding of this variability is essential for effective water resource management, agricultural planning, and the design of climate adaptation strategies that are tailored to basin-specific conditions (Wagesho et al. 2013; Ayehu et al. 2021).

3.4. Temporal and spatial precipitation trends

Analysis of both gauge observations and CHIRPS data indicates that rainfall trends across Ethiopia are predominantly positive at seasonal and annual scales. Increasing trends are observed in most basins, particularly during the Kiremit season, which largely controls annual rainfall totals (Table 4; Fig. 5, 6, 7, and 9).

3.4.1. Bega

Rainfall during the Bega season (October-January) shows pronounced year-to-year variability across Ethiopian river basins. Periods of reduced rainfall commonly coincide with strong El Niño events, while wetter conditions are generally observed during La Niña years, highlighting the influence of large-scale climate drivers on Bega rainfall (Fig. 5).

Despite this interannual variability, long-term trends from 1981 to 2023 indicate a generally stable to slightly increasing pattern. Analysis of rainfall records from 158 stations shows that about 88% of the

time series exhibit positive trends during Bega, although most of these trends are not statistically significant (Table 4). Areas with localized decreases are limited and scattered, and the magnitude of decline is small. In contrast, five stations show statistically significant increasing trends, and nearly half of the stations in southern and southeastern Ethiopia record significant increases in Bega rainfall.

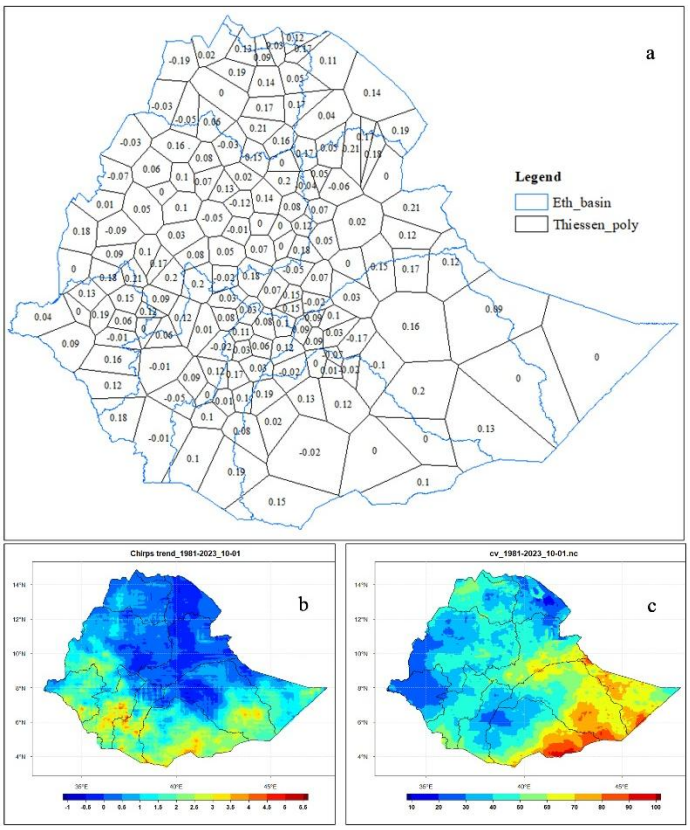

Fig. 5. (a) Bega areal mean precipitation trends based on gauge observations shown using Thiessen polygons and Kendall's Tau values, (b) corresponding CHIRPS-based precipitation trends (mm yr^{-1}), and (c) the coefficient of variation.

Overall, the results do not indicate any widespread or systematic decline in Bega precipitation at the basin scale. Instead, the observed patterns suggest that Bega rainfall remains relatively stable, with modest increases in some regions, particularly in the southern and southeastern basins.

3.5.2. Belg

Between 1981 and 2023, Belg rainfall (February-May) shows strong spatial and temporal variability across Ethiopian river basins. Analysis of the 158 gauge time series indicates a mixed pattern, with 57% of stations showing increasing trends and 43% showing declines. This contrast is most evident between the eastern and southern parts of the country. CHIRPS data confirm a widespread decline in Belg rainfall over eastern basins, including Awash, Genale, the Rift Valley, and Wabishebele–Ogaden, along with localized decreases in parts of the Abay and Baro basins. At the same time, many areas continue to show stable or increasing trends, particularly in southern and southeastern Ethiopia (Fig. 6).

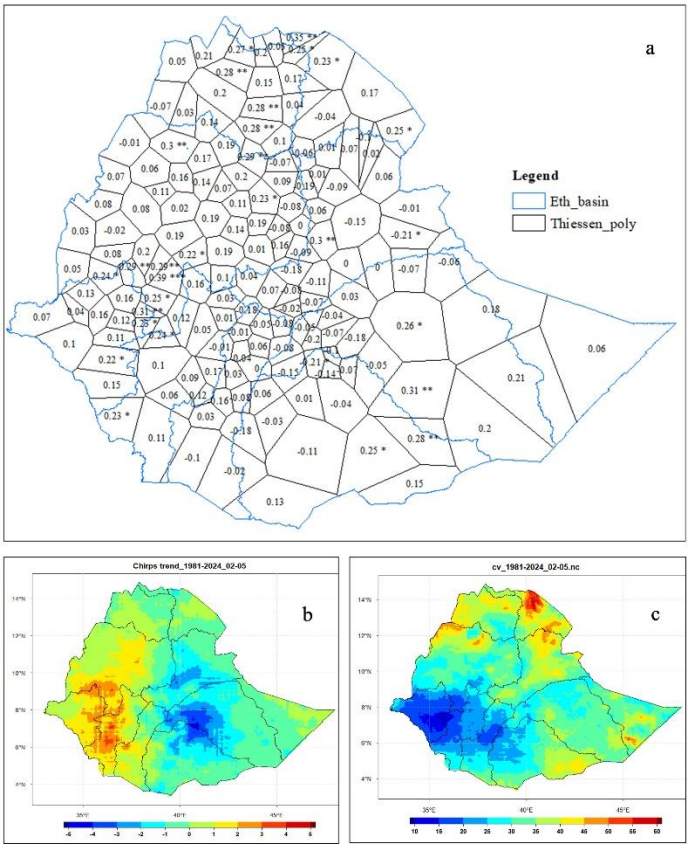

Fig. 6. (a) Belg areal mean precipitation trends based on gauge observations shown using Thiessen polygons and Kendall's Tau values, (b) corresponding CHIRPS-based precipitation trends (mm yr^{-1}), and (c) the coefficient of variation.

The strongest trend signals highlight the uneven nature of Belg rainfall change. Nekemte shows a highly significant positive trend ($p \leq 0.01$), while Adele and Bale Robe exhibit highly significant negative trends at the same confidence level (Fig. 6a). At a less strict significance threshold ($p \leq 0.1$), 15 stations (9.5%) display strong negative trends, whereas 16 stations (10.1%) show strong positive trends. Overall, about one-quarter of the stations record statistically significant increases in Belg rainfall, mainly concentrated in southern and southeastern basins (Table 4).

Because Belg rainfall is critical for land preparation, early crop establishment, and the transition to the main Kiremit season, these trends have direct implications for agricultural planning (Diro et al. 2011). Declining Belg rainfall in eastern basins increases the risk of early-season drought and water stress, while increasing trends in southern Ethiopia may enhance cropping opportunities and seasonal water availability. These contrasting patterns reinforce the need for region-specific water management and adaptive strategies that reflect local rainfall behavior (Gudina et al. 2025).

3.5.3. Kiremit

Kiremit (June-September) is Ethiopia's main rainy season and plays a central role in agriculture, hydropower generation, and overall water availability. Analysis of areal mean Kiremit rainfall trends from

1981 to 2023, based on both gauge observations and CHIRPS data, reveals pronounced spatial variability across Ethiopian river basins.

Most basins show a tendency toward increasing Kiremit rainfall. The Abay Basin, in particular, exhibits a clear upward trend, despite some local declines, reinforcing its importance for rain-fed agriculture and its contribution to the Blue Nile system. The Baro-Akobo Basin also shows a consistent increase in rainfall, which supports both transboundary river flows and agricultural water supply. Similarly, the Omo-Gibe Basin displays increasing rainfall trends, with positive implications for hydropower generation and farming activities. The Tekeze Basin shows moderately positive trends, while the Awash and Genale-Dawa basins exhibit mixed behavior, with increasing rainfall in upstream and midstream areas but declines in downstream sections (Fig. 7).

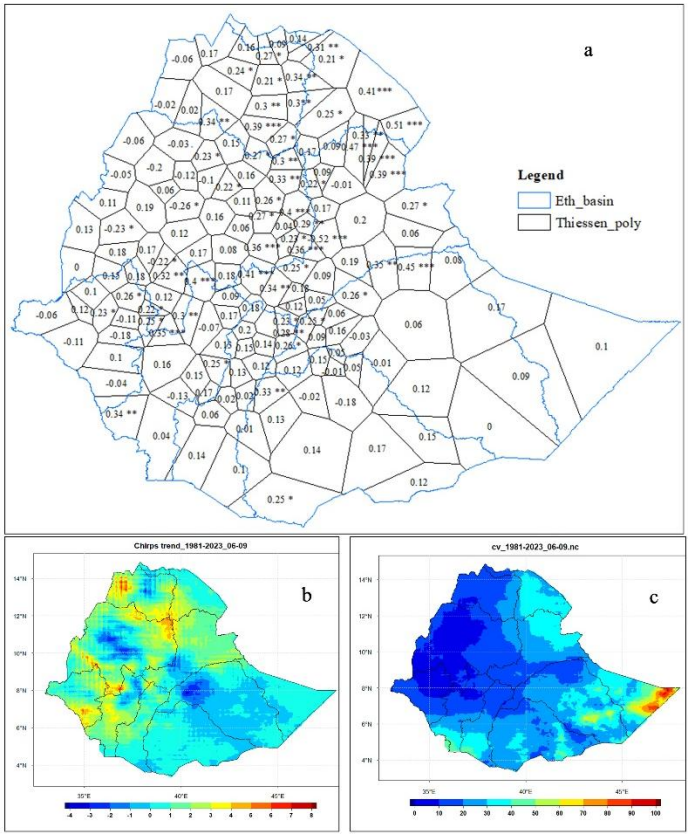

Fig. 7. (a) Kiremit areal mean precipitation trends based on gauge observations shown using Thiessen polygons and Kendall's Tau values, (b) corresponding CHIRPS-based precipitation trends (mm yr^{-1}), and (c) the coefficient of variation.

In contrast, Kiremit rainfall shows declining tendencies in the Rift Valley and Wabishebele basins. Given existing water scarcity and the dependence of local livelihoods on seasonal rainfall, these declines are a cause for concern. Reduced Kiremit rainfall in these basins may increase drought risk, limit irrigation potential, and place additional pressure on water supply systems.

Statistical testing confirms the dominance of increasing trends during the Kiremit season. The Mann–Kendall test indicates that 130 time series (82%) show increasing trends, while 26 (16%) show decreases.

Strong positive trends at the highest confidence level ($p \leq 0.01$) are observed at 29 stations, mainly in the Abay, Awash, and Wabishebele basins. Strong negative trends at the same level are rare and are observed only at the Shewa Robit station in the Abay Basin. At a lower significance threshold ($p \leq 0.1$), strong positive trends occur at 63 stations, particularly in the Abay, Tekeze, and Denakil basins, while strong negative trends are limited to seven stations (Table 4). Overall, the results indicate that increasing Kiremit rainfall is the dominant signal across Ethiopia, although localized declines point to emerging water stress in some basins.

3.5.4. Annual precipitation trend

Trends in areal mean annual precipitation over Ethiopia from 1981 to 2023 were assessed using both gauge observations and CHIRPS data, applying the modified Mann–Kendall test. Trend direction and significance were evaluated using the Tau statistic and associated p-values. Results from both datasets indicate an overall increase in annual rainfall, although the level of significance differs between them. The gauge data show a highly significant upward trend ($p < 0.001$), while CHIRPS indicates a moderately significant increase
($p < 0.05$), suggesting a persistent long-term rise in annual precipitation across the country (Fig. 9).

Spatial patterns derived from gauge data are illustrated using Thiessen polygons, where each polygon represents the area closest to a rainfall station (Fig. 9a). Tau values range from −0.47 to 0.50, with positive values indicating increasing rainfall and negative values indicating declines. Most stations show positive trends, and 21 gauges exhibit significant increases (Tau ≈ 0.36-0.52). The strongest increases are observed at Amde Work in the northeastern Abay Basin, consistently identified by both gauge and satellite datasets. In contrast, only one station, Shewa Robit, shows a strong and significant decreasing trend (Tau = −0.47) (Table 4; Fig. 8).

Table 4. Summary of gauge-based temporal precipitation trends.

Trend	Qualifying	a	Bega	%	Belg	%	Kiremit	%	Annual	%
Positive (increasing)	exceptionally likely	≤1%	4	3	13	8	29	18	45	28
	extremely likely	≤5%	11	7	27	17	54	34	70	44
	very likely	≤10%	29	18	40	25	63	40	83	53
	total increasing		125	79	105	66	130	82	133	84
Negative (decreasing)	total decreasing		27	17	49	31	26	16	23	15
	very likely	≤10%	1	1	8	5	7	4	2	1
	extremely likely	≤5%	0	0	2	1	4	3	1	1
	exceptionally likely	≤1%	0	0	0	0	1	1	1	1

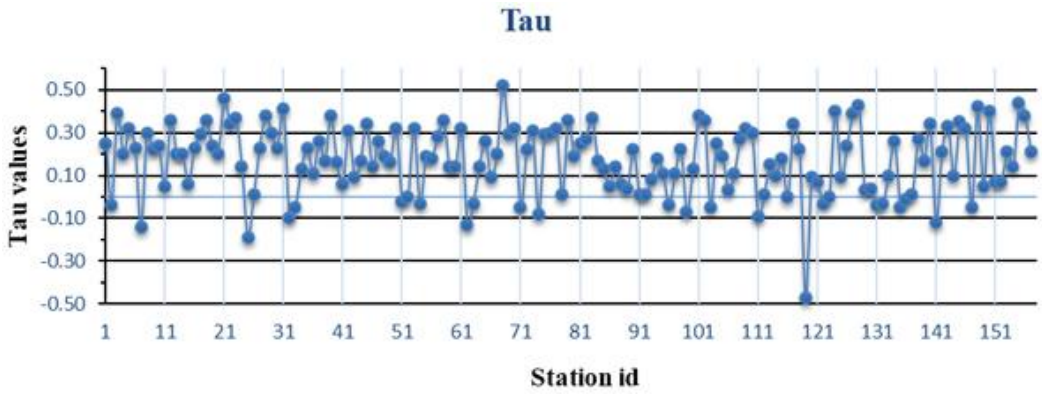

Fig. 8. Modified Mann–Kendall test Tau values for annual precipitation (1981-2023) based on 158 rain gauge stations.

The gauge-based analysis reveals marked spatial variability. Strong positive trends dominate northeastern, central, and southeastern Ethiopia, while parts of the western region show weaker or mixed signals. This spatial heterogeneity reflects regional differences in climate forcing and has important implications for basin-level water availability and agricultural planning.

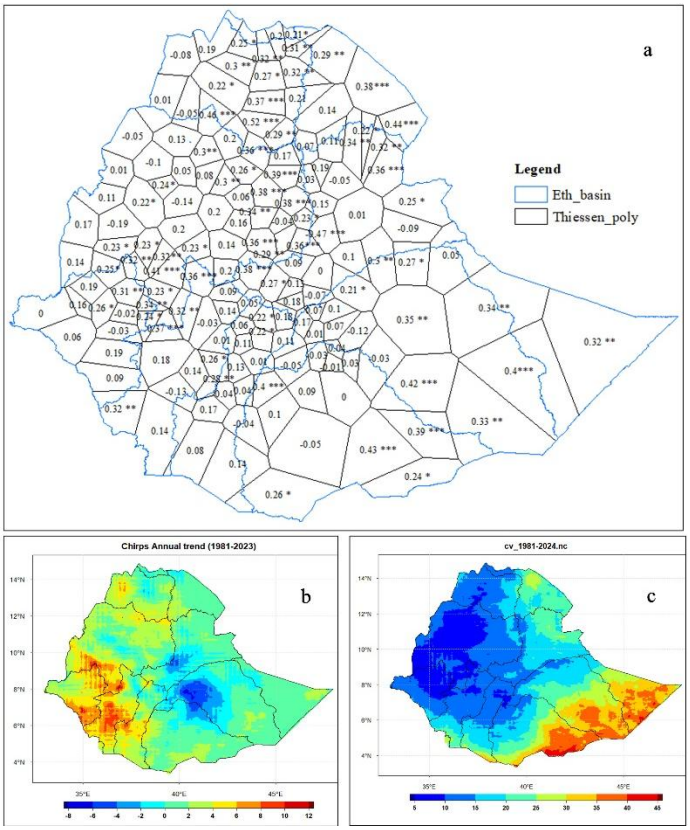

Fig. 9. Annual areal mean precipitation trends based on gauge observations shown using Thiessen polygons and Kendall's Tau values, (b) corresponding CHIRPS-based precipitation trends (mm yr^{-1}), and (c) the coefficient of variation (c).

CHIRPS-based trend maps (Fig. 9b) provide a broader spatial perspective and generally support the gauge-based findings. Western and southwestern Ethiopia show the strongest increases, reaching up to 12 mm per year. Central Ethiopia exhibits mixed trends, while eastern regions mostly show weak increases or near-stable conditions. Although local variations remain, both datasets consistently indicate a general increase in annual precipitation across Ethiopia, with the most pronounced changes occurring in the western basins.

3.6. Basin-scale areal mean precipitation trends

Analysis of areal mean precipitation trends at the basin scale reveals clear contrasts in how rainfall is changing across Ethiopia. The Abay Basin shows a statistically significant increase in both annual and Bega rainfall, along with a notable upward trend during the Kiremit season. In contrast, the Awash Basin does not exhibit any statistically significant trends across seasons or in the annual series.

The Baro Basin stands out for showing consistent and significant increases across all time scales, including annual, Kiremit, Belg, and Bega rainfall. The Denakil Basin shows a significant increase only during the Kiremit season, while the Genale Basin exhibits a significant increasing trend during Bega. The Omo Basin records significant increases in annual and Bega rainfall, and the Rift Valley Basin shows similar significant increases in both annual and Bega precipitation.

By comparison, the Wabishebele and Tekeze basins do not show statistically significant trends in any season or in the annual totals (Table 5). These basin-specific differences highlight the uneven nature of rainfall change across Ethiopia and reinforce the importance of considering individual basin characteristics when assessing climate impacts on water resources and planning adaptation strategies.

Table 5. Temporal trends in areal mean precipitation across Ethiopian river basins.

Basin	Annual			Kiremit			Belg			Bega		
	Tau	p_value	Signif.	Tau	p_value	Signif.	Tau	p_value	Signif.	Tau	p_value	Signif.
Abay	0.289	0.00651	**	0.205	0.05415		0.154	0.14867		0.220	0.03825	*
Awash	0.076	0.47668		0.189	0.07522		–0.176	0.09822		0.010	0.93328	
Baro	0.362	0.00065	***	0.229	0.03109	*	0.327	0.00209	**	0.234	0.02797	*
Dankal	0.194	0.06861		0.216	0.04233	*	–0.039	0.72197		–0.021	0.85058	
Genala	0.043	0.69086		0.032	0.76950		–0.136	0.20168		0.249	0.01907	*
Omo	0.327	0.00209	**	0.174	0.10255		0.134	0.20917		0.236	0.02651	*
Riftvally	0.262	0.01352	*	0.15	0.16081		0.043	0.69086		0.300	0.00472	**
Shebele-Ogaden	–0.025	0.81791		–0.003	0.98330		–0.176	0.09822		0.161	0.13181	
Tekeze-Mereb	0.136	0.20168		0.13	0.22475		0.003	0.98330		0.167	0.11646	

Note: Shebeleo = Shebele-Ogaden; Tekezem = Tekeze-Mereb

4. Summary and conclusion

This study examined the spatial and temporal variability of seasonal and annual rainfall across Ethiopia's major river basins using gauge observations and CHIRPS data for 1981-2023. The results confirm that

Ethiopia's rainfall regime is highly variable, shaped by complex interactions among large-scale circulation systems, including the seasonal migration of the ITCZ, the Somali Jet, and tropical easterly flows.

The main findings can be summarized as follows:

- Ethiopia's mean annual rainfall is 813.8 mm, with strong regional contrasts. The western basins – Abay, Baro, and Omo – receive 52.7% of the country's total precipitation, while the Abay Basin alone accounts for 28.6%, underscoring its dominant role in national and downstream water availability.
- Kiremit is the primary rainy season, contributing about 58.2% of annual rainfall nationwide. Belg and Bega provide critical rainfall in specific basins, particularly in the Rift Valley, Genale, and Shebele-Ogaden, where livelihoods depend on rainfall outside the main Kiremit season.
- Trend analysis shows that rainfall has generally increased across most basins and seasons, with 88% of the time series exhibiting positive trends. The strongest increases occur in the Abay and Baro basins, with annual rainfall rising by up to 8.1 mm per year.
- In contrast, Belg rainfall shows declining trends in eastern basins such as Awash, Genale, and Shebele-Ogaden, where rainfall is essential for early crop establishment and pasture availability. The Shebele-Ogaden Basin also exhibits a consistent decline in annual and Kiremit rainfall, indicating increasing vulnerability to water stress.
- Variability analysis highlights marked spatial differences. The Abay and Baro basins show relatively stable rainfall regimes (CV ~ 0.09), whereas the Tekeze-Mereb and Denakil basins experience much higher variability (CV > 0.3).
- Reliability for agriculture and water resources was further supported by the CV analysis, which showed significant spatial variability: the Abay and Baro basins had the most stable rainfall regimes (CV ~0.09), while the Tekeze-Mereb and Denakil basins had the highest annual rainfall variability (CV > 0.3).

These findings have direct implications for water resource management and climate adaptation in Ethiopia. Increasing rainfall in western basins offers opportunities for improved water storage, irrigation development, and hydropower generation. At the same time, declining and highly variable rainfall in eastern basins highlights the need for targeted adaptation measures, including drought preparedness, improved pasture management, and investment in water-harvesting infrastructure.

Overall, this study provides a basin-scale perspective on Ethiopia's rainfall dynamics that can support evidence-based planning and climate-resilient water management. Future work should integrate hydrological modeling with higher-resolution climate projections to better assess impacts on streamflow, agriculture, and water security.

References

Abbate E., Bruni P., Sagri M., 2015, Geology of Ethiopia: a review and geomorphological perspectives, [in:] Landscapes and Landforms of Ethiopia, P. Billi (ed.), Springer, Dodrecht, 33-64, DOI: 10.1007/978-94-017-8026-1_2.

Abebe B.A., Grum B., Degu A.M., Goitom H., 2022, Spatio-temporal rainfall variability and trend analysis in the Tekeze-Atbara river basin, northwestern Ethiopia, Meteorological Applications, 29 (2), DOI: 10.1002/met.2059.

Abebe S.T., Cirella G.T., 2023, Shocks from the COVID-19 Crisis in Ethiopia, [in:] Uncertainty Shocks in Africa: Impact and Equilibrium Strategies for Sound Economic and Social Development, G.T. Cirella (ed.), Springer, 65-81, DOI: 10.1007/978-3-031-21885-9_4.

Alexandersson H., Moberg A., 1998, Homogenization of Swedish temperature data. Part I: Homogeneity test for linear trends, International Journal of Climatology, 17 (1), 25-34, DOI: 10.1002/(SICI)1097-0088(199701)17:1<25::AID-JOC103>3.0.CO;2-J.

Aniley E., Zemen A., Belay M., Birku B., Taye H., 2025, Evaluating rainfall forecasting capability of multi-source weather (MSWX) product over rainfall regimes of Ethiopia, Geocarto International, 40 (1), DOI: 10.1080/10106049.2025.2480298.

Awulachew S.B., Yilma A.D., Loulseged M., Loiskandl W., Ayana M., Alamirew T., 2007, Water Resources and Irrigation Development in Ethiopia, Working Paper 123, International Water Management Institute, Colombo, Sri Lanka, 78 pp.

Ayehu G.T., Tadesse T., Gessesse B., 2021, Spatial and temporal trends and variability of rainfall using long-term satellite product over the Upper Blue Nile Basin in Ethiopia, Remote Sensing in Earth Systems Sciences, 4 (3), 199-215, DOI: 10.1007/s41976-021-00060-3.

Blöschl G., Sivapalan M., 1997, Process controls on regional flood frequency: Coefficient of variation and basin scale, Water Resources Research, 33 (12), 2967-2980, DOI: 10.1029/97WR00568.

Camberlin P., 2018, Climate of Eastern Africa, [in:] Oxford Research Encyclopedia of Climate Science, DOI: 10.1093/acrefore/9780190228620.013.512.

D'Souza A., Jolliffe D., 2017, A profile of food insecurity dynamics in rural and small town Ethiopia, Ethiopian Journal of Economics, 25 (2), 77-112, DOI: 10.22004/ag.econ.259504.

de Sherbinin A., VanWey L.K., McSweeney K., Aggarwal R., Barbieri A., Henry S., Hunter L.M., Twine W., Walker R., 2008, Rural household demographics, livelihoods and the environment, Global Environmental Change, 18 (1), 38-53, DOI: 10.1016/j.gloenvcha.2007.05.005.

Ding Y., Sikka D., 2006, Synoptic systems and weather, [in:] The Asian Monsoon, Springer Praxis Books, Springer, Berlin, Heidelberg, 131-201, DOI: 10.1007/3-540-37722-0_4.

Dinku T., Faniriantsoa R., Islam S., Nsengiyumva G., Grossi A., 2022, The climate data tool: enhancing climate services across Africa, Frontiers in Climate, 3, DOI: 10.3389/fclim.2021.787519.

Diro G.T., Grimes D.I.F., Black E., 2011, Teleconnections between Ethiopian summer rainfall and sea surface temperature: part II. Seasonal forecasting, Climate Dynamics, 37 (1), 121-131, DOI: 10.1007/s00382-010-0896-x.

Fazzini M., Bisci C., Billi P., 2015, The Climate of Ethiopia, [in:] Landscapes and Landforms of Ethiopia, P. Billi (ed.), Springer, Dordrecht, 65-87, DOI: 10.1007/978-94-017-8026-1_3.

Funk C., Peterson P., Landsfeld M., Pedreros D., Verdin J., Shukla S., Husak G., Rowland J., Harrison L., Hoell A., 2015, The climate hazards infrared precipitation with stations – a new environmental record for monitoring extremes, Scientific Data, 2 (1), DOI: 10.1038/sdata.2015.66.

Gashaw T., Wubaye G.B., Worqlul A.W., Dile Y.T., Mohammed J.A., Birhan D.A., Tefera G.W., van Oel P.R., Haileslassie A., Chukalla A.D., Taye M.T., Bayabil H.K., Zaitchik B., Srinivasan R., Senamaw A., Bantider A., Adgo E., Seid A., 2023, Local and regional climate trends and variabilities in Ethiopia: Implications for climate change adaptations, Environmental Challenges, 13, DOI: 10.1016/j.envc.2023.100794.

Gissila T., Black E., Grimes D.I.F., Slingo J.M., 2004, Seasonal forecasting of the Ethiopian summer rains, International Journal of Climatology, 24 (11), 1345-1358, DOI: 10.1002/joc.1078.

Gudina L.B., Zhang J., Lu Y., Xin X., Wu T., Game A.T., Zhang X., Waza M.A., Liu C., 2025, Leading modes of Belg rainfall variability in Ethiopia, Climate Dynamics, 63 (4), DOI: 10.1007/s00382-025-07694-9.

Hamed K.H., Rao A.R., 1998, A modified Mann-Kendall trend test for autocorrelated data, Journal of Hydrology, 204 (1-4), 182-196, DOI: 10.1016/S0022-1694(97)00125-X.

Harris I., Osborn T.J., Jones P., Lister D., 2020, Version 4 of the CRU TS monthly high-resolution gridded multivariate climate dataset, Scientific Data, 7 (1), DOI: 10.1038/s41597-020-0453-3.

Jury M.R., 2010, Ethiopian decadal climate variability, Theoretical and Applied Climatology, 101, 29-40, DOI: 10.1007/s00704-009-0200-3.

Jury M.R., 2018, Characteristics of Ethiopia air chemistry and its meteorological context, Earth Interactions, 22 (12), DOI: 10.1175/EI-D-17-0009.1.

Jury M.R., 2022, Representing the Indian Ocean Dipole, Physical Oceanography, 29 (4), 417-432, DOI: 10.22449/1573-160X-2022-4-417-432.

Jury M.R., 2023, Characterizing Northeast Africa drought and its drivers, Climate, 11 (6), DOI: 10.3390/cli11060130.

Jury M.R., Funk C., 2013, Climatic trends over Ethiopia: regional signals and drivers, International Journal of Climatology, 33 (8), 1924-1935, DOI: 10.1002/joc.3560.

Kobe F.T., 2023, Understanding climate change in Ethiopia: impacts and solutions, International Journal of Big Data Mining for Global Warming, 5 (2), DOI: 10.1142/S2630534823300014.

Korecha D., Barnston A.G., 2007, Predictability of June-September rainfall in Ethiopia, Monthly Weather Review, 135 (2), 628-650, DOI: 10.1175/MWR3304.1.

Maidment R., Black E., Greatrex H., Young M., 2020, TAMSAT, [in:] Satellite Precipitation Measurement, V. Levizzani, C. Kidd, D.B. Kirschbaum, C.D. Kummerow, K. Nakamura, F.J. Turk (eds.), Advances in Global Change Research, 67, 393-408, DOI: 10.1007/978-3-030-24568-9_22.

Mair A., Fares A., 2011, Comparison of rainfall interpolation methods in a mountainous region of a tropical island, Journal of Hydrologic Engineering, 16 (4), 371-383, DOI: 10.1061/(ASCE)HE.1943-5584.0000330.

Mera G.A., 2018, Drought and its impacts in Ethiopia, Weather and Climate Extremes, 22, 24-35, DOI: 10.1016/j.wace.2018.10.002.

Mishra A.K., Singh V.P., 2011, Drought modeling – A review, Journal of Hydrology, 403 (1-2), 157-175, DOI: 10.1016/j.jhydrol.2011.03.049.

Moges D.M., Bhat H.G., 2021, Climate change and its implications for rainfed agriculture in Ethiopia, Journal of Water and Climate Change, 12 (4), 1229-1244, DOI: 10.2166/wcc.2020.058.

Mudelsee M., 2019, Trend analysis of climate time series: A review of methods, Earth-Science Reviews, 190, 310-322, DOI: 10.1016/j.earscirev.2018.12.005.

Nicholson S.E., 2017, Climate and climatic variability of rainfall over eastern Africa, Reviews of Geophysics, 55 (3), 590-635, DOI: 10.1002/2016RG000544.

Nicholson S.E., 2018, The ITCZ and the seasonal cycle over equatorial Africa, Bulletin of the American Meteorological Society, 99 (2), 337-348, DOI: 10.1175/BAMS-D-16-0287.1.

Pedersen L., Jensen N.E., Christensen L.E., Madsen H., 2010, Quantification of the spatial variability of rainfall based on a dense network of rain gauges, Atmospheric Research, 95 (4), 441-454, DOI: 10.1016/j.atmosres.2009.11.007.

Segele Z.T., Lamb P.J., 2005, Characterization and variability of Kiremt rainy season over Ethiopia, Meteorology and Atmospheric Physics, 89 (1), 153-180, DOI: 10.1007/s00703-005-0127-x.

Shortridge J., 2019, Observed trends in daily rainfall variability result in more severe climate change impacts to agriculture, Climatic Change, 157 (3), 429-444, DOI: 10.1007/s10584-019-02555-x.

Stojanovic M., Mulualem G. M., Sorí R., Vázquez M., Nieto R., Gimeno L., 2022, Precipitation moisture sources of Ethiopian river basins and their role during drought conditions, Frontiers in Earth Science, 10, DOI: 10.3389/feart.2022.929497.

Taylor J.R., 2022, An Introduction to Error Analysis. The Study of Uncertainties in Physical Measurements, University Science Books, 392 pp.

Thiessen A.H., 1911, Precipitation averages for large areas, Monthly Weather Review, 39 (7), 1082-1089, DOI: 10.1175/1520-0493(1911)39<1082b:PAFLA>2.0.CO;2.

Trenberth K.E., Shea D.J., 2005, Relationships between precipitation and surface temperature, Geophysical Research Letters, 32 (14), DOI: 10.1029/2005GL022760.

Viste E., Sorteberg A., 2013, Moisture transport into the Ethiopian highlands, International Journal of Climatology, 33 (1), 249-263, DOI: 10.1002/joc.3409.

Wagesho N., Goel N.K., Jain M.K., 2013, Temporal and spatial variability of annual and seasonal rainfall over Ethiopia, Hydrological Sciences Journal, 58 (2), 354-373, DOI: 10.1080/02626667.2012.754543.

WBG, 2018, Ethiopia Economic Update: The Inescapable Manufacturing-Services Nexus: Exploring the Potential of Distribution Services, World Bank Group, 90 pp.

WBG, 2021, Ethiopia Economic Update, No. 8: Ensuring Resilient Recovery from COVID-19, World Bank Group, DOI: 10.1596/35550.

Williams F.M., 2016, Understanding Ethiopia, Springer International Publishing, Australia. 343 pp., DOI: 10.1007/978-3-319-02180-5.

World Bank, 2018, The Ethiopia economic update: The inescapable manufacturing-services nexus, World Bank, Washington DC, available online at https://www.tralac.org/news/article/13055-ethiopia-economic-update-the-inescapable-manufacturing-services-nexus.html (data access 02.02.2026).

Yitayew M., Melesse A.M., 2011, Critical Water Resources Issues in the Nile River Basin, [in:] Nile River Basin: Hydrology, Climate and Water Use, A.M. Melesse (ed.), Springer, Dordrecht, 401-416, DOI: 10.1007/978-94-007-0689-7_20.

Yue S., Wang C., 2004, The Mann-Kendall test modified by effective sample size to detect trend in serially correlated hydrological series, Water Resources Management, 18 (3), 201-218, DOI: 10.1023/B:WARM.0000043140.61082.60.

Zeleke T.T., Damtie B., 2017, Temporal and Spatial Climate Variability and Trends Over Abay (Blue Nile) River Basin, [in:] Social and Ecological System Dynamics. AESS Interdisciplinary Environmental Studies and Sciences Series, Springer, Cham., 59-75, DOI: 10.1007/978-3-319-45755-0_6.

Zerssa G., Feyssa D., Kim D.-G., Eichler-Löbermann B., 2021, Challenges of smallholder farming in Ethiopia and opportunities by adopting climate-smart agriculture, Agriculture, 11 (3), DOI: 10.3390/agriculture11030192.

Projected CMIP6 temperature changes over Sudan under SSP2-4.5 and SSP5-8.5 for mid- and late-21st century

Khalid Hilal

Independent researcher

Abstract

Understanding future temperature changes in Sudan is essential for climate-risk assessment and adaptation planning in this highly vulnerable and data-scarce region. This study evaluates robust projected changes in near-surface air temperature at both annual and seasonal scales in summer (June-September) and winter (December-February) relative to the historical baseline period (1995-2014). Projections are provided for the mid-century (2041-2060) and late-century (2081-2100) under the moderate SSP2-4.5 and high-emission SSP5-8.5 scenarios, based on a bias-corrected ensemble of CMIP6 climate models. Bias correction was applied using Equidistant Quantile Mapping (EQM) for historical simulations and Delta Quantile Mapping (DQM) for future projections to ensure consistency with observed climatology. The results indicate pronounced, scenario-dependent warming across all seasons. By mid-century, annual mean temperatures are projected to rise by 1.68°C under SSP2-4.5 and 2.17°C under SSP5-8.5, reaching 2.68°C and 4.87°C, respectively, by late-century. Seasonal analysis reveals the most intense and variable warming during summer, while winter exhibits more stable increases with narrower inter-model uncertainties. Spatially, northern and central Sudan are expected to experience the strongest warming, with high inter-model agreement. These findings underscore escalating heat-stress risks and highlight the urgent need for emissions mitigation and targeted adaptation strategies to support climate-resilient planning and sustainable development in Sudan.

Keywords

CMIP6, climate change, temperature projections, bias correction, seasonal warming, multi-model ensemble, emissions scenarios.

Submitted 24 September 2025, revised 19 January 2026, accepted 3 February 2026

DOI: 10.26491/mhwm/217736

1. Introduction

Sudan is situated at the intersection of North Africa and the eastern Sahel, encompassing a broad range of climatic zones from hyper-arid deserts in the north to semi-arid savannahs in the south. This geographic and climatic diversity renders the country highly sensitive to variations in temperature and precipitation. Rising temperatures, intensified heat extremes, and shifts in seasonal climate patterns pose significant risks to food security, water availability, energy demand, and public health. With more than 80 % of the population dependent on rain-fed agriculture and pastoral livelihoods, even modest warming can substantially disrupt crop yields, livestock productivity, and hydrological systems (NUPI, SIPRI 2022; WBG 2023).

Historically, Sudan's climate exhibits pronounced spatial and seasonal gradients. Mean annual temperatures are high across the country, ranging from approximately 22°C in the southern regions to >28°C in the northern deserts, with summer (June-September) and winter (December-February) as the two dominant seasonal periods affecting agricultural and water-resource planning. Observational analyses indicate a consistent warming trend across Sudan over the past five decades, in line with regional and global signals of anthropogenic climate change (NUPI, SIPRI 2022). Nevertheless, high-resolution projections of future seasonal temperatures remain limited, hindering robust adaptation planning.

Global climate models (GCMs) from the Coupled Model Intercomparison Project Phase 6 (CMIP6) provide a state-of-the-art framework for assessing potential future climates under alternative socioeconomic and emissions pathways. The Shared Socioeconomic Pathways (SSPs) describe internally consistent scenarios linking demographic, economic, and technological developments with greenhouse-gas emissions. Of particular relevance to mid- and late-century planning are SSP2-4.5, a "middle-of-the-road" scenario representing intermediate mitigation, and SSP5-8.5, a high-emission trajectory reflecting limited mitigation efforts (Almazroui et al. 2020). These scenarios encompass plausible futures for Sudan's climate and provide a foundation for evaluating adaptation strategies.

Although numerous studies have examined climate trends across the broader Sahel, most focus on precipitation or annual mean temperature and often employ coarse spatial resolution. Seasonal-scale temperature projections for Sudan, particularly those that resolve sub-national gradients and inter-model uncertainty, remain scarce. Recent African climate assessments highlight warming trends but often aggregate Sudan into larger sub-regions, obscuring spatial patterns critical for local adaptation (NUPI, SIPRI 2022; WMO 2024). The spread between models, internal climate variability, and systematic biases further complicate interpretation if not addressed through bias correction and ensemble analysis.

To address these knowledge gaps, this study applies high-resolution (0.5°) bias-corrected CMIP6 simulations to quantify projected seasonal and annual temperature over or mid-century (2041-2060) and end-of-century (2081-2100). Bias correction is performed using Equidistant Quantile Mapping (EQM), a well-established statistical approach that reduces systematic model errors while preserving projected climate signals (Cannon et al. 2015). By focusing on annual, summer, and winter anomalies relative to the 1995-2014 baseline, and explicitly assessing inter-model agreement and spread, this study provides a scientifically rigorous, high-resolution assessment of future temperature changes over Sudan.

The primary objectives of this study are to quantify projected seasonal temperature changes across Sudan for the periods 2041-2060 and 2081-2100 under the SSP2-4.5 and SSP5-8.5 scenarios, respectively, and to evaluate the spatial distribution of warming to identify regions and seasons most vulnerable to increasing temperatures. By achieving these objectives, this work delivers a robust, high-resolution assessment of mid- and late-century temperature change over Sudan.

2. Data and study area

2.1. Data sources

Near-surface air temperature data were derived from two primary sources. Observational data were obtained from the Climate Research Unit (CRU) monthly dataset, version 4.09 (Harris et al. 2023) at 0.5° × 0.5° resolution for 1995-2014, providing a robust baseline for model evaluation and bias correction. Historical and future projections for the mid-century (2041-2060) and late-century (2081-2100) periods were obtained from ten CMIP6 models under the SSP2-4.5 (moderate emissions) and SSP5-8.5 (high emissions) scenarios. CMIP6 datasets were accessed via https://data.ceda.ac.uk/badc/cmip6/data/CMIP6/.

All CMIP6 datasets were re-gridded to the CRU grid (0.5° × 0.5°) to ensure spatial consistency and were subsequently bias-corrected against the observational reference. Only models with complete monthly coverage over the historical period were included. A full list of models, along with their horizontal resolutions, variant labels, and key references, is provided in Table 1. These datasets were used to evaluate projected changes in near-surface air temperature over Sudan.

Table 1. CMIP6 models used in this study, with horizontal resolution, variant label, and source institute.

No.	CMIP6 Model	Institute/Country	Resolution (°)	Variant label	Reference
1	ACCESS-ESM1-5	CSIRO & Bureau of Meteorology/Australia	1.9° × 1.3°	r1i1p1f1	Ziehn et al. (2020)
2	BCC-CSM2-MR	Beijing Climate Center/China	1.1° × 1.1°	r1i1p1f1	Wu et al. (2019)
3	FIO-ESM-2-0	First Institute of Oceanography/China	1.3° × 0.9°	r1i1p1f1	Bao et al. (2019)
4	GISS-E2-1-G	NASA Goddard Institute for Space Studies/USA	2° × 2.5°	r1i1p1f1	Kelley et al. (2020)
5	HadGEM3-GC31-LL	Met Office Hadley Centre/UK	1.9° × 1.3°	r1i1p1f3	Jones et al. (2024)
6	INM-CM4-8	Institute of Numerical Mathematics/Russia	2° × 1.5°	r1i1p1f1	Volodin et al. (2023)
7	KACE-1-0-G	Korea Meteorological Administration/South Korea	1.3° × 0.9°	r1i1p1f1	Byun et al. (2023)
8	MPI-ESM1-2-HR	Max Planck Institute for Meteorology/Germany	0.9° × 0.9°	r1i1p1f1	Gutjahr et al. (2019)
9	TaiESM1	Research Center for Environmental Changes/Taiwan	1.3° × 0.9°	r1i1p1f1	Lee et al. (2020)
10	UKESM1-0-LL	Met Office Hadley Centre & UK partners/UK	1.9° × 1.3°	r1i1p1f2	Sellar et al. (2019)

2.2. Study area

The study encompasses the entire territory of Sudan, which extends from approximately 8° N to 23.5° N in latitude and from 21° E to 39° E in longitude. Sudan spans a broad climatic gradient, ranging from hyper-arid deserts in the north to semi-arid plains and savannah landscapes in the central and southern regions. This gradient produces pronounced spatial differences in temperature, rainfall, and seasonal climate patterns, resulting in distinct hot-dry and cooler-wet periods across the country (Funk et al. 2011; WBG 2023).

Mean annual temperatures generally range from around 22°C in the southern savannahs to above 28°C in the northern deserts. Topography and elevation strongly influence local and regional temperature regimes and climate variability. Elevation ranges from roughly 200 m above sea level in the southern plains to approximately 1,800 m in the northern and eastern highlands, with the Jebel Marra volcanic massif in western Sudan rising above 3,000 m (Fig. 1). These topographic differences, along with land cover, soil properties, and proximity to rivers, shape local and topo-climatic conditions and modulate the distribution of heat across the country (WMO 2024).

Sudan's sensitivity to climate variability, reliance on rain-fed agriculture, limited water resources, and exposure to extreme heat events make understanding seasonal temperature variability particularly important. Characterizing temperature changes across these diverse climatic zones provides essential information for

agricultural planning, water-resource management, and public-health preparedness. A spatially explicit understanding of warming patterns is therefore critical for informing adaptation strategies and mitigating the impacts of projected mid-century temperature increases (NUPI, SIPRI 2022; WBG 2023).

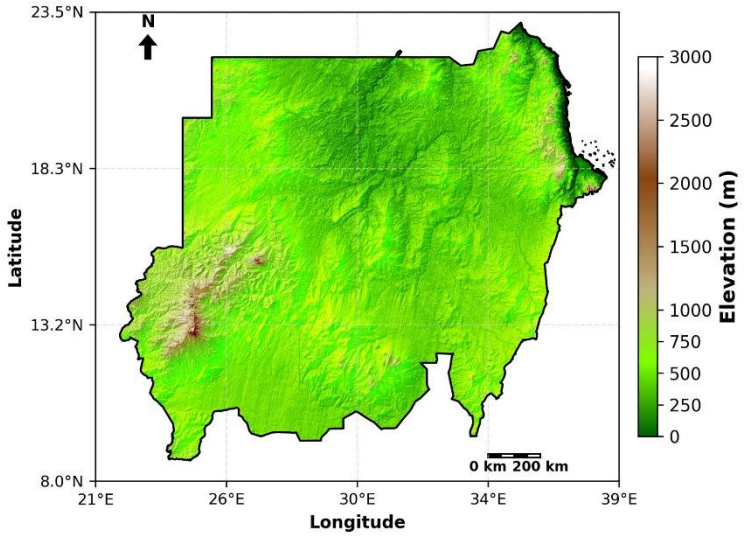

Fig. 1. Topographic map of Sudan illustrating elevation gradients from 200 m in the southern plains to 1,800 m in the northern and eastern highlands, with Jebel Marra exceeding 3,000 m.

3. Methodology

3.1. Bias correction

CMIP6 model outputs were bias-corrected against CRU TS 4.09 observations to reduce systematic deviations in historical simulations and improve the reliability of future projections. Two complementary methods were employed: Empirical Quantile Mapping (EQM) for historical simulations and Delta Quantile Mapping (DQM) for future projections.

EQM is a non-parametric technique that adjusts the cumulative distribution of simulated values to match the observed distribution. For a raw model value X_{raw}, the bias-corrected value is defined as:

$$X_{corrected} = F_{obs}^{-1}\left(F_{mod}(X_{raw})\right) \quad (1)$$

where F_{mod} represents the empirical cumulative distribution function (CDF) of the model data, and F_{obs}^{-1} is the inverse CDF of the observational data (Gudmundsson et al. 2012). Applying EQM ensures that historical simulations accurately reflect observed climatology, providing a validated baseline for subsequent analyses.

Delta Quantile Mapping (DQM) was applied to future projections to adjust biases while preserving the projected climate signal. For a future model value X_{fut}, the corrected value is given by:

$$X_{fut,corr} = X_{fut} + \left(F_{obs}^{-1}(p) - F_{mod,hist}^{-1}(p)\right) \quad (2)$$

where p represents the percentile of the future value within the historical model distribution $F_{mod,hist}$ (Xavier et al. 2022). This method preserves anomalies relative to the historical period while adjusting for systematic biases. Comparative evaluations have shown that quantile-based methods such as DQM maintain the climate change signal more reliably than traditional quantile mapping techniques (Lehner et al. 2023).

Using both EQM and DQM provides a robust framework for assessing projected temperature changes. EQM ensures the historical baseline is accurate, while DQM allows future projections to retain their physical consistency, enabling reliable quantification of seasonal and annual temperature anomalies as well as inter-model uncertainty over Sudan.

3.2. Data processing, ensemble statistics, and model agreement

Monthly mean near-surface air temperature (TAS) from ten CMIP6 GCMs and CRU observational data (CRU TS 4.09; Harris et al. 2023) were aggregated into annual, summer, and winter climatologies for the 1995-2014 baseline period. To ensure spatial consistency with observations, all CMIP6 outputs were re-gridded to the CRU 0.5° × 0.5° latitude–longitude grid using conservative remapping in the Climate Data Operators (CDO) and masked to Sudan's national boundary.

Future projections under SSP2-4.5 and SSP5-8.5 were evaluated for the mid-century (2041-2060) and late-century (2081-2100) periods. For each SSP and season, the multi-model ensemble mean was used to represent the central tendency of projected monthly mean TAS changes, while the ensemble standard deviation quantified inter-model spread. Grid cells where at least two-thirds of models projected warming of the same sign were classified as regions of likely change (≥66 % model agreement), following standard CMIP6 assessment protocols (Eyring et al. 2016; IPCC 2021).

Projected changes were tested for statistical significance at each grid cell using a two-sample Student's t-test, comparing the historical baseline period (1995-2014) with the mid- and late-century periods. Grid cells with $p < 0.05$ were considered significant. Significance hatching in figures is applied only where both the t-test criterion and the ≥66 % model-agreement criterion are satisfied, ensuring that displayed changes reflect robust forced signals rather than natural variability (IPCC 2021; Harris et al. 2023).

3.3. Bias correction evaluation metrics

The fidelity of CMIP6 simulations over the 1995-2014 baseline was evaluated using the Pearson correlation coefficient, the modified Kling-Gupta Efficiency (KGE'), and Taylor diagrams (Taylor 2001; Kling et al. 2012; Enyew et al. 2024).

The modified Kling-Gupta Efficiency (KGE') combines correlation, variability ratio, and coefficient-of-variation ratio into a single metric, providing a robust assessment of model skill relative to CRU observations:

$$KGE' = 1 - \sqrt{(r-1)^2 + (\alpha - 1)^2 + \left(\frac{CV_{mod}}{CV_{obs}} - 1\right)^2} \quad (4)$$

where r is the spatial correlation between model and observations, $\alpha = \frac{\sigma_{\text{mod}}}{\sigma_{\text{obs}}}$ is the ratio of model to observed standard deviation (variability ratio), and

$$CV_{mod}/\,CV_{obs} = \frac{\sigma_{mod}/\mu_{mod}}{\sigma_{obs}/\mu_{obs}}$$

is the ratio of coefficients of variation (CV), with σ denoting the standard deviation and μ the mean. Specifically, $CV_{mod} = \frac{\sigma_{mod}}{\mu_{mod}}$ represents the relative variability of the model data, $CV_{obs} = \frac{\sigma_{obs}}{\mu_{obs}}$ represents the relative variability of the observational data. KGE' values closer to 1 indicate higher agreement with observations, whereas values closer to 0 indicate lower model skill.

Taylor diagrams were employed to visualize the spatial correlation, normalized standard deviation, and centered root-mean-square difference (CRMSD) for individual models and the ensemble mean. EQM bias-corrected outputs were included in this evaluation to illustrate improvements in model performance following systematic bias correction.

4. Results

4.1. Temperature climatology and annual cycle (1995-2014)

The spatial distribution and temporal variability of mean annual temperature across Sudan during 1995-2014 are shown in Figure 2a. Observed mean annual temperatures exhibit substantial spatial variability, ranging from 17.9°C to 30.33°C. The coolest conditions (<20°C) occur in the northern desert regions, whereas the warmest conditions (>30°C) are observed in the central and southern parts of the country. The national mean temperature is 27.76°C, with a median of 28.31°C and a standard deviation of 1.80°C, reflecting moderate variability across Sudan.

The annual cycle of observed and simulated temperatures over Sudan is illustrated in Figure 2b. The CMIP6 ensemble successfully reproduces the characteristic seasonal evolution of temperatures across the country; however, noticeable departures from observations persist throughout the year. The ensemble shows a slight warm anomaly during the peak summer season (+0.55°C), marking the only period in which simulated temperatures exceed the CRU observations. During winter, the ensemble underestimates temperatures by −1.33°C (CRU: 22.21°C; Ensemble: 20.88°C), representing the most pronounced cold deviation of the year. For the other seasons, the simulated annual temperature cycle in the CMIP6 ensemble is within approximately 1°C of the observations. On the annual scale, the ensemble mean (26.65°C) remains close to the CRU estimate (27.03°C), resulting in a modest annual bias of −0.38°C.

Taken together, these results demonstrate that, while the ensemble captures the overarching structure and timing of Sudan's annual temperature cycle, persistent but seasonally distinct deviations remain – most notably the summer warm excess contrasted with the larger winter cold bias. This integrated view of spatial climatology and seasonal evolution provides a robust baseline for evaluating climate model performance and bias-correction procedures.

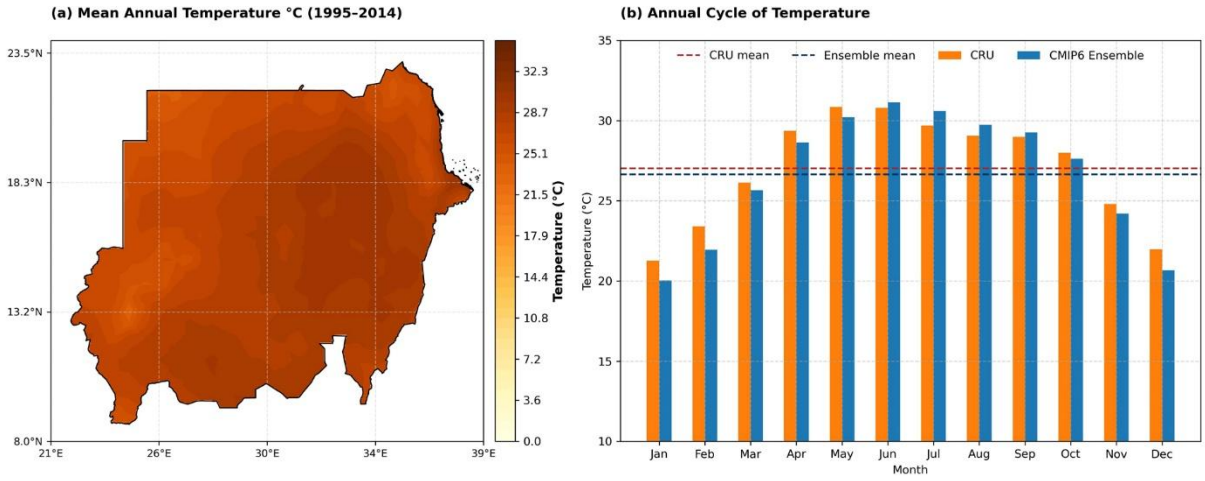

Fig. 2. Mean annual temperature over Sudan (1995-2014): (a) spatial distribution based on CRU observations; (b) annual cycle comparing CRU observations with the ensemble mean of 10 CMIP6 models.

4.2. Evaluation of temperature bias correction

The Empirical Quantile Mapping (EQM) method substantially improves the performance of CMIP6 temperature simulations over Sudan during 1995-2014 (Fig. 3). After correction, model standard deviations converge to a narrow range (3.32-3.37°C), nearly matching the CRU reference (3.34°C) and contrasting with the broader spread in the raw simulations (3.28-4.56°C). CRMSD values decrease markedly from 1.35-1.77°C in the raw data to 0.90-0.97°C after correction, indicating closer alignment with the observed spatio-temporal temperature structure. Correlation coefficients remain high (≈0.96), showing that EQM reduces systematic biases without altering the underlying temporal signal.

The largest improvement is observed in the Kling-Gupta Efficiency *(KGE)* metric, where raw models range widely (0.37-0.88), but all EQM-corrected models achieve consistently high values (0.96). As illustrated in Figure 3, corrected models cluster tightly around the observational benchmark, emphasizing the strength and consistency of the improvement. Overall, EQM provides a robust enhancement of model skill, yielding corrected datasets that are more reliable for historical assessment and future projections.

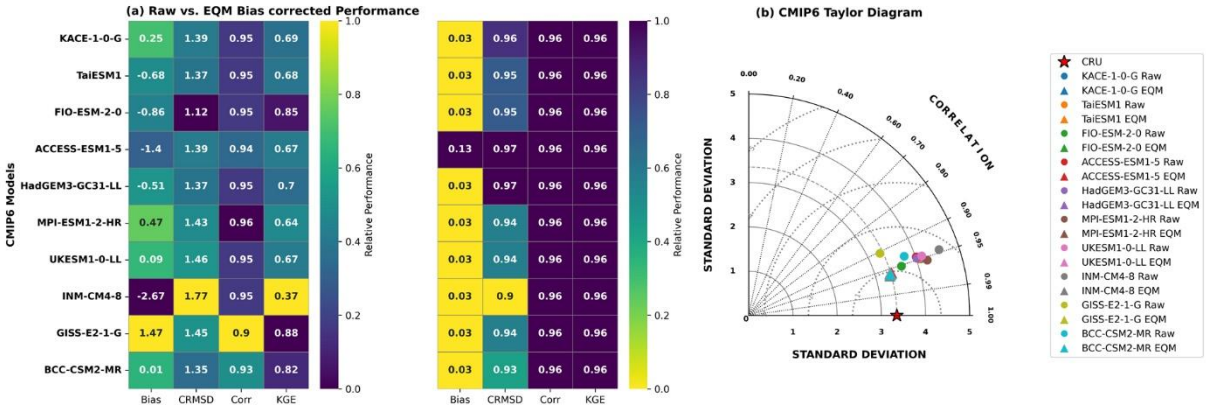

Fig. 3. Evaluation of CMIP6 temperature simulations over Sudan (1995-2014). Left: heatmaps of raw and EQM-corrected model performance (Bias, CRMSD, correlation, KGE). Right: Taylor diagram showing improved agreement with CRU after bias correction.

Figure 4 illustrates the spatial patterns of temperature biases in raw and ΔBias-corrected CMIP6 simulations over Sudan. In the raw simulations, annual temperatures are modestly underestimated relative to CRU observations (mean −0.59°C; SD = 0.87°C). Summer biases are predominantly positive (mean +0.45°C; SD = 0.76°C), while winter exhibits the strongest cold bias (mean −1.52°C; SD = 1.31°C).

Following ΔBias correction, median biases are substantially reduced across all seasons (annual: −0.65°C; summer: +0.48°C; winter: −1.51°C), accompanied by narrower interquartile ranges (annual: 1.88°C; summer: 1.46°C; winter: 2.73°C), indicating improved agreement with observations. The fraction of grid cells with positive biases (annual: 25%; summer: 73%; winter: 12%) highlights pronounced seasonal asymmetries, likely linked to regional climate processes, particularly the influence of the West African monsoon during summer.

Hatched areas denote residual extremes outside the central 66% range, identifying localized regions where bias correction remains less effective. Overall, ΔBias correction markedly reduces both the magnitude and spatial extent of temperature biases, with the greatest improvements observed for annual and summer, while winter retains some localized cold bias.

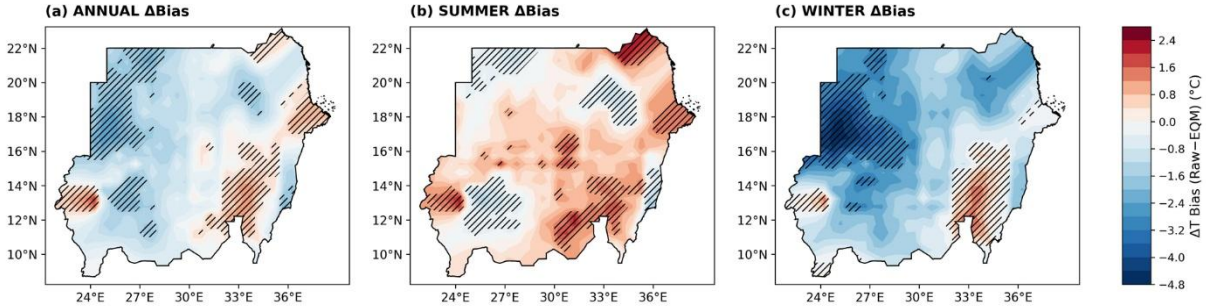

Fig. 4. Spatial patterns of raw and ΔBias-corrected temperature biases in CMIP6 simulations over Sudan for annual, summer, and winter seasons. ΔBias correction substantially reduces biases across all seasons. Cross-hatched areas indicate regions of model agreement of 66% or greater.

Figure 5 presents the ensemble mean changes in annual near-surface air temperature relative to the 1995-2014 baseline for mid-century (2041-2060) and late-century (2081-2100) under the SSP2-4.5 (moderate emissions) and SSP5-8.5 (high emissions) scenarios. Panels show (a) mid-century SSP2-4.5, (b) mid-century SSP5-8.5, (c) late-century SSP2-4.5, and (d) late-century SSP5-8.5.

By mid-century, ensemble mean warming over Sudan is projected to reach 1.65°C under SSP2-4.5 and 2.16°C under SSP5-8.5, with corresponding 66% likely ranges of 1.12-1.97°C and 1.55-2.48°C, respectively. Warming intensifies substantially by late-century, increasing to 2.67°C (66% range: 1.89-3.30°C) under SSP2-4.5 and 5.00°C (66% range: 3.92-6.01°C) under SSP5-8.5. These results underscore the strong scenario dependence of future warming in Sudan, with high-emission pathways leading to markedly greater temperature increases. Hatched regions denote areas of robust warming where both statistical significance ($p < 0.05$) and strong inter-model agreement (≥66%) are satisfied. The 66% likely ranges quantify inter-model uncertainty, and the corresponding numerical statistics are summarized in Table 2.

Figure 6 shows the ensemble time series of annual mean near-surface air temperature anomalies over Sudan for 2041-2100 under SSP2-4.5 and SSP5-8.5. Solid lines represent the ensemble mean, shaded envelopes indicate the 66% likely range, and dashed lines show the inter-model minimum and maximum. Under SSP2-4.5, anomalies increase gradually from 1.68°C in 2041-2060 to 2.68°C by 2081-2100, with the 66% likely range widening from 1.34-2.15°C to 2.02-3.52°C. The associated linear warming trend is 0.247°C decade^{-1}. In contrast, SSP5-8.5 exhibits much stronger warming, rising from 2.18°C in 2041-2060 to 4.87°C by late-century, with the 66% likely range expanding from 1.84-2.67°C to 4.11-6.17°C, corresponding to a linear trend of 0.703°C decade^{-1}.

Overall, these projections are broadly consistent with IPCC AR6 Working Group I assessments, which report likely warming of approximately 1.5-2.5°C under SSP2-4.5 and 2.5-4.0°C under SSP5-8.5 for East Africa and the Sahel by mid-century (IPCC 2021). The slightly narrower uncertainty ranges in this study reflect the use of a bias-corrected subset of CMIP6 models focused specifically on Sudan. Nevertheless, the magnitude, spatial distribution, and temporal evolution of projected warming closely align with the broader multi-model patterns reported by the IPCC.

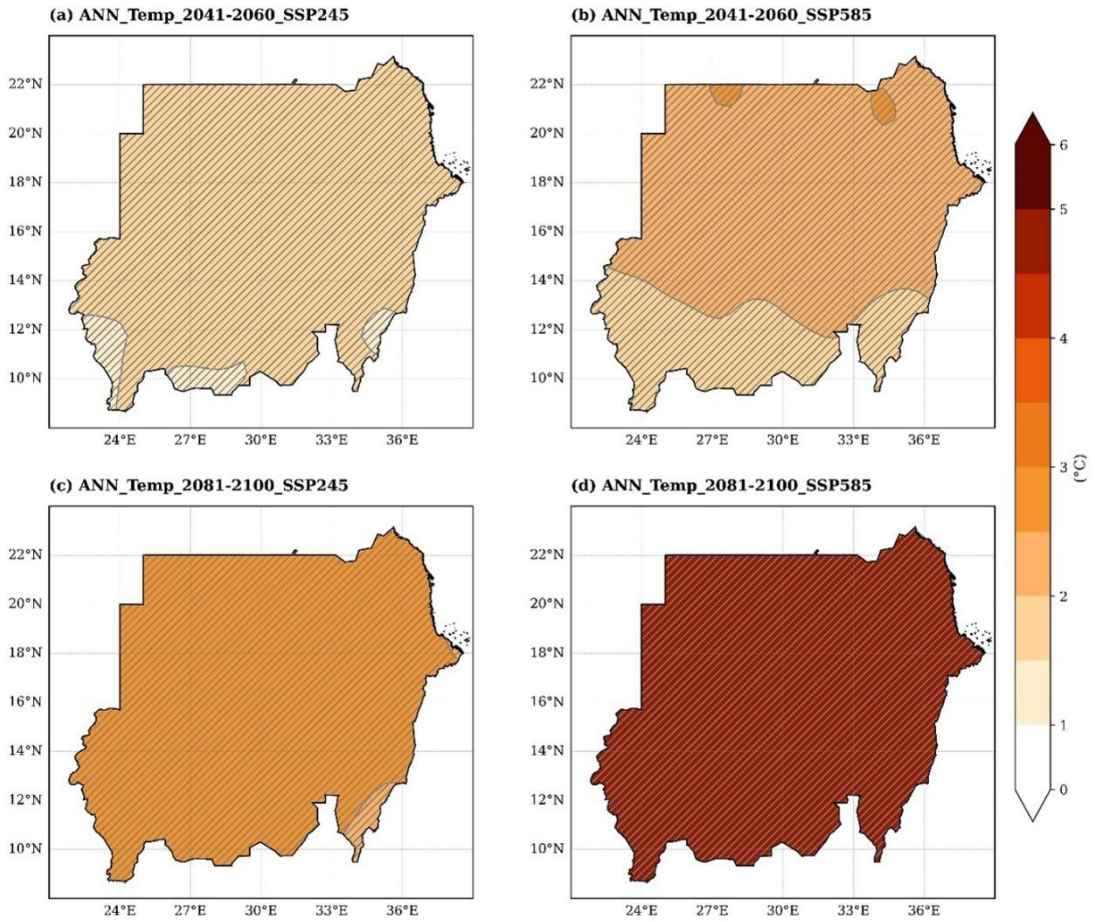

Fig. 5. Ensemble mean annual temperature anomalies relative to the 1995-2014 baseline for the mid- and late-century periods under SSP2-4.5 and SSP5-8.5. Cross-hatched areas indicate regions of model agreement of 66% or greater.

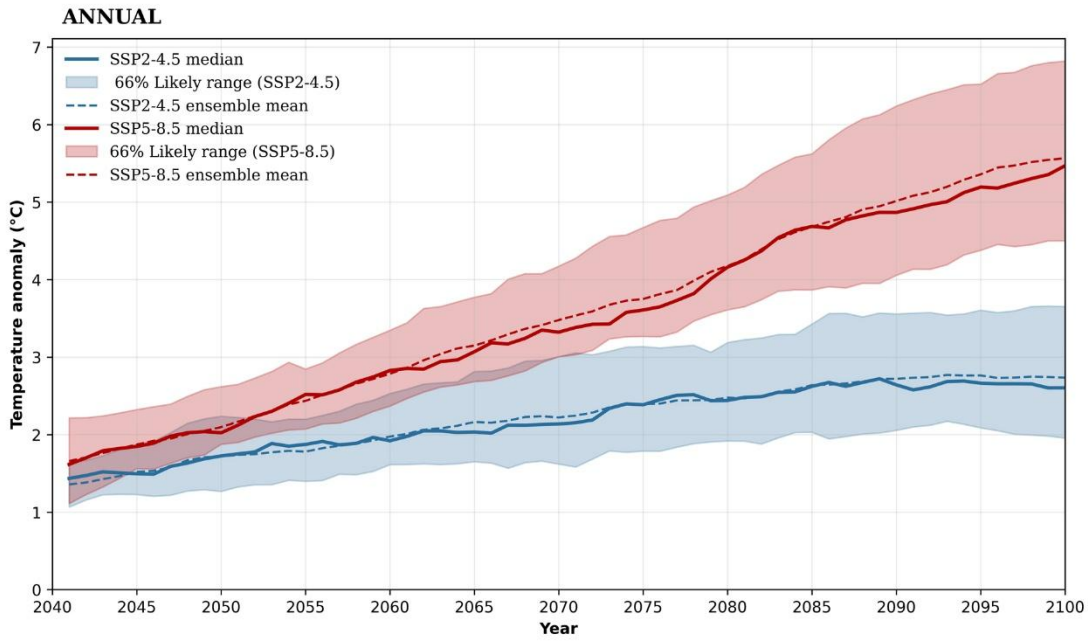

Fig. 6. Ensemble time series of annual mean near-surface air temperature anomalies over Sudan for 2041-2100 under SSP2-4.5 and SSP5-8.5. Solid lines represent the ensemble median, dashed lines indicate the ensemble mean, and shaded areas show the 66% likely range.

Table 2. Ensemble statistics of future annual and seasonal temperature anomalies (°C) over Sudan under SSP2-4.5 and SSP5-8.5 for mid- and late-century.

Season	Scenario	Mean Anomaly (°C)	Median (°C)	Std (°C)	Min (°C)	Max (°C)	66% likely range (°C)
ANNUAL	SSP245 (2041-2060)	1.68	1.65	0.15	1.45	1.91	1.12-1.97
	SSP585 (2041-2060)	2.17	2.16	0.23	1.78	2.51	1.55-2.48
	SSP245 (2081-2100)	2.68	2.67	0.13	2.45	2.92	1.89-3.30
	SSP585 (2081-2100)	4.87	5.00	0.16	4.50	5.00	3.92-6.01
SUMMER	SSP245 (2041-2060)	1.78	1.68	0.29	1.41	2.26	1.49-2.18
	SSP585 (2041-2060)	2.30	2.16	0.44	1.74	3.06	1.88-2.90
	SSP245 (2081-2100)	2.80	2.69	0.28	2.47	3.27	2.53-3.21
	SSP585 (2081-2100)	4.79	5.00	0.24	4.35	5.00	4.47-5.00
WINTER	SSP245 (2041-2060)	1.58	1.60	0.06	1.45	1.72	1.51-1.64
	SSP585 (2041-2060)	1.98	1.98	0.11	1.73	2.29	1.89-2.07
	SSP245 (2081-2100)	2.57	2.56	0.08	2.31	2.77	2.51-2.63
	SSP585 (2081-2100)	4.90	5.00	0.15	4.37	5.00	4.75-5.00

4.4. Future seasonal warming

Summer projections are shown in Figure 7, which presents the ensemble mean changes in near-surface air temperature relative to the 1995-2014 baseline for the mid-century (2041-2060) and late-century (2081-2100) periods under the SSP2-4.5 and SSP5-8.5 scenarios. Panels (a-d) correspond to mid- and late-century projections for both emissions pathways.

During the mid-century period, ensemble mean summer warming is projected to reach 1.78°C under SSP2-4.5 and 2.30°C under SSP5-8.5, with 66% likely ranges of 1.49-2.18°C and 1.88-2.90°C, respectively. By late-century, warming intensifies further, increasing to 2.80°C (66% range: 2.53-3.21°C) under SSP2-4.5 and 4.79°C (66% range: 4.47-5.00°C) under SSP5-8.5.

Hatched regions indicate areas of robust warming where both statistical significance ($p < 0.05$) and strong inter-model agreement (≥66%) are satisfied. These results demonstrate that future summer warming in Sudan is strongly scenario dependent, with higher emissions leading to substantially greater temperature increases. The detailed numerical statistics for these projections are summarized in Table 2.

Winter projections are presented in Figure 8, with panels (a-d) corresponding to mid- and late-century projections under the SSP2-4.5 and SSP5-8.5 scenarios. During the mid-century period, ensemble mean winter warming is projected to reach 1.58°C under SSP2-4.5 and 1.98°C under SSP5-8.5, with 66% likely ranges of 1.51-1.64°C and 1.89-2.07°C, respectively. By late-century, winter warming intensifies to 2.57°C (66% range: 2.51-2.63°C) under SSP2-4.5 and 4.90°C (66% range: 4.75-5.00°C) under SSP5-8.5.

Compared to summer, winter warming exhibits greater temporal stability and narrower uncertainty intervals, reflecting reduced inter-model spread. Hatched regions denote areas of robust warming, defined by both statistical significance ($p < 0.05$) and strong inter-model agreement (≥66%), consistent with the criteria applied to annual and summer projections.

Overall, these results indicate that while both seasons experience substantial warming, the magnitude and variability are consistently higher during the summer months. Corresponding winter statistics are summarized in Table 2.

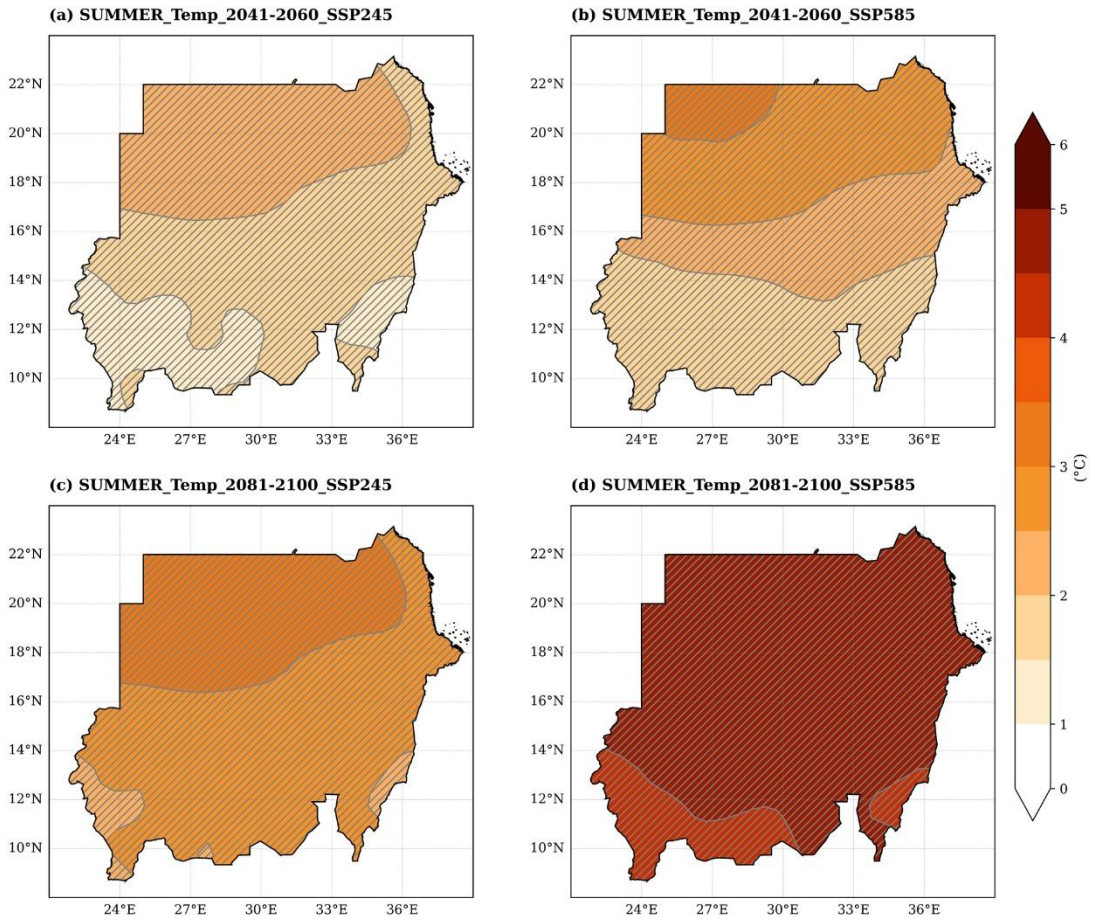

Fig. 7. Ensemble mean summer near-surface air temperature anomalies relative to the 1995-2014 baseline for the mid-century and late-century periods under SSP2-4.5 and SSP5-8.5. Cross-hatched areas indicate regions of model agreement of 66% or greater.

Figure 9 illustrates the seasonal evolution of near-surface air temperature anomalies over Sudan from 2041 to 2100. Panel (a) presents summer anomalies, which display a pronounced upward trajectory. Under SSP5-8.5, the 66 % likely ranges progressively widen, indicating accelerated warming and increased inter-model divergence during the monsoon season. Panel (b) shows winter anomalies, which also increase over time but follow a more stable trend with narrower uncertainty intervals, consistent with the reduced model spread identified in the statistical analysis.

Seasonal warming rates over 2041-2100 are estimated at approximately 0.265°C per decade (summer) and 0.243°C per decade (winter) under SSP2-4.5, and 0.742°C per decade (summer) and 0.718°C per decade (winter) under SSP5-8.5. These projections indicate that Sudan will continue to experience sustained warming throughout the 21st century in both seasons, with summer warming occurring at a faster rate and exhibiting greater variability than winter warming.

Overall, the results align closely with regional projections reported in the IPCC AR6, underscoring strong scenario-dependent warming across northern and north-eastern Africa.

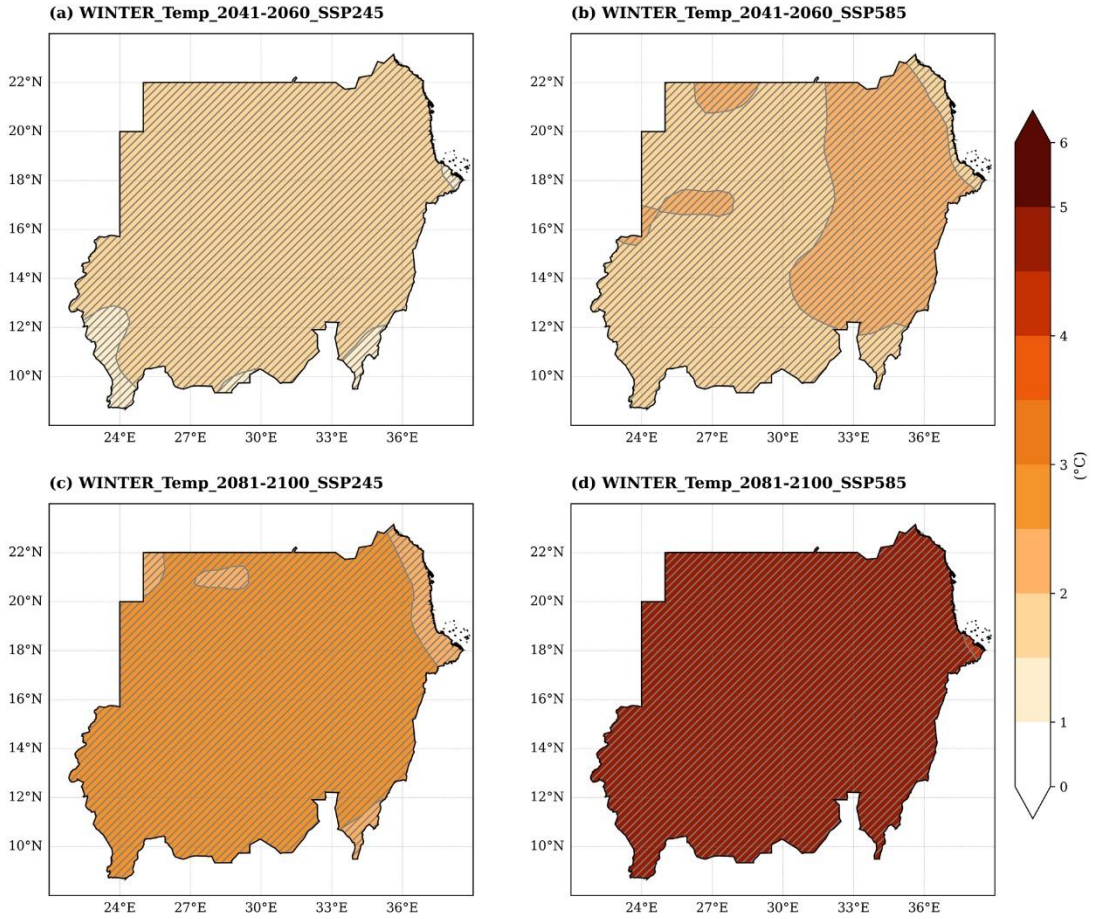

Fig. 8. Ensemble mean winter near-surface air temperature anomalies relative to the 1995-2014 baseline for the mid-century and late-century periods under SSP2-4.5 and SSP5-8.5. Cross-hatched areas indicate regions of model agreement of 66% or greater.

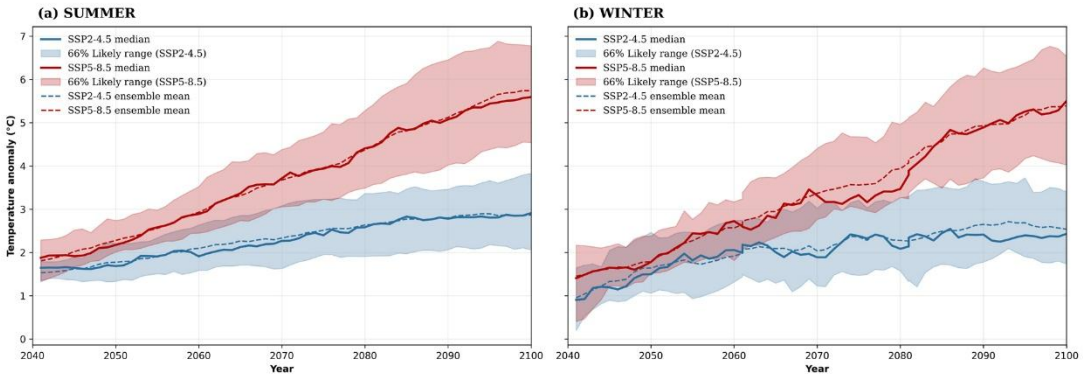

Fig. 9. Ensemble time series of seasonal near-surface air temperature anomalies over Sudan for 2041-2100 under SSP2-4.5 and SSP5-8.5. (a) summer anomalies, (b) winter anomalies. Solid lines represent the ensemble median, dashed lines indicate the ensemble mean, and shaded areas show the 66% likely range.

4.5. Scenario divergence

The temperature differences between the moderate- and high-emission pathways exhibit a clear, increasingly pronounced divergence from mid-century to late-century (Fig. 10a-c). During the mid-century period (2041-2060), the separation between scenarios is already detectable, with consistently positive warming differences across all seasons. Annual differences remain modest yet robust, with a mean increase of 0.49°C and a narrow 66% likely range of 0.38-0.58°C, indicating strong inter-model agreement. Seasonal patterns follow a similar structure: winter differences average 0.41°C, while summer shows a larger response of 0.53°C, reflecting enhanced land-atmosphere coupling during hotter months. The tight uncertainty ranges across all mid-century estimates underscore the stability and consistency of the modeled scenario divergence.

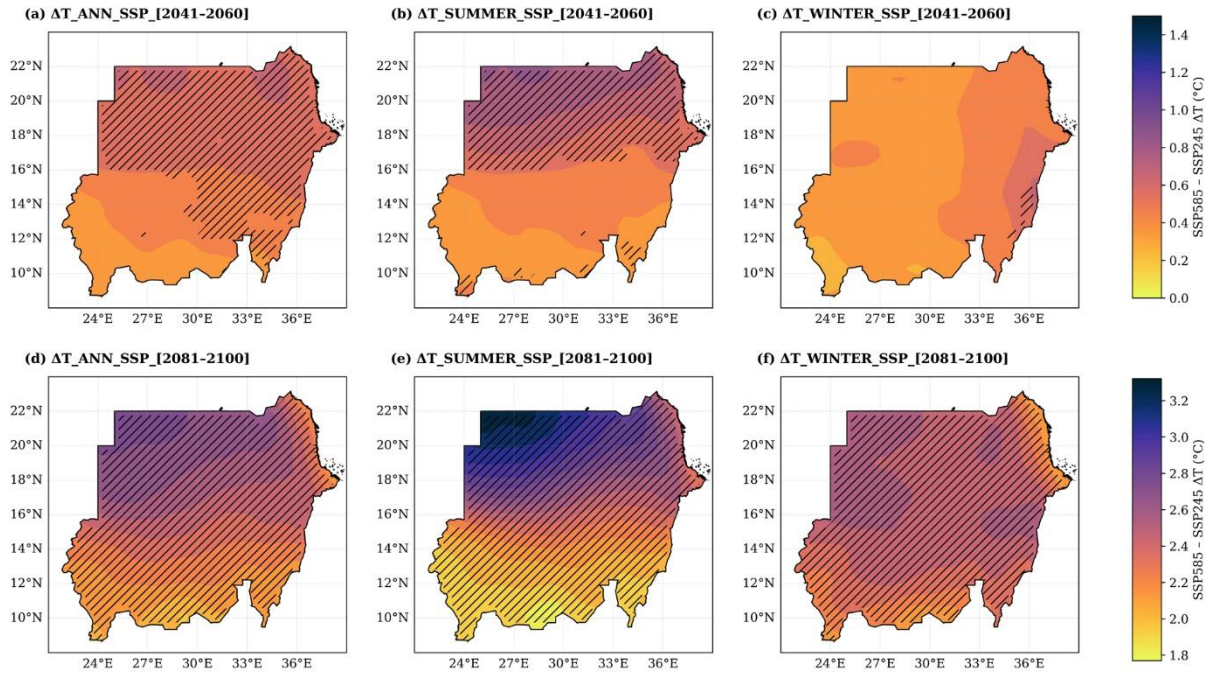

Fig. 10. Projected temperature differences (SSP5-8.5 minus SSP2-4.5) over Sudan. Panels a-c show mid-century (2041-2060) annual, winter, and summer differences; panels d-f show late-century (2081-2100) differences. Color shading indicates mean differences, and cross-hatched areas indicate regions of model agreement of 66% or greater.

By the late-century period (2081-2100), the contrast between emissions pathways intensifies substantially (Fig. 10d-f). Annual differences increase to a mean of 2.36°C, with a constrained 66% likely range of 2.13-2.63°C, highlighting the dominant influence of cumulative greenhouse-gas emissions on long-term warming. Seasonal differences reach comparable magnitudes, with winter and summer increases of 2.37°C and 2.39°C, respectively. Although inter-model spread widens slightly, particularly during summer due to amplified radiative forcing and surface feedbacks, warming remains consistently higher under the high-emission scenario across all models.

Overall, these results demonstrate that while mid-century scenario separation is moderate and tightly bounded, late-century divergence becomes pronounced and climatically significant. The persistence of

positive differences, combined with narrow mid-century uncertainty and coherent late-century ranges, provides high confidence that Sudan's future thermal conditions, particularly summer heat stress, will be strongly governed by the global emissions trajectory.

5. Discussion and conclusions

This study provides a detailed assessment of projected annual and seasonal temperature changes over Sudan for the mid-century (2041-2060) and late-century (2081-100) periods under the SSP2-4.5 and SSP5-8.5 scenarios, using bias-corrected CMIP6 multi-model ensembles. The results indicate a robust and consistent warming signal across all seasons, with a strong dependence on future emissions pathways.

For annual mean temperature, the mid-century ensemble median warming is projected to reach 1.65°C under SSP2-4.5 (66% likely range: 1.12-1.97°C) and 2.16°C under SSP5-8.5 (66% likely range: 1.55-2.48°C). By late-century, annual warming intensifies substantially to 2.67°C (66% range: 1.89-3.30°C) under SSP2-4.5 and 5.00°C (66% range: 3.92-6.01°C) under SSP5-8.5 (Table 2) (IPCC 2021; World Bank 2023). The corresponding linear warming trends of 0.247°C per decade and 0.703°C per decade, respectively, illustrate the accelerated temperature increase associated with high-emission pathways (Fig. 6).

Summer exhibits the fastest and most variable warming. Mid-century median summer anomalies are projected at 1.68°C under SSP2-4.5 (66% range: 1.49-2.18°C) and 2.16°C under SSP5-8.5 (66% range: 1.88-2.90°C). By late-century, summer warming reaches 2.69°C (66% range: 2.53-3.21-°C) under SSP2-4.5 and 5.00°C (66% range: 4.47-5.00°C) under SSP5-8.5 (Table 2; Fig. 7). Corresponding warming rates of approximately 0.265°C per decade and 0.742°C per decade reflect strong land–atmosphere feedback during the hottest months.

Winter warming is comparatively more stable. Mid-century median anomalies reach 1.60°C (66% range: 1.51-1.64°C) under SSP2-4.5 and 1.98°C (66% range: 1.89-2.07°C) under SSP5-8.5. By late-century, winter warming increases to 2.56°C (66% range: 2.51-2.63°C) and 5.00°C (66% range: 4.75-5.00°C), respectively, with linear trends of 0.243°C per decade and 0.718°C per decade (Table 2; Fig. 8). Compared to summer, winter projections exhibit narrower uncertainty ranges, indicating reduced inter-model spread and greater seasonal stability.

Spatially, northern and central Sudan are projected to experience stronger warming than southern regions, consistent with heterogeneous climate regimes, land–atmosphere interactions, and topographic influences. The 66% likely ranges provide a quantitative measure of inter-model uncertainty, indicating robust warming signals across most regions. These findings are consistent with regional assessments for East Africa and the Sahel reported in IPCC AR6 WGI (IPCC 2021) and complement recent analyses of climate-related peace and security risks in Sudan (NUPI, SIPRI 2022).

Scenario divergence is already evident by mid-century. Annual temperature differences between SSP5-8.5 and SSP2-4.5 average 0.49°C (66% likely range: 0.38-0.58°C), with summer differences of 0.53°C (66%

range: 0.30-0.84°C) and winter differences of 0.40°C (66% range: 0.24-0.63°C). By late-century, these contrasts become climatically significant, with annual differences of 2.37°C (66% range: 1.91-2.83°C), summer divergences reaching 2.40°C (66% range: 1.77-3.32°C), and winter divergences of 2.39°C (66% range: 2.01-2.63°C) (Fig. 10). This confirms that cumulative greenhouse-gas emissions will strongly govern future thermal conditions, particularly extreme summer heat stress (IPCC 2021; NUPI, SIPRI 2022; WBG 2023).

Bias correction using Equidistant Quantile Mapping (EQM) and Delta Quantile Mapping (DQM) substantially reduces systematic model errors, improves Kling-Gupta Efficiency (KGE'), and constrains inter-model spread, thereby enhancing confidence in the projections. Nevertheless, several limitations remain. CMIP6 models' coarse spatial resolution (~100-200 km) may underestimate local warming hotspots; EQM assumes stationary bias structures that may not fully hold under future climate conditions; and sparse observational coverage in northern Sudan introduces uncertainty into the reference climatology (IPCC 2021).

The projected warming has significant socioeconomic implications. Enhanced summer temperatures are likely to exacerbate heat stress, reduce agricultural productivity, intensify water scarcity, and challenge hydropower generation. Northern and central Sudan appear particularly vulnerable to compounded heatwave and drought risks. These findings underscore the urgent need for targeted adaptation strategies, including climate-resilient crops, improved water-resource management, and strengthened early-warning systems, consistent with broader climate risk and security assessments (NUPI, SIPRI 2022; WBG 2023).

In conclusion, Sudan is projected to experience substantial annual and seasonal warming throughout 2041-2100, with summer exhibiting the fastest and most variable increases. The growing divergence between moderate- and high-emission pathways highlights the critical importance of global mitigation efforts, while strong multi-model agreement provides robust guidance for national adaptation planning. Bias-corrected CMIP6 ensembles offer actionable insights for policymakers and stakeholders, supporting evidence-based climate risk assessments and long-term adaptation strategies (IPCC 2021; NUPI, SIPRI 2022; WBG 2023).

References

Almazroui M., Saeed F., Saeed S., Islam M.N., Ismail M., Klutse N.A.B., Siddiqui M.H., 2020, Projected change in temperature and precipitation over Africa from CMIP6, Earth Systems and Environment, 4, 455-475, DOI: 10.1007/s41748-020-00161-x.

Bao Y., Song Z., Qiao F., 2019, FIO-ESM Version 2.0: Model description and evaluation, Journal of Geophysical Research: Oceans, 125 (6), DOI: 10.1029/2019JC016036.

Byun Y.-H., Lim Y.-J., Sung H.-M., Kim J., Sun M., Kim B.-H., 2023, IPCC DDC: NIMS-KMA KACE1.0-G model output prepared for CMIP6 CMIP, World Data Center for Climate (WDCC) at DKRZ, DOI: 10.26050/WDCC/AR6.C6CMNKK1.

Cannon A.J., Sobie S.R., Murdock T.Q., 2015, Bias correction of GCM precipitation by quantile mapping: How well do methods preserve changes in quantiles and extremes?, Journal of Climate, 2817, 6938-6959, DOI: 10.1175/JCLI-D-14-00754.1.

Enyew F.B., Sahlu D., Tarekegn G.B., Hama S., Debele S.E., 2024, Performance evaluation of CMIP6 climate model projections for precipitation and temperature in the Upper Blue Nile Basin, Ethiopia, Climate, 12 (11), DOI: 10.3390/cli12110169.

Eyring V., Bony S., Meehl G.A., Senior C.A., Stevens B., Stouffer R.J., Taylor K.E., 2016, Overview of the Coupled Model Intercomparison Project Phase 6 CMIP6 experimental design and organization, Geoscientific Model Development, 9 (5), 1937-1958, DOI: 10.5194/gmd-9-1937-2016.

Funk C.C., Eilerts G., Verdin J., Rowland J., Marshall M., 2011, A climate Trend Analysis of Sudan, USGS Fact Sheet 2011-3072, U.S. Geological Survey, available online at https://pubs.usgs.gov/fs/2011/3072/ (data access 04.02.2026).

Gudmundsson L., Bremnes J.B., Haugen J.E., Engen-Skaugen T., 2012, Technical Note: Downscaling RCM precipitation to the station scale using statistical transformations – a comparison of methods, Hydrology and Earth System Sciences Discussions, 16 (9), 3383-3390, DOI: 10.5194/hessd-9-6185-2012.

Gutjahr O., Putrasahan D., Lohmann K., Jungclaus J.H., von Storch J.-S., Brüggemann N., Haak H., Stössel A., 2019, Max Planck Institute Earth System Model MPI-ESM1.2 for the High Resolution Model Intercomparison Project HighResMIP, Geoscientific Model Development, 127 (7), 3241-3281, DOI: 10.5194/gmd-12-3241-2019.

Harris I.C., Jones P.D., Osborn T.J., 2023, CRU TS4.09: Monthly climate dataset of high-resolution gridded observations, Centre for Environmental Data Analysis CEDA, available online at https://catalogue.ceda.ac.uk/uuid/9cf07e92afaa405da4f40b6733f362d3 (data access 04.02.2026).

IPCC, 2021, Climate Change 2021: The Physical Science Basis, Contribution of Working Group I to the Sixth Assessment Report of the IPCC, Cambridge University Press.

Jones G.S., Andrews M.B., Andrews T., Blockley E., Ciavarella A., Christidis N., Cotterill D.F., Lott F.C., Ridley J., Stott P.A., 2024, The HadGEM3-GC3.1 contribution to the CMIP6 Detection and Attribution MIP, Journal of Advances in Modeling Earth Systems, 168 (8), DOI: 10.1029/2023MS004135.

Kelley M., Schmidt G.A., Nazarenko L.S., Bauer S.E., Ruedy R., Russell G.L., Ackerman A.S., Aleinov I., Bauer M., Bleck R., Canuto V., Cesana G., Cheng Y., Clune T.L., Cook B.I., Cruz C.A., Del Genio A.D., Elsaesser G.S., Faluvegi F.G., Kiang N.Y., Kim D., Lacis A.A., Leboissetier A., LeGrande A.N., Lo K.K., Marshall J., Matthews E.E., McDermid S., Mezuman K., Miller R.L., Murray L.T., Oinas V., Orbe C., Garcia-Pando C.P., Perlwitz J.P., Puma M.J., Rind D., Romanou A., Shindell D.T., Sun S., Tausnev N., Tsigaridis K., Tselioudis G., Weng E., Wu J., Yao M.-S., 2020, GISS-E2.1: Configurations and climatology, Journal of Advances in Modeling Earth Systems, 12 (8), DOI: 10.1029/2019MS002025.

Kling H., Fuchs M., Paulin M., 2012, Runoff conditions in the upper Danube basin under an ensemble of climate change scenarios, Journal of Hydrology, 424-425, 264-277, DOI: 10.1016/j.jhydrol.2012.01.011.

Lee W.-L., Wang Y.-C., Shiu C.-J., Tsai I.-C., Tu C.-Y., Lan Y.-Y., Chen J.-P., Pan H.-L., Hsu H.-H., 2020, Taiwan Earth System Model Version 1: description and evaluation of mean state, Geoscientific Model Development, 13, 3887-3904, DOI: 10.5194/gmd-13-3887-2020.

Lehner F., Nadeem I., Formayer H., 2023, Evaluating skills and issues of quantile-based bias adjustment for climate change scenarios. Advances in Statistical Climatology, Meteorology and Oceanography, 9, 29-48, DOI: 10.5194/ascmo-9-29-2023.

NUPI, SIPRI, 2022, Climate, Peace and Security Fact Sheet: Sudan, SIPRI Publications, available online at https://www.sipri.org/publications/2025/partner-publications/climate-peace-and-security-fact-sheet-south-sudan-2025 (data access 04.02.2026).

Sellar A.A., Jones C.G., Mulcahy J.P., Tang Y., Yool A., Wiltshire A., O'Connor F.M., Stringer M., Hill R., Palmieri J., Woodward S., de Mora L., Kuhlbrodt T., Rumbold S.T., Kelley D.I., Ellis R., Johnson C.E., Walton J., Abraham N.L., Andrews M.B., Andrews T., Archibald A.T., Berthou S., Burke E., Blockley E., Carslaw K., Dalvi M., Edwards J., Folberth G.A., Gedney N., Griffiths P.T., Harper A.B., Hendry M.A., Hewitt A.J., Johnson B., Jones A., Jones C.D., Keeble J., Liddicoat S., Morgenstern O., Parker R.J., PRedoi V., Robertson E., Siahaan A., Smith R.S., Swaminathan R., Woodhouse M.T., Zeng G., Zerroukat M., 2019, UKESM1: Description and evaluation of the U.K. Earth System Model, Journal of Advances in Modeling Earth Systems, 11 (12), 4513-4558, DOI: 10.1029/2019MS001739.

Taylor K.E., 2001, Summarizing multiple aspects of model performance in a single diagram, Journal of Geophysical Research: Atmospheres, 106 (D7), 7183-7192, DOI: 10.1029/2000JD900719.

Volodin E., Mortikov E., Gritsun A., Lykossov V., Galin V., Diansky N., Gusev A., Kostrykin S., Iakovlev N., Shestakova A., Emelina S., 2023, IPCC DDC: INM INM-CM4-8 model output prepared for CMIP6 CMIP, World Data Center for Climate (WDCC) at DKRZ, DOI: 10.26050/WDCC/AR6.C6CMINIC8.

WBG, 2023, Sudan – Climate Change Knowledge Portal, World Bank Group, available online at https://climateknowledgeportal.worldbank.org/country/sudan (data access 04.02.2026).

WMO, 2024, Africa faces disproportionate burden from climate change and adaptation costs, WMO Press release, available online at https://public.wmo.int/news/media-centre/africa-faces-disproportionate-burden-from-climate-change-and-adaptation-costs (data access 04.02.2026).

Wu T., Lu Y., Fang Y., Xin X., Zhang J., Li L., Li W., Jie W., Zhang J., Liu Y., Zhang L., Zhang F., Zhang Y., Wu F., Li J., Chu M., Wang Z., Shi X., Liu X., Wei M., Huang A., Zhang Y., Liu X., 2019, The Beijing Climate Center Climate System Model: Progress from CMIP5 to CMIP6, Geoscientific Model Development, 12 (4), 1573-1600, DOIL 10.5194/gmd-12-1573-2019.

Xavier A.C.F., Martins L.L., Rudke A.P., de Morais M.V.B., Martins J.A., Blain G.C., 2022, Evaluation of quantile delta mapping (QDM) as a bias-correction method in maximum rainfall datasets from downscaled models in São Paulo state (Brazil), International Journal of Climatology, 42 (1), 175-190, DOI: 10.1002/joc.7238.

Ziehn T., Chamberlain M.A., Law R.M., Lenton A., Bodman R.W., Dix M., Stevens L., Wang Y.-P., Srbinovsky J., 2020, The Australian Earth System Model: ACCESS-ESM1.5, Journal of Southern Hemisphere Earth Systems Science, 70 (1), 193-214, DOI: 10.1071/ES19035.

Climate change impacts on high-altitude Himalayan hydrology: A review with special reference to modeling applications

Arushi Sharma[1,2], Kapil Kesarwani[1], Vandita Srivastava[3]

[1] Hemvati Nandan Bahuguna Garhwal University, India

[2] National Institute of Hydrology, India

[3] Department of Physics, Kanahiya Lal D.A.V. (P.G.) College, India

Abstract

Climate change has increasingly altered the environment, specifically in high-mountain regions. This change is posing a significant challenge to water resources and downstream socioeconomic systems. The Himalayan cryosphere plays a critical role in sustaining river flow for the majority of the downstream population. The Himalayan region is considered one of the most critical areas globally when assessing the social and economic consequences of glacier shrinkage. Consequently, the Himalayan system is highly sensitive to changes in temperature and precipitation regimes. To understand the climate-driven impacts on high-altitude hydrology, hydrological modeling has become a key tool for assessing glacier melt contributions, watershed hydrological processes, and streamflow variability across the Himalayan region. This review aims to synthesize current understanding of climate change impacts on the cryosphere and high-altitude hydrology, with main emphasis on temperature and precipitation variability and their representation in hydrological models. The study examines various modeling approaches, including lumped, semi-distributed, and fully distributed models, as well as emerging machine-learning and hybrid frameworks. Studies conducted within the Indian Himalayan Region (IHR) are critically reviewed to evaluate model performance, data requirements, and scenarios, focusing on compatibility. Furthermore, the review discusses primary sources of uncertainty and limitations of gridded climate products, specifically in parameter estimation and process representation for complex high-altitude terrain. Although multiple models are available and perform well enough, generating results that are consistent with observed discharge data, the major challenge lies in selecting the most suitable model for a specific scenario and identifying the necessary input parameters. The study also outlines future directions, including the integration of AI/machine learning approaches to improve climate impact assessments and hydrological predictions in data-scarce, high-altitude Himalayan basins.

Keywords

Climate change impacts, high-altitude Himalayan hydrology, hydrological modeling, cryosphere response, climate variability, model uncertainty, Indian Himalayan Region.

Submitted 15 September 2025, revised 10 January 2026, accepted 29 January 2026

DOI: 10.26491/mhwm/217540

1. Introduction – overview of climate change implications on high-altitude regions

Climate change has emerged as the biggest threat in the past 40 years and has been responsible for impeding nations' abilities to achieve sustainable development goals (IPCC 2007). Evidence of the impacts and risks associated with climate change is strongest for natural systems (IPCC 2017). It has been projected for the Hindu Kush Himalaya (HKH) that by the end of the 21st century, the median annual air temperature will further increase by 0.8-5.7°C (Dahri et al. 2021). Future projections for the Himalayan regions are highly conflicting and spatially variable (Dahri et al. 2021). In India, glaciers cover a region from 26°N, 72°E to 36°N, 96°E (Raina, Srivastava 2008), providing water to 50-60% of the population living downstream. The Himalayan region is potentially one of the most critical parts of the world when considering the social and economic impacts of glacier shrinkage (Barnett et al. 2005). A study observed

that between 2003 and 2009, Himalayan glaciers lost an estimated 174 gigatons of water each year and retreated at a rate of 0.3 to 1.0 meters per year (with the most extreme melting occurring in the east), a rate faster than the global average ice mass melt (Mani 2021). Climate change is responsible not only for temperature and precipitation variation but also disturbs the hydrological cycle. This variation impacts glacier mass by causing melting and loss of seasonal snow, thereby affecting the stability of water resources in the region. Any changes in water resources, including reduction in availability or variation in flow patterns resulting from altered seasonal precipitation, will directly influence the water supply and consequently reduce water availability for agriculture or domestic use. Thinning of glaciers may also affect hydropower production, a key source of renewable energy for the region. Factors that will affect future water availability in Himalayan rivers include glacier melt, groundwater extraction, reservoir construction, decline in precipitation, population growth, snowmelt, springs, and permafrost thaw. These concerns have made the Himalayan region a focus of research for the past decade (Chandel, Ghosh 2021). In short, the melting induced by climate change will cause a cascading effect, making the region more vulnerable to disasters such as flash floods, landslides, soil erosion, and glacial lake outburst floods. Initially, melting glaciers may increase groundwater levels downstream, but over time, glaciers will retreat and generate less meltwater, exacerbating water shortages and endangering the lives of the downstream population (Ó Dochartaigh et al. 2019). With the fast-growing need for fresh water and increasing awareness of its sustainable use, studies on snow, ice, and glaciers have acquired considerable importance (Kesarwani et al. 2015). Knowledge of snow and glacier-fed watersheds and associated glaciological elements is significant for the sustainable use and protection of Himalayan water resources. The purpose of this literature review is to systematically examine existing research related to the impacts of climate change on high-altitude regions. It is critical to study glacio-hydrological functions and their impact on water availability. Although numerous studies have attempted to analyze recent climate change, project future changes, and model the underlying impacts on the hydrological regime and water availability for the Himalayan region, there are still significant gaps in data, information, and knowledge that limit our understanding of the basin's hydro-meteorological regime. The present study is an attempt to understand temperature and precipitation trends in the Himalayas for improved understanding of climate change impacts on regional hydrology. The study also explores the suitability of various hydrological models used in the region. The study highlights climate-driven changes that influence hydrological processes, while also discussing key challenges in Himalayan hydrological studies, such as data scarcity, complex terrain, limited long-term observations, and uncertainties associated with climate inputs, model structure, and parameterization.

2. Literature review – methodology

To understand the impacts of climate change on high-altitude regions, relevant literature was identified through online databases such as Scopus and Google Scholar. The initial identification of literature was based on titles and keywords. The keywords included, but were not limited to: climate change, high altitude, hydrology, hydrological modeling, glaciers, and temperature and precipitation variation in the Himalayas. The literature review methodology is explained in Figure 1a. A few papers were excluded based

on the study areas, and language of the paper. Literature with insufficient information was also excluded. Finally, a total of 206 documents was selected for this review, including original articles (76%), books, book chapters and reports (12%), review articles (7%), and technical reports and theses (6%). These 206 documents were then broadly categorized by their study areas, such as the Himalayan region, HKH (Hindu Kush Himalaya), and IHR (Indian Himalayan Region) as depicted in Figure 1b. For a broader perspective, global studies were also included for general explanation. Further classification was done based on research themes (Fig. 1c). The main research themes we focused on were: climate change impact on hydrology, hydrological modeling, climate change impact on glaciers, glacio-hydrological modeling, glaciers and glacier hazards, geographic information system (GIS) applications for the assessment of climate change, climate change impacts, and temperature and precipitation variation associated with climate change. The main aim was to review literature focused on climate change impacts on high-altitude regions by altering cryospheric and hydrological components. This structured methodology ensures comprehensive coverage and minimizes bias by following a systematic, repeatable, and transparent process.

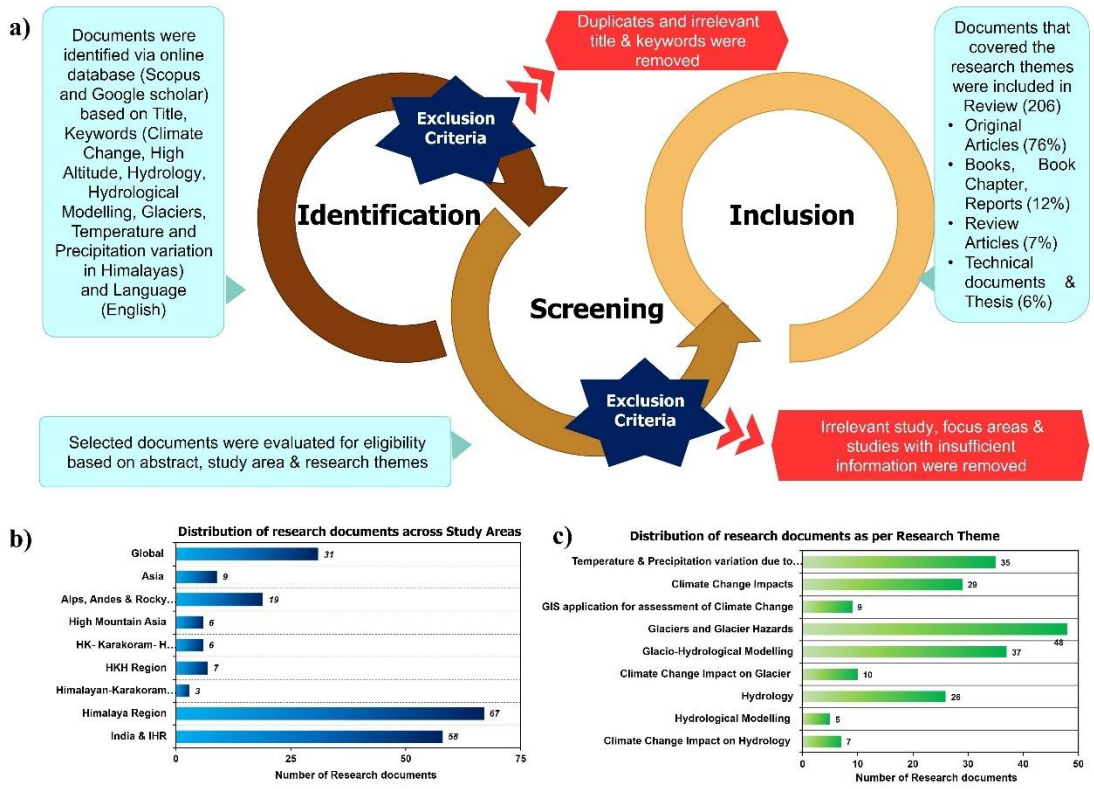

Fig. 1. Literature review methodology detailing the stages of identification, screening, and inclusion criteria. The figure also illustrates the distribution of literature categorized by study area and research theme.

3. High-altitude Himalayan hydrology – key features

The Himalayan region is characterized by elevation variation, diverse precipitation patterns, and temperature profiles from the foothills to the Himalayan crest, with average elevation in the Tibetan plateau (Chandel, Ghosh 2021). The foothills are warm, and the higher altitudes are cooler. The region

receives rainfall from two precipitation systems: the Indian summer monsoon and western disturbances. The central and eastern parts of the Himalayas receive rainfall from the Indian summer monsoon from June to September, whereas western disturbances and the Indian summer monsoon contribute to precipitation in the western Himalayas (Bookhagen, Burbank 2010). The high-altitude Himalayan region acts as a barrier and is responsible for precipitation in the foothills. The majority of basins in the region are of the summer accumulation type, but the western Himalayas are of the winter accumulation type (Lutz et al. 2014). Snow and glaciers are important hydrological components in the Himalayas, affecting the livelihood of about a billion people residing in the basins of the Indus, Ganges, and Brahmaputra rivers (Wester et al. 2019). The water from these rivers not only contributes to the water requirements of the downstream populations but is also essential for food production, energy production, and ecosystem sustenance. The water resources generated from these rivers are responsible for the gross domestic products (GDP) of India, Nepal, Pakistan, and China (Chandel, Ghosh 2021). Snowpacks and glaciers are considered highly sensitive indicators of global climate change. They are predominantly sensitive to the rising temperatures affecting the Himalayan hydrology in several ways, namely, glacier retreat, permafrost degradation, lesser snowfall, reduced mountain snowpack, and early onset of melt, which consequently alter the patterns of river flow (Immerzeel et al. 2010; Beniston, Stoffel 2014; Lutz et al. 2014; Lutz et al. 2016). Various studies have confirmed that the majority of glaciers in the region is facing decline in their mass and even worse conditions are predicted for the future (Brun et al. 2017; Azam et al. 2018; Chandel, Ghosh 2021; Schmale et al. 2017).

4. Climate change in the Himalayas

The task of understanding climate change trends starts with the basic understanding of the term 'climate,' which refers to the long-term average of weather conditions (temperature, precipitation, humidity, wind speed, and direction) observed at a given location (Shekhar, Singh 2014). Climate change refers to any long-term deviation in these climate parameters caused by natural variability or human activities. The phrase 'long-term' is consistent with the definition of climate as an average of its parameters over a duration of 30 years (WMO 2017). All available records of temperature and climate models show a near-surface temperature increase, particularly in recent decades (IPCC 2007; IPCC 2018).

4.1. Historical climate observations and trends in the IHR region

Various studies have confirmed that elevated warming negatively affects the glacio-hydrology of snow and ice-fed river catchments, especially in the high-altitude Himalayan region (Shekhar, Singh 2014; Wester et al. 2019). This impact is also seen in the hydrological balance of many watersheds globally (Xu et al. 2009; Immerzeel et al. 2010). It is now well-established that the Earth's surface has warmed over the past 100 years, primarily due to anthropogenic activities (IPCC 2021). Changes in many components of the climate system, such as precipitation, snow cover, sea ice, and extreme weather events, have also been observed (NOAA 2020). These changes exhibit remarkable regional variations around the globe. Various studies have shown that high-altitude regions are especially sensitive to climate change because they experience

higher mean annual rates of warming (IPCC 2007; Xu et al. 2009; Lesher 2011; Pepin et al. 2015). Studies assessing past temperature trends in the Himalayan region indicate that surface air temperatures have increased in the Himalayas since 1970 (Bhutiyani et al. 2007; Immerzeel et al. 2010). Future predictive studies estimate an increase of 0.01°C to 0.75°C per year by 2050 (Xu et al. 2009; Kraaijenbrink et al. 2017). Bhutiyani et al. (2007) observed historical temperatures from three meteorological stations and reported higher rates of warming during winters in the northwestern Himalayas. Temperature trends observed by various studies are given in Table 1.

Assessment of historical precipitation in the Himalayas shows both positive and negative trends (Ye et al. 2007a; Immerzeel et al. 2010) (Table 2). A study by Nepal (2016) based on model assessments showed variation in snowfall patterns, snowmelt, discharge, and evapotranspiration, estimating that these variations are due to sensitivity to climate change. Studies conducted over the entire Indian Himalayan Region (IHR) suggest that increasing human activities have led to unprecedented changes in the earth's delicate climate system (Sharma et al. 2019). Changes in temperature and precipitation patterns will significantly impact high-altitude hydrology in the region. The net hydrologic impacts of climate change on high-altitude lakes have also been observed, showing dependence on their proximity to glaciers, lake elevation, and whether climate changes are predominantly in temperature or precipitation (Thayyen, Gergan 2010; Ahmed et al. 2022). Our understanding of hydro-meteorological regimes, particularly at the sub-basin scale, is limited by the lack of significant data and information, and knowledge gaps. In the western Himalayas, numerous studies have been conducted to examine recent climate change, project future changes, and model the impacts on the hydrological regime and water availability (Immerzeel et al. 2013; Hasson et al. 2017; Hasson et al. 2019; Lutz et al. 2019; Dahri et al. 2021). However, accurate assessments are challenging because in situ observations are very scarce and the strong influence of the innately complex climate systems interacting with very high orographic features (Dahri et al. 2021).

Table 1. Summary of reported historical and projected temperature changes across the various Himalayan regions based on observational records, satellite and reanalysis datasets, and climate model projections. Values represent mean or extreme temperature trends over different analysis periods as reported in the cited studies.

Study area	Study period	Temperature change	Variable	Data collection method	Source
Himalayan region	1950 to 1999	+2.5°C	Mean temperature	Observation and IPCC-AR4	Rao et al. (2016)
	21st century	+9°C	Mean temperature	Projected: IPCC-AR4	Rao et al. (2016)
	21st century	+0.3-0.9°C	Mean temperature	Projected: RCP8.5 model	Dimri et al. (2018)
	1982-2006	+1.5°C	Mean temperature	Observations	Shrestha et al. (2012)
Hindu Kush Himalayas (HKH)	1901-2014	0.1°C/decade	Mean temperature	Observations	Sabin et al. (2020)
	21st century	+2.6-4.6°C	Mean temperature	Projected: CMIP5	Sabin et al. (2020)
Karakoram and Northwest Himalaya	2066-2095	+1.6-1.8°C	Mean temperature	Projected: RCP8.5	Sanjay et al. (2017)
Indian Himalayan Region (IHR)	1971-2003	+0.22°C/decade	Mean temperature	Observed: Station data	Kothawale, Rupa Kumar (2005)
	1986-2015	+0.15°C /decade	Mean temperature	Observed: Station data	Le Masson, Nair (2012)
	2080	+3.84°C	Mean temperature	Projected: Climate Model	Krishnan et al. (2019) Negi et al. (2021)
	2011-2040	+1.18°C	Maximum temperature	Projected: General Circulation Models (GCMs)	Sharma, Goyal (2020)
	2011-2040	+0.54°C	Mean temperature	Projected: General Circulation Models (GCMs)	Sharma, Goyal (2020)
	2011-2040	+1.92°C	Minimum temperature	Projected: General Circulation Models (GCMs)	Sharma, Goyal (2020)
Western Himalaya	1901-2003	+0.9°C	Minimum temperature	Observed & Reanalysis Modelled data	Dash et al. (2007)
	1901-2003	+1.9°C	Minimum temperature	Observed & Reanalysis Modelled data	Dash et al. (2007)
	1985-2009	+1.41°C	Maximum temperature	Space based Observations (GIOVANNI)	Kumar et al. (2014)
	1985-2009	+1.63°C	Minimum temperature	Space based Observations (GIOVANNI)	Kumar et al. (2014)
	1985-2009	+1.49°C	Mean temperature	Space based Observations (GIOVANNI)	Kumar et al. (2014)
	1979-2007	+0.26 ±0.09°C/ decade	Mean temperature	Space based observation	Gautam et al. (2010)
Northwest Himalaya	1901-2000	+0.16°C	Mean temperature	Observation and Space based (NOAA) study	Bhutiyani et al. (2007)
	1876-2006	+0.11°C	Mean temperature	Observation (IMD, SASE and IAF Stations)	Bhutiyani et al. (2007)
	20th century	+0.009-0.064°C	Mean temperature	Observation (IMD Stations)	Singh et al. (2008a)
Eastern Himalaya	1960-2000	+0.1°C to 0.9°C	Maximum temperature	Observation (Tocklai Tea Research Association (Jorhat))	Jhajharia, Singh (2011)
	1960-2000	+0.2°C to 0.8°C	Mean temperature	Observation (Tocklai Tea Research Association (Jorhat))	Jhajharia, Singh (2011)
	1960-2000	+0.1°C to 0.6°C	Minimum temperature	Observation (Tocklai Tea Research Association (Jorhat))	Jhajharia, Singh (2011)
	1900-2002	+0.6°C	Mean temperature	Modelling based study (Climate Research Unit (CRU) dataset)	Immerzeel (2008)
	2050	+2.9°C	Mean temperature	Projected: Modelling based study (HadRM2 Simulations)	Shrestha, Devkota (2010)
	2050	+4.3°C	Mean temperature	Projected: Modelling based study (PRECIS simulations)	Shrestha, Devkota (2010)

Table 2. Reported trends in precipitation across the Himalayan, Hindu Kush–Himalayan, and associated sub-regions based on observational records and climate model projections. The table summarizes study periods and the direction of precipitation change (increasing or decreasing) as documented in the cited literature.

Study area	Study period	Precipitation variation	Source
Himalayas	1982-2006	Increasing	Shrestha et al. (2012)
Hindu Kush Himalayas (HKH)	1951-2014	Increasing	Krishnan et al. (2019)
	1901-2099	Increasing	Panday et al. (2015)
Indian Himalayan Region (IHR)	2011-2040	Increasing	Sharma, Goyal (2020)
Western Himalaya	1951-2007	Increasing	Krishnan et al. (2019)
	1998-2016	Increasing	Krishnan et al. (2019)
	1975-2006	Decreasing	Guhathakurta, Rajeevan (2008) Dimri, Dash (2012)
	1866-2006	Decreasing	Bhutiyani et al. (2009)
Eastern Himalayas	2000-2100	Increasing	Immerzeel (2008)
	1979-2100	Decreasing	Singh, Goyal (2016)
	1951-2007	Decreasing	Saikia et al. (2013)

4.2. Evidence of temperature rise, precipitation changes, and extreme events

Temperature can represent the energy exchange between longwave and shortwave radiation; therefore, temperature change is considered a good indicator of changing climate globally (Bhutiyani et al. 2007). Meteorological observations worldwide show an increase of 0.85°C from 1885 to 2012 and an increasing trend of 0.05°C per decade in global mean temperature (Diaz, Bradley 1997; Easterling et al. 1997; Barry 2001; Folland et al. 2001; IPCC 2013; NOAA 2020). The warming trend is not uniform globally, with inconsistencies observed in mountainous regions due to the unavailability of sufficient long-term in situ observations and complex topographic conditions (Pepin et al. 2015). Studies based on instrumental data suggest that the Himalayan region has experienced a warming trend more than twofold greater than the global average (Shrestha et al. 1999; Kothawale, Rupa Kumar 2005; Bhutiyani et al. 2007; Kothawale et al. 2010; Krishnan et al. 2020). The temperature trend has increased in the past decades, with this unusual warming trend attributed to anthropogenic greenhouse gas (GHG) emissions and deforestation, which are suggested to be dominant climate forcing agents (Shrestha et al. 1999; Kothawale et al. 2010; Zemp et al. 2019). In a study to understand past temperature trends, increases in average annual temperature and average annual maximum temperature have been reported (Huddleston et al. 2003; Bhutiyani et al. 2007; Palazzi et al. 2019). This increase is several-fold higher than the rise in the global average temperature. Another study based on previous meteorological data sets from the Indus and Ganges basins suggested rises of 0.50°C and 0.44°C, respectively (Singh et al. 2008a). A study conducted over the western IHR for the period from 1971 to 2007 suggested a warming rate of 0.46°C per decade, higher than the 0.20°C per decade observed for the rest of India (Kothawale, Rupa Kumar 2005; Sharma, Goyal 2020).

In recent decades, several studies have been conducted for the northwestern Himalayas using reanalysis datasets; the result shows an increased rate of warming in the region (Dimri, Dash 2012; Kumar et al. 2014). A study conducted in the central Himalayas for the period 1967-2007 using a meteorological

dataset suggests an increase in the annual mean temperature of 0.49°C (Singh et al. 2013). A study conducted by Singh et al. (2016) found that precipitation is a relatively less-studied parameter for assessment of climate change. Since the precipitation data is limited no visible trend is observed for IHR precipitation, unlike temperature. Few studies suggest that, in comparison to moderate rainfall events, extreme rainfall events have increased significantly in IHR. Whereas in the northwestern Himalayas in the Indus basin (IHR) a significant increase in precipitation has been observed (Shrestha et al. 2000; Goswami et al. 2006; Nandargi, Dhar 2011). In another study conducted by (Bhutiyani et al. 2009) in northwestern IHR using the meteorological dataset from 10 weather stations suggests a decrease in annual and monsoon precipitation and an increase in winter precipitation. Whereas another study (Dimri, Dash 2012) reported a contrasting trend, indicating an insignificant decrease in winter precipitation. The study conducted for Uttarakhand & Himachal Pradesh shows a significant decrease in annual precipitation. Whereas the study for the western (Jammu & Kashmir, J&K) and eastern parts of IHR shows an increasing trend in precipitation (Singh, Goyal 2016). Studies conducted by (Kothawale et al. 2010), have also suggested temperature variations in the region. The temperature trends across the central Himalayan region (Nepal) exhibit significant spatial variation. There is a visible warming trend over the majority of the Himalayan and middle mountainous areas. On the contrary, the Terai and Siwalik regions display comparatively smaller warming trends, and in some cases, there are even observable cooling trends. This spatial distribution of maximum temperature trends, as highlighted by Shrestha et al. (1999), underscores the complexity of climate patterns in the central Himalayas, with distinct warming patterns in mountainous terrains and varying trends in the lowland regions. A study conducted in the central Himalayas (Nepal) from 1971 to 1994 using the temperature data from 49 stations shows a warming trend of 0.068 to 0.128°C in most of the middle mountain and Himalayan regions. The study revealed that the southern plain region shows a warming trend of 0.038°C per year, along with increased variation in rainfall patterns in the region. Global warming and its impact on the hydrological cycle and nature of hydrological events have posed an additional threat to the region (Mall et al. 2006).

Extreme events like flash floods, flooding from monsoon rainfall, lake outbursts, landslides, and avalanches may be induced by climate change (National Research Council 2012). Mainly, the monsoon flood is caused by heavy rains, but other factors such as snowmelt and changes in land use may enhance the scale of the event, making it more disastrous (Pramanik, Bhaduri 2016). The water resources of snow-dominated regions such as the Himalayas are adversely impacted by climate change (Barnett et al. 2005; Piao et al. 2010; Chen et al. 2016; Roe et al. 2017; Huss, Hock 2018; Chandel, Ghosh 2021). Increasing warmth and humidity in daily weather, erratic rainfall patterns, extension of the normal winter season, and increasing incidences of floods, drought, and cyclones are some of the common observations, reflecting changes in normal atmospheric circulation and climate change predictions (IPCC 2007). Many studies have been conducted to observe a particular trend in precipitation patterns over this region. The results suggest that precipitation trends are sensitive to location and the methodology used for assessment, along with the elevation of the meteorological stations that have been used for collection of data. It has been

observed that the region has sparse meteorological stations, and the available stations are at low altitudes (Palazzi et al. 2013). This situation results in low-altitude bias, and snow measurements at all altitudes are typically fairly error-prone (Winiger et al. 2005; Hunt et al. 2020).

4.3. Impact of climate change on cryosphere dynamics

Himalayan glaciers are valley-type glaciers and account for about 70% of non-polar glaciers (Nandy et al. 2006). Earlier studies have estimated that an area of about 32,000 km² is permanently covered by ice and snow in the Himalayas (Negi 1991). According to the Geological Survey of India, there are 9,575 glaciers in the Indian Himalayas, distributed among the three river basins – Indus, Ganga, and Brahmaputra. Most of these glaciers (approximately 90%) are small to very small, being less than 5 km in length and smaller than 5 km² in area. Only a few glaciers, such as Siachen, Gangotri, Milam, and Zemu, are larger than 10 km². The IHR serves as an important source of freshwater for the densely populated areas downstream. The region is particularly vulnerable to climate change because it is highly dependent on snow and glacier-melt runoff to meet its freshwater demands (Singh, Goyal 2016). Due to their latitudinal and altitudinal positions, the Himalayan glaciers react to even minute changes in temperature and precipitation patterns (Kumar et al. 2009; Messerli et al. 2009; Immerzeel et al. 2010; Bajracharya, Shrestha 2011). In recent decades, climate change has induced various glacio-hydrological changes, such as changes in terminus and areal extent of the glaciers, glacier mass balance, and streamflow in downstream areas. The ablation and accumulation of glaciers are directly affected by changes in temperature and precipitation patterns. Air temperature is crucial since it is a major component of energy exchanges that control snow and ice melts. Among various parameters for assessing climate impact, glacier length is a major parameter for observing such changes. The recession in length or snout of a glacier depends on the increase in temperature, with the warming trend shifting the snout and ELA towards higher altitudes. Pandey and Venkataraman (2013) conducted a study from 1980 to 2010 over the western IHR (Chandra-Bhaga basin) and found a glacier area loss of 2.5%. Another study conducted in the Garhwal Himalayas from 1968 to 2006 reported an overall reduction in glacial area from 4.6% to 2.8% (Bhambri et al. 2011). An increased rate of retreat was observed from 1990-2006. A study conducted by Basnett et al. (2013) in the Teesta River basin showed a reduction in area from 3.3% to 0.8% from 1989-1990 to 2010. Another study by Racoviteanu et al. (2015) in the Sikkim Himalayas observed an areal loss from 20.1% to 8% from 1962 to 2000. Studies in various parts of the IHR suggest a reduction in glacierized area, with an increased rate after 1990 (Bahuguna et al. 2007; Berthier et al. 2007; Chalise et al. 2003; Ye et al. 2007b). A survey conducted by Ageta et al. (2003) over Himalayan glaciers in India, Bhutan, and Nepal reported a concerning trend: nearly all measured glaciers exhibited signs of retreat. This observation is particularly pronounced for summer-accumulation type glaciers in regions characterized by elevated precipitation and warmer temperatures, as highlighted by Ageta et al. (2003). Data from the past 100 years generated from glacier studies show that the glaciers in the Himalayas have been, by and large, shrinking and retreating continuously (IPCC 2013; Pramanik, Bhaduri 2016). The findings underscore the vulnerability of

Himalayan glaciers to climate change, emphasizing that not only are these glaciers retreating, but the rate of retreat is notably accelerated in certain glacier types and geographical settings.

A few studies also concluded that the changes are observed only in glacier length and area, showing only the horizontal variation and not representing any volume change in the amount of ice present in the glacier. Hence, it cannot be concluded that observed changes are the effects of climate change; other underlying factors may be responsible for such variations. In addition, there can be several other factors that can change the length of a glacier, including bed topography, aspect, and slope, which primarily control the flow and dynamics of glaciers and hence the changes that occur. Apart from these factors, debris cover, a characteristic of Himalayan glaciers, can also be responsible for anomalous behaviour of the snout position of the glaciers (Singh et al. 2016). It has been evident that variation in precipitation and temperature due to climate change over the Himalayan region plays a dominant role in influencing glacier sensitivity and affects the melting process. Glaciers in the Himalayas are under the influence of westerlies that show a decreasing trend from west to east, along with the influence of the Indian and Asian monsoons, showing a decreasing trend from the eastern Himalayas to the west (Burbank et al. 2003; Bookhagen, Burbank 2006; 2010). This complex climate diversity results in a varying pattern of glacier response to climate variables (Fujita, Nuimura 2011; Scherler et al. 2011; Bolch et al. 2012; Gardelle et al. 2013; Gardner et al. 2013; Tayal, Sarkar 2019). Therefore, it is important to understand the impact of climate change on glacial regions. To understand these impacts, it is essential first to identify the probable issues in terms of climate change drivers and human dependence on Himalayan resources. Once these issues are understood, probable solutions can be assessed by applying various disciplinary sciences and developing suitable approaches that aid in a better and more robust understanding of such systems (Fig. 2).

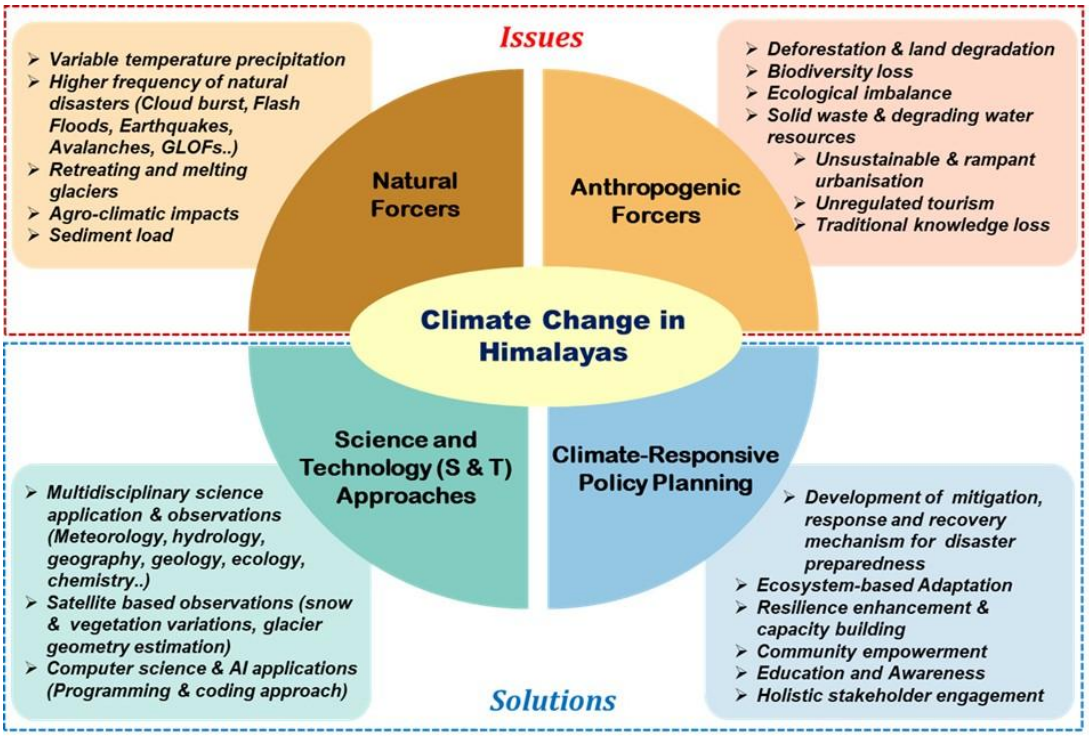

Fig. 2. Climate change in the Himalayas – issues and probable solutions.

5. Hydrological response of glaciers to climate change

Studies conducted over the Himalayan regions have observed the impact of climate change on river flow. Many underlying scenarios affect the hydrology of the region, and several factors contribute to increased melt rates in glaciers. Understanding these dynamics is crucial for comprehending the impact of global warming on these icy landscapes. Recognizing these varied factors contributes to a more comprehensive understanding of the intricate interplay between climate variables and glacier behaviour in the face of global warming. Because of variability in glacier characteristics and differences in climate, high-altitude regions respond differently to climatic changes across the world (Bliss et al. 2014). Therefore, assessing the climate impact on glaciers is crucial for estimating water availability and maintaining ecosystem balance (IPCC 2013; Pramanik, Bhaduri 2016). Various studies have recognized the Himalayan region as a 'hotspot' of climate change due to significant transformations in its hydro-meteorological regime (Bhutiyani et al. 2009; Shrestha, Aryal 2011; Wijngaard et al. 2018; Krishnan et al. 2019; Lutz et al. 2019). An authentic assessment of climate change, its variability, and its underlying impacts on the hydrological regime in the basin is seriously constrained by the paucity of observed data and detailed hydro-meteorological investigations (Dahri et al. 2021).

5.1. Glacier melt contributions to river discharge

Glaciers, by acting as buffers, play a crucial role in maintaining the hydrological cycle and ecosystem stability. This role is well documented by studies conducted in the region. Glaciers regulate the water supply from mountains to the plains during both dry and wet spells (Pramanik, Bhaduri 2016). Under a warming climate, glaciers and seasonal snow cover experience changes in their water storage capacity. A negative mass balance leads to an increased contribution of meltwater to river flows. However, this increased melt is not permanent; as the glacier volume decreases, the total meltwater generated from glaciers will ultimately decrease. Various studies have established that, depending on the state of glacier retreat, a warming climate may lead to either rising or decreasing river flows (Pellicciotti et al. 2010; Ragettli et al. 2016). In a related study, Ren et al. (2007) employed three distinct coupled General Circulation Models (GCMs) to estimate glacier melt rates specifically in the Greater Himalaya (GH). Their modeling exercise estimated a spatially averaged glacier depth reduction of approximately 2 meters for the 2001-2030 period in areas located below 4000 meters. Averaged over the entire GH region, the melting rate is accelerating at about 5 mm per year (Lesher 2011). This modeling approach provides valuable insights into dynamic changes within the glacier systems, offering a quantitative understanding of the thinning process. Furthermore, a study conducted in the Koshi River basin provides insights on hydrological implications of glacier melt. The research indicates that, on average, snow and glacier melt contribute approximately 34% to the total discharge annually. Notably, during the pre-monsoon season (March to May), this contribution rises significantly to 63%. Projections from the model used in this study suggest a potential 13% increase in annual discharge by mid-century, followed by a slight decrease in subsequent years. These anticipated changes in discharge underscore the intricate relationship between glacier melt and river basin hydrology, with potential implications for downstream water resources and

ecosystems (Nepal 2016). Studies conducted by Immerzeel et al. (2013) and Lutz et al. (2014) have contributed valuable insights into the complex dynamics of water resources in the Himalayan region. Their research indicates that the combined effects of increasing precipitation and glacier melt are expected to lead to an overall increase in annual runoff for Himalayan watersheds. Thus, at least in the near term, there may be a positive impact on water availability in these regions. According to the findings, water availability is projected to remain relatively constant until mid-century. However, it is important to note that stability in overall water availability does not necessarily imply a consistent distribution throughout the year. Extreme events linked to climate change are anticipated to have a notable impact on the seasonal water availability in downstream areas (IPCC 2007; Nepal 2016).

These projections underscore the intricate nature of the hydrological system in the Himalayan region, where the interplay of increased precipitation, glacier melt, and the influence of climate change-induced extremes contributes to a nuanced understanding of water resource dynamics. Balancing these factors becomes crucial for sustainable water management, particularly in the context of potential challenges posed by variability in seasonal water availability in downstream areas.

5.2. Alterations in snowmelt patterns and timing

A study conducted by Gusain et al. (2014) from 1976 to 2011 using the station data showed that the majority of stations below 4000 m recorded declining trends in seasonal snowfall. Similarly, a study from 1987-2009 showed that the majority of stations at 3250 m elevations also showed a decreasing trend in seasonal snowfall (Singh et al. 2015). Another study conducted by Nepal (2016) observed that snowfall is projected to decrease substantially with rising temperature, the basin will lose snow storage capacity, and there will be a marked decrease in snowmelt runoff from non-glaciated areas. Various studies have shown that the contribution of glaciers (snow and glacier melt) in IHR increases from east to west (Barnett et al. 2005; Alford, Armstrong 2010; Armstrong 2010; Immerzeel et al. 2010; Racoviteanu 2011; Nepal 2016).The escalating contribution of glacier melt to the total volume of meltwater raises substantial concerns, particularly when contrasted with the replenishable nature of snowmelt. Unlike the annual renewal of snowpack through seasonal snowfall, glaciers evolve over extended periods and are not easily replenished (Barnett et al. 2005). This fundamental difference underscores the vulnerability of glacier-dependent water resources and highlights the need for a diligent approach to water management in the face of changing climate conditions. In the context of the diverse climatic patterns within the IHR, it becomes evident that the relative contributions of rain, snowmelt, and glacier melt to river discharge will vary significantly. This variability is anticipated, given the wide range of climates present in the region (Pramanik, Bhaduri 2016). Each river system within the IHR is likely to exhibit distinct hydrological responses based on its specific geographical and climatic characteristics. Numerous studies have emphasized the critical role of temperature change in shaping the contributions of snow and glacier melt to river discharge. The impact extends beyond just the quantity; it also affects the form of precipitation, distinguishing between liquid and solid forms, and the timing of their contributions to the overall

discharge. These findings collectively highlight the intricate interactions between climate variables and water resource dynamics in the Himalayan region, emphasizing the need for comprehensive assessments to inform adaptive strategies for sustainable water management in this crucial and vulnerable environment.

6. Role of hydrological models for high-altitude regions

Researchers have undertaken extensive efforts to evaluate the effects of climate change on glacierized mountainous catchments worldwide, employing cryospheric and hydrologic models (Nolin et al. 2010; Gascoin et al. 2011; Nepal 2016; Soncini et al. 2016; Zhang et al. 2016; Li et al. 2019; Bhatta et al. 2020), in addition to investigations specifically focused on the Himalayan region (Rees, Collins 2006; Immerzeel et al. 2010, 2012; Lutz et al. 2014, 2016; Shea et al. 2015; Azam et al. 2019; Chandel, Ghosh 2021). The studies have explored various models for assessing streamflow components in both glacierized and non-glacierized catchments. Current research emphasizes the importance of selecting a modeling strategy rather than relying on a single model, due to the complex and site-specific nature of high-altitude hydrology. A common trend in recent studies is the adoption of a coupled approach, integrating Geographic Information System (GIS) datasets, meteorological parameters, and glacio-hydrological models. This holistic method aims to provide a more accurate assessment of the streamflow component and the overall impact of climate change on the region. The synergy of these various datasets and models allows researchers to capture the complex interactions and dynamics within high-altitude catchments, contributing to a more comprehensive understanding of the hydrological implications of climate change in mountainous regions (Fig. 3).

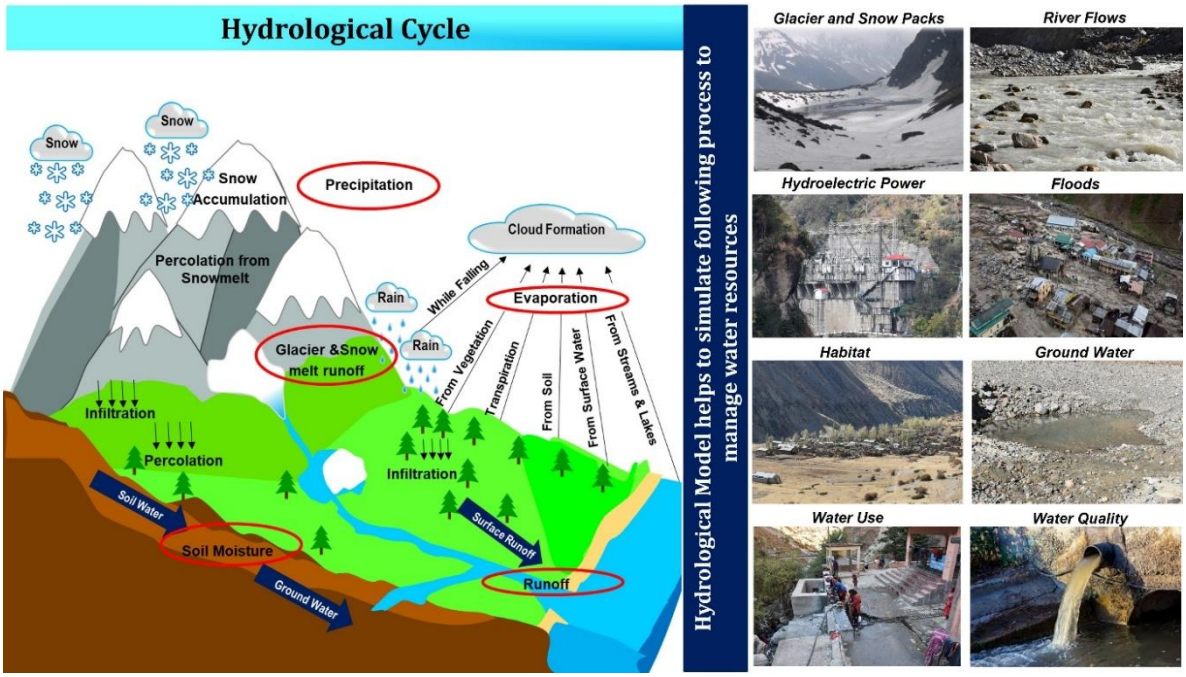

Fig. 3. Illustration of the hydrological cycle: A comprehensive overview of precipitation, evaporation, and runoff dynamics in the water cycle, highlighting the importance of hydrological models for understanding and predicting hydrological processes in various environments.

6.1. Types of hydrological models

According to (Moradkhani, Sorooshian 2008), a model is a simplified representation of a real-world system. The best model is the one that gives results close to reality with the fewest parameters and least model complexity. Models are mainly used for predicting system behavior and understanding various hydrological processes. A model consists of various parameters that define the characteristics of the model. A runoff model can be defined as a set of equations that helps in the estimation of runoff as a function of various parameters used for describing watershed characteristics. The two important inputs required for all models are rainfall data and drainage area. Along with these, watershed characteristics such as soil properties, vegetation cover, watershed topography, soil moisture content, and characteristics of groundwater aquifers are also considered. Hydrologic models are simplified, conceptual representations of a part of the hydrologic cycle.

These models are primarily used for hydrologic prediction and for understanding hydrologic processes. They are currently considered important and necessary tools for water and environmental resource management. Three major types of hydrologic models can be distinguished (Fig. 4). The major hydrological models used in various studies and details of their applications are listed in Table. 3.

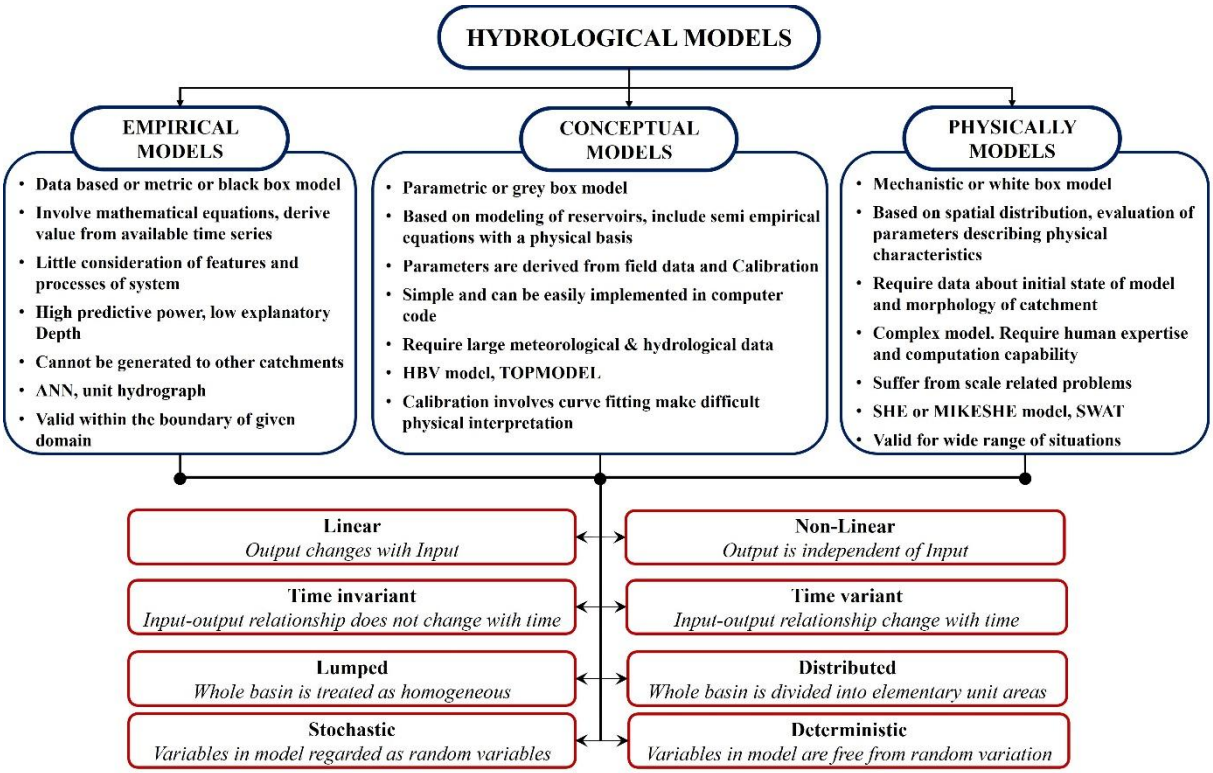

Fig. 4. Classification of hydrological models along with their characteristics (Source: Devi et al. 2015).

6.1.1. Empirical models (metric model)

These are observation-oriented models that take only the information from existing data without considering the features and processes of the hydrological system, and hence these models are also called data-driven models (Devi et al. 2015). They involve mathematical equations derived from concurrent input

and output time series, and not from the physical processes of the catchment. These models are valid only within the boundaries. Unit hydrograph is an example of this method. Statistically based methods use regression and correlation models to find the functional relationship between inputs and outputs.

6.1.2. Conceptual methods (parametric models)

This type of model describes all of the component hydrological processes. It consists of a set of interconnected reservoirs that represent the physical elements in a catchment in which they are recharged by rainfall, infiltration, and percolation and are emptied by evaporation, runoff, and drainage. Semi-empirical equations are used in this method, and the model parameters are assessed not only from field data but also through calibration. A large number of meteorological and hydrological records is required for calibration. The calibration involves curve fitting, which makes the interpretation difficult and hence the effect of land use change cannot be predicted with much confidence. Stanford Watershed Model IV (SWM) is the first major conceptual model developed by Crawford and Linsley in 1966, with 16 to 20 parameters. Many conceptual models have been developed with varying degrees of complexity.

6.1.3. Physically based models

Physically based models are mathematically idealized representations of real phenomena. These models are also called mechanistic models; they include the principles of physical processes. They use state variables that are measurable and are functions of both time and space. The hydrological processes of water movement are represented by finite difference equations. Calibration does not require extensive hydrological and meteorological data, but the evaluation of a large number of parameters describing the physical characteristics of the catchment is required, including soil moisture content, initial water depth, topography, topology, river network geometries, and dimensions (Abbott et al. 1986 (1)). Physical models can overcome many defects of the other two models because the parameters have physical interpretations. They can provide a large amount of information even outside the boundary and can be applied for a wide range of situations. SHE/ MIKE SHE model is an example of a physically based model (Abbott et al. 1986 (1 & 2)). The above three models can be divided further into subcategories according to the variability of their input and output parameters with space and time, as discussed below.

a) Linear and Non-linear – A model is linear in the system-theory sense if it satisfies the principle of superposition: i.e., any change in input must be reciprocated in output. If not, it is a non-linear model.
b) Time invariant and Time variant – A model is time-invariant if its input-output relationship does not change with time. The form of the output depends only on the form of the input and not on the time at which the input is applied. Models that do not have this property are called time-variant. Most hydrologic systems are time-variant to accommodate variations in solar activity during the day and seasonal variations during the year. Yet, for simplicity, they are assumed to be time invariant.
c) Lumped and distributed – In lumped models, the whole basin is treated as homogeneous. Here parameters are independent of space. In distributed models, which attempt to calculate flow contributions from separate areas or sub-basins that are treated as homogeneous within themselves, to

fully distributed models, in which the whole basin is divided into elementary unit areas like a grid net and flows are passed from one grid point to another as water drains through the basin.

d) Stochastic and Deterministic – If any of the variables in the model are regarded as random variables having probability distributions, then the model is stochastic. If all variables in the equation are regarded as free from random variation, so that none is thought of as having a probability distribution, then the model is deterministic.

Table 3. Description of various models along with their application details.

Model/Model type	Input	Application	Snow/Glacial melt	Source
Snowmelt runoff model (SRM)/Semi-Distributed Model	Snow cover area and ancillary data: temperature, precipitation, and runoff	Simulate and forecast daily streamflow in mountain basins where snowmelt is a major runoff factor	Computes snow melt, glacier module is not included	Martinec et al. (1994)
Snowmelt Model (SNOWMOD)/Distributed Model	Snow covered area, elevation bands and their areas, altitude of meteorological stations, precipitation, air temperatures, streamflow data, and information on the initial soil moisture status of the basin	Simulate daily streamflow for mountainous basins having contributions from both snowmelt and rainfall	Computes snow melt, glacier module is not included	Singh, Jain (2003)
Water flow and balance simulation model (WaSiM)/distributed, deterministic, physically based model	Precipitation and temperature, raster data for topography, land use, and soil properties.	Grid-based tool for investigating the spatial and temporal variability of hydrological processes in complex river basins	Glacier module is not included, computes short-term (floods) and long-term simulations (long-term water balance simulations)	Hess, Counsell (2000)
GEOtop/distributed model	Georeferenced maps, elevation (DTM), soil-type map, land-use map, weather (hourly) data time series	Simulate interaction between energy balance (evapotranspiration, heat transfer) and hydrological cycle (water, glacier, and snow) for relatively large mountain catchments	Computes snow cover dynamics	Endrizzi et al. (2014)
Hydrologiska Byråns Vattenbalansavdelning/semi-distributed model	Daily rainfall, temperature, and potential evaporation	Simulates daily discharge for glaciarized as well as non-glaciarized catchments	Glacier module is included	Seibert, Vis (2012)
Tracer Aided Catchment Model, Distributed (TACD)/distributed model	Precipitation, temperature, and evapotranspiration	Applicable in process-based runoff generation	Glacier module is included but computation of melt of debris-covered glaciers is treated the same way as that of debris-free glaciers	Uhlenbrook et al. (2004)
Soil and Water Assessment Tool (SWAT)/semi-distributed model	Daily rainfall data, maximum and minimum air temperature, solar radiation, relative air humidity & wind speed, DEM, and land use/land cover maps	Simulates different hydrologic responses for a river basin or watershed using process-based equations	Computes snow accumulation and snowmelt	Douglas-Mankin et al. (2010)

Model/Model type	Input	Application	Snow/Glacial melt	Source
University of British Columbia Watershed Model (UBC)/semi-distributed model	Precipitation, temperature, and elevation bands information	Designed primarily for mountainous watersheds; calculates the total contribution from both snowmelt and rainfall runoff	A separate calculation can also be made for runoff occurring from glacier-covered areas	Loukas, Vasiliades (2014)
Hydrologic Engineering Center - Hydrologic Modeling System (HEC-HMS)/semi-distributed model	DEM, precipitation, temperature, stream, and watershed characteristics	Suitable only for events not for long-term hydrological simulations	Computes Snow Melt	Visweshwaran (2017)
Mike-SHE/distributed model	Model extent - typically as a polygon, topography, precipitation, evapotranspiration, air temperature, solar radiation, sub-catchment delineation, river morphology (geometry + cross-sections), land use distribution, soil distribution, subsurface geology	Simulates the complete land phase of the hydrologic cycle	Computes snow melt	Soltani et al. (2017)
Variable Infiltration Capacity (VIC)/large-scale, semi-distributed	Daily rainfall, daily maximum and minimum temperature, soil map, land cover map, vegetation properties, lake and wetland features, digital elevation model, streamflow data	Subgrid variability, macroscale model; large-scale effects	Computes snow melt	Liang et al. (1994)
Spatial Processes in Hydrology model (SPHY)/spatially distributed	Digital Elevation Model (DEM), land use type, glacier cover, reservoirs and soil characteristics. precipitation, temperature, and evapotranspiration	Simulate terrestrial hydrology at flexible scales, under various land use and climate conditions	Glacier module is included	Terink et al. (2015)

6.2. Integration of remote sensing and GIS data in modeling

With the advent of various GIS-based hydrological models, remote sensing and GIS-based techniques are being integrated widely into studies. To understand the variation of glaciers (snow cover, ELA, snout, GLOFs, etc.) satellite imagery is being used in the studies. Gardelle et al. (2011) used Landsat Thematic Mapper (TM) and Enhanced Thematic Mapper Plus (ETM+) imagery to compare the evolution of lakes throughout the HKH and found that in the wetter, more eastern region, which is influenced by the Indian summer monsoon (India, Nepal, and Bhutan), glacial lakes are more numerous, larger, and are growing in size, while in the more western, drier region (Pakistan and Afghanistan), glacial lakes are decreasing in size. Glacier length is one of the most widely available datasets for the Himalaya (Lesher 2011). This parameter can be easily reported using remote sensing observations. Uttarakhand has the maximum number of observations of changes in glacier length. All the glaciers are retreating with an average rate of about 18

m/year (Singh et al. 2016). Various studies include DEM datasets for snow cover estimation. Surprisingly, apart from the shrinkage reported by various glaciological studies using remote sensing, a study by Bahuguna et al. (2014) using the same method suggests that 86.8% of 2018 glaciers mapped in Karakoram, Himachal Pradesh, Zanskar, Uttarakhand, Nepal, and Sikkim regions of the HKH were stable not retreating between 2000/2001 and 2010/2011 (Singh et al. 2016). Remote sensing has been used extensively for mapping changes in the area covered by glaciers and snow in the IHR. Mapping of Chhota Shigri, Patsio, and Samudra Tapu glaciers in the Chenab basin, Parbati glacier in the Parbati basin, and Shaune Garang glacier in the Baspa basin, has reported an overall deglaciation of 21% from 1962 to 2001 (Kulkarni et al. 2007). A study from western IHR suggests a loss of glacier area of 19 and 9% from two nearby river basins (Brahmbhatt et al. 2012). Moreover, various distributed grid-based hydrological models (VIC, MIKESHE) require DEM datasets, LULC, Soil maps, and glacier area extent. All of these parameters are computed with the help of remote sensing & GIS techniques. The Soil and Water Assessment Tool (SWAT) has been widely accepted as a suitable model for hydrological analysis in Himalayan watersheds (Swain et al. 2022). As a semi-distributed model, SWAT requires elevation-wise area information for glacierized and non-glacierized regions, which have been derived in previous Himalayan studies using GIS spatial analysis. These applications highlight the importance of accurate representation of elevation-dependent land cover and cryospheric processes in mountainous basins.

7. Case studies: hydrological model applications in the Himalayas

Numerous studies worldwide, including in the Himalayas, have focused on quantifying the contributions of different streamflow components (Alford, Armstrong 2010; Racoviteanu et al. 2013; Brown et al. 2014; Mimeau et al. 2019b; Kayastha et al. 2020; Kayastha, Kayastha 2020). The relative roles of glacier melt, snowmelt, rainfall runoff, and baseflow have been assessed across high-altitude catchments (Singh, Jain 2002; Immerzeel et al. 2010, 2012; Racoviteanu et al. 2013; Zhang et al. 2013; Lutz et al. 2014; Nepal et al. 2014; Savéan et al. 2015; Azam et al. 2019). These studies typically employ glacio-hydrological models to separate and quantify streamflow components. Several physically based distributed models have been applied in Himalayan catchments. Examples include SPHY (Spatial Processes in Hydrology) (Lutz et al. 2014; 2016), TOPKAPI-ETH (Ragettli et al. 2013; 2016), HBV (Stahl et al. 2008; Jost et al. 2012; Etter et al. 2017), Variable Infiltration Capacity (VIC) (Zhang et al. 2013; Zhao et al. 2013), the Distributed Hydrology Soil Vegetation Model (DHSVM) (Wigmosta et al. 2002; Naz et al. 2014; Frans et al. 2015, 2016; Mimeau et al. 2019a), and Glacier Evolution Runoff Model (GERM) (Huss et al. 2014). These tools provide insights into glacier mass balance, runoff partitioning, and the role of snow and ice melt under changing climate conditions. Hybrid approaches have also been developed. VIC has been integrated with glacier models to predict runoff (Zhang et al. 2013; Zhao et al. 2013; Ren et al. 2018; Yun et al. 2020). Temperature-index models are sometimes combined with VIC outputs using area-weighted factors to simulate glacier melt (Chandel, Ghosh 2021; Zhang et al. 2013). Remote sensing products have also supported hydrological modeling; for example, MODIS snow cover and TRMM precipitation estimates, were attributed to enhanced glacier runoff under warming conditions (Immerzeel et al. 2009). However,

significant uncertainties persist in climate-forcing datasets, particularly for high-altitude hydrometeorology. Earlier studies in the Indus Basin relied on lumped or temperature-index models, which often oversimplify glacier-hydrology interactions. More recent work has emphasized distributed and process-based approaches that capture catchment heterogeneity (Bhanja et al. 2023; Dwivedi et al. 2025). Hydrological modeling has also been extended to non-glacierized basins to assess future scenarios; for example, the J2000 model applied in the Koshi River basin projected declining snowfall and reduced snow storage capacity under warming, leading to decreased snowmelt runoff from non-glaciated areas (Nepal 2016).

In glacierized basins, models generally project increasing glacier melt until mid-century, followed by declining melt contributions as glacier volumes shrink (Nepal 2016). Across Himalayan watersheds, climate change is expected to intensify both precipitation and glacier melt (Immerzeel et al. 2013; Lutz et al. 2014). While annual water availability may remain stable in the near term, the frequency of hydrological extremes such as floods and droughts is projected to increase (IPCC 2007). Representative Concentration Pathways (RCPs) are standardized greenhouse gas emission scenarios used in climate modeling, defined by their radiative forcing levels by 2100. Comparative analyses in Nepal and the Andes under RCP 4.5 and RCP 8.5 suggest consistent glacier retreat, with debris-free glaciers most sensitive, whereas debris-covered glaciers with stagnant, low-gradient termini exhibit relative stability (Ragettli et al. 2016). At the basin scale, semi-distributed conceptual models have been applied to quantify streamflow components. In the Gangotri glacier catchment (central Himalayas), snowmelt contributed 55.5% of total streamflow, followed by glacier melt (29.7%) and rainfall runoff (14.7%) (Arora et al. 2024). The model, calibrated with in situ records (2013-2016) and validated for 2016-2019, performed well overall, though performance declined during months of abrupt precipitation and temperature shifts. In the Chandra-Bhaga Basin, SPHY was applied for 1950-2022, calibrated against in situ runoff (1973-2006) and MODIS snow cover (2003-2018), and validated with Chhota Shigri runoff (2010-2015). Modeled mean annual runoff was 60.21 ± 6.17 m^3/s, with glacier runoff contributing 39%, snowmelt from non-glacierized areas and baseflow contributing 25% each, and rainfall runoff contributing 11% (Srivastava et al. 2024). The SWAT model applied to the Satluj Basin (1986-2005) showed that snowmelt runoff was the dominant contributor, accounting for 68-71% of mean annual discharge at Rampur. Water yield averaged ~600 mm annually, ~50% of precipitation, mostly generated during early summer; actual evapotranspiration accounted for ~14% of precipitation (Shukla et al. 2021). Shared Socioeconomic Pathways (SSPs) are future climate scenarios that combine socioeconomic development trajectories with greenhouse gas forcing levels. In the Jhelum sub-basin, future projections indicate substantial glacier area loss (34.7 ±12.1% under the SSP245 scenario and 55.3 ±16.1% under the SSP585 scenario by the 2080s), accompanied by reduced glacier streamflow and declining water availability, with significant implications for agriculture and hydropower (Abdulla et al. 2025).

Studies across the IHR indicate that as much as 70% of summer flow in the Ganges and 0-60% in other major rivers originates from glacier melt (Barnett et al. 2005). Although reported values vary (Alford, Armstrong 2010; Armstrong 2010; Racoviteanu 2011), there is consensus that glacier contribution to

streamflow increases from east to west across the IHR (Immerzeel et al. 2010). In the Central Himalaya, modeling at Dokriani Glacier revealed a linear relationship between increases in temperature, precipitation, and runoff, with higher runoff linked to the glacier's proximity to the watershed outlet and its relatively high glacial cover (Singh et al. 2006).

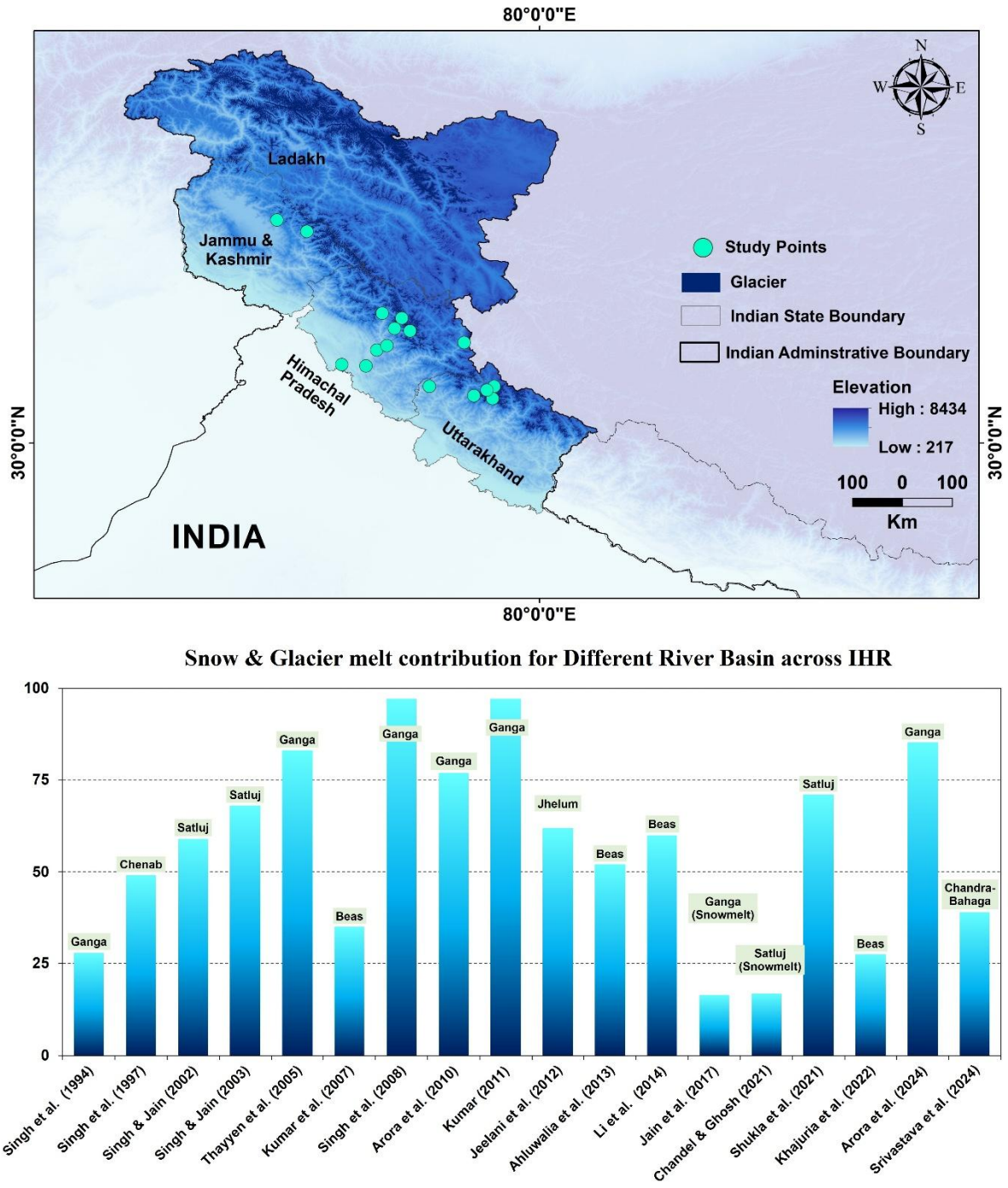

Fig. 5. Study area map of the Indian Himalayan Region (IHR) showing glacierized zones, elevation distribution, and locations of selected study points across Ladakh, Jammu & Kashmir, Himachal Pradesh, and Uttarakhand (top panel), along with a comparative synthesis of reported snow and glacier melt contributions (%) to streamflow for major Himalayan river basins compiled from previous studies (bottom panel).

Table 4. Basin-wise estimates of snow and glacier melt contributions to river discharge across major Himalayan catchments, derived using modelling approaches over different study periods, as reported in the cited literature.

Rivers (basins)	Study period	Duration	Melt contribution (%)	Contributors	Approach/Method	References
Beas	1987-2005	Annual	60	Snow and Glacier Melt	Hydrological Modelling	Li et al. (2013)
	1990-2004	Annual	35	Snow and Glacier Melt	Temperature Index Modelling	Kumar et al. (2007)
	1993-1997	Annual	39	Snow and Glacier Melt	Hydrological Modelling	Jain et al. (2010)
	2010-2011	(Apr.-Mar.)	52	Snow and Glacier Melt	Temperature Index Modelling	Saran Ahluwalia et al. (2015)
	2015-2018	Annual	10 to 45	Snow Melt	Temperature Index Modelling	Khajuria et al. (2022)
Satluj	1981-1993	Annual	16.9	Glacier Melt	Hydrological Modelling	Chandel, Ghosh (2021)
	1985-1999	Annual	68	Snow Melt	Temperature Index Modelling	Singh, Jain (2003)
	1986-1996	Annual	59	Snow and Glacier Melt	Temperature Index Modelling	Singh, Jain (2002)
	1986-2005	Annual	71	Snow Melt	Hydrological Modelling	Shukla et al. (2021)
Jhelum	1901-2010	Annual	62	Snow and Glacier Melt	Temperature Index Modelling	Jeelani et al. (2012)
Chenab	1982-1992	Annual	49	Snow and Glacier Melt	Temperature Index Modelling	Singh, Kumar (1997)
Chandra-Bhaga	1950-2022	Annual	39	Glacier Melt	Hydrological Modelling	Srivastava et al. (2024)
Ganga	1982-1992	Annual	28	Snow and Glacier Melt	Hydrological Modelling	Singh, Hasnain (1998)
	1992-2005	Annual	13-20	Snowmelt	Hydrological Modelling	Jain et al. (2017)
	1994, 1998-2000	(May-Oct.)	76-90	Snow and Glacier Melt	Hydrological Modelling	Thayyen et al. (2005)
	1999-2002, 1983-1984, 1987	(May-Oct.)	77	Snow and Glacier Melt	Temperature Index Modelling	Arora et al. (2010)
	2000-2003	(May-Oct.)	97	Snow and Glacier Melt	Temperature Index Modelling	Singh et al. (2008a)
	2004-2006	(May-Sep.)	97	Snow and Glacier Melt	Temperature Index Modelling	Kumar (2011)
Bhagirathi River/ Gangotri	2013-2016	Annual	86	Snow and Glacier Melt	Hydrological Modelling	Arora et al. (2024)

8. Hydrological processes most impacted by climate change

The Himalayan region contains the largest volume of ice outside the polar zones and serves as a crucial freshwater source for downstream populations (Immerzeel et al. 2012; Ragettli et al. 2016). Climate change is altering key hydrological processes in these basins, particularly snow accumulation, snowmelt timing, glacier melt, and rainfall-runoff dynamics. Variations in forest cover further influence water availability, sediment load, and seasonal river flows, leading to environmental, socioeconomic, and ecological vulnerabilities. In such rapidly changing conditions, accurate meteorological forcing data and appropriate hydrological models are essential for evaluating catchment-scale water budgets. Degree-day or temperature-index models remain limited because they poorly represent the energy balance that drives snow and glacier melt (Dahri et al. 2021).

A significant climate-related concern in the region is the sharp rise in extreme rainfall events, which enhances the risk of floods, landslides, and other natural hazards (Singh et al. 2016). Combined with anthropogenic pressures such as land-use change, infrastructure expansion, and encroachment, these changes degrade ecosystem services and intensify hydrological instability (Wakeel et al. 2005; Sharma et al. 2007; Raman, Punia 2012; Boykoff, Yulsman 2013). To address these challenges, long-term monitoring of snow, ice, and water is essential, along with improved datasets to understand shifts in water demand and socioeconomic vulnerability (Pramanik, Bhaduri 2016).

Major uncertainties persist in quantifying the contributions of glacial melt, snow melt, and rainfall to total river discharge, especially in high-altitude catchments with heterogeneous terrain (Bolch et al. 2012; Cogley 2012). Studies already indicate declining snowfall, increasing melt rates, and shifts in melt season timing, processes that strongly influence streamflow seasonality and water security. Field measurement remains difficult due to logistical and accessibility constraints, prompting increased reliance on remote sensing for snow cover, glacier area, and ice volume mapping (Kääb et al. 2012; Gardelle et al. 2013; Shangguan et al. 2014). However, with climate change rapidly altering these environments, cryospheric measurements are urgently needed (Rohrer et al. 2013; Ragettli et al. 2015).

Overall, climate change is reshaping the hydrological regime of the Indian Himalayan region by affecting snowfall patterns, melt processes, rainfall extremes, and downstream water availability. Strengthening observational networks and improving process-based modeling will be critical for understanding and managing these evolving hydrological risks.

9. Data limitations and gaps in high-altitude hydrology

Various observations made so far have made it clear that assessment of high-altitude hydrology is a challenging task. Several factors can be responsible, including complex topography, limited availability of in-situ data, and uncertainties in modeling approaches. It has been observed that due to the scarcity of in-situ data, modeling studies have been conducted based on modeled data with numerous uncertainties, and hence, the results obtained from such studies will also have a certain level of ambiguity. High-altitude hydrology remains poorly understood, along with all the possible changes that will be observed in river flow in the near future. This lack of understanding can be attributed to high meteorological variability, physical inaccessibility, and the complex interactions between cryospheric and hydrological processes under the influence of climate change (Ragettli et al. 2016). Several hydrological studies have been conducted to quantify the impacts of climate change on the hydrological systems in the Himalaya (Sharma et al. 2000; Singh et al. 2016). The major constraint in the IHR is the unavailability of climate data, which results in limited meteorological input for hydrological modeling. The poor availability of in-situ parameters makes it necessary to use modeled data (e.g., IPCC GCMs) or averaged data from stations within the region or at similar elevations, and therefore, the direct and indirect effects of climate change in the more remote areas are poorly understood (Lesher 2011). To estimate the contribution of streamflow components (glacier melt, snowmelt, and runoff) to the total runoff, numerous hydrological model applications have been conducted over various catchments. Few

studies use models that are data-intensive (Zhao et al. 2013; Ren et al. 2018); that is, they require more input parameters and thus become difficult to implement on a large spatial scale in a data-limited region such as the Himalayas. Moreover, most of the hydrological models do not include a glacier module to compute the glacier melt contribution. Earlier models did not include debris-covered glaciers, and few of the models include the effects of the topography of glaciers, a proper volume-area scaling formulation, and the impact of debris cover (Zhang et al. 2013). The major drawback that has been observed in hydrological modeling studies over glacierized catchments is that many studies have not included observations about the cryosphere other than initial glacier outlines (Prasch et al. 2013; Ragettli et al. 2013; Nepal et al. 2014). The use of fewer response variables in the modeling increases the risk of predictive uncertainty in the results (Beven 2000). Most of the meteorological stations are situated at lower altitude, i.e., ~3000 m above sea level (m.a.sl); there are very few stations in alpine zones. As a result, it has been observed that the meteorological data that have been used in modeling studies are being collected from stations below glacier elevation (Leng et al. 2023). There is limited consideration of debris thickness impacts on glacier melt in such studies, mainly due to data scarcity at higher elevations. The correct representation of internal states and process dynamics in glacio-hydrological models often cannot be verified because of missing in situ measurements (Ragettli et al. 2015). Retreating glaciers not only affect the environment and hydrological regimes but also have livelihood and economic impacts on the downstream population. These implications will disturb the traditional knowledge and beliefs of the local communities (Allison 2015). It has been evident from the few studies carried out for IHR that difficult terrain and weather conditions also contribute to data scarcity in the region. This has increased the uncertainties and restricted the understanding of the probable impacts of changing climate in the region. Therefore, it is important to carry out studies that will help to generate a database and reduce the uncertainties about the changes observed in the IHR (Singh et al. 2016). A large knowledge gap exists related to the impact of climate change on water resources. In the present scenario, climate change effects on water resources and related hazards in the Himalayas and their downstream river basins are poorly understood.

9.1. Uncertainties in modeling climate change impacts

Uncertainties in modeling studies and delicate hydro-meteorological investigations have posed a serious constraint in assessing the impact of climate change on the hydrometeorology (Dahri et al. 2021). Numerous studies have attempted to assess and model the hydrological regime of the high-altitude western Himalayas (Archer 2003; Hasson 2016; Lutz et al. 2016; Hasson et al. 2019), yet there are significant uncertainties, and our understanding of the basin's hydrological regime remains poor. The greatest uncertainties are associated with the use of non-representative (mostly underestimated) precipitation in the higher altitude areas, which receive the bulk of precipitation and make major contributions to streamflow. In the case of a glacierized basin that is predominantly a snow and glacier-fed system, the temperature-index or degree-day based hydrological models may not accurately simulate the prevailing energy balance, which is the main driving force for streamflow generation from the snow and glacier systems. Their application is mainly limited to simulation of melt rates at daily or coarser resolution (Hock 2003; Pellicciotti et al. 2005). Assessment of the future hydrological regime is primarily constrained

by very high uncertainties in the GCM outputs for the study domain. Specific knowledge of IHR with respect to climate change indicators is lacking due to both the inaccessibility of the location and the insufficient theoretical attention given to the complex interactions of spatial scales in weather and climate phenomena in mountain areas.

The Ministry of Environment & Forest (MoEF) discussion paper reported that over the past 100 years, the Himalayan glaciers have shown an erratic pattern. A study conducted for Sonapani glacier revealed that the glacier has retreated by about 500 m during the past 100 years, whereas another study for Kangriz glaciers has not shown any reasonable retreat in the same period; the glacier has retreated less than an inch. A study reported that the Siachen glacier increased in length by 700 m from 1862 to 1909, retreated from 1929 to 1958 (400 m), and for the past 50 years, negligible retreat has been observed. Gangotri glacier showed a significant and rapid retreat of 20 m per year, but has slowed more recently (National Research Council 2012). A similar trend has been observed for Bhagirath Kharak and Zemu glaciers. There are numerous underlying factors, physical features, and a complex interplay of climatic factors that may be responsible for such contrasting behavior. Besides such statements, there are a few studies that have reported that one of the major impacts of climate change over the glacierized region has been an increase in the formation of glacier lakes. The remote nature and lack of meteorological stations and stream flow data in many high-altitude lakes in the Himalayas limit the availability of data required to model the water balance of a watershed or lake, and therefore, few lakes in the Himalayas have been modeled (Lesher 2011). To understand the complex glacier and hydrology interaction, glacio-hydrological models are considered indispensable tools. This coupled approach makes it easy to understand the characteristics of a catchment and its response to climate. But this modeling approach also has its fair share of uncertainty and complications that make the application of such models at high altitudes a challenging task. They are subject to several factors that include: (1) a lack of representative data to force the models (Huss et al. 2014; Pellicciotti et al. 2014), (2) simplifications in model structure due to insufficient process understanding and the scarcity of detailed information about glacio-hydrological processes (Huss et al. 2014), and (3) parametric uncertainty due to insufficient quality or quantity of data for model calibration and validation (Ragettli et al. 2013; 2015).

Given the multitude of control factors, often acting at relatively fine scales, current projections of global glacier change models do not adequately constrain the mechanisms underlying the variations in river flow from high-altitude catchments. It is therefore uncertain whether such models can correctly capture the response times and the magnitudes of future changes. (Marzeion et al. 2012; Huss, Hock 2015; Ragettli et al. 2016). Due to a lack of observed meteorological data and extremely complex orography interacting with synoptic-scale atmospheric circulation, it can be concluded that significant uncertainties still exist to hamper precise representation of the basin's hydrometeorological regime (Andermann et al. 2012; Lutz et al. 2014). The greatest uncertainties in the higher-altitude areas are associated with the spatiotemporal distribution of precipitation and the dynamics of glacial ice mass. Structural limitations of the climate and

hydrological modeling frameworks, and lack of reliable and representative observations for bias corrections and validations also impose limitations.

9.2. Data scarcity: implications for model uncertainties and calibration

Hydrological modeling in data-scarce regions such as the Himalayan river basins is fundamentally constrained by the limited availability of reliable meteorological observations. Basic variables such as precipitation, temperature, humidity, and snow parameters are either sparsely measured or completely absent across high-altitude regions due to harsh terrain, inaccessibility, and logistical challenges (Immerzeel et al. 2014; Nepal et al. 2017). As a result, modelers often rely on interpolated or gridded meteorological datasets to drive hydrological models. While these datasets offer spatially continuous coverage, they come with inherent uncertainties related to coarse resolution, interpolation algorithms, and biases arising from sparse ground-truth observations (Huffman et al. 2010; Karger et al. 2017). Interpolated gridded temperature and precipitation products are commonly applied in large-scale hydrological models; however, their quality is typically evaluated only by cross-validation using the limited station network available (Freudiger et al. 2016). This limitation raises critical concerns regarding their representativeness in high-altitude catchments where observation density is extremely low (Freudiger et al. 2016). For example, precipitation in the Himalayas exhibits considerable spatial variability due to elevation, aspect, and orographic effects and patterns that are often poorly captured by coarse-resolution datasets. Conventional gauge-based rainfall estimates may be accurate locally, but interpolations to ungauged regions in complex terrain often yield approximations that deviate substantially from actual rainfall (Bookhagen, Burbank 2010; Palazzi et al. 2013).

Remote sensing products and global reanalysis datasets have emerged as valuable substitutes in data-sparse regions such as the Indian Himalayan Region (IHR). Studies increasingly utilize products such as ERA-Interim, ERA5, JRA-55, and APHRODITE for hydrological simulations. ERA-Interim and JRA-55 precipitation has been used along with observed datasets. It has been reported that these gridded datasets overestimate precipitation because of spatial variability, and this effect transfers to streamflow predictions. JRA-55 produced higher peaks, and ERA-Interim results were comparatively closer to station-driven simulations. Similar findings have been reported across the Himalayas, where reanalysis datasets frequently overestimate winter precipitation and underestimate convective summer rainfall, adversely affecting calibration and validation outcomes (Soncini et al. 2017; Sabin et al. 2020). These biases directly translate into uncertainties in simulated streamflow, snowmelt contributions, and extreme event estimation. Consequently, hydrological models such as SWAT, VIC, and HBV require careful bias-correction and multi-dataset intercomparison to ensure reliable performance in such regions (Ménégoz et al. 2013; Dahri et al. 2018). The scarcity of observed hydro-meteorological data in the IHR continues to be a major source of uncertainty in hydrological modeling. Improving station density, integrating multisource products, and adopting calibration strategies such as regionalization or multi-objective optimization remain essential for reducing uncertainties and strengthening model reliability.

9.3. Application of bias-corrected and downscaled climate projections in Himalayan hydrologic models

The complex spatial climatic characteristics of the Himalayas pose significant challenges for regional climate models (RCMs), making some form of correction essential before applying RCM simulations for hydrological assessments. In recent years, simple bias-correction techniques have been complemented or replaced by more advanced methods. Several studies across the IHR have applied both simple (linear scaling) and more complex (quantile mapping) bias-correction techniques for temperature and precipitation. Bias correction substantially improved the wetter and colder RCM estimates, and hydrological model responses further demonstrated its importance. However, many studies observed no major difference between the outputs of linear scaling and quantile mapping, because both techniques exhibit almost identical performance, suggesting that simpler methods may be sufficient in certain Himalayan applications (Shrestha et al. 2017). SWAT has also been confirmed as a suitable model for hydrological analysis in Himalayan basins at both monthly and daily time scales (Shrestha et al. 2017; Swain et al. 2022). Further work projecting future hydrological changes using a multi-GCM, multi-bias correction method (BCM) and multi-parameter ensembles, identified three major sources of uncertainty: GCM selection, bias collection methods, and model parameterization. Studies highlight that GCM-related uncertainty can be substantially reduced through bias correction, indicating that the number of GCMs used becomes less critical once they are corrected. Although using more GCMs is generally recommended, it also incurs significant computational cost. Notably, Wang et al. (2020) found that uncertainty trends remained largely unchanged when more than two GCMs were included. Similar conclusions were drawn in recent analysis over the western Himalayas, demonstrating that uncertainty from GCMs, bias-correction techniques, and hydrological model structure collectively influences future hydrological projections (Mehboob, Kim 2024).

A few studies have applied CMIP6 global climate model outputs in Himalayan regions, where projections have been statistically downscaled using tools such as SDSM, and bias-corrected with CMhyd to improve their suitability for hydrological applications (IPCC 2021; Alasqah et al. 2025). Although downscaling provides a reasonable fit, CMIP6 models still exhibit uncertainty-related biases, particularly in precipitation, due to strong variability in spatial patterns and emission scenarios. Projections generally indicate rising temperatures, with potential decreases in rainfall in arid regions and increases in humid areas, offering useful insights into future water resource conditions. However, studies across the Himalayas have shown that non-linear bias correction techniques significantly improve precipitation estimates, especially for extremes, which are often underrepresented in widely used gridded datasets. Overall, while CMIP5 and CMIP6 projections are valuable for climate and hydrological assessments in the Himalayas, their effective use requires robust downscaling and bias correction to reduce persistent uncertainty in complex mountain terrain (Alasqah et al. 2025).

10. Implications for decision-makers and stakeholders

Hydrological modeling in the Himalayan river basin offers critical support for informed water resource planning, particularly in regions that are highly sensitive to climatic variability and limited by scarce observational data. Integrated modeling tools enable the estimation of natural and altered flow conditions, including dry-season recession flows, and can incorporate locally available observations to improve simulation accuracy. GIS-based interfaces further streamline catchment delineation and flow assessment, allowing water managers to quickly generate transparent, reproducible outputs that guide the design and placement of irrigation systems, hydropower projects, and other water resource interventions. Such tools are also effective for multi-stakeholder dialogues, helping decision-makers communicate the implications of various water-use scenarios in a clear and accessible manner.

For policymakers, the use of hydrological models enhances understanding of spatial and temporal variations in water availability, aids drought preparedness, and informs long-term investment in climate-resilient practices. Although numerous models exist, careful consideration is needed to determine which modeling approaches and datasets are most appropriate for Himalayan conditions, especially in snow and glacier-fed catchments. Equally important is assessing how model outputs translate into societal impacts, such as implications for downstream communities, equity in water distribution, and the capacity of local institutions to adapt to changing hydrological regimes. Strengthening hydrological modeling and integrating its insights into planning processes will be crucial for building resilience and supporting sustainable water management across the IHR.

11. Conclusion – research needs and future directions

Hydrological research in the Himalayas urgently requires improved observational networks, long-term in situ measurements, and standardized data collection to reduce uncertainties in modeling snow and glacier-fed catchments. Future studies should prioritize high-resolution climate datasets, process-based hydrological models, and integrated remote sensing approaches to better capture the complex hydro-climatic dynamics of the region. Strengthening interdisciplinary collaborations and enhancing monitoring of snow, ice, and runoff will be essential for developing reliable projections and effective climate-adaptation strategies for the Himalayan basin.

11.1. Future research opportunities

Climate change is expected to exert significant impacts on snowmelt and glacier runoff across the Himalayas (Brock et al. 2000; Immerzeel et al. 2014; Ragettli et al. 2016). Minimum temperature, an important control on precipitation type in mountainous terrain, is among the least studied parameters in the IHR, with limited long-term observations except for a few studies (Bhutiyani et al. 2007). The rapid rise in minimum temperature observed, particularly in the western IHR, warrants continued investigation using extended instrumental records. Future studies should further examine the relationships between climatic variables, glacier discharge, and basin-scale hydrology, along with improved projections of streamflow variability (Singh et al. 2016). High-resolution, process-based modeling efforts remain essential

for capturing the complex hydro-climatic behaviour of high-altitude catchments (Viviroli et al. 2011; Fernández, Mark 2016; Ragettli et al. 2016). Strengthening coordination among research organizations is also necessary to guide climate adaptation, forest conservation, and soil erosion control efforts across the region (Pramanik, Bhaduri 2016).

Glaciological studies continue to face major challenges from limited accessibility and sparse field data; hence, most predictive assessments still rely on secondary datasets. Establishing long-term monitoring stations and standardizing measurement protocols are critical for reducing uncertainties in hydrological research outcomes (Pramanik, Bhaduri 2016). Despite advances in climate modeling, substantial uncertainty persists in simulating current and future climate processes in the Himalayas, marking this as an ongoing research priority (Knutti, Sedláček 2013; Dahri et al. 2021).

In addition, emerging opportunities lie in applying machine learning (ML) and hybrid physics-ML models for snow cover mapping, glacier mass balance reconstruction, streamflow forecasting, and gap-filling sparse hydro-meteorological datasets. ML approaches – when combined with physically based models and remote sensing inputs – can significantly enhance predictive skill in data-scarce Himalayan basins and help reduce model uncertainties (Ouyang et al. 2025).

11.2. Recommended models for Himalayan basins

Comparing fully distributed and semi-distributed hydrological models such as SPHY, HBV, and HEC-HMS provides a robust basis for discharge estimation in Himalayan catchments. Semi-distributed models like HBV-Light and HEC-HMS often outperform SPHY in data-scarce regions because their parameterization requirements are relatively modest, making them more suitable for the limited observational network available. Future simulations can be further improved by integrating satellite-based products and reanalysis datasets to supplement sparse in situ observations (Abbaspour et al. 2015; Arora et al. 2024). With ongoing climatic changes affecting snow and glacier energy balance, the need for enhanced ground-based measurements and models that can incorporate such observations is increasingly emphasized (Rohrer et al. 2013; Ragettli et al. 2015).

While semi-distributed glacio-hydrological models have yielded satisfactory results across many Himalayan basins, the region's high spatial heterogeneity and sensitivity to climate forcing underscore the importance of adopting coupled approaches. These approaches integrate field observations, physically based modeling, and advanced Artificial Intelligence (AI), Machine Learning (ML)/Deep Learning (DL), capture complex, nonlinear processes, and handle diverse, multi-source datasets: capabilities that traditional models often lack (Maity et al. 2024). Emerging research demonstrates promising applications of AI/ML/DL in precipitation forecasting, evapotranspiration estimation, groundwater variability assessment, and extreme event prediction (floods or compound events).

Furthermore, the adoption of Explainable AI (XAI) and transfer learning can enhance interpretability, improve cross-basin adaptability, and support stakeholder trust in these advanced models (Ouyang et al. 2025). Overall, integrating AI/ML/DL with conventional process-based hydrological models represents a

transformative shift toward more accurate, scalable, and reliable hydrological predictions for the Himalayan region.

Conflict of interest statement

The authors declare that the research was conducted in the absence of any commercial or financial relationships that could be construed as a potential conflict of interest.

References

Abbaspour K.C. Rouholahnejad E., Vaghefi S., Srinivasan R., Yang H., Kløve B., 2015, A continental-scale hydrology and water quality model for Europe: Calibration and uncertainty of a high-resolution large-scale SWAT model, Journal of Hydrology, 524, 733-752, DOI: 10.1016/j.jhydrol.2015.03.027.

Abbott M.B., Bathurst J.C., Cunge J.A., O'Connell P.E., Rasmussen J., 1986a, An introduction to the European Hydrological System – Systeme Hydrologique Europeen,"SHE", 1: History and philosophy of a physically-based, distributed modelling system, Journal of Hydrology, 87 (1-2), 45-59, DOI: 10.1016/0022-1694(86)90114-9.

Abbott M.B., Bathurst J.C., Cunge J.A., O'Connell P.E., Rasmussen J., 1986b, An introduction to the European Hydrological System – Systeme Hydrologique Europeen, "SHE", 2: Structure of a physically-based, distributed modelling system, Journal of Hydrology, 87 (1-2), 61-77, DOI: 10.1016/0022-1694(86)90115-0.

Abdullah T., Bashir J., Romshoo S.A., 2025, Assessing glacier changes and hydrological impacts in the upper Indus Basin under CMIP6 climate scenarios, iScience, 28 (8), DOI: 10.1016/j.isci.2025.113200.

Ageta Y., Naito N., Iwata S., Yabuki H., 2003, Glacier distribution in the Himalayas and glacier shrinkage from 1963 to 1993 in the Bhutan Himalayas, Bulletin of Glaciological Research, 20, 29-40.

Ahmed R., Rawat M., Wani G.F., Ahmad S.T., Ahmed P., Jain S.K., Meraj G., Mir R.A., Rather A.F., Farooq M., 2022, Glacial lake outburst flood hazard and risk assessment of Gangabal Lake in the Upper Jhelum Basin of Kashmir Himalaya using geospatial technology and hydrodynamic modeling, Remote Sensing, 14 (23), DOI: 10.3390/rs14235957.

Alasqah A., Tayyeh H.K., Mohammed R., Hussein A.M., Khedher K.M., Benzougagh B., 2025, Integrating double techniques of statistical downscaling and bias correction to reduce bias in projections trends of future climate datasets, Scientific Reports, 15 (1), DOI: 10.1038/s41598-025-15483-x.

Alford D., Armstrong R., 2010, The role of glaciers in stream flow from the Nepal Himalaya, The Cryosphere Discussions, 4 (2), 469-494, DOI: 10.5194/tcd-4-469-2010.

Ali S.N., Shekhar M., Pandey P., Bhardwaj A., Singh S., 2014, Indian Himalayan capacity and adaptation programme: capacity-building in Himalayan glaciology, Current Science, 106 (3).

Allison E., 2015, The spiritual significance of glaciers in an age of climate change, Wiley Interdisciplinary Reviews: Climate Change, 6 (5), 493-508, DOI: 10.1002/wcc.354.

Andermann C., Longuevergne L., Bonnet S., Crave A., Davy P., Gloaguen R., 2012, Impact of transient groundwater storage on the discharge of Himalayan rivers, Nature Geoscience, 5(2), 127-132.

Archer D., 2003, Contrasting hydrological regimes in the upper Indus Basin, Journal of Hydrology, 274 (1-4), 198-210, DOI: 10.1016/S0022-1694(02)00414-6.

Armstrong R.L., 2010, The glaciers of the Hindu Kush-Himalayan region: a summary of the science regarding glacier melt/retreat in the Himalayan Hindu Kush Karakoram Pamir, and Tien Shan mountain ranges, International Centre for Integrated Mountain Development (ICIMOD).

Arora M., Goel N.K., Kesarwani K., 2024, Integrated hydrological modelling and streamflow characterization of Gangotri Glacier meltwater, Applied Water Science, 14, DOI: 10.1007/s13201-024-02283-3.

Arora M., Rathore D.S., Singh R..D., Kumar R., Kumar A., 2010, Estimation of melt contribution to total streamflow in River Bhagirathi and River DhauliGanga at Loharinag Pala and Tapovan Vishnugad project sites, Journal of Water Resource and Protection, 2 (7), 636-643, DOI: 10.4236/jwarp.2010.27073.

Azam M.F., Wagnon P., Berthier E., Vincent C., Fujita K., Kargel J., 2018, Review of the status and mass changes of Himalayan-Karakoram glaciers, Journal of Glaciology, 64 (243), 61-74, DOI: 10.1017/jog.2017.86.

Azam M.F., Wagnon P., Vincent C., Ramanathan A., Kumar N., Srivastava S., Pottakkal J.G., Chevallier P., 2019, Snow and ice melt contributions in a highly glacierized catchment of Chhota Shigri Glacier (India) over the last five decades, Journal of Hydrology, 574, 760-773, DOI: 10.1016/j.jhydrol.2019.04.075.

Bahuguna I.M., Kulkarni A.V., Nayak S., Rathore B.P., Negi H.S., Mathur P., 2007, Himalayan glacier retreat using IRS 1C PAN stereo data, International Journal of Remote Sensing, 28 (2), 437-442, DOI: 10.1080/01431160500486674.

Bahuguna I.M., Rathore B.P., Brahmbhatt R., Sharma M., Dhar S., Randhawa S.S., Kumar K., Romshoo S., Shah R.D., Ganjoo R.K., 2014, Are the Himalayan glaciers retreating?, Current Science, 106 (7), 1008-1013.

Bajracharya S.R., Shrestha B.R., 2011, The status of glaciers in the Hindu Kush-Himalayan region, International Centre for Integrated Mountain Development (ICIMOD), DOI: 10.53055/ICIMOD.551.

Barnett T.P., Adam J.C., Lettenmaier D.P., 2005, Potential impacts of a warming climate on water availability in snow-dominated regions, Nature, 438 (7066), 303-309, DOI: 10.1038/nature04141.

Barry R., 2001, Mountain climate change and cryospheric responses: a review, World Mountain Symposium 2001.

Basnett S., Kulkarni A., Bolch T., 2013, The influence of debris cover and glacial lakes on the recession of glaciers in Sikkim Himalaya, India, Journal of Glaciology, 59 (218), 1035-1046, DOI: 10.3189/2013JoG12J184.

Beniston M., Stoffel M., 2014, Assessing the impacts of climatic change on mountain water resources, Science of the Total Environment, 493, 1129-1137, DOI: 10.1016/j.scitotenv.2013.11.122.

Benn D., Lehmkuhl F., 2000, Mass balance and equilibrium-line altitude of glaciers in high mountain environments, Quaternary International, 65-66, 15-29, DOI: 10.1016/S1040-6182(99)00034-8.

Berthier E., Arnaud Y., Kumar R., Ahmad S., Wagnon P., Chevallier P., 2007, Remote sensing estimates of glacier mass balances in the Himachal Pradesh (Western Himalaya India), Remote Sensing of Environment, 108 (3), 327-338, DOI: 10.1016/j.rse.2006.11.017.

Beven K., 2000, Uniqueness of place and process representations in hydrology modelling. Hydrology and Earth Systems Science, 4 (2), 203-213, DOI: 10.5194/hess-4-203-2000.

Bhambri R., Bolch T., Chaujar R., Kulshreshta S.C., 2011, Glacier changes in the Garhwal Himalaya India, from 1968 to 2006 based on remote sensing, Journal of Glaciology, 57 (203), 543-556, DOI: 10.3189/002214311796905604.

Bhanja S.N., Coon E.T., Lu D., Painter S.L., 2023, Evaluation of distributed process-based hydrologic model performance using only a priori information to define model inputs, Journal of Hydrology, 618, DOI: 10.1016/j.jhydrol.2023.129176.

Bhatta B., Shrestha S., Shrestha P.K., Talchabhadel R., 2020, Modelling the impact of past and future climate scenarios on streamflow in a highly mountainous watershed: A case study in the West Seti River Basin Nepal, Science of The Total Environment, 740, DOI: 10.1016/j.scitotenv.2020.140156.

Bhutiyani M., Kale V., Pawar N.J., 2007, Long-term trends in maximum, minimum and mean annual air temperatures across the Northwestern Himalaya during the twentieth century, Climatic Change, 85 (1), 159-177, DOI: 10.1007/s10584-006-9196-1.

Bhutiyani M.R., Kale V.S., Pawar N.J., 2009, Climate change and the precipitation variations in the northwestern Himalaya: 1866-2006, International Journal of Climatology, 30 (4), 535-548, DOI: 10.1002/joc.1920.

Bliss A., Hock R., Radić V., 2014, Global response of glacier runoff to twenty-first century climate change, Journal of Geophysical Research: Earth Surface, 119 (4), 717-730, DOI: 10.1002/2013JF002931.

Bolch T., Kulkarni A., Kääb A., Huggel C., Paul F., Cogley J.G., Frey H., Kargel J.S., Fujita K., Scheel M., 2012, The state and fate of Himalayan glaciers, Science, 336 (6079), 310-314, DOI: 10.1126/science.1215828.

Bookhagen B., Burbank D.W., 2006, Topography, relief, and TRMM-derived rainfall variations along the Himalaya, Geophysical Research Letters, 33 (8), DOI: 10.1029/2006GL026037.

Bookhagen B., Burbank D.W., 2010, Toward a complete Himalayan hydrological budget: Spatiotemporal distribution of snowmelt and rainfall and their impact on river discharge, Journal of Geophysical Research: Earth Surface, 115 (F3), DOI: 10.1029/2009JF001426

Boykoff M.T., Yulsman T., 2013, Political economy, media, and climate change: sinews of modern life, Wiley Interdisciplinary Reviews: Climate Change, 4 (5), 359-371, DOI: 10.1002/wcc.233.

Brahmbhatt R.M., Bahuguna I.M., Rathore B.P., Kulkarni A..V., Nainwal H.C., Shah R.D., Ajai, 2012, A comparative study of deglaciation in two neighbouring basins (Warwan and Bhut) of Western Himalaya, Current Science, 103, 298-304.

Brock B.W., Willis I.C., Sharp M.J., 2000, Measurement and parameterization of albedo variations at Haut Glacier d'Arolla, Switzerland, Journal of Glaciology, 46 (155), 675-688, DOI: 10.3189/172756500781832675.

Brown M.E., Racoviteanu A.E., Tarboton D.G., Sen Gupta A., Nigro J., Policelli F., Habib S., Tokay M., Shrestha M.S., Bajracharya S., Hummel P., Gray M., Duda P., Zaitchik B., Mahat B., Artan G., Tokar S., 2014, An integrated modeling system for estimating glacier and snow melt driven streamflow from remote sensing and earth system data products in the Himalayas, Journal of Hydrology, 519, 1859-1869, DOI: 10.1016/j.jhydrol.2014.09.050.

Brun F., Berthier E., Wagnon P., Kääb A., Treichler D., 2017, A spatially resolved estimate of High Mountain Asia glacier mass balances from 2000 to 2016, Nature Geoscience, 10, 668-673, DOI: 10.1038/ngeo2999.

Burbank D.W., Blythe A.E., Putkonen J., Pratt-Sitaula B., Gabet E., Oskin M., Barros A., Ojha T.P., 2003, Decoupling of erosion and precipitation in the Himalayas, Nature, 426 (6967), 652-655, DOI: 10.1038/nature02187.

Chalise S.R., Kansakar S.R., Rees G., Croker K., Zaidman M., 2003, Management of water resources and low flow estimation for the Himalayan basins of Nepal, Journal of Hydrology, 282 (1-4), 25-35, DOI: 10.1016/S0022-1694(03)00250-6.

Chandel V.S., Ghosh S., 2021, Components of Himalayan river flows in a changing climate, Water Resources Research, 57 (2), DOI: 10.1029/2020WR027589.

Chen Y., Li W., Deng H., Fang G., Li Z., 2016, Changes in Central Asia's water tower: past, present and future, Scientific Reports, 6 (1), DOI: 10.1038/srep35458.

Cogley J.G., 2012, Himalayan glaciers in the balance, Nature, 488 (7412), 468-469, DOI: 10.1038/488468a.

Dahri Z.H., Ludwig F., Moors E., Ahmad S., Ahmad B., Ahmad S., Riaz M., Kabat P., 2021, Climate change and hydrological regime of the high-altitude Indus basin under extreme climate scenarios, Science of the Total Environment, 768, DOI: 10.1016/j.scitotenv.2020.144467.

Dahri Z.H., Moors E., Ludwig F., Ahmad S., Khan A., Ali I., Kabat P., 2018, Adjustment of measurement errors to reconcile precipitation distribution in the high-altitude Indus basin, International Journal of Climatology, 38 (10), 3842-3860, DOI: 10.1002/joc.5539.

Dash S.K., Jenamani R.K., Kalsi S.R., Panda S.K., 2007, Some evidence of climate change in twentieth-century India, Climatic Change, 85 (3-4), 299-321, DOI: 10.1007/s10584-007-9305-9.

Devi G.K., Ganasri B.P., Dwarakish G.S., 2015, Applications of remote sensing in satellite oceanography: A review, Aquatic Procedia, 4, 579-584, DOI: 10.1016/j.aqpro.2015.02.075.

Diaz H.F., Bradley R.S., 1997, Temperature variations during the last century at high elevation sites, Climatic Change, 36 (3-4), 253-279, DOI: 10.1023/A:1005335731187.

Dimri A.P., Dash S.K., 2012, Wintertime climatic trends in the western Himalayas, Climatic Change, 111 (3-4), 775-800, DOI: 10.1007/s10584-011-0201-y.

Dimri A.P., Kumar D., Choudhary A., Maharana P., 2018, Future changes over the Himalayas: maximum and minimum temperature, Global and Planetary Change, 162, 212-234, DOI: 10.1016/j.gloplacha.2018.01.015.

Douglas-Mankin K.R., Srinivasan R., Arnold J.G., 2010, Soil and Water Assessment Tool (SWAT) model: Current developments and applications, Transactions of the ASABE, 53 (5), 1423-1431, DOI: 10.13031/2013.34915.

Dwivedi D., Poeppl R.E., Wohl E., 2025, Hydrological connectivity: a review and emerging strategies for integrating measurement, modeling, and management, Frontiers in Water, 7, DOI: 10.3389/frwa.2025.1496199.

Easterling D.R., Horton B., Jones P.D., Peterson T.C., Karl T.R., Parker D.E., Salinger M.J., Razuvayev V., Plummer N., Jamason P., 1997, Maximum and minimum temperature trends for the globe, Science, 277 (5324), 364-367, DOI: 10.1126/science.277.5324.364.

Endrizzi S., Gruber S., Dall'Amico M., Rigon R., 2014, GEOtop 2.0: simulating the combined energy and water balance at and below the land surface accounting for soil freezing, snow cover and terrain effects, Geoscientific Model Development, 7 (6), 2831-2857, DOI: 10.5194/gmd-7-2831-2014.

Etter S., Addor N., Huss M., Finger D., 2017, Climate change impacts on future snow, ice and rain runoff in a Swiss mountain catchment using multi-dataset calibration, Journal of Hydrology: Regional Studies, 13, 222-239, DOI: 10.1016/j.ejrh.2017.08.005.

Fernández A., Mark B.G., 2016, Modeling modern glacier response to climate changes along the Andes Cordillera: A multiscale review, Journal of Advances in Modeling Earth Systems, 8 (1), 467-495, DOI: 10.1002/2015MS000482.

Folland C.K., Rayner N.A., Brown S.J., Smith T.M., Shen S.S.P., Parker D.E., Macadam I., Jones P.D., Jones R.N., Nicholls N., 2001, Global temperature change and its uncertainties since 1861, Geophysical Research Letters, 28 (13), 2621-2624, DOI: 10.1029/2001GL012877.

Frans C., Istanbulluoglu E., Lettenmaier D.P., Clarke G., Bohn T.J., Stumbaugh M., 2016, Implications of decadal to century scale glacio-hydrological change for water resources of the Hood River basin, OR, USA, Hydrological Processes, 30 (23), 4314-4329, DOI: 10.1002/hyp.10872.

Frans C., Istanbulluoglu E., Lettenmaier D.P., Naz B.S., Clarke G.K.C., Condom T., Burns P., Nolin A.W., 2015, Predicting glacio-hydrologic change in the headwaters of the Zongo River, Cordillera Real, Bolivia, Water Resources Research, 51 (11), 9029-9052, DOI: 10.1002/2014WR016728.

Freudiger D., Frielingsdorf B., Stahl K., Steinbrich A., Weiler M., Griessinger N., Seibert J., 2016, The potential of meteorological gridded datasets for hydrological modeling in alpine basins, Hydrologie und Wasserbewirtschaftung, 60 (6), 353-367, DOI: 10.5675/HyWa_2016,6_1.

Fujita K., 2008, Influence of precipitation seasonality on glacier mass balance and its sensitivity to climate change, Annals of Glaciology, 48, 88-92, DOI: 10.3189/172756408784700824.

Fujita K., Nuimura T., 2011, Spatially heterogeneous wastage of Himalayan glaciers, Proceedings of the National Academy of Sciences, 108 (34), 14011-14014, DOI: 10.1073/pnas.1106242108.

Gabbi J., Huss M., Bauder A., Cao F., Schwikowski M., 2015, The impact of Saharan dust and black carbon on albedo and long-term mass balance of an Alpine glacier, The Cryosphere, 9 (4), 1385-1400, DOI: 10.5194/tc-9-1385-2015.

Gardelle J., Arnaud Y., Berthier E., 2011, Contrasted evolution of glacial lakes along the Hindu Kush Himalaya mountain range between 1990 and 2009, Global and Planetary Change, 75 (1-2), 47-55, DOI: 10.1016/j.gloplacha.2010.10.003.

Gardelle J., Berthier E., Arnaud Y., Kääb A., 2013, Region-wide glacier mass balances over the Pamir-Karakoram-Himalaya during 1999-2011, The Cryosphere, 7 (4), 1263-1286, DOI: 10.5194/tc-7-1263-2013.

Gardner A.S., Moholdt G., Cogley J.G., Wouters B., Arendt A.A., Wahr J., Berthier E., Hock R., Pfeffer W.T., Kaser G., Ligtenberg S.R.M., Nolsch T., Sharp M.J., Hagen J.O., Van Den Broeke M.R., Paul F., 2013, A reconciled estimate of glacier contributions to sea level rise: 2003 to 2009, Science, 340 (6134), 852-857, DOI: 10.1126/science.1234532.

Gascoin S., Kinnard C., Ponce R., Lhermitte S., MacDonell S., Rabatel A., 2011, Glacier contribution to streamflow in two headwaters of the Huasco River, Dry Andes of Chile, The Cryosphere, 5 (4), 1099-1113, DOI: 10.5194/tc-5-1099-2011.

Gautam R., Hsu N.C., Lau K., 2010, Premonsoon aerosol characterization and radiative effects over the Indo-Gangetic Plains: Implications for regional climate warming, Journal of Geophysical Research: Atmospheres, 115 (D17), DOI: 10.1029/2010JD013819.

Goswami B.N., Venugopal V., Sengupta D., Madhusoodanan M.S., Xavier P.K., 2006, Increasing trend of extreme rain events over India in a warming environment, Science, 314 (5804), 1442-1445, DOI: 10.1126/science.1132027.

Guhathakurta P., Rajeevan M., 2008, Trends in the rainfall pattern over India, International Journal of Climatology, 28 (11), 1453-1469, DOI: 10.1002/joc.1640.

Gusain H.S., Mishra V.D., Bhutiyani M.R., 2014, Winter temperature and snowfall trends in the cryospheric region of north-west Himalaya, Mausam, 65 (3), 425-432, DOI: 10.54302/mausam.v65i3.1053.

Hasson S., 2016, Seasonality of precipitation over Himalayan watersheds in CORDEX South Asia and their driving CMIP5 experiments, Atmosphere, 7 (10), DOI: 10.3390/atmos7100123.

Hasson S., Böhner J., Lucarini V., 2017, Prevailing climatic trends and runoff response from Hindukush-Karakoram-Himalaya, upper Indus Basin, Earth System Dynamics, 8 (2), 337-355, DOI: 10.5194/esd-8-337-2017.

Hasson S., Saeed F., Böhner J., Schleussner C.-F., 2019, Water availability in Pakistan from Hindukush-Karakoram-Himalayan watersheds at 1.5°C and 2°C Paris Agreement targets, Advances in Water Resources, 131, DOI: 10.1016/j.advwatres.2019.06.010.

Hess T.M., Counsell C., 2000, A water balance simulation model for teaching and learning – WaSim, ICID British Section Irrigation and Drainage Research Day, 29 March 2000, HR Wallingford.

Hock R., 2003, Temperature index melt modelling in mountain areas, Journal of Hydrology, 282 (1-4), 104-115, DOI: 10.1016/S0022-1694(03)00257-9.

Huddleston B., Ataman E., De Salvo P., Zanetti M., Bloise M., Bel J., Francheschini G., Fed'Ostiani L., 2003, Towards a GIS-based analysis of mountain environments and populations, Environment and Natural Resources Working Paper, 10, 26 pp.

Huffman G.J., Adler R.F., Bolvin D.T., Nelkin E.J., 2010, The TRMM Multi-satellite Precipitation Analysis (TMPA), [in:] Satellite Applications for Surface Hydrology, [eds.: F. Hossain, M. Gebremichael), Springer Verlag, 3-22.

Hunt K.M.R., Turner A.G., Shaffrey L.C., 2020, The impacts of climate change on the winter water cycle of the western Himalaya, Climate Dynamics, 55 (7-8), 2287-2307, DOI: 10.1007/s00382-020-05383-3.

Huss M., Hock R., 2015, A new model for global glacier change and sea-level rise, Frontiers in Earth Science, 3, DOI: 10.3389/feart.2015.00054.

Huss M., Hock R., 2018, Global-scale hydrological response to future glacier mass loss, Nature Climate Change, 8 (2), 135-140, DOI: 10.1038/s41558-017-0049-x.

Huss M., Zemp M., Joerg P.C., Salzmann N., 2014, High uncertainty in 21st century runoff projections from glacierized basins, Journal of Hydrology, 510, 35-48, DOI: 10.1016/j.jhydrol.2013.12.017.

Immerzeel W., 2008, Historical trends and future predictions of climate variability in the Brahmaputra basin, International Journal of Climatology, 28 (2), 243-254, DOI: 10.1002/joc.1528.

Immerzeel W.W., Droogers P., de Jong S.M., Bierkens M.F.P., 2009, Large-scale monitoring of snow cover and runoff simulation in Himalayan river basins using remote sensing, Remote Sensing of Environment, 113 (1), 40-49, DOI: 10.1016/j.rse.2008.08.010.

Immerzeel W.W., Pellicciotti F., Bierkens M.F.P., 2013, Rising river flows throughout the twenty-first century in two Himalayan glacierized watersheds, Nature Geoscience, 6 (9), 742-745, DOI: 10.1038/ngeo1896.

Immerzeel W.W., Petersen L., Ragettli S., Pellicciotti F., 2014, The importance of observed gradients of air temperature and precipitation for modeling runoff from a glacierized watershed in the Nepalese Himalayas, Water Resources Research, 50 (3), 2212-2226, DOI: 10.1002/2013WR014506.

Immerzeel W.W., Van Beek L.P.H., Bierkens M.F.P., 2010, Climate change will affect the Asian water towers, Science, 328 (5984), 1382-1385, DOI: 10.1126/science.1183188.

Immerzeel W.W., Van Beek L.P.H., Konz M., Shrestha A.B., Bierkens M.F.P., 2012, Hydrological response to climate change in a glacierized catchment in the Himalayas, Climatic Change, 110, 721-736, DOI: 10.1007/s10584-011-0143-4.

IPCC, 2007, Climate Change 2007: Impacts, Adaptation and Vulnerability, Contribution of Working Group II to the Fourth Assessment Report of the IPCC, Cambridge University Press.

IPCC, 2013, Climate Change 2013: The Physical Science Basis, Contribution of Working Group I to the Fifth Assessment Report of the Intergovernmental Panel on Climate Change, Cambridge University Press, Cambridge, United Kingdom and New York, NY, USA, 1535 pp.

IPCC, 2017, Climate Change 2014: Impacts Adaptation, and Vulnerability. Part A: Global and Sectoral Aspects, Contribution of Working Group II to the Fifth Assessment Report of the Intergovernmental Panel on Climate Change, Cambridge University Press.

IPCC, 2018, Global Warming of 1.5°C, An IPCC special report on the impacts of global warming of 1.5°C above pre-industrial levels and related global greenhouse gas emission pathways.

IPCC, 2021, Climate Change 2021: The Physical Science Basis, Contribution of Working Group I to the Sixth Assessment Report of the Intergovernmental Panel on Climate Change, Cambridge University Press, Cambridge, United Kingdom and New York, NY, USA, DOI: 10.1017/9781009157896.

Jain S.K., Goswami A., Saraf A.K., 2010, Assessment of snowmelt runoff using remote sensing and effect of climate change on runoff, Water Resources Management, 24, 1763-1777, DOI: 10.1007/s11269-009-9523-1.

Jain S.K., Jain S.K., Jain N., Xu C.-Y., 2017, Hydrologic modeling of a Himalayan mountain basin by using the SWAT mode, Hydrology and Earth System Sciences Discussions, DOI: 10.5194/hess-2017-100.

Jeelani G., Feddema J.J., van der Veen C.J., Stearns L., 2012, Role of snow and glacier melt in controlling river hydrology in Liddar watershed (western Himalaya) under current and future climate, Water Resources Research, 48 (12), DOI: 10.1029/2011WR011590.

Jhajharia D., Singh V.P., 2011, Trends in temperature, diurnal temperature range and sunshine duration in Northeast India, International Journal of Climatology, 31 (9), 1353-1367, DOI: 10.1002/joc.2164.

Jost G., Moore R.D., Menounos B., Wheate R., 2012, Quantifying the contribution of glacier runoff to streamflow in the upper Columbia River Basin Canada, Hydrology and Earth System Sciences, 16 (3), 849-860, DOI: 10.5194/hess-16-849-2012.

Kääb A., Berthier E., Nuth C., Gardelle J., Arnaud Y., 2012, Contrasting patterns of early twenty-first-century glacier mass change in the Himalayas, Nature, 488 (7412), 495-498, DOI: 10.1038/nature11324.

Karger D.N., Conrad O., Böhner J., Kawohl T., Kreft H., Soria-Auza R.W., Zimmermann N.E., Linder H.P., Kessler M., 2017, Climatologies at high resolution for the earth's land surface areas, Scientific Data, 4 (1), DOI: 10.1038/sdata.2017.122.

Kayastha R.B., Kayastha R., 2020, Glacio-Hydrological Degree-Day Model (GDM) useful for the Himalayan river basins, [in:] Himalayan Weather and Climate and Their Impact on the Environment, [eds.: A. Dimri, B. Bookhagen, M. Stoffel, T. Yasunari], 379-398, DOI: 10.1007/978-3-030-29684-1_19.

Kayastha R.B., Steiner N., Kayastha R., Mishra S.K., McDonald K., 2020, Comparative study of hydrology and icemelt in three Nepal river basins using the Glacio-Hydrological Degree-Day Model (GDM) and observations from the Advanced Scatterometer (ASCAT), Frontiers in Earth Science, 7, DOI: 10.3389/feart.2019.00354.

Kesarwani K., Dobhal D.P., Durgapal A., Mehta M., 2015, High altitude meteorology and cloud cover conditions: a study from Chorabari glacier catchment Central Himalaya India, Himalayan Geology, 36 (2), 134-142.

Khajuria V., Kumar M., Gunasekaran A., Rautela K.S., 2022, Snowmelt runoff estimation using combined terra-aqua MODIS improved snow product in Western Himalayan River Basin via degree day modelling approach, Environmental Challenges, 8, DOI: 10.1016/j.envc.2022.100585.

Knutti R., Sedláček J., 2013, Robustness and uncertainties in the new CMIP5 climate model projections, Nature Climate Change, 3 (4), 369-373, DOI: 10.1038/nclimate1716.

Kothawale D.R., Munot A.A., Kumar K.K., 2010, Surface air temperature variability over India during 1901-2007, and its association with ENSO, Climate Research, 42 (2), 89-104, DOI: 10.3354/cr00857.

Kothawale D.R., Rupa Kumar K., 2005, On the recent changes in surface temperature trends over India, Geophysical Research Letters, 32 (18), DOI: 10.1029/2005GL023528.

Kraaijenbrink P.D., Bierkens M.F.P., Lutz A.F., Immerzeel W.W., 2017, Impact of a global temperature rise of 1.5 degrees Celsius on Asia's glaciers, Nature, 549 (7671), 257-260, DOI: 10.1038/nature23878.

Krishnan R., Sanjay J., Gnanaseelan C., Mujumdar M., Kulkarni A., Chakraborty S. (eds.), 2020, Assessment of Climate Change over the Indian Region: A Report of the Ministry of Earth Sciences (MoES) Government of India, Springer, DOI: 10.1007/978-981-15-4327-2.

Krishnan R., Shrestha A.B., Ren G., Rajbhandari R., Saeed S., Sanjay J., Syed M.A., Vellore R., Xu Y., You Q., 2019, Unravelling climate change in the Hindu Kush Himalaya: rapid warming in the mountains and increasing extremes, [in:] The Hindu Kush Himalaya Assessment: Mountains Climate Change Sustainability and People, [eds.: P. Wester, A. Mishra, A. Mukherji, A. Shrestha], 57-97, DOI: 10.1007/978-3-319-92288-1_3.

Kulkarni A.V., Bahuguna I.M., Rathore B.P., Singh S.K., Randhawa S.S., Sood R.K., Dhar S., 2007, Glacial retreat in Himalaya using Indian remote sensing satellite data, Current Science, 92 (1), 69-74.

Kumar A., 2011, Modelling of stream flow and sediment delivery characteristics of Gangotri glacier basin Himalayas, PhD Thesis.

Kumar R., Areendran G., Rao P., 2009, Witnessing Change: Glaciers in the Indian Himalayas, Pilani WWF-India and Birla Institute of Technology, 38 pp.

Kumar R., Singh S., Randhawa S.S., Singh K.K., Rana J.C., 2014, Temperature trend analysis in the glacier region of Naradu Valley, Himachal Himalaya, India, Comptes Rendus Geoscience, 346 (9-10), 213-222, DOI: 10.1016/j.crte.2014.09.001.

Kumar V., Singh P., Singh V., 2007, Snow and glacier melt contribution in the Beas River at Pandoh dam, Himachal Pradesh, India, Hydrological Sciences Journal, 52 (2), 376-388, DOI: 10.1623/hysj.52.2.376.

Le Masson V., Nair K. 2012, Does climate modeling help when studying adaptation to environmental changes? The case of Ladakh, India, [in:] Climate Change Modeling for Local Adaptation in the Hindu Kush-Himalayan Region, [eds.: A. Lamadrid, I. Kelman], Emerald Group Publishing Limited, 75-94, DOI: 10.1108/S2040-7262(2012)0000011011.

Leng R., Harrison S., Anderson K., 2023, Himalayan alpine ecohydrology: An urgent scientific concern in a changing climate, Ambio, 52, 390-410, DOI: 10.1007/s13280-022-01792-2.

Lesher R.S., 2011, Climate change impacts to a high altitude lake in the Indian Himalaya, Arts and Letters.

Li L., Engelhardt M., Xu C.-Y., Jain S.K., Singh V.P., 2013, Comparison of satellite-based and re-analysed precipitation as input to glacio-hydrological modelling for Beas River basin, northern India, IAHS-AISH Publication, 360, 45-52.

Li L., Shen M., Hou Y., Xu C.-Y., Lutz A.F., Chen J., Jain S.K., Li J., Chen H., 2019, Twenty-first-century glacio-hydrological changes in the Himalayan headwater Beas River basin, Hydrology and Earth System Sciences, 23 (3), 1483-1503, DOI: 10.5194/hess-23-1483-2019.

Liang X., Lettenmaier D.P., Wood E.F., Burges S.J., 1994, A simple hydrologically based model of land surface water and energy fluxes for general circulation models, Journal of Geophysical Research, 99 (D7), 14415-14428, DOI: 10.1029/94JD00483.

Loukas A., Vasiliades L., 2014, Streamflow simulation methods for ungauged and poorly gauged watersheds, Natural Hazards and Earth System Sciences, 14 (7), 1641-1661, DOI: 10.5194/nhess-14-1641-2014.

Lutz A.F., Immerzeel W.W., Kraaijenbrink P.D.A., Shrestha A.B., Bierkens M.F.P., 2016, Climate change impacts on the upper Indus hydrology: sources, shifts and extremes, PloS One, 11 (11), DOI: 10.1371/journal.pone.0165630.

Lutz A.F., Immerzeel W.W., Shrestha A.B., Bierkens M.F.P., 2014, Consistent increase in High Asia's runoff due to increasing glacier melt and precipitation, Nature Climate Change, 4 (7), 587-592, DOI: 10.1038/nclimate2237.

Lutz A.F., ter Maat H.W., Wijngaard R.R., Biemans H., Syed A., Shrestha A.B., Wester P., Immerzeel W.W., 2019, South Asian river basins in a 1.5°C warmer world, Regional Environmental Change, 19, 833-847, DOI: 10.1007/s10113-018-1433-4.

Maity R., Srivastava A., Sarkar S., Khan M.I., 2024, Revolutionizing the future of hydrological science: Impact of machine learning and deep learning amidst emerging explainable AI and transfer learning, Applied Computing and Geosciences, 24, DOI: 10.1016/j.acags.2024.100206.

Mall R.K., Gupta A., Singh R., Singh R.S., Rathore L.S., 2006, Water resources and climate change: An Indian perspective, Current Science, 90 (12), 1610-1626.

Mani M, 2021, Glaciers of the Himalayas: Climate Change, Black Carbon, and Regional Resilience, World Bank Publications, DOI: 10.1596/978-1-4648-0099-3.

Martinec J., Rango A., Roberts R., 1994, Snowmelt Runoff Model (SRM) User's Manual, Department of Geography, University of Bern.

Marzeion B., Jarosch A.H., Hofer M., 2012, Past and future sea-level change from the surface mass balance of glaciers, The Cryosphere, 6 (6), 1295-1322, DOI: 10.5194/tc-6-1295-2012.

Mehboob M.S., Kim Y., 2024, Impact of climate change on the hydrological projections over a western Himalayan river basin and the associated uncertainties, Journal of Hydrology, 628, DOI: 10.1016/j.jhydrol.2023.130460.

Ménégoz M., Gallée H., Jacobi H.W., 2013, Precipitation and snow cover in the Himalaya: from reanalysis to regional climate simulations, Hydrology and Earth System Sciences, 17 (10), 3921-3936, DOI: 10.5194/hess-17-3921-2013.

Messerli B, Korner C., Sharma E., Tshering K., Schaaf T., Ramakrishan P.S., Zomer R., Jianchu X., Baker C., Trisal C., 2009, Biodiversity and Climate Change in the Himalaya, Integrated Mountain Development, No. 55, International Centre for Integrated Mountain Development (ICIMOD).

Mimeau L., Esteves M., Jacobi H.-W., Zin I., 2019a, Evaluation of gridded and in situ precipitation datasets on modeled glacio-hydrologic response of a small glacierized Himalayan catchment, Journal of Hydrometeorology, 20 (6), 1103-1121, DOI: 10.1175/JHM-D-18-0157.1.

Mimeau L., Esteves M., Zin I., Jacobi H.-W., Brun F., Wagnon P., Koirala D., Arnaud Y., 2019b, Quantification of different flow components in a high-altitude glacierized catchment (Dudh Koshi Himalaya): some cryospheric-related issues, Hydrology and Earth System Sciences, 23 (9), 3969-3996, DOI: 10.5194/hess-23-3969-2019.

Moradkhani H., Sorooshian S., 2008, General review of rainfall-runoff modeling: model calibration, data assimilation, and uncertainty analysis, [in:] Hydrological Modelling and Water Cycle, vol. 63, [eds.: S. Sorooshian, K.L. Hsu, E. Coppola, B. Tomassetti, M. Verdecchia, G. Visconti], Springer, Berlin, Heidelberg, DOI: 10.1007/978-3-540-77843-1_1.

Nandargi S., Dhar O.N., 2011, Extreme rainfall events over the Himalayas between 1871 and 2007, Hydrological Sciences Journal, 56 (6), 930-945, DOI: 10.1080/02626667.2011.595373.

Nandy S.N., Dhyani P.P., Samal P.K., 2006, Resource information database of the Indian Himalaya.

National Research Council, 2012, Himalayan Glaciers: Climate Change Water Resources, and Water Security, Washington, DC, The National Academies Press, DOI: 10.17226/13449.

Naz B.S., Frans C.D., Clarke G.K.C., Burns P., Lettenmaier D.P., 2014, Modeling the effect of glacier recession on streamflow response using a coupled glacio-hydrological model, Hydrology and Earth System Sciences, 18 (2), 787-802, DOI: 10.5194/hess-18-787-2014.

Negi H.S., Kumar A., Kanda N., Thakur N.K., Singh K.K., 2021, Status of glaciers and climate change of East Karakoram in early twenty-first century, Science of the Total Environment, 753, DOI: 10.1016/j.scitotenv.2020.141914.

Negi S.S., 1991, Himalayan Rivers, Lakes, and Glaciers, Indus Publishing, New Delhi, 182 pp.

Nepal S., 2016, Impacts of climate change on the hydrological regime of the Koshi river basin in the Himalayan region, Journal of Hydro-Environment Research, 10, 76-89, DOI: 10.1016/j.jher.2015.12.001.

Nepal S., Flügel W.-A., Shrestha A.B., 2017, Upstream-downstream linkages of hydrological processes in the Himalayan region, Ecological Processes, 6, DOI: 10.1186/s13717-014-0019-4.

Nepal S., Krause P., Flügel W.-A., Fink M., Fischer C., 2014, Understanding the hydrological system dynamics of a glaciated alpine catchment in the Himalayan region using the J2000 hydrological model, Hydrological Processes, 28 (3), 1329-1344, DOI: 10.1002/hyp.9627.

NMSHE, 2010, National Mission for Sustaining the Himalayan Ecosystem, National Action Plan on Climate Change Mission, Document, 51.

NOAA, 2020, Global Climate Report for Annual, National Centers for Environmental Information, available online at https://www.ncei.noaa.gov/access/monitoring/monthly-report/global/202013 (data access 02.02.2026).

Nolin A.W., Phillippe J., Jefferson A., Lewis S.L., 2010, Present-day and future contributions of glacier runoff to summertime flows in a Pacific Northwest watershed: Implications for water resources, Water Resources Research, 46 (12), DOI: 10.1029/2009WR008968.

Ó Dochartaigh B.É., MacDonald A.M., Black A.R., Everest J., Wilson P., Darling W.G., Jones L., Raines M., 2019, Groundwater-glacier meltwater interaction in proglacial aquifers, Hydrology and Earth System Sciences, 23 (11), 4527-4539, DOI: 10.5194/hess-23-4527-2019.

Östrem G., 1959, Ice melting under a thin layer of moraine, and the existence of ice cores in moraine ridges, Geografiska Annaler, 41 (4), 228-230.

Ouyang W., Zhang C., Ye L., Zhang H., Meng Z., Chu J., 2025, Dive into transfer-learning for daily rainfall-runoff modeling in data-limited basins, Journal of Hydrology, 657, DOI: 10.1016/j.jhydrol.2025.133063.

Palazzi E., Mortarini L., Terzago S., von Hardenberg J., 2019, Elevation-dependent warming in global climate model simulations at high spatial resolution, Climate Dynamics, 52, 2685-2702, DOI: 10.1007/s00382-018-4287-z.

Palazzi E., von Hardenberg J., Provenzale A., 2013, Precipitation in the Hindu-Kush Karakoram Himalaya: observations and future scenarios, Journal of Geophysical Research: Atmospheres, 118 (1), 85-100, DOI: 10.1029/2012JD018697.

Panday P.K., Thibeault J., Frey K.E., 2015, Changing temperature and precipitation extremes in the Hindu Kush-Himalayan region: An analysis of CMIP3 and CMIP5 simulations and projections, International Journal of Climatology, 35 (10), 3058-3077, DOI: 10.1002/joc.4192.

Pandey P., Venkataraman G., 2013, Changes in the glaciers of Chandra-Bhaga basin, Himachal Himalaya, India, between 1980 and 2010 measured using remote sensing, International Journal of Remote Sensing, 34 (15), 5584-5597, DOI: 10.1080/01431161.2013.793464.A

Pellicciotti F., Bauder A., Parola M., 2010, Effect of glaciers on streamflow trends in the Swiss Alps, Water Resources Research, 46 (10), DOI: 10.1029/2009WR009039.

Pellicciotti F., Brock B., Strasser U., Burlando P., Funk M., Corripio J., 2005, An enhanced temperature-index glacier melt model including the shortwave radiation balance: development and testing for Haut Glacier d'Arolla, Switzerland, Journal of Glaciology, 51 (175), 573-587, DOI: 10.3189/172756505781829124.

Pellicciotti F., Ragettli S., Carenzo M., McPhee J., 2014, Changes of glaciers in the Andes of Chile and priorities for future work, Science of the Total Environment, 493, 1197-1210, DOI: 10.1016/j.scitotenv.2013.10.055.

Pepin N., Bradley R.S., Diaz H.F., Baraer M., Caceres E.B., Forsythe N., Fowler H., Greenwood G., Hashmi M.Z., Liu X.D., Miller J.R., Ning L., Ohmura A., Palazzi E., Rangwala I., Schöner W., Severskiy I., Shahgedanova M., Wang M.B., Williamson S.N., Yang D.Q., 2015, Elevation-dependent warming in mountain regions of the world, Nature Climate Change, 5 (5), 424-430, 10.1038/nclimate2563.

Piao S., Ciais P., Huang Y., Shen Z., Peng S., Li J., Zhou L., Liu H., Ma Y., Ding Y., Friedlingstein P., Liu C., Tan K., Yonqiang Y., Zhang T., Fang J., 2010, The impacts of climate change on water resources and agriculture in China, Nature, 467 (7311), 43-51, DOI: 10.1038/nature09364.

Pramanik P., Bhaduri D., 2016, Impact of climate change on water resources in Indian Himalaya, [in:] Conservation Agriculture: An Approach to Combat Climate Change in Indian Himalaya, [eds.: J.K. Bisht. V.S. Meena, P.K. Mishra, A. Pattanayak], 487-507, Springer, Singapore, DOI: 10.1007/978-981-10-2558-7_19.

Prasch M., Mauser W., Weber M., 2013, Quantifying present and future glacier melt-water contribution to runoff in a central Himalayan river basin, The Cryosphere, 7 (3), 889-904, DOI: 10.5194/tc-7-889-2013.

Racoviteanu A., 2011, Himalayan glaciers: combining remote sensing, field techniques and indigenous knowledge to understand spatio-temporal patterns of glacier changes and their impact on water resources, University of Colorado at Boulder, available online at https://scholar.colorado.edu/concern/graduate_thesis_or_dissertations/fb494849k (data access 02.02.2026).

Racoviteanu A.E., Armstrong R., Williams M.W., 2013, Evaluation of an ice ablation model to estimate the contribution of melting glacier ice to annual discharge in the Nepal Himalaya, Water Resources Research, 49 (9), 5117-5133, DOI: 10.1002/wrcr.20370.

Racoviteanu A.E., Arnaud Y., Williams M.W., Manley W.F., 2015, Spatial patterns in glacier characteristics and area changes from 1962 to 2006 in the Kanchenjunga-Sikkim area, eastern Himalaya, The Cryosphere, 9 (2), 505-523, DOI: 10.5194/tc-9-505-2015.

Ragettli S., Immerzeel W.W., Pellicciotti F., 2016, Contrasting climate change impact on river flows from high-altitude catchments in the Himalayan and Andes Mountains, Proceedings of the National Academy of Sciences, 113 (33), 9222-9227, DOI: 10.1073/pnas.1606526113.

Ragettli S., Pellicciotti F., Bordoy R., Immerzeel W.W., 2013, Sources of uncertainty in modeling the glaciohydrological response of a Karakoram watershed to climate change, Water Resources Research, 49 (9), 6048-6066, DOI: 10.1002/wrcr.20450.

Ragettli S., Pellicciotti F., Immerzeel W.W., Miles E.S., Petersen L., Heynen M., Shea J.M., Stumm D., Joshi S., Shrestha A., 2015, Unraveling the hydrology of a Himalayan catchment through integration of high resolution in situ data and remote sensing with an advanced simulation model, Advances in Water Resources, 78, 94-111, DOI: 10.1016/j.advwatres.2015.01.013.

Raina V.K., Srivastava D., 2008, Glacier Atlas of India. Bangalore, Geological Society of India, 315 pp.

Raman R., Punia M., 2012, Land use dynamics and landscape fragmentation in higher Garhwal Himalaya. India, Asian Journal of Geoinformatics, 12 (1).

Rao V.B., Franchito S.H., Gerólamo R.O.P., Giarolla E., Ramakrishna S.S.V.S., Rao B.R.S., Naidu C.V., 2016, Himalayan warming and climate change in India, American Journal of Climate Change, 5 (4), 558-574, DOI: 10.4236/ajcc.2016.54038.

Rees H.G., Collins D.N., 2006, Regional differences in response of flow in glacier-fed Himalayan rivers to climatic warming, Hydrological Processes, 20 (10), 2157-2169, DOI: 10.1002/hyp.6209.

Ren D., Karoly D.J., Leslie L.M., 2007, Temperate mountain glacier-melting rates for the period 2001-30: estimates from three coupled GCM simulations for the greater Himalayas, Journal of Applied Meteorology and Climatology, 46 (6), 890-899, DOI: 10.1175/JAM2499.1.

Ren Z., Su F., Xu B., Xie Y., Kan B., 2018, A coupled glacier-hydrology model and its application in Eastern Pamir, Journal of Geophysical Research: Atmospheres, 123 (24), 13,629-13,713, DOI: 10.1029/2018JD028572.

Roe G.H., Baker M.B., Herla F., 2017, Centennial glacier retreat as categorical evidence of regional climate change, Nature Geoscience, 10 (2), 95-99, DOI: 10.1038/ngeo2863.

Rohrer M., Salzmann N., Stoffel M., Kulkarni A.V., 2013, Missing (in-situ) snow cover data hampers climate change and runoff studies in the Greater Himalayas, Science of the Total Environment, 468-469, S60-S70, DOI: 10.1016/j.scitotenv.2013.09.056.

Sabin T.P., Krishnan R., Vellore R., Priya P., Borgaonkar H.P., Singh B.B., Sagar A., 2020, Climate change over the Himalayas, [in:] Assessment of Climate Change over the Indian Region: A Report of the Ministry of Earth Sciences (MoES), [eds.: R. Krishnan, J. Sanjay, C. Gnanaseelan, M. Mujumdar, A. Kulkarni, S. Chakraborty, Government of India, 207-222.

Saikia U.S., Goswami B., Rajkhowa J., Venkatesh A., Ramachandran K., Rao V.U.M., Venkateswarlu B., Ngachan S.V., 2013, Shift in monsoon rainfall pattern in the North Eastern region of India post 1991, Journal of Agrometeorology, 15 (2), 162-164, DOI: 10.54386/jam.v15i2.1467.

Sanjay J., Krishnan R., Shrestha A.B., Rajbhandari R., Ren G.-Y., 2017, Downscaled climate change projections for the Hindu Kush Himalayan region using CORDEX South Asia regional climate models, Advances in Climate Change Research, 8 (3), 185-198, DOI: 10.1016/j.accre.2017.08.003.

Saran Ahluwalia R., Rai S.P., Jain S.K., Dobhal D.P., Kumar A., 2015, Estimation of snow/glacier melt contribution in the upper part of the Beas River basin Himachal Pradesh, using conventional and SNOWMOD modeling approach, Journal of Water and Climate Change, 6 (4), 880-890, DOI: 10.2166/wcc.2015.107.

Savéan M., Delclaux F., Chevallier P., Wagnon P., Gonga-Saholiariliva N., Sharma R., Neppel L., Arnaud Y., 2015, Water budget on the Dudh Koshi River (Nepal): uncertainties on precipitation, Journal of Hydrology, 531, 850-862, DOI: 10.1016/j.jhydrol.2015.10.040.

Scherler D., Bookhagen B., Strecker M.R., 2011, Spatially variable response of Himalayan glaciers to climate change affected by debris cover, Nature Geoscience, 4 (3), 156-159, DOI: 10.1038/ngeo1068.

Schmale J., Flanner M.G., Kang S., Sprenger M., Zhang Q., Guo J., Li Y., Schwikowski M., Farinotti D., 2017, Modulation of snow reflectance and snowmelt from Central Asian glaciers by anthropogenic black carbon, Scientific Reports, 7, DOI: 10.1038/srep40501.

Seibert J., Vis M.J., 2012, Teaching hydrological modeling with a user-friendly catchment-runoff-model software package, Hydrology and Earth System Sciences, 16 (9), 3315-3325, DOI: 10.5194/hess-16-3315-2012.

Shangguan D., Liu S., Ding Y., Wu L., Deng W., Guo W., Wang Y., Xu J., Yao X., Guo Z., Zhu W., 2014, Glacier changes in the Koshi River basin, central Himalaya, from 1976 to 2009, derived from remote-sensing imagery, Annals of Glaciology, 55 (66), 61-68, DOI: 10.3189/2014AoG66A057.

Sharma A., Goyal M., 2020, Assessment of the changes in precipitation and temperature in Teesta River basin in Indian Himalayan Region under climate change, Atmospheric Research, 231, DOI: 10.1016/j.atmosres.2019.104670.

Sharma E., Bhuchar S., Xing M., Kothyari B.P., 2007, Land use change and its impact on hydro-ecological linkages in Himalayan watersheds, Tropical Ecology, 48 (2), 151-161.

Sharma E., Molden D., Rahman A., Khatiwada Y.R., Zhang L., Singh S.P., Yao T., 2019, Introduction to the Hindu Kush Himalaya Assessment, [in:] The Hindu Kush Himalaya Assessmen. Mountains Climate Change Sustainability, and People, [eds.: P. Wester, P. Mishra, A. Mukherji, A. Shrestha], Springer, Cham, 1-16, DOI: 10.1007/978-3-319-92288-1_1.

Sharma K.P., Vorosmarty C.J., Moore B., 2000, Sensitivity of the Himalayan hydrology to land-use and climatic changes, Climatic Change, 47, 117-139, DOI: 10.1023/A:1005668724203.

Shea J.M., Immerzeel W.W., Wagnon P., Vincent C., Bajracharya S., 2015, Modelling glacier change in the Everest region, Nepal Himalaya, The Cryosphere, 9 (3), 1105-1128, DOI: 10.5194/tc-9-1105-2015.

Shekhar M., Singh S., 2014, Climate Science, Current Science, 106 (7), p. 10.

Shrestha A.B., Aryal R., 2011, Climate change in Nepal and its impact on Himalayan glaciers, Regional Environmental Change, 11 (1), 65-77, DOI: 10.1007/s10113-010-0174-9.

Shrestha A.B., Devkota L.P., 2010, Climate change in the Eastern Himalayas: Observed Trends and Model Projections, Climate Change Impact and Vulnerability in the Eastern Himalayas – Technical Report 1, International Centre for Integrated Mountain Development (ICIMOD), DOI: 10.53055/ICIMOD.520.

Shrestha A.B., Wake C.P., Dibb J.E., Mayewski P.A., 2000, Precipitation fluctuations in the Nepal Himalaya and its vicinity and relationship with some large scale climatological parameters, International Journal of Climatology, 20 (3), 317-327, DOI: 10.1002/(SICI)1097-0088(20000315)20:3<317::AID-JOC476>3.0.CO;2-G.

Shrestha A.B., Wake C.P., Mayewski P.A., Dibb J.E., 1999, Maximum temperature trends in the Himalaya and its vicinity: an analysis based on temperature records from Nepal for the period 1971-94, Journal of Climate, 12 (9), 2775-2786, DOI: 10.1175/1520-0442(1999)012<2775:MTTITH>2.0.CO;2.

Shrestha M., Acharya S.C., Shrestha P.K., 2017, Bias correction of climate models for hydrological modelling-are simple methods still useful?, Meteorological Applications, 24 (3), 531-539, DOI: 10.1002/met.1655.

Shrestha U.B., Gautam S., Bawa K.S., 2012, Widespread climate change in the Himalayas and associated changes in local ecosystems, PloS One, 7 (5), DOI: 10.1371/journal.pone.0036741.

Shukla S., Jain S.K., Kansal M.L., 2021, Hydrological modelling of a snow/glacier-fed western Himalayan basin to simulate the current and future streamflows under changing climate scenarios, Science of the Total Environment, 795, DOI: 10.1016/j.scitotenv.2021.148871.

Singh A.K., Hasnain S.I., 1998, Major ion chemistry and weathering control in a high altitude basin: Alaknanda River, Garhwal Himalaya, India, Hydrological Sciences Journal, 43 (6), 825-843, DOI: 10.1080/02626669809492181.

Singh D., Sharma V., Juyal V., 2015, Observed linear trend in few surface weather elements over the Northwest Himalayas (NWH) during winter season, Journal of Earth System Science, 124 (3), 553-565, DOI: 10.1007/s12040-015-0560-2.

Singh O., Arya P., Chaudhary B.S., 2013, On rising temperature trends at Dehradun in Doon valley of Uttarakhand India. Journal of Earth System Science, 122 (3), 613-622, DOI: 10.1007/s12040-013-0304-0.

Singh P., Arora M., Goel N.K., 2006, Effect of climate change on runoff of a glacierized Himalayan basin, Hydrological Processes, 20 (9), 1979-1992, DOI: 10.1002/hyp.5991.

Singh P., Jain S.K., 2002, Snow and glacier melt in the Satluj River at Bhakra Dam in the western Himalayan region, Hydrological Sciences Journal, 47 (1), 93-106, DOI: 10.1080/02626660209492910.

Singh P., Jain S.K., 2003, Modelling of streamflow and its components for a large Himalayan basin with predominant snowmelt yields, Hydrological Sciences Journal, 48 (2), 257-276, DOI: 10.1623/hysj.48.2.257.44693.

Singh P., Kumar N., 1997, Effect of orography on precipitation in the western Himalayan region, Journal of Hydrology, 199 (1-2), 183-206, DOI: 10.1016/S0022-1694(96)03222-2.

Singh P., Kumar V., Thomas T., Arora M., 2008a, Basin-wide assessment of temperature trends in northwest and central India, Hydrological Sciences Journal, 53 (2), 421-433, DOI: 10.1623/hysj.53.2.421.

Singh S., Kumar R., Bhardwaj A., Sam L., Shekhar M., Singh A., Kumar R., Gupta A., 2016, Changing climate and glacio-hydrology in Indian Himalayan Region: a review, Wiley Interdisciplinary Reviews: Climate Change, 7 (3), 393-410, DOI: 10.1002/wcc.393.

Singh S.K., Rai S.K., Krishnaswami S., 2008b, Sr and Nd isotopes in river sediments from the Ganga Basin: sediment provenance and spatial variability in physical erosion, Journal of Geophysical Research: Earth Surface, 113 (F3), DOI: 10.1029/2007JF000909.

Singh V., Goyal M.K., 2016, Analysis and trends of precipitation lapse rate and extreme indices over north Sikkim eastern Himalayas under CMIP5ESM-2M RCPs experiments, Atmospheric Research, 167, 34-60, DOI: 10.1016/j.atmosres.2015.07.005.

Slariya M.K., 2013, Development and water resources in Indian Himalayan region: an invitation to disaster – a study of hydroelectric power developmental projects in Himachal Pradesh, Scholarly Research Journal for Interdisciplinary Studies, 1 (1), 1464-1475.

Snehmani Bhardwaj A., Singh M.K., Gupta R.D., Joshi P.K., Ganju A., 2015, Modelling the hypsometric seasonal snow cover using meteorological parameters, Journal of Spatial Science, 60 (1), 51-64, DOI: 10.1080/14498596.2014.943310.

Soltani S.S., Cvetkovic V., Destouni G., 2017,. Simple Kinematic Pathway Approach (KPA) to catchment-scale travel time and water age distributions, [in:] AGU Fall Meeting Abstracts, vol. 2017.

Soncini A., Bocchiola D., Azzoni R.S., Diolaiuti G., 2017, A methodology for monitoring and modeling of high altitude Alpine catchments, Progress in Physical Geography: Earth and Environment, 41 (4), 393-420, DOI: 10.1177/0309133317710832.

Soncini A., Bocchiola D., Confortola G., Minora U., Vuillermoz E., Salerno F., Viviano G., Shrestha D., Senese A., Smiraglia C., Diolaiuti G., 2016, Future hydrological regimes and glacier cover in the Everest region: The case study of the upper Dudh Koshi basin, Science of the Total Environment, 565, 1084-1101, DOI: 10.1016/j.scitotenv.2016.05.138.

Srivastava S., Azam M.F., Thakur P.K., 2024, Linking basin-scale hydrology with climatic parameters in western Himalaya: Application of satellite data, temperature index modelling and in-situ observations, Geoscience Frontiers, 15 (6), DOI: 10.1016/j.gsf.2024.101936.

Stahl K., Moore R.D., Shea J.M., Hutchinson D., Cannon A.J., 2008, Coupled modelling of glacier and streamflow response to future climate scenarios, Water Resources Research, 44 (2), DOI: 10.1029/2007WR005956.

Swain S., Mishra S.K., Pandey A., Pandey A.C., Jain A., Chauhan S.K., Badoni A.K., 2022, Hydrological modelling through SWAT over a Himalayan catchment using high-resolution geospatial inputs, Environmental Challenges, 8, DOI: 10.1016/j.envc.2022.100579.

Tayal S., Sarkar S.K., 2019, Climate Change Impacts on Himalayan Glaciers and Implications on Energy Security of the Country, TERI Discussion Paper, The Energy and Resources Institute, New Delhi, India, 30 pp.

Terink W., Lutz A.F., Simons G.W.H., Immerzeel W.W., Droogers P., 2015, SPHY v2. 0: Spatial processes in hydrology, Geoscientific Model Development, 8 (7), 2009-2034, DOI: 10.5194/gmd-8-2009-2015.

Thayyen R.J., Gergan J.T., 2010, Role of glaciers in watershed hydrology: A preliminary study of a "Himalayan catchment", The Cryosphere, 4 (1), 115-128, DOI: 10.5194/tc-4-115-2010.

Thayyen R.J., Gergan J.T., Dobhal D.P., 2005, Monsoonal control on glacier discharge and hydrograph characteristics, a case study of Dokriani Glacier, Garhwal Himalaya, India, Journal of Hydrology, 306 (1-4), 37-49, DOI: 10.1016/j.jhydrol.2004.08.034.

Uhlenbrook S., Roser S., Tilch N., 2004, Hydrological process representation at the meso-scale: the potential of a distributed, conceptual catchment model, Journal of Hydrology, 291 (3-4), 278-296, DOI: 10.1016/j.jhydrol.2003.12.038.

Visweshwaran R., 2017, Application of the HEC-HMS model for runoff simulation in the Krishna basin, Master's Thesis, National Institute of Technology Karnataka, Surathkal, India.

Viviroli D., Archer D.R., Buytaert W., Fowler H.J., Greenwood G.B., Hamlet A.F., Huang Y., Koboltschnig G., Litaor M.I., López-Moreno J.I., Lorentz S., Schadler B., Schreier H., Schwaiger K., Vuille M., Woods R., 2011, Climate change and mountain water resources: overview and recommendations for research, management and policy, Hydrology and Earth System Sciences, 15 (2), 471-504, DOI: 10.5194/hess-15-471-2011.

Wakeel A., Rao K.S., Maikhuri R.K., Saxena K.G., 2005, Forest management and land use/cover changes in a typical micro watershed in the mid elevation zone of Central Himalaya India, Forest Ecology and Management, 213 (1-3), 229-242, DOI: 10.1016/j.foreco.2005.03.061.

Wang H.-M. Chen J., Xu C.-Y., Zhang J., Chen H., 2020, A framework to quantify the uncertainty contribution of GCMs over multiple sources in hydrological impacts of climate change, Earth's Future, 8 (8), DOI: 10.1029/2020EF001602.

WEF, 2016, World Economic Forum Annual Meeting 2016. Mastering the Fourth Industrial Revolution, Davos-Klosters, Switzerland, available online at: https://www.weforum.org/publications/world-economic-forum-annual-meeting-2016-mastering-the-fourth-industrial-revolution/ (data access 02.02.2026).

Wester P., Mishra A., Mukherji A., Shrestha A.B. (eds.), 2019, The Hindu Kush Himalaya Assessment. Mountains, Climate Change, sustainability and People, Springer Cham, 627 pp., DOI: 10.1007/978-3-319-92288-1.

Wigmosta M.S., Nijssen B., Storck P., Singh V.P., Frevert D.K., 2002, The distributed hydrology soil vegetation model, [in:] Mathematical Models of Small Watershed Hydrology and Applications, [eds.: V.P. Singh, D. Frevert], Water Resources Publications, LLC, Colorado, USA, 7-42.

Wijngaard R.R., Biemans H., Lutz A.F., Shrestha A.B., Wester P., Immerzeel W.W., 2018, Climate change vs. socio-economic development: understanding the future South Asian water gap, Hydrology and Earth System Sciences, 22 (12), 6297-6321, DOI: 10.5194/hess-22-6297-2018.

Winiger M., Gumpert M., Yamout H., 2005, Karakorum-Hindukush-western Himalaya: assessing high-altitude water resources, Hydrological Processes, 19 (12), 2329-2338, DOI: 10.1002/hyp.5887.

Wisal K., Asif K., Ullah K.A., Mujahid K., 2020, Evaluation of hydrological modeling using climatic station and gridded precipitation dataset, Mausam, 71 (4), 717-728, DOI: 10.54302/mausam.v71i4.63.

WMO, 2017, WMO Guidelines on the Calculation of Climate Normals, WMO-No. 1203.

Xu J., Grumbine R.E., Shrestha A., Eriksson M., Yang X., Wang Y., Wilkes A., 2009, The melting Himalayas: cascading effects of climate change on water, biodiversity, and livelihoods, Conservation Biology, 23 (3), 520-530, DOI: 10.1111/j.1523-1739.2009.01237.x.

Ye H., Fetzer E.J., Bromwich D.H., Fishbein E.F., Olsen E.T., Granger S.L., Lee S.-Y., Chen L., Lambrigtsen B.H., 2007a, Atmospheric total precipitable water from AIRS and ECMWF during Antarctic summer, Geophysical Research Letters, 34 (19), DOI: 10.1029/2006GL028547.

Ye Q., Zhu L., Zheng H., Naruse R., Zhang X., Kang S., 2007b, Glacier and lake variations in the Yamzhog Yumco basin, southern Tibetan Plateau, from 1980 to 2000 using remote-sensing and GIS technologies, Journal of Glaciology, 53 (183), 673-676, DOI: 10.3189/002214307784409261.

Yun X., Tang Q., Wang J., Liu X., Zhang Y., Lu H., Wang Y., Zhang L., Chen D., 2020, Impacts of climate change and reservoir operation on streamflow and flood characteristics in the Lancang-Mekong River Basin, Journal of Hydrology, 590, DOI: 10.1016/j.jhydrol.2020.125472.

Zemp M., Huss M., Thibert E., Eckert N., McNabb R., Huber J., Barandun M., Machguth H., Nussbaumer S.U., Gärtner-Roer I., Thomson L., Paul F., Maussion F., Kutuzov S., Cogley J.G., 2019, Global glacier mass changes and their contributions to sea-level rise from 1961 to 2016, Nature, 568 (7752), 382-386, DOI: 10.1038/s41586-019-1071-0.

Zhang G., Kang S., Cuo L., Qu B., 2016, Modeling hydrological process in a glacier basin on the central Tibetan Plateau with a distributed hydrology soil vegetation model, Journal of Geophysical Research: Atmospheres, 121 (16), 9521-9539, DOI: 10.1002/2016JD025434.

Zhang G., Yao T., Shum C.K., Yi S., Yang K., Xie H., Feng W., Bolch T., Wang L., Behrangi A., 2017, Lake volume and groundwater storage variations in Tibetan Plateau's endorheic basin, Geophysical Research Letters, 44 (11), 5550-5560, DOI: 10.1002/2017GL073773.

Zhang L., Su F., Yang D., Hao Z., Tong K., 2013, Discharge regime and simulation for the upstream of major rivers over Tibetan Plateau, Journal of Geophysical Research: Atmospheres, 118 (15), 8500-8518, DOI: 10.1002/jgrd.50665.

Zhao Q., Ye B., Ding Y., Zhang S., Yi S., Wang J., Shangguan D., Zhao C., Han H., 2013, Coupling a glacier melt model to the Variable Infiltration Capacity (VIC) model for hydrological modeling in north-western China, Environmental Earth Sciences, 68, 87-101, DOI: 10.1007/s12665-012-1718-8.

Estimation of snow cover melting characteristics from Vernadsky weather station data (Antarctica)

Borys Khrystiuk[1], Liudmyla Gorbachova[1], Vitalii Shpyg[1], Denys Pishniak[2], Sergiy Klok[3]

[1] Ukrainian Hydrometeorological Institute

[2] National Antarctic Scientific Center of Ukraine

[3] Boryspil Institute of Municipal Management at the Interregional Academy of Personnel Management, Ukraine

Abstract

In Antarctica, snowmelt processes determine the volume and mass of ice sheets and ice shelves. The tempo, extent, and duration of surface snowmelt are increasing under climate change. Thus, investigating snowmelt characteristics is an important way to better understand the state of ice sheets and ice shelves. However, previous to this study, Vernadsky weather station data had not been applied to research on snowmelt processes. The most common approaches to determining the amount of snow melting are the heat balance method, calculation via the melting coefficient, or via the water balance of the snow cover. The application of such approaches to the conditions of Antarctica has its own specific features, related to the geographical location and the availability of the necessary observation data. At the Vernadsky weather station, observations of snow cover characteristics and solar radiation elements have gaps. This article reports the characteristics of snow cover melting based on observations of snow depth and air temperature (at 2 m height) for the Vernadsky weather station data for the period 1997-2025. During 1997-2025 at the Vernadsky Station, the observed snow accumulation season was from March to December, and the snowmelt season lasted from December to February. The multi-annual mean date of maximum snow depth is October 31 (±6 days), and the multi-annual mean maximum snow depth is 211 (±9) cm. The duration of snowmelt ranged from 50 to 117 days, with a multi-annual mean of 78 (±3) days. The amount of snow melting ranged from 108 to 287 cm; the multi-annual mean was 162 (±8) cm. The mean intensity of snowmelt ranged from 0.96 to 3.26 cm/day, in water equivalent approximately 3.45 to 11.7 mm/day, with a multi-annual mean of 7.68 (±0.36) mm/day.

Keywords

Snow cover, snowmelt, Vernadsky Station, surface air temperature, water equivalent, Antarctic Peninsula.

Submitted 5 November 2025, revised 27 January 2026, accepted 29 January 2026

DOI: 10.26491/mhwm/217541

1. Introduction

In hydrology, snowmelt processes are investigated as integral to the formation of river runoff (Marks et al. 1998; Vafakhah et al. 2014). In river catchments, snowmelt involves the complex processes of energy and water transfer between the atmosphere and snow, between different snow layers, and between snow layers and soil (WMO 2009). The most common approaches to determining snowmelt are the heat-balance method, the melting-coefficient method, and the water-balance method of the snow cover (Holko et al. 2011; Zhou et al. 2021). Machine learning methods are widely used in modern research (Thapa et al. 2020). All of these approaches are used in mathematical models of runoff formation when calculating snowmelt in river catchments. The application of such approaches under the conditions in Antarctica has its own specific features, related to the geographical location and the availability of the necessary observation data (Liston, Winther 2005; Zhu et al. 2023).

In Antarctica, research into snow accumulation and snowmelt processes is important because it determines the volume and mass of the terrestrial ice sheet and ice shelves. Bell et al. (2018) reported three modes by which meltwater could impact Antarctic mass balance: increased runoff, meltwater injection to the bed, and meltwater-induced ice-shelf fracture. Banwell et al. (2021) showed that in 2019-2020, surface melt on the northern George VI Ice Shelf on the Antarctic Peninsula was a 32-year record-high. Zhu et al. (2023) reported that both the extent and duration of snowmelt increased in the Antarctic Peninsula from 2015 to 2021 and that snowmelt was significantly more intense on the western side. In general, capturing more detailed information about snowmelt processes is an important way to better understand the state of the ice sheet and ice shelves in Antarctica under climate change (Nagler et al. 2016; Luis et al. 2022).

Ukrainian scientists were given the opportunity to carry out glaciological research in Antarctica by the transfer of the Faraday Station to Ukraine by the United Kingdom in 1996. Now this station is named the Ukrainian Antarctic Akademik Vernadsky Station (hereinafter the Vernadsky Station). Of great scientific importance was the creation of a glaciological polygon by the Ukrainian scientist Govorukha (1997a; 1997b) on the Woozle Hill that is situated on Galindez Island (in Ukrainian scientific literature it is named Domashnii ice cap). Here, 44 snow stakes were installed: 30 main and 14 additional (on the slopes of the glacier). Snow density was measured with a standard snow gauge (Tymofeyev, Grishchenko 2010). There are significantly fewer stakes now. Based on mass-balance measurements it was shown that general evolution of the glacier agrees well with the decadal changes of the mean air temperatures: accumulation dominated in the 1950s and early 60s in conditions of slight cooling; a near-equilibrium state with first signs of ablation was observed in the 1970s, when the first indicators of climate warming appeared; then ablation continued through the 1980s, with further acceleration in the 1990s (Tymofeyev, Grishchenko 2010). The contribution of tropospheric circulation to the mass balance on glaciers is shown, as well as its importance to the formation of ocean currents and sea-ice transport through the Bransfield Strait across the coastal zone of Graham Land (Grischenko et al. 2005). Data from the glaciological polygon and data from two snow stakes at the Vernadsky Station's meteorological observatory were used (Tymofeyev, Grishchenko 2010), showing an increase in snow depth and positive mass balance of the glacier under negative temperature anomalies and ablation and snow cover reduction under positive ones. Results of further investigations using such data types are reported in (Tymofeyev et al. 2021). Periodical and irregular components of variations in snow cover thickness at Galindez Island, the Argentine Islands archipelago, were statistically analyzed (Belokrinitskaya et al. 2006). Mean annual snow cover duration was estimated (Klok 2016; Shpyg et al. 2024). The dates of snow cover formation and its full melting, fluctuations in snow cover parameters, moisture content estimates, etc., were described (Grischenko et al. 2005; Klok 2016; Klok, Afteniuk 2017; Klok et al. 2021; Shpyg et al. 2024). The influence of wind, temperature, and precipitation phases on snow depth was estimated, revealing that wind speed and direction have crucial roles in changes of snow cover on a daily temporal scale in the location of the Vernadsky Station (Shpyg et al. 2024). For the case of an intense atmospheric river with a related extreme warm event and record-high surface melt, which occurred in February 2022 over the Antarctic Peninsula,

the maximum daily extent of melt was calculated using the accumulated snowmelt (Gorodetskaya et al. 2023). However, research on snowmelt processes using the Vernadsky weather station data was not conducted. At the same time, many researchers use information from the Vernadsky Station on meteorological parameters, including snow cover, to study general trends on both the Antarctic Peninsula and Antarctica (Liston, Winther 2005; Turner et al. 2020; Andres-Martin et al. 2024). Typically, snowmelt research is conducted using satellite data and reanalysis, which allows for spatial distribution and overcomes certain limitations of weather station data (Zhu et al. 2023; Ning et al. 2024). However, this approach overgeneralizes and simplifies the characteristics of snowmelt processes. Note that, as shown by Barrand et al. (2013) and Ning et al. (2024), regional climate models frequently struggle to resolve localized surface melt in regions with highly complex terrain. This problem is characteristic of both the Antarctic Peninsula and Galindez Island, where Vernadsky Station is located. As noted by Kaplan Pastíriková et al. (2025), the use of reanalysis data may lead to unrealistic results for snow depth compared to ground-based data. Therefore, ground-based observations are important, reliable sources of information.

The objective of this paper is to determine snow melting characteristics from the Vernadsky weather station data and to analyze the results. In accordance with it, the following tasks were undertaken.

1. Analysis of observational data for determining snowmelt characteristics.
2. Creating complex graphs to determine the snow cover characteristics.
3. Determining the dates of initial snow accumulation, the maximum snow depth, initial and final snow melting, and also the snow depth for these dates.
4. Determining near-surface air temperature during the snowmelt period.
5. Calculation of snow melting characteristics.
6. Analysis of the results.

2. Data and methodology

The Vernadsky Station is located off the western coast of the Antarctic Peninsula on Galindez Island, Argentine Islands Archipelago (Fig. 1). The climate of the Station is marine subantarctic, which is formed by large-scale circumpolar circulation in the atmosphere and ocean (King, Tuner 1997).

On the Antarctic Peninsula, including the Vernadsky Station, stable trends in surface air temperature increase are observed (Silva et al 2020; Turner et al. 2020; Khrystiuk et al. 2023).

In this research, we used the series of meteorological observations of near-surface air temperature and snow cover depth spanning nearly 28 years (1997-2025) from the Vernadsky Station. These data were obtained from the archive of the State Institution "National Antarctic Scientific Center" of the Ministry of Education and Science of Ukraine (NASC). These data are free to access. For 2011-2025, the data are posted on the website (http://meteodata.uac.gov.ua/), and for 1997-2010, the data can be obtained upon request (gorbachova@uhmi.org.ua). Near-surface air temperature (2 m) was recorded by automatic meteorological stations (AWS): MAWS (Modular Automatic Weather Station), Mobile Meteorological Complex "Troposphere" (this complex was developed and manufactured in Ukraine), and Vaisala AWS-

310. The data were collected every three hours at standard times (00, 03, 06, 09, 12, 15, 18, and 21 UTC). The daily data for snow cover depth is measured by two snow stakes, which are installed on the meteorological site of the Vernadsky Station. This system of observation better accounts for the snow cover changes due to the topography of Galindez Island and strong winds. Snow cover depth values are read from these snow stakes by a meteorologist at 13 UTC every day.

Fig. 1. Location of the Vernadsky Station (background graphic from Klok, Kornus 2021).

Unfortunately, at Vernadsky Station, snow courses and research on snow characteristics at different depths are not conducted systematically. The archive of the NASC has this information for 2012-2019 (Table 1). Its analysis shows that digging snow holes did not always occur during the season of snowmelt. This limits the use of these data, since for this research, data about the density of snow cover is needed precisely during the snowmelt season. Although it should be noted that the values of snow cover density during the snow accumulation and the snowmelt seasons do not show significant fluctuations (Table 1). The exception is snow cover density, which was 0.60 g/cm^3 as determined by data from November 5, 2018 on the dome of the Woozle Hill glacier. However, this value cannot be considered reliable, since it indicated that two of the snow layers had densities exceeding 1.0 g/cm^3. This is an erroneous value, because the maximum density of ice is only 0.92 g/cm^3 (Montero de Hijes et al. 2024). The lowest value of snow cover density was 0.32 g/cm^3 as determined by data from October 31, 2015. The highest value of snow cover density was 0.39 g/cm^3 as determined by data from November 22, 2012.

Determining snowmelt characteristics is possible using solar radiation observation data. This approach is widely used in various snowmelt models (Bartelt, Lehning 2002; Corona et al. 2015; Chen et al. 2020; Keenan et al. 2021). Due to the financial and technical difficulties that occurred in Ukraine in the late 20th

and first two decades of the 21st century, it took years to replace expensive meteorological equipment (which had broken down) designed to measure the characteristics of solar radiation and radiation balance. Only the data series of sunlight duration were and remain continuous. The use of models requires quantitative values for the solar radiation reaching the Earth's surface. Obtaining that data became possible only in February 2019, with the installation of the Vaisala AWS-310 automatic meteorological station at the Vernadsky Station, and the configuration of the corresponding modules in 2020. With these considerations, simulating snowmelt processes using modern models is impossible for 1997-2025. Therefore, research on snowmelt processes was carried out by calculating their characteristics based on daily observation data for the snow depth and near-surface air temperature (2-m height) for 1997-2025. Characteristics such as the duration, amount, and intensity of snow melting were determined.

Table 1. Results of research on snow and ice holes on Galindez Island in the Antarctic from the Vernadsky Station.

Snowmelt period	Location	Date	Snow depth (cm)	Snow density* (g/cm^3)	Note
2012-2013	The dome of the Woozle Hill glacier	22.11.2012	105	0.39	Snowmelt period was 26.11.2012 to 16.02.2013. Snow depth observations were discontinued 15.01.2013.
2013-2014	-//-	22.11.2013	76	0.35	Snowmelt period was from 12.12.2013 to 17.02.2014. Snow depth observations were discontinued 31.12.2014.
2015-2016	The Vernadsky weather station	31.10.2015	142	0.32	Snowmelt period was from 09.12.2015 to 03.02.2016.
2017-2018	The dome of the Woozle Hill glacier	27.05.2017	32	0.33	Snowmelt period was from 10.12.2017 to 29.01.2018.
	-//-	24.06.2017	33	0.35	
	-//-	25.07.2017	37	0.38	
	-//-	29.08.2017	40	0.34	
	-//-	26.10.2017	66	0.37	
2018-2019	-//-	05.11.2018	85	0.60	Snowmelt period was from 09.12.2018 to 03.02.2019. Two of the snow layers have a density exceeding 1.0 g/cm^3!

Note: * – the mean snow cover density from all snow layers in the holes.

The duration of the snowmelt season was defined as the number of days from the beginning of the snowmelt process to its completion. The amount of snow melting was calculated as the difference in snow depth at the beginning and end of the melting season. Complex graphs were used to determine initial snow accumulation dates, as well as the dates of the beginning and end of snowmelt; an example is shown in Figure 2.

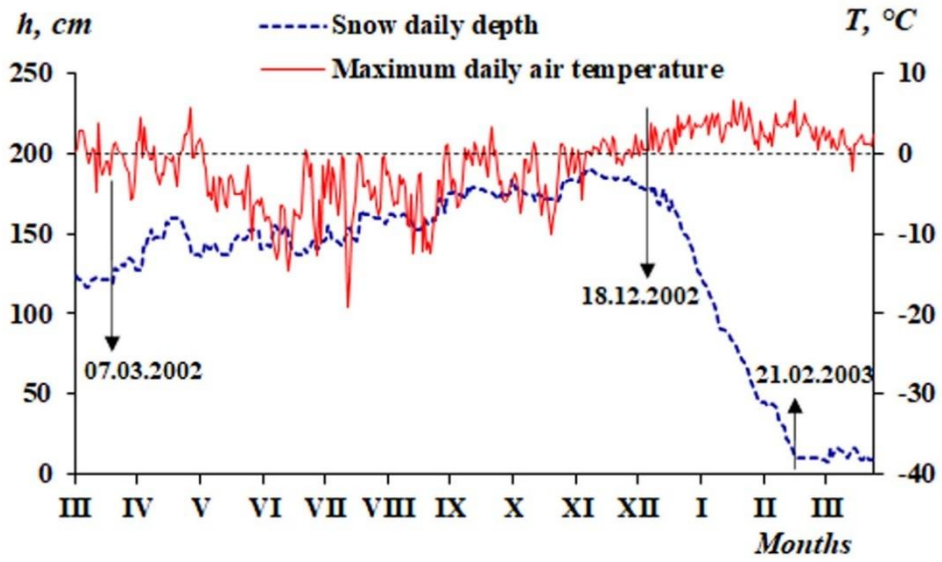

Fig. 2. Example graph for determining snow cover characteristics (representing 2002-2003 at Vernadsky Station); 07.03.2002 is the initial date of snow accumulation; 18.12.2002 is the initial date of snow melting; 21.02.2003 is the final date of snow melting.

The beginning of the snowmelt period was determined from the date when there was a stable transition of the maximum daily air temperature through zero to positive air temperatures. The final date of snowmelt was taken as the date of complete clearing of the surface from snow cover, or the date when the snowmelt process stopped, but some snow cover remained. The intensity of snow melting (I, cm/day) was determined by the formula (Anderson 1968):

$$I = L/D \quad (1)$$

where: L is the amount of snow melting (cm); D is the duration of the melting season (day).

Given that data on snow cover density are available only for the period 2012-2019 (Table 1), the determination of snowmelt intensity in water equivalent for the entire research period was carried out as follows. Information from Table 1 was used for the seasons of thawing in which measurements were made in the research snow and ice holes. The data for the snowmelt season 2018-2019 were unreliable, and thus not used. For the snowmelt season 2017-2018, the snow cover density value determined according to data from 26.10.2017 was used. For other snowmelt seasons, the mean snow cover density value for the period 2012-2018 is used, which is 0.36 g/cm^3.

The intensity of snowmelt in water equivalent (I_w, mm) was calculated by the formula (Anderson 1968):

$$I_w = 10 \cdot I \cdot P \quad (2)$$

where P is the weighted-average snow density (g/cm^3).

The multi-year mean values of snow cover characteristics were calculated as the arithmetic mean of a series. The standard error of multi-annual mean value (SEM) was calculated by the formula (Wilks 2020):

$$SEM = \pm\sigma/\sqrt{n} \quad (3)$$

where σ is the standard deviation; n is the number of observations.

3. Results

According to complex graphs (example in Fig. 2), the dates of initial snow accumulation, the maximum snow depth, the snow melting beginning and end (Fig. 3), and the snow depth were determined (Fig. 4). During the observation period 1997-2025, the mean snow accumulation beginning date is March 29 (±3 days). The earliest initial snow accumulation occurred on 24.02.2015, and the latest occurred on 01.05.2020. Typically, the increase in snow depth occurred before the beginning of snowmelt. During the observation period 1997-2025, only in 24% of cases did the new snow cover form on a surface free from last year's snow, while in most years new snow accumulation occurred on top of the remnants of snow cover from the previous season.

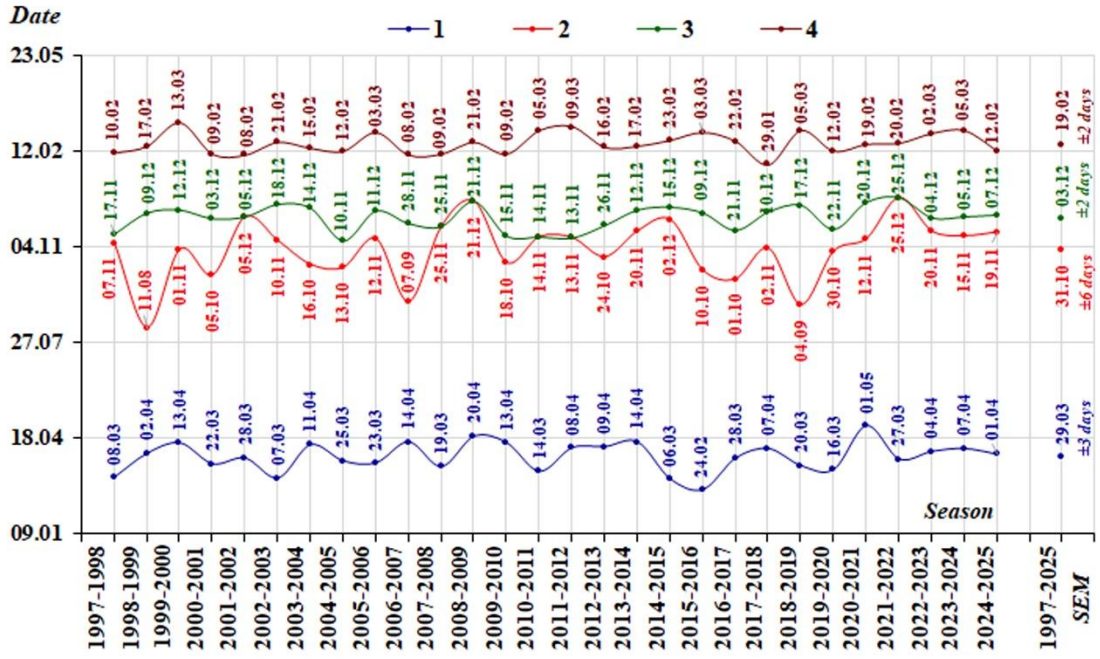

Fig. 3. Dates of initial snow accumulation. (1) the maximum snow depth, (2) the beginning, (3) and end (4) of snow melting at the Vernadsky Station for 1997-2025.

In particular, at the beginning of April 2022, the remnants of last year's snow cover reached 138 cm (Fig. 4). The multi-annual mean date of maximum snow depth is October 31 (±6 days), and the multi-annual mean maximum snow depth is 211 (±9) cm. The greatest snow depth was observed from the second decade of August to the end of December, and notably on November 20, 2022, it was 350 cm. The lowest snow depth was 134 cm, observed on 18.10.2009 (Fig. 3, 4).

Analysis of initial snow accumulation dates shows that the earliest date is 10.11.2004, and the latest is 25.12.2021. The earliest date of final snow melting is 29.01.2018, and the latest is March 12.03.2000. In summary, snow melting began between the first half of November and the end of December, continuing until the end of January to early March (Fig. 3). The multi-annual mean date of initial snowmelt is December 3 (±2 days), and its end is February 19 (±2 days). Initially, snow melting occurred under the influence of positive air temperatures during the daytime, and later the intensity of melting increased due to the transition of the mean daily air temperature through 0°C, when melting occurred throughout the day.

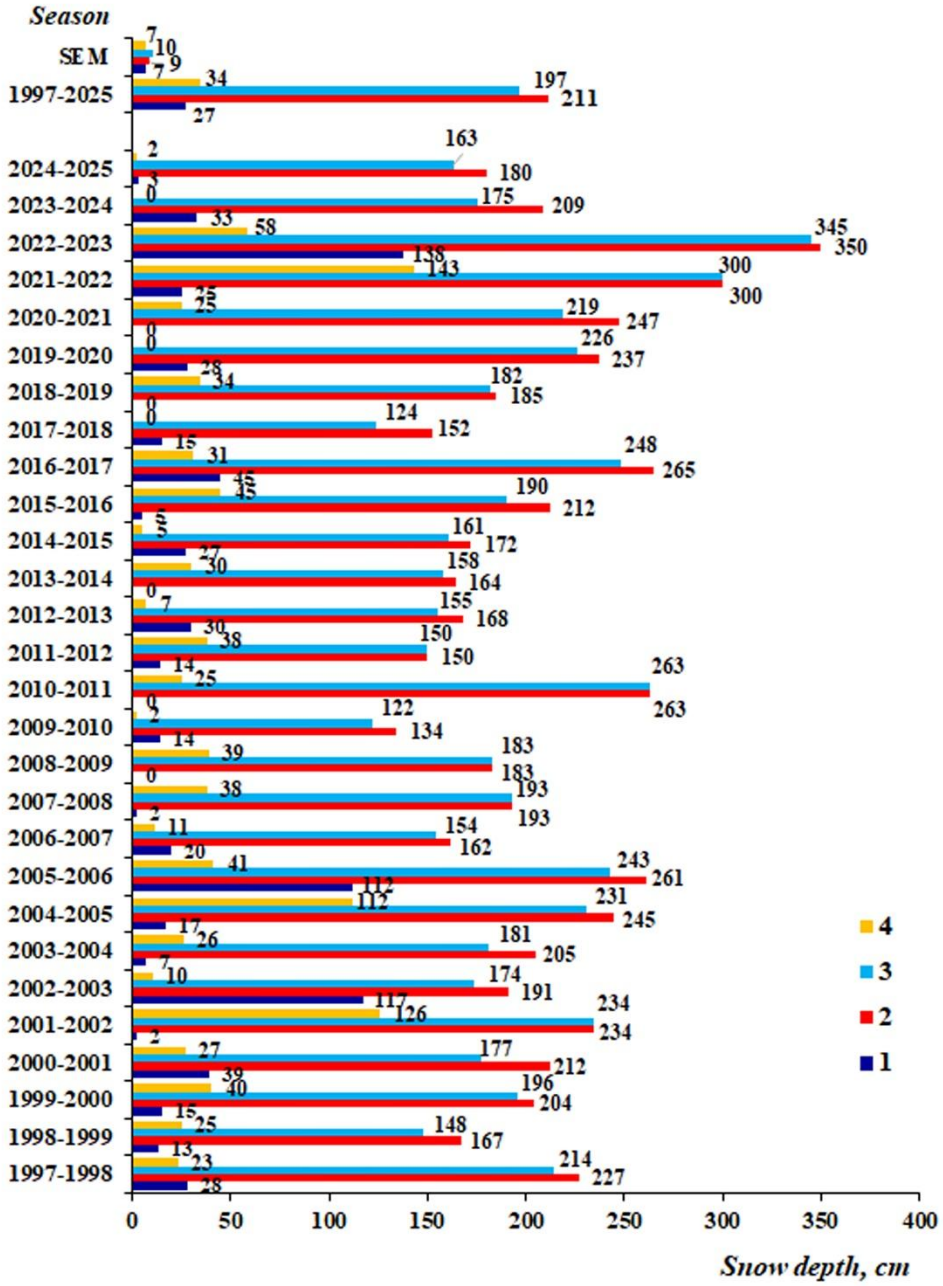

Fig. 4. Snow depth at the Vernadsky Station for 1997-2025 (1– initial accumulation; 2 – maximum value; 3 – initial melting; 4 – final melting).

The results (Figs. 3 and 4) supported calculation of the duration, amount, and mean intensity of snowmelt for 1997-2025 (Table 2). The mean intensity of snowmelt (cm/day) was calculated by formula (1).

Table 2. Characteristics of snowmelt and near-surface air temperature at the Vernadsky Station for 1997-2025.

Snowmelt season	Snowmelt duration (day)	Amount of snow melting (cm)	Mean intensity of snowmelt		Mean air temperature during the snowmelt season (°C)		
			cm/day	mm/day	minimal	maximum	mean daily
1997-1998	85	191	2.25	8.09	–0.2	2.2	0.8
1998-1999	70	123	1.76	6.33	–0.4	1.9	0.6
1999-2000	92	156	1.70	6.10	–0.9	1.1	0.0
2000-2001	68	150	2.21	7.94	0.8	3.1	1.8
2001-2002	65	108	1.66	5.98	–1.0	2.1	0.4
2002-2003	65	164	2.52	9.08	0.8	3.3	1.8
2003-2004	63	155	2.46	8.86	0.1	3.1	1.5
2004-2005	94	119	1.27	4.56	–1.5	1.6	–0.1
2005-2006	82	202	2.46	8.86	–0.1	2.6	1.1
2006-2007	72	143	1.99	7.15	0.4	2.9	1.5
2007-2008	76	155	2.04	7.34	–0.7	1.6	0.3
2008-2009	62	144	2.32	8.36	0.1	2.5	1.2
2009-2010	86	120	1.40	5.02	0.3	2.9	1.5
2010-2011	111	238	2.14	7.72	–0.5	2.8	1.0
2011-2012	117	112	0.96	3.45	–1.2	1.6	0.1
2012-2013	82	148	1.80	7.04*	–0.2	2.3	0.9
2013-2014	67	128	1.91	6.69*	–0.9	1.8	0.3
2014-2015	70	156	2.23	8.02	–0.4	1.6	0.5
2015-2016	85	145	1.71	5.46*	–0.9	1.4	0.1
2016-2017	93	217	2.33	8.40	–0.7	2.0	0.6
2017-2018	50	124	2.48	9.18*	–0.4	2.0	0.7
2018-2019	78	148	1.90	6.83	–1.3	1.9	0.1
2019-2020	82	226	2.76	9.92	–0.4	2.2	0.8
2020-2021	61	194	3.18	11.4	–0.1	2.3	1.0
2021-2022	57	157	2.75	9.92	–0.7	1.8	0.4
2022-2023	88	287	3.26	11.7	0.2	2.4	1.2
2023-2024	91	175	1.92	6.92	0.2	2.3	1.1
2024-2025	67	161	2.40	8.65	–0.2	2.2	0.9
Mean for the period	78	162	2.13	7.68	–0.4	2.2	0.8
SEM	±3	±8	±0.10	±0.36	±0.1	±0.1	±0.1

Note: * – calculated using the snow cover density values from Table 1 for the snowmelt seasons in which measurements were made of the snow layers in the research holes.

The multi-annual mean duration of snowmelt is 78 (±3) days. Depending on the air temperature regime during the snowmelt season, its duration ranged from 50 to 117 days. The amount of snow melting ranged from 108-287 cm, with a multi-annual mean of 162 (±8) cm. The mean intensity of snowmelt ranged from 0.96 to 3.26 cm/day. The lowest melting intensity (0.96 cm/day) was observed in the snowmelt season of 2011-2012, which was characterized by the longest duration (117 days), as well as relatively low air

temperatures. In addition, during the season of 2011-2012, a temporary slowdown in snowmelt during the return of cold weather, as well as snowfall, was observed. The highest melting intensity (3.26 cm/day) was observed in the snowmelt season of 2022-2023, which was characterized by the highest snow depth (350 cm) (Fig. 4) and the largest amount of snow melting (287 cm), as well as relatively high air temperatures. The multi-annual mean of snowmelt intensity is 2.13 (±0.10) cm/day.

For the period 1997-2025, the intensity of snowmelt in water equivalent was calculated by the formula (2) using data on snow cover density from Table 1. In calculations for the seasons in which snow density was not measured, the mean snow density for the period 2012-2018 was used. The intensity of snowmelt in water equivalent ranged from 3.45 to 1.7 mm/day; the multi-annual mean was 7.68 (±0.36) mm/day.

4. Discussion

Based on ground observations over a long period, the amount, duration, and mean intensity of snowmelt at the Vernadsky Station were determined for the first time, supplying new knowledge of these characteristics. The approximation of the intensity of snowmelt in water equivalent is also the first reliable knowledge of this variable. The results allow us to assess the reliability of snowmelt characteristics obtained using other methods. Luis et al. (2022) used Scatterometer-based backscatter data and showed that on the Antarctic Peninsula, the mean snowmelt duration was 70 days during 2000-2018. This result is in good agreement with the calculations given in Table 2 for the Vernadsky Station; specifically, the mean snowmelt duration was 78 days. Zhu et al. (2023), using SAR images, showed that from 2015 to 2021, the extent and duration of snowmelt have been increasing in the Antarctic Peninsula. Therefore, the next step of the research is to determine the trends in snowmelt characteristics, which are given in Table 2, as well as their comparison with trends obtained by other methods.

We emphasize that separate data about snow density are not sufficient either for understanding its formation or for use in any modeling of snowmelt processes. The results of this study yield only approximate knowledge about the processes and values of snowmelt at Vernadsky Station. The situation can only be improved by organizing systematic observations from snow holes.

5. Conclusions

Typically, in Antarctica, snowmelt studies are conducted using satellite data and reanalysis, which conveys the spatial distribution of snowmelt characteristics and eliminates certain limitations of ground-based observations. However, remote approaches still have difficulties in determining snowmelt values in regions with complex terrain, typical of Galindez Island, where the Vernadsky Station is located. Ground-based observations remain an important and reliable source of information. In this article, the characteristics of snow cover melting were determined based on observations of snow depth and air temperature (at 2-m height) at the Vernadsky Station for 1997-2025.

The multi-annual mean initial snow accumulation date is March 29 (±3 days). The multi-annual mean date of maximum snow depth is October 31 (±6 days), and the multi-annual mean maximum snow depth is

211 (±9) cm. The multi-annual mean date of initial snowmelt is December 3 (±2 days), and its end is February 19 (±2 days). The duration of snowmelt ranged from 50 to 117 days; the multi-annual mean was 78 (±3) days. The amount of snow melting ranged from 108-287 cm, with a multi-annual mean of 162 (±8) cm. The mean intensity of snowmelt ranged from 0.96 to 3.26 cm/day, in water equivalent approximately 3.45 to 11.7 mm/day; the multi-annual mean was 7.68 (±0.36) mm/day.

At Vernadsky Station, observations of snow cover density need to be improved. Further, the results obtained in this research represent the first knowledge about snowmelt characteristics at the Vernadsky Station. The approach used in our article, despite its apparent simplicity, ensures the reliability of the conclusions, as it uses ground-based observation data. These results can be used in other investigations, for example, for the comparison and generalization of snowmelt processes on the Antarctic Peninsula, etc.

Acknowledgment

The investigation was conducted within project № H/11-2024 from 23.08.2024 "Relations between parameters of solar radiation, snow cover and surface near Akademik Vernadsky Station" that was funded by the State Institution "National Antarctic Scientific Center" of the Ministry of Education and Science of Ukraine.

References

Anderson E.A., 1968, Development and testing of snow pack energy balance equations, Water Resources Research, 4 (1), 19-37, DOI: 10.1029/WR004i001p00019.

Andres-Martin M., Azorin-Molina C., Serrano E., González-Herrero S., Guijarro J.A., Bedoya-Valestt S., Utrabo-Carazo E., Serrano V.S.M., 2024, Near-surface wind speed trends and variability over the northern Antarctic Peninsula, 1979-2022, Atmospheric Research, 309, 107568, DOI: 10.1016/j.atmosres.2024.107568.

Banwell A.F., Datta R.T., Dell R.L., Moussavi M., Brucker L., Picard G., Shuman C.A., Stevens L.A., 2021, The 32-year record-high surface melt in 2019/2020 on the northern George VI Ice Shelf, Antarctic Peninsula, The Cryosphere, 15 (2), 909-925, DOI: 10.5194/tc-15-909-2021.

Barrand N.E., Vaughan D.G., Steiner N., Tedesco M., Kuipers Munneke P., Van den Broeke M.R., Hosking J.S., 2013, Trends in Antarctic Peninsula surface melting conditions from observations and regional climate modeling, Journal of Geophysical Research: Earth Surface, 118 (1), 315-330, DOI: 10.1029/2012JF002559.

Bartelt P., Lehning M., 2002, A physical SNOWPACK model for the Swiss avalanche warning: Part I: numerical model, Cold Regions Science and Technology, 35 (3), 123-145, DOI: 10.1016/S0165-232X(02)00074-5.

Bell R.E., Banwell A.F., Trusel L.D., Kingslake J., 2018, Antarctic surface hydrology and impacts on ice-sheet mass balance, Nature Climate Change, 8, 1044-1052, DOI: 10.1038/s41558-018-0326-3.

Belokrinitskaya L.M., Grischenko V.F., Ivchenko V.N., Klock S.V., Kruchenitsky G.M., 2006, Long-term and seasonal variability of snow blanket thickness at the Galindez glacier, (in Russian), Ukrainian Antarctic Journal, 4-5, 295-300, DOI: 10.33275/1727-7485.4-5.2006.557.

Chen T., Pan J., Chang S., Xiong C., Shi J., Liu M., Tao Che T., Lifu Wang L., Liu H., 2020, Validation of the SNTHERM model applied for snow depth, grain size, and brightness temperature simulation at meteorological stations in China, Remote Sensing, 12 (3), DOI: 10.3390/rs12030507.

Corona J.A.I., Muñoz J., Lakhankar T., Romanov P., Khanbilvardi R., 2015, Evaluation of the Snow Thermal Model (SNTHERM) through continuous in situ observations of snow's physical properties at the CREST-SAFE field experiment, Geosciences, 5 (4), 310-333, DOI: 10.3390/geosciences5040310.

Govorukha L.S., 1997a, Brief geographical and glaciological characteristics of Argentine Islands archipelago, (in Russian), Bulletin of Ukrainian Antarctic Center, 1, 17-19.

Govorukha L.S., 1997b, Glaciological research on Galindez Island, (in Russian), Bulletin of Ukrainian Antarctic Center, 1, 67-76.

Gorodetskaya I.V., Durán-Alarcón C., González-Herrero S., Clem K.R., Zou X., Rowe P., Imazio P.R., Campos D., Leroy-Dos Santos C., Dutrievoz N., Wille J.D., Chyhareva A., Favier V., Blanchet J., Pohl B., Cordero R.R., Park S.-J., Colwell S., Lazzara M.A., Carrasco J., Gulisano A.M., Krakovska S., Ralph F.M., Dethinne T., Picard G., 2023, Record-high Antarctic Peninsula temperatures and surface melt in February 2022: a compound event with an intense atmospheric river, NPJ Climate and Atmospheric Science, 6, 202, DOI: 10.1038/s41612-023-00529-6.

Grischenko V.F., Timofeyev V.E., Klock S.V., 2005, Impacts of components of glaciosphere to climate change at the Antarctic Penisnula region, (in Russian), Ukrainian Antarctic Journal, 3, 99-107, DOI: 10.33275/1727-7485.3.2005.574.

Holko L., Gorbachova L., Kostka Z., 2011, Snow hydrology in Central Europe, Geography Compass, 5 (4), 154-218, DOI: 10.1111/j.1749-8198.2011.00412.x.

Kaplan Pastíriková L., Hrbáček F., Matějka M., 2025, Validation of ERA5-Land-based reconstructed air temperature and near-surface ground temperature on James Ross Island, Polar Geography, 48 (2), DOI: 10.1080/1088937X.2024.2434744.

Keenan E., Wever N., Dattler M., Lenaerts J.T.M., Medley B., Kuipers Munneke P., Reijmer C., 2021, Physics-based SNOWPACK model improves representation of near-surface Antarctic snow and firn density, The Cryosphere, 15 (2), 1065-1085, DOI: 10.5194/tc-15-1065-2021.

Khrystiuk B., Gorbachova L., Shpyg V., Pishniak D., 2023, Changes in extreme temperature indices at the Ukrainian Antarctic Akademik Vernadsky station, 1951-2020, Meteorology Hydrology and Water Management, 10 (1), 95-106, DOI: 10.26491/mhwm/150883.

King J.C., Turner J., 1997, Antarctic meteorology and climatology, Cambridge University Press, DOI: 10.1017/CBO9780511524967.

Klok S., 2016, Analysis of the major Formation Dates and selected characteristics of the snow cover at the region of the Ukrainian Antarctic base Academic Vernadsky, (in Russian), Ukrainian Antarctic Journal, 15, 35-40, DOI: 10.33275/1727-7485.15.2016.90.

Klok S.V., Afteniuk A.A., 2017, Features of stratigraphy and dynamics of the snow thickness in the region of Ukrainian Antarctic Station "Academic Vernadsky", Book of Abstract of the VIII International Antarctic Conference, Kyiv, 16-18 May, 2017, 151.

Klok S.V., Kornus A.O., 2021, Intra-annual and long-periodic components in the changes of precipitation over the Antarctic Peninsula and their possible causes, Journal of Geology, Geography and Geoecology, 30 (3), 490-490, DOI: 10.15421/112144.

Klok S.V., Kornus A.O., Kornus O.H., 2021, The components of seasonal variability of the snow depth in the area of the Ukrainian Antarctic Akademik Vernadsky Station, Book of Abstract of the X International Antarctic Conference, Kyiv, 11-13 May, 2021, 89-90, available online at http://uac.gov.ua/wp-content/uploads/2021/05/Abstracts-X-IAC-2021.pdf, (data access 25.10.2025).

Liston G.E., Winther J-G., 2005, Antarctic surface and subsurface snow and ice melt fluxes, Journal of Climate, 18 (10), 1469-1481, DOI: 10.1175/JCLI3344.1.

Luis A.J., Alam M., Jawak S.D., 2022, Spatiotemporal change analysis for snowmelt over the Antarctic ice shelves using scatterometers, Frontiers in Remote Sens, 3, DOI: 10.3389/frsen.2022.953733.

Marks D., Kimball J., Tingey D., Link T., 1998, The sensitivity of snowmelt processes to climate conditions and forest cover during rain-on-snow: A case study of the 1996 Pacific Northwest flood, Hydrological Processes, 12 (10-11), 1569-1587, DOI: 10.1002/(SICI)1099-1085(199808/09)12:10/11<1569::AID-HYP682>3.0.CO;2-L.

Montero de Hijes P., Dellago C., Jinnouchi R., Kresse G., 2024, Density isobar of water and melting temperature of ice: Assessing common density functionals, The Journal of Chemical Physics, 161 (13), DOI: 10.1063/5.0227514.

Nagler T., Rott H., Ripper E., Bippus G., Hetzenecker M., 2016, Advancements for snowmelt monitoring by means of Sentinel-1 SAR, Remote Sens, 8 (4), DOI: 10.3390/rs8040348.

Ning W., Wang Y., Zhang W., Zhou M., 2024, What recent global atmospheric reanalyses and regional climate models can represent observed snow accumulation on Antarctica? Atmospheric Research, 300, DOI: 10.1016/j.atmosres.2024.107260.

Shpyg V., Shchehlov O., Pishniak D., 2024, Snow cover at the Akademik Vernadsky station: response on wind, temperature and precipitation variations, Ukrainian Antarctic Journal, 22 (1), 6-23, DOI: 10.33275/1727-7485.1.2024.724.

Silva A.B., Arigony-Neto J., Braun M.H., Espinoza J.M.A., Costi J., Jaña R., 2020, Spatial and temporal analysis of changes in the glaciers of the Antarctic Peninsula, Global and Planetary Change, 184, DOI: 10.1016/j.gloplacha.2019.103079.

Thapa S., Zhao Z., Li B., Lu L., Fu D., Shi X., Tang B., Qi H., 2020, Snowmelt-driven streamflow prediction using machine learning techniques (LSTM, NARX, GPR, and SVR), Water, 12 (6), 1734, DOI: 10.3390/w12061734.

Turner J., Marshall G.J., Colwell S., Phillips T., Lu H., 2020, Antarctic temperature variability and change from station data, International Journal of Climatology, 40 (6), 2986-3007, DOI: 10.1002/joc.6378.

Tymofeyev V.E., Grishchenko V.F., 2010, Regional changes of climate and atmospheric circulation and balanse of mass of small glacier at Galindez Island, (in Russian), Ukrainian Antarctic Journal, 9, 249-262, DOI: 10.33275/1727-7485.9.2010.412.

Tymofeyev V.E., Mazepa O.V., Tatarchuk O.G., 2021, Current state of glacioclimate at the North Antarctic Peninsula, Book of Abstracts of the X International Antarctic Conference, Kyiv, 11-13 May, 2021, 88-89, available online at http://uac.gov.ua/wp-content/uploads/2021/05/Abstracts-X-IAC-2021.pdf, (data access 25.10.2025).

Vafakhah M., Sedighi F., Javadi M.R., 2014, Modeling the rainfall-runoff data in snow-affected watershed, International Journal of Computer and Electrical Engineering, 6, 40-43.

Wilks D.S., 2020, Statistical Methods in the Atmospheric Sciences, Fourth Edition, Elsevier, DOI: 10.1016/C2017-0-03921-6.

WMO, 2009, Guide to hydrological practices, Volume II: Management of water resources and application of hydrological practices, 6th ed., WMO-No. 168, World Meteorological Organization, Geneva.

Zhou G., Cui M., Wan J., Zhang S., 2021, A Review on snowmelt models: progress and prospect, Sustainability, 13, 11485, DOI: 10.3390/su132011485.

Zhu Q., Guo H., Zhang L., Liang D., Liu X., Zhou H., Gou Y., 2023, High-resolution spatio-temporal analysis of snowmelt over Antarctic Peninsula ice shelves from 2015 to 2021 using SAR images, International Journal of Digital Earth, 16 (1), 825-846, DOI: 10.1080/17538947.2023.2181991.


METEOROLOGY HYDROLOGY
AND WATER MANAGEMENT
IMGW-PIB Science Journal since 2013